Development and Calibration of Cyclic Loading Models for Monopile Foundations in Clays

Toby D. Balaam

Wolfson College

University of Oxford

A thesis submitted for the degree of

Doctor of Philosophy

Trinity 2020

Development and Calibration of Cyclic Loading Models for Monopile Foundations in Clays

Toby D. Balaam

Wolfson College, University of Oxford

A thesis submitted for the degree of Doctor of Philosophy

Trinity 2020

Monopiles are currently the most common foundation for offshore wind turbines. Recent research, such as in the PISA project, have produced new design methods for calculating the ultimate monotonic capacity of monopiles under lateral loading, leading to more efficient designs. However, monopiles are also subject to cyclic lateral loading from wind and waves. This aspect is not yet properly understood or accounted for in design. Better understanding of the cyclic response is important for both serviceability and fatigue design considerations, as cyclic loading can cause permanent foundation rotation, as well as changes to the stiffness and energy dissipation response.

A new approach to modelling of cyclic loading, 'Hyperplastic Accelerated Ratcheting Model' (HARM), can capture pile response to cyclic lateral loading on a cycle-by-cycle basis for many cycles. Previous research demonstrates that this approach to modelling compares well to experimental data at a macro-scale, such as the full pile moment-rotation response. However, for design, it would be more appropriate for calibration parameters to be developed for site-specific conditions from laboratory element tests. To facilitate this approach, a database of cyclic laboratory tests in fine-grained soils has been acquired from the literature and private communication. Results of the tests are summarised to establish important features of behaviour and inform the formulation of a 0D, multi-surface, kinematic-hardening, rate-dependent, hyperplasticity model in total stress space which is calibrated to each data set.

The model is then applied to more complex cases. Firstly it is used to generate synthetic contour diagrams, well used by the industry, to demonstrate prediction of the development of strain across the full constant-amplitude cyclic stress space. Secondly it is used to predict more realistic, multi-amplitude, element tests undertaken at the Norwegian Geotechnical Institute. Both these exercises serve as tests of the underlying mechanisms of the model.

At monopile scale, the PISA project resulted in an extended Winkler model with monotonic reaction curves along the length and at the base of the pile; this approach is subsequently extended to incorporate a total stress, 0D hyperplasticity model in place of each reaction curve. The resulting 1D model is capable of predicting the cyclic response along the pile length, including ratcheting. Cyclic tests at Cowden are modelled, with parameters compared to those at element level to investigate the potential mapping of response at different levels of detail. By exploring mobilisation of lateral pressure down the pile for typical operational loading, an element-testing regime is proposed to better reflect the realistic conditions around the pile.

The 0D total-stress model predicts the shear behaviour for fine-grained soils well. However, the possible effects of effective stress changes are modelled by softening of the yield surfaces in the total stress model. A better approach would be to capture realistically effective stress changes due to cyclic loading. A preliminary extension of the 0D model to capture effective stresses, based on Modified Cam-Clay, is presented at development stage.

Acknowledgements

This work was supported by grant EP/L016303/1 for Cranfield University and the University of Oxford, Centre for Doctoral Training in Renewable Energy Marine Structures - REMS (http://www.rems-cdt.ac.uk/) from the UK Engineering and Physical Sciences Research Council (EPSRC).

Firstly, I am deeply grateful to my supervisors, Guy Houlsby and Byron Byrne for their invaluable advice and continuous support. Their enthusiasm was a constant source of encouragement throughout.

Being part of the Civil Engineering Group at Oxford has been a pleasure and I am grateful for the opportunity to spend time with so many inspiring people. In particular, I would like to thank Iona Richards for the many valuable discussions and and Christelle Abadie, who gave up much of her time to help with explanations and advice during the early stages of this project. I would also like to thank friends from the Jenkin Building and the REMS group for making the experience so enjoyable.

I am grateful to many at NGI (Norwegian Geotechnical Institute) for facilitating a short but extremely productive visit in 2019. Thanks to Ana Page for investing in making the trip so enjoyable and for the interesting discussions alongside Hans Peter Jostad, Knut Andersen and Kristoffer Skau. For the provision of data which facilitated much of the work, I would like to acknowledge the financial support by the Norwegian Research Council and the industrial partners Equinor, Innogy, EDF, Vattenfall and Multiconsult through the project Wave loads And Soil support for eXtra Large monopiles (WAS-XL), Grant No. 268182.

I am also grateful to Kris Wessel Andersen and Amin Aghakouchak of Ørsted for taking such a keen interest in my work early on and providing invaluable data which aided my understanding immensely.

Outside of Engineering, I am thankful to the many friends I made during my time in such a great city; those of the Wolfson football team, Share Oxford and elsewhere.

I thank my family for all the support over the years, particularly during the final push. Last but not least, Sophie, thank you for everything you do.

Contents

Nomenclature

Variables - Greek alphabet

α	Internal variables (hyperplasticity) Empirical rate of strength increase with strain rate (rate-dependency)
$\alpha_k, \alpha_\eta, \alpha_R$	Experimental power-law exponent: stiffness, energy loss factor, ratcheting
β	Hardening parameter (hyperplasticity)
χ	Generalised stress (hyperplasticity)
η	Energy loss factor (cycle definitions) Quality of fit metric Viscous constant (rate-dependency)
η_{10}	Logarithmic (base 10) viscous constant (rate-dependency)
η_I	Integrated Energy loss factor (proposed cycle definitions)
η_{sd}	Small displacement quality of fit
η_{ult}	Ultimate quality of fit
γ	Shear strain
κ, κ^*	Swelling line (linear-log,log-log) (MCC)
κ_{fac}	Factor on swelling line (MCC - multi-surface hyperplasticity)
κ_{ref}	Reference strength reduction (hyperplasticity)
λ, λ^*	Virgin consolidation line (linear-log,log-log) (MCC)
μ	Viscosity of surface (hyperplasticity - rate process theory)
ν	Poisson's ratio
Ω	Local weighting factor (MCC - multi-surface hyperplasticity)
$\overline{\chi}$	Dissipative generalised stress (hyperplasticity)
σ	General stress-type variable
σ_a	Axial stress in CU conditions
σ_e	Radial stress in CU conditions

$\sigma_{v,c}$	Normal consolidation stress in DSS conditions
σ_v	Normal stress in DSS conditions
τ	Shear stress
θ	Rotation of pile
ε	General strain-type variable
ε_a	Axial strain in triaxial conditions
ε_q	Deviatoric strain in triaxial conditions
ε_r	Radial strain in triaxial conditions
ε_v	Volumetric strain in triaxial conditions
ξ	Damping ratio
ζ_b	Load amplitude characterisation parameter
ζ_c	Load asymmetry characterisation parameter

Variables - Latin alphabet

ε_N	Mean strain at average load (proposed cycle definitions)
A	Area under monotonic curve
a	Curvature paramter for 'Jeanjean' function
A_k, A_η, A_R	Experimental power-law coefficient: stiffness, energy loss factor, ratcheting
A_u, A_0, A_e, A_n	Correction factors: initial stiffness, ultimate stress, ultimate strain, curvature (1D FE Model - PISA curves)
B_{Eff}	Experimental logarithmic coefficient: effective stress change
D	Diameter Stiffness Matrix (OxPile)
d	Dissipation function (hyperplasticity)
E_0	Initial stiffness (pile)
E_E	Maximum elastic energy (cycle definitions)
E_H	Loop area (cycle definitions)
E_t	Tangent stiffness with active surfaces (hyperplasticity - kinematic hardening)
f	Helmholtz free energy function (hyperplasticity)
f_0	First natural frequency
f_{1p},f_{3p}	Rotor frequency and blade passing frequency
$F_{\beta,G}$	Global softening development factor (hyperplasticity)

$F_{\beta,R}$	Ratcheting development factor (hyperplasticity - HARM)
F_{β}	Softening development factor (hyperplasticity)
F_{η}	Rate surface factor (hyperplasticity)
F_{κ}	Softening type factor (hyperplasticity)
F_{ext}	Vector of external forces (1D FE Model)
F_{int}	Vector of internal forces (1D FE Model)
G	Tangential stiffness (laboratory tests)
g	Gibbs free energy function (hyperplasticity)
g	Shear modulus number (MCC)
H	Horizontal load applied to pile Surface stiffness (hyperplasticity - kinematic hardening)
i	Surface Index (hyperplasticity)
I_p	Plasticity index
K	Surface strength (hyperplasticity - kinematic hardening)
k	Secant stiffness (general cycle definitions)
K_0	Co-efficient of earth pressure at rest
k_f	Secant stiffness (proposed cycle definitions)
L	Embedded length
M	Moment applied to pile
M	Slope of critical state line
m_{κ}	Softening exponent (hyperplasticity)
M_c,M_e	Slope of critical state line in compression or extension
m_r	Exponent of history dependency (hyperplasticity - HARM)
m_s	Exponent of stress dependency (hyperplasticity - HARM)
N	Specific volume at $p = 1kPa$ (MCC)
n	Number of cycles Curvature parameter for PISA function
N_f	Number of cycles to failure (or end)
N_{int}	Number of internal variables (hyperplasticity)
N_{max}	Maximum number of cycles applied
N_s	Number of surfaces (hyperplasticity)
N_y	Number of surfaces currently yielding (hyperplasticity)

OCR	Overconsolidation ratio
p	Mean pressure in triaxial conditions Horizontal pressure around pile
p_c	Mean effective stress at maximum of yield surface on isotropic axis (MCC)
p_x	Mean effective stress at centre of yield surface on isotropic axis(MCC)
q	Deviatoric Stress
R_0	Ratcheting constant (hyperplasticity - HARM)
R_{ref}	Reference ratcheting rate reduction (hyperplasticity - HARM)
S, E, T	Stress and strain switch matrices and rate array for general control (hyperplasticity - MCC)
s_u	Undrained shear strength (general)
$s_{u,c}$,$s_{u,e}$	Undrained shear strength CU compression and CU extension
$s_{u,DSS}$	Undrained shear strength in DSS conditions
T	Period of cyclic loading
t	Thickness Time Time constant (hyperplasticity - rate process theory)
T_u	Test time to failure (hyperplasticity - rate process theory)
u	Lateral displacement of pile
v	Lateral displacement (PISA) Specific volume
w	Flow potential function (hyperplasticity)
X_{ref}	Reference value of X which occurs at point of linear-log rate dependency (hyperplasticity - rate process theory)
y	Lateral displacement of pile (in p-y type methods) Yield function (hyperplasticity)
z	Depth below ground level

Other abbreviations

CD	Consolidated Drained Triaxial test
CO_2	Carbon Dioxide
CU	Consolidated Undrained Triaxial test
CU_{cyc}	Cyclic Consolidated Undrained Triaxial test
DSS	Direct Simple Shear test

DSS_{cyc}	Cyclic Direct Simple Shear test
API	American Petroleum Institute
CSL	Critical State Line
DNV-GL	Det Norske Veritas Germanischer Lloyd
FEA	Finite Element Analysis
FLS	Fatigue Limit State
HARM	Hyperplastic Accelerated Ratcheting Model
MCC	Modified Cam Clay
NC	Normally Consolidated
NCL	Normal Consolidation Line
NGI	Norwegian Geotechnical Institute
OC	Over-Consolidated
OWF	Offshore Wind Farm
OWT	Offshore Wind Turbine
PISA	Pile Soil Analysis
SI	Site Investigation
SLS	Serviceability Limit State
ULS	Ultimate Limit State
WAS-XL	Wave loads and soil support for extra-large monopiles

Subscripts, superscripts and diacritics

$\bar{X}$	Normalised value of X (1D FE Model)
ΔX	Accumulated value of X (related to monotonic)
$\dot{X}$	Rate (time derivative) of X
X'	Effective value of X (referring to stress)
X^*	Corected value of X (1D FE Model)
$X_{0.1D}$	Value of X at ground level pile displacement of 0.1D
X_0	Initial value of X
X_ψ	X corresponding to rotation (1D FE Model)
X_{av}, X_a	Average value of X
X_a	Value of X at average force on loading (cycle definitions)
X_{BB}	Value of X corresponding to monotonic (backbone) response
X_b	Value of X at average force on unloading (cycle definitions)

X_{cyc}, X_{cy}	Cyclic amplitude of X
X_c	Value of X after consolidation (element testing)
X_{diff}	Absolute difference between measured and predicted X
X_e	Value of X at extremum (cycle definitions)
X_G	Variable X at ground level
X_i	Value of X at corresponding surface index (hyperplasticity)
X_l	Value of X at minimum load on loading (cycle strain definitions) Value of X on loading (cycle definitions)
X_{max}	Maximum value of X
X_{meas}	Measured value of X
X_{min}	Minimum value of X
X_M	Value of X as an average of loading and unloading (cycle definitions)
X_{Ns}	Value of X at final surface (hyperplasticity)
X_n	Value of X at cycle n Value of X at most negative (previous cycle definitions)
$X_{p,0}$	Value of strain-type X after pre-cycling (NGI cyclic definitions)
X_{par}	X related to parallel kinematic hardening models (hyperplasticity)
X_{pred}	Predicted value of X
X_p	Value of X at peak (previous cycle definitions)
X_q	X corresponding to deviatoric strain (MCC)
X_{recal}	Recalibrated value of X (hyperplasticity - backbone recalibration)
X_R	Reference value of X (cycle definitions)
X_r	Value of X at reversal (cycle definitions)
X_{ser}	X related to series kinematic hardening models (hyperplasticity)
$X_{u,pc}$	Ultimate value of X post cycles
X_u	Ultimate value of X Value of X at minimum load on unloading (cycle definitions) Value of X on unloading (cycle definitions)
X_v	X corresponding to displacement (1D FE Model) X corresponding to volumetric strain (MCC)
$X_{x\to 0}$	Value as X as x tends to 0
X_y	Value of X at yield

Functions

$\langle X \rangle$	Macauley Brackets	$\begin{pmatrix} X \leq 0 \rightarrow \langle X \rangle = 0 \\ X > 0 \rightarrow \langle X \rangle = X \end{pmatrix}$
$\mathcal{H}(X)$	Modified Heaviside Function	$\begin{pmatrix} X < 0 \rightarrow \mathcal{H}(X) = 0 \\ X > 0 \rightarrow \mathcal{H}(X) = 1 \\ X = 0 \rightarrow 0 \leq \mathcal{H}(X) \leq 1 \end{pmatrix}$
$S(X)$	Modified Signum Function	$\begin{pmatrix} X < 0 \rightarrow S(X) = 1 \\ X > 0 \rightarrow S(X) = -1 \\ X = 0 \rightarrow -1 \leq S(X) \leq 1 \end{pmatrix}$

Chapter 1

Introduction

1.1 Context

Average atmospheric carbon dioxide levels are higher today than at any point in the past 800,000 years, amplifying the Earth's natural greenhouse effect and causing warming (Figure 1.1). In 2019, the mean annual temperature was nearly 1°C above the pre-industrial baseline (1850-1900), with 20 of the hottest years on record occurring in the preceding 21 years (WMO, 2019).

Long-term temperature increases are causing extreme weather, ocean acidification and sea level rise with wide-ranging impacts expected to have catastrophic effects (IPCC, 2014). This has led to global movements to reduce the extent of change, most notably the 'Paris Agreement' in which 196 countries pledged to reduce CO_2 emissions in order limit average temperature rise to below 2°C (United Nations, 2015). To meet this target, a key element will be a rapid, global transition from fossil fuels to renewable energy generation (IEA, 2015).

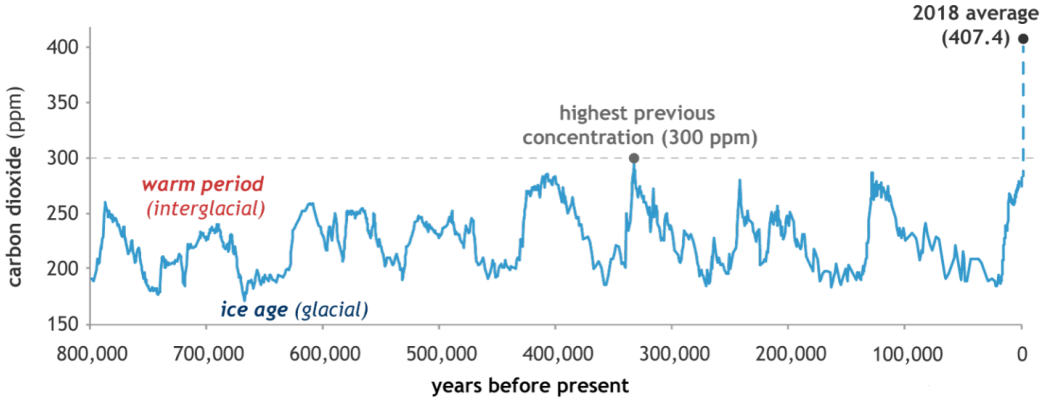

Figure 1.1: Global atmospheric carbon dioxide concentrations (CO_2) in parts per million (ppm) for the past 800,000 years, based upon ice core data (Lindsey, 2020)

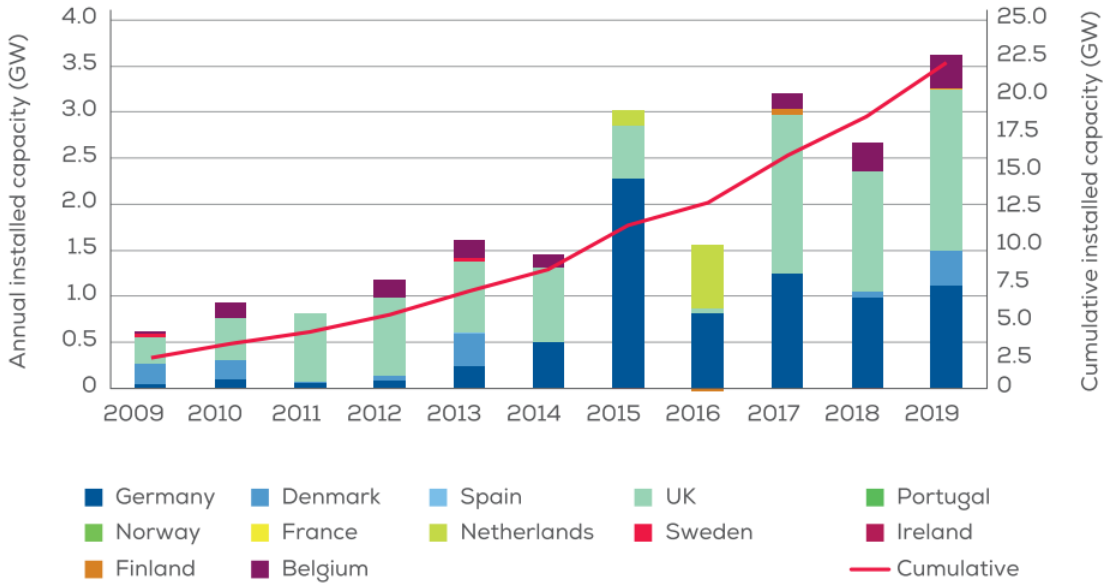

Figure 1.2: Annual offshore wind installations by country (left axis) and cumulative capacity (right axis) (Wind Europe, 2020a)

1.1.1 Offshore wind energy

In 2019 wind energy generated over 15% of the electricity demand in the EU, 10 years earlier this was less than 5%. Offshore production is increasing, accounting for roughly a quarter of newly installed capacity over the last three years (Wind Europe, 2020a; Wind Europe, 2020b). Offshore Wind Turbines (OWTs) benefit from higher wind yield, more reliable availability, a greater number of potential sites with fewer size limitations, and typically spark less opposition.

Concerns with cost and the challenging offshore environment are reducing as the industry gains experience. The cost of offshore wind is continuing to fall at rates far exceeding original targets, with recent winning bids for Doggerbank hitting £39.65 per megawatt-hour (Evans, 2019). Meanwhile, costs of conventional energy show little signs of falling. Combined with an increasing awareness of the need to protect our environment, the demand for offshore wind farms looks set to continue to rise (Figure 1.2). There are still, however, cost savings to be made.

1.1.2 Offshore wind turbine foundations

Foundations form a high proportion (up to 30% NREL, 2018) of the capital cost of an offshore wind farm. Figure 1.3 shows a range of possible support structure and

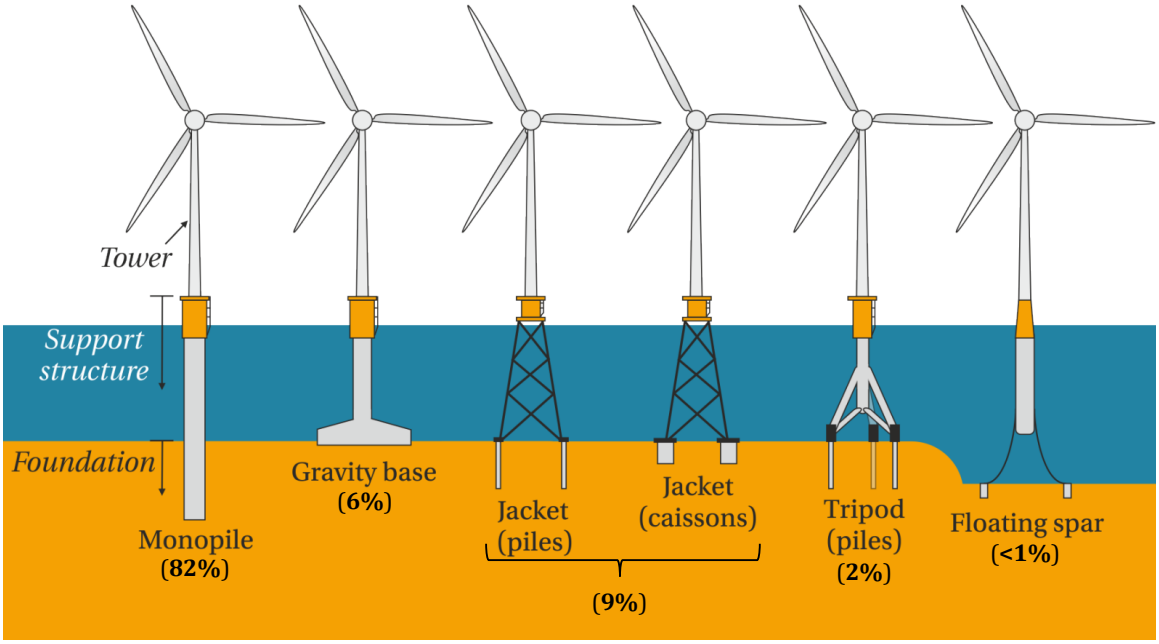

Figure 1.3: Possible support structures for OWTs. Figure edited from Richards (2020) with percentage share of grid-connected turbines in the EU, data from Wind Europe (2020a)

foundation choices alongside the percentage share of EU grid-connected turbines. Monopiles are by far the most prevalent, accounting for 82% of all installed substructures. Jacket structures remain a cost-effective solution at some sites (accounting for 29% of installed foundations in 2019); with suction caisson foundations offering the potential for quicker, quieter installation. Floating support structures, currently in development stage, have the opportunity to exploit sites with deeper water.

The popularity of monopiles is predominantly due to their suitability for mass fabrication, an established supply chain, applicability to most soil conditions and proven track record. However the size and cost of steel can be substantial. At the Gode Wind farm, 7.5m diameter, 100mm thick monopiles, weighing up to 1000 tonnes, were used to support 6MW turbines in up to 35m water depth (Schroeder et al., 2015). Such large piles result in expense in material and fabrication, but also in lengthy installation with expensive machinery. Thus, there is great focus within the industry to improve monopile design, to reduce costs and potentially extend the range of water depths in which they can be deployed.

In Europe, the majority (77%) of installed capacity is in the North Sea (Wind Europe, 2020a), where soil conditions range from stiff clays to dense sands, layered soils and bedrock (Anusic et al., 2016; Arany et al., 2016; Kallehave et al., 2015a).

New markets such as Taiwan bring new environmental challenges (extreme winds and earthquakes), differing soil conditions (silty, highly compressible soils, Leblanc Thilstead, 2019), and potentially new design drivers and choices. For now, at least, monopiles dominate.

1.2 Monopile design

1.2.1 Loading and variables

OWTs are subject to lateral loads from wind and waves as well as operational loads from the rotor (Figure 1.4a). The self-weight of the structure is relatively small, meaning that lateral loads can be in the order of 60% of the vertical (Houlsby, 2016). This creates a design problem dominated by the combination of moment M and horizontal loading H (Figure 1.4b).

The applied load components are pseudo-random, increasing and decreasing with time (e.g. Figure 1.4e). This is often termed 'cyclic loading'. In reality, however, the resulting combined load is irregular and complex due to variations in:

- Loading frequency - where load components vary by orders of magnitudes between 0.001–10Hz (Arany et al., 2017) and interact with the dynamic response of the structure.
- Magnitude of loading - resulting in millions of low amplitude cycles and hundreds of extreme events over the lifetime of the turbine (Leblanc et al., 2010b).
- Directionality - spatial variation of wind and waves induce loads in differing directions which vary temporally and may not always be co-linear (Van Vledder, 2013).
- Resulting lever arm (M/H) - as the relative contribution of load components vary, so too does the ratio of M to H.

Due to their simple shape, monopiles have only a few design parameters (Figure 1.4b), which may be adjusted to resist the induced loads: embedded length, L, diameter D, and wall thickness t which may differ along the length. Currently, typical monopiles have diameters up to 8m, with L/D ratios between 3 and 6 and D/t ratios between 80

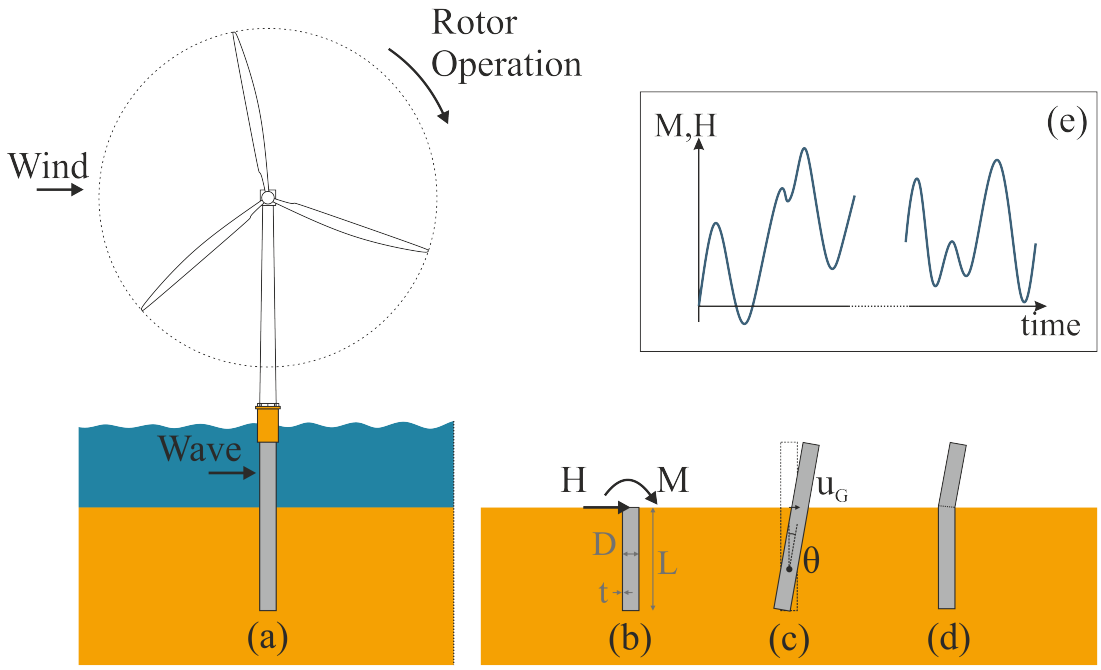

Figure 1.4: (a) Illustration of lateral loading components on a monopile foundation (b) as idealised combined Moment and Horizontal load (c) soil 'failure', excessive rotation θ and ground level displacement u_G (d) pile failure and material yield (e) Indicative pseudo-random loading

and 100 (Sánchez et al., 2019; Schroeder et al., 2015). L/D ratios look set to remain close to 3, although diameters are continuing to increase as turbines get larger. Future monopiles may be closer to 10m in diameter as the new generation of 12MW turbines are employed (Knight, 2019).

Short, stubby monopiles (with low L/D ratios) tend to behave less flexibly than the laterally loaded piles often seen in oil and gas structures, rotating as a rigid body as shown in Figure 1.4c. Parameters are chosen to limit horizontal displacement u and rotation θ (soil 'failure') and to withstand material yield and failure of the pile (Figure 1.4d). These requirements are discussed in more detail in the following sections.

1.2.2 Design criteria and current methods

Design criteria are taken from the DNVGL-ST-0126 standard 'Support structures for wind turbines' (DNVGL, 2018), with particular focus on 7.6.2 'Design criteria for laterally loaded piles'. This is referred to as 'DNVGL' in this section. Where possible design methods specifically described by DNVGL are considered. Failing that, best-practice tools are considered.

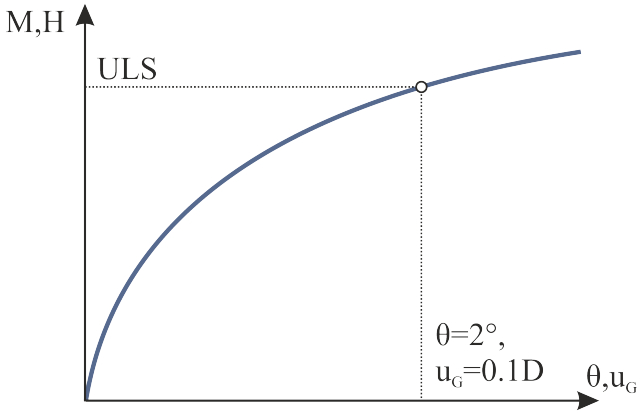

Figure 1.5: Illustration of a typical monopile response and ULS Limit

1.2.2.1 Monotonic response

Under maximum combined lateral and moment loading in the Ultimate Limit State (ULS), DNVGL 7.6.2.5 specifies that sufficient lateral pile resistance (pile capacity) should be ensured. This includes both pile yield (Figure 1.4d) and soil 'failure' (Figure 1.4c). Only the latter is considered here.

An idealised example of pile response to a monotonic increase in lateral load is shown in Figure 1.5 in general terms of M-θ or H-u_G. This is invariably non-linear and without an obvious plastic 'failure' until exceedingly large deflections. Instead ULS pile capacity is considered to be achieved at some specified pile displacement u_G or rotation θ. DNVGL do not specify these limits, but convention appears to be $u_{G,ULS} = 0.1D$ or $\theta_{ULS} = 2°$ (see Byrne et al., 2019b).

ULS is typically considered using the p-y method, as recommended in DNVGL. The monopile is modelled as a beam supported by springs representing lateral soil reaction. The reaction, p, is described as a function of lateral displacement, y at varying depths down the pile. The empirical p-y relationships (found in DNVGL F.2 or in 8.5 of API, 2011) were derived for long slender piles so their use for short-stubby monopiles involves significant extrapolation. In fact DNVGL 7.6.2.6 states that "Use of p-y curves for design of piles with diameters of more than 1.0 m (for example monopiles) is recommended to be validated for such use, e.g. by means of FE analysis".

The PISA project (Byrne et al., 2017; Byrne et al., 2019b), presented a model which includes the distributed lateral load, moments due to vertical shear stresses as-

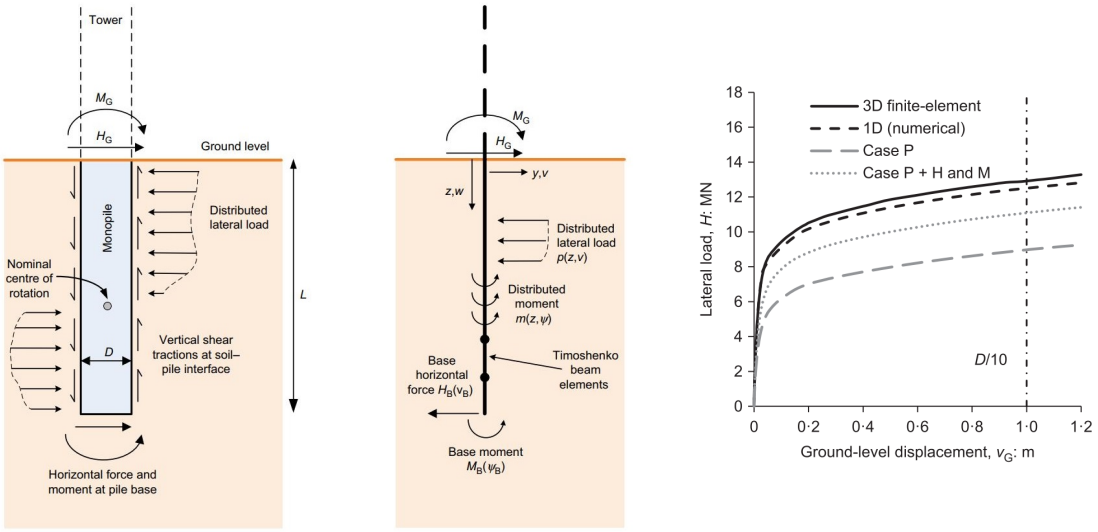

(a) **(b)**

Figure 1.6: PISA design model after Byrne et al. (2019b) (a) soil reaction components (b) PISA 1D FE model as employed in OxPile (c) Comparison of load-ground level response from an example FEA analysis and 1D PISA FE Model at a clay site along with contribution of various soil reactions. Case P refers the 1D model with distributed lateral soil reactions only. Case P+H and M refers to the addition of base soil reactions

sociated with local pile rotation, and a shear force and moment at the base of the pile (Figure 1.6a). The model has been validated against large-scale field testing at realistic L/D ratios. Byrne et al. (2019b) present a 'rule-based' and a 'numerical-based' method, in which the curves are derived from empirical parameters or calibrated by a suite of 3D FEA analyses. The resulting 1D PISA model and design approach reduces design conservatism by better calculating the ultimate monotonic capacity under lateral loads. Additionally, initial stiffness is better predicted which is important in dynamic response, covered in Section 1.2.2.3.

1.2.2.2 Response to repeated loading

The combined action of millions of loading cycles (briefly introduced section 1.2.1) can cause the foundation to accumulate rotation progressively and affect the strength and stiffness of the soil.

Serviceability limit state is considered in DNVGL 7.6.2.7, in which it is stated that permanent deformations must not exceed design criteria for normal use. This tolerance is "typically derived from visual requirements and requirements for the operation of the wind turbine" and corresponds to an allowable permanent rotation which occurs due to:

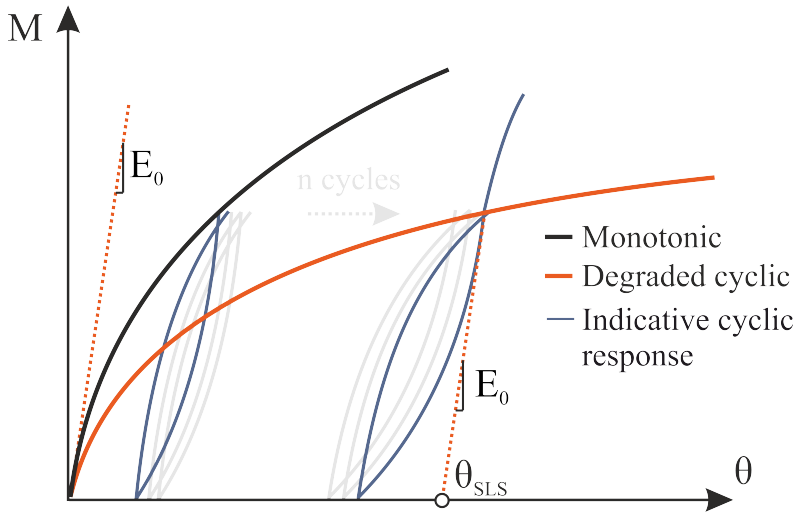

Figure 1.7: Illustration of cyclic response after n cycles of constant amplitude loading. Indicative 'ideal' degraded curve with elastic unloading to find permanent deformation (after Long and Vanneste (1994) and Carswell et al. (2016))

- installation misalignment
- accumulation of rotation (due to soil deformations) caused by repeated loading about a non-zero mean

Limits are defined by the turbine manufacturer, and are considered separately with with independent limits of 0.25° (Peralta et al., 2017). As well as this, guidance in DNVGL 7.6.2.5 states that "cyclic degradation effects in the lateral resistance" must be considered for the ULS conditions outlined in 1.2.2.1.

Empirical 'modifications' are presented (DNVGL F.2 or in 8.5 of API, 2011) to cater for cyclic loading by reducing the *p-y* curves by a constant factor (Reese et al., 1974).Long and Vanneste (1994) and Rajashree and Sundaravadivelu (1996) provide approaches in which the reduction is dependent upon number of cycles. However both are based upon a limited number of long, slender pile tests with relatively few cycles so have inherent uncertainties.

Modified '*p-y*' curves allow for a calculation of rotation at peak load but there is no consensus on an accepted methodology to predict permanent rotation for SLS (Arany et al., 2017). One option is to assume an elastic unload to zero, similar to the method described by Carswell et al., 2016). Figure 1.7 shows an idealised response to constant amplitude loading with a non-zero bias alongside an example modified prediction with the elastic unload tracking the initial stiffness of the pile. In this

figure the p-y degradation is assumed to match the peak accumulated rotation due to the applied n cycles.

Using this method, accumulated rotation is poorly addressed and bears no resemblance to the true pile behaviour. It does not trace the loading history and therefore does not predict the continuous response, which is a more accurate representation of the evolution of changes to pile strength and stiffness. Adaptation for realistic, multi-amplitude and multi-directional loads is unclear.

1.2.2.3 Dynamic response

DNVGL 3.6.2.2 specifies that OWT structures are designed such that the first mode of natural frequency, f_0 avoids the f_{1p} (rotor) and f_{3p} (blade passing) excitation frequencies as defined by the bands of cut-in and rated rotor speeds. The objective of this is to minimise the dynamic amplification of displacements and to reduce the associated fatigue damage (Fatigue Limit State, FLS) in the structure. Typically monopile supported OWTs are designed as 'soft-stiff', such that f_0 lies between f_{1p}, and f_{3p}, this is shown schematically in Figure 1.8.

An OWT can be simplified one-dimensionally as a mass (nacelle and blades), m, atop a beam of length, L, and flexural rigidity, EI, founded by a 'macro' spring (representing the soil), k. f_0 can then be estimated as (Byrne and Houlsby, 2003):

$$f_0 = \frac{1}{2\pi}\sqrt{\frac{1}{m\left(\frac{L^3}{3EI} + \frac{L^2}{k}\right)}} \tag{1.1}$$

Hence f_0 is sensitive to soil stiffness k as shown by Kallehave et al. (2015b).

The dynamic response of the structure is also governed by damping, a measure of energy dissipation. Damping reduces the natural frequency of the turbine and limits and decays the rotation from dynamic loads. Damping on a wind turbine structure consists of: aerodynamic, hydrodynamic, structural and soil damping, of which soil damping is the greatest and most uncertain (Beuckelaers, 2015). Active mass dampers (Brodersen et al., 2017) can also be installed to increase total damping and further reduce excitation at natural frequencies. This may become necessary as turbines increase in size and f_{1p} reduces, therefore increasing the intersection of the the wave frequency distribution and soft-stiff f_0.

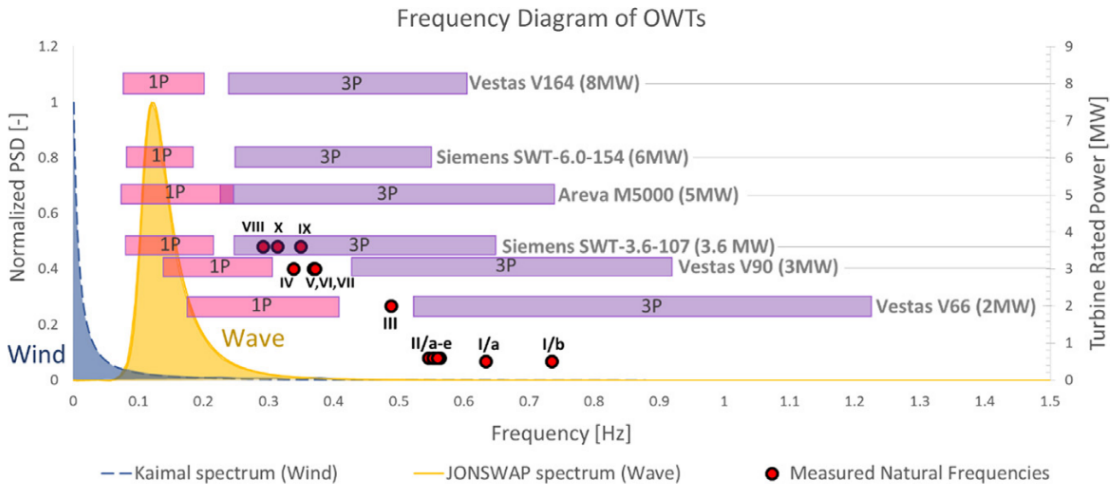

Figure 1.8: Typical wind and wave spectra, rotational speed (1P) and blade passing (3P) frequency bands for six commercial turbines alongside some measured natural frequencies (Arany et al., 2016)

Arany et al. (2016) state that the total damping ratio, ξ, of an operational turbine is typically $2-8\%$ from which the damped frequency, $\tilde{f}_1$, calculated by:

$$\tilde{f}_1 = f_1\sqrt{1-\xi^2} \tag{1.2}$$

could reduce by 0.32%.

Single element 'macro' models can be constructed which include lateral, rotational and cross-coupling components (Arany et al., 2016) or with a series of non-linear soil reaction curves ('p-y' or PISA methods discussed in 1.2.2.1). Both can be built to include dissipative behaviour (Page et al., 2018; Beuckelaers, 2015). Integrated dynamic analyses may then be undertaken to calculate f_0 and further natural frequencies.

In contrast to most engineering problems, there is no obvious conservative side when considering frequency, hence accurate description of soil stiffness is paramount. Stiffness is likely to change with cyclic loading (discussed in section 1.3.3). Scour of soil around the monopile is also known to affect stiffness and reduce natural frequency (Mayall et al., 2018), preventative scour protection is therefore commonplace.

1.2.3 Summary

Monopiles have few design variables owing to their simple shape. Embedded length, L, is typically governed by overturning capacity (ULS) and maximum allowable tilt (SLS). Diameter, D, is dependent upon the required natural frequency, f_0, of the

turbine, linked to the stiffness of the soil. Whilst the wall thickness, t, will typically be dictated by buckling during installation or fatigue loads (FLS) (Kallehave et al., 2015b; Arany et al., 2017).

In short, long term cyclic loading affects FLS and SLS and, as strength of the surrounding soil is reduced, ULS. As monotonic design improves and turbines near the end of their design life, such that lifetime extension is considered, SLS and FLS design are becoming increasingly important. Current accepted design methods of cyclic degradation are ill-defined, possibly over conservative and ill-equipped for dealing with multi-amplitude or multi-directional loads.

Any improvement to the accuracy of cyclic foundation design for OWTs should consider:

- Accumulation of rotation (ratcheting)
- Changes to stiffness of surrounding soil, and with it changes to overall capacity (strength) and dissipative behaviour

Accurate prediction of the above gives confidence in design and can reduce conservatism and cost.

1.3 Cyclic response of fine-grained soils - research review

Section 1.2 showed the importance of understanding the effects of long-term cyclic loading in monopile design. In this section relevant research is reviewed from micro to macro scale. From mechanical observations of the soil fabric, to standard laboratory tests on soil elements, and finally experimental findings at model, increased gravity and full scale. Proposed improved methodologies to quantify the response in monopile geotechnical design are reviewed.

The primary focus of this thesis is fine-grained (clay) soils. Therefore this section is centred around research in clays. Coarse-grained materials (sands) are, however, considered at a high level. Throughout this section particular weight will be given to **strain (rotation), stiffness, capacity and dissipative behaviour**.

1.3.1 Micro scale

The soil matrix is an assemblage of solid particles and voids. Offshore, the voids are typically fully occupied by water. Behaviour of a soil subject to cyclic stress is dependent on the boundary conditions, but also on drainage and frequency of loading. Clays typically drain slowly and behave with apparent cohesion. Conversely, in sands significant drainage may occur in a few cycles. Both accumulate irreversible strain with application of many stress cycles (Di Prisco and Wood, 2012).

Cyclic loading will break down the soil structure and cause volumetric compression. In undrained conditions the contraction of the soil is prevented by the compressibility of the water. Stresses carried by the soil skeleton are transferred to the water causing the effective stress to decrease (Andersen, 2015). If the shear stresses are large, so too is reduction of effective stress which in turn reduces shear strength strength and stiffness. Alongside this, repeated shearing causes the particle structure to break down (destructuration, e.g. Okur and Ansal, 2007). The combined action of the two and is often termed 'cyclic softening' or 'degradation'. The more softening, the higher the shear strains. Cyclic shear strains in clays are also rate dependent. The undrained shear strength of saturated clay increases with strain rate, at approximately 10% per order of magnitude, (Mitchell and Soga, 2005). This increases with plasticity of clays and is considerably less for sands.

1.3.2 Element tests

Simple laboratory tests can be undertaken on soil samples retrieved offshore to ascertain soil properties for design. This is true of both monotonic and cyclic properties and the following section briefly covers cyclic tests and relationships in literature (in undrained conditions for clays and drained for sands). Tests may be controlled with cycles of stress or strain. The former appears to be more widely used in OWT design. Hollow Cylinder (HCA) tests are not considered as they are complex, expensive and rarely used by industry.

In an 'NGI-type' cyclic simple shear (DSS_{cyc}) test, Figure 1.9a, a cylindrical specimen (usually 50-75mm in diameter and 20-30mm high) is constrained horizontally by a series of stacked metal rings (which are free to move across each other) or a reinforced rubber membrane and vertically by two plates (e.g. Bjerrum, 1967). In stress

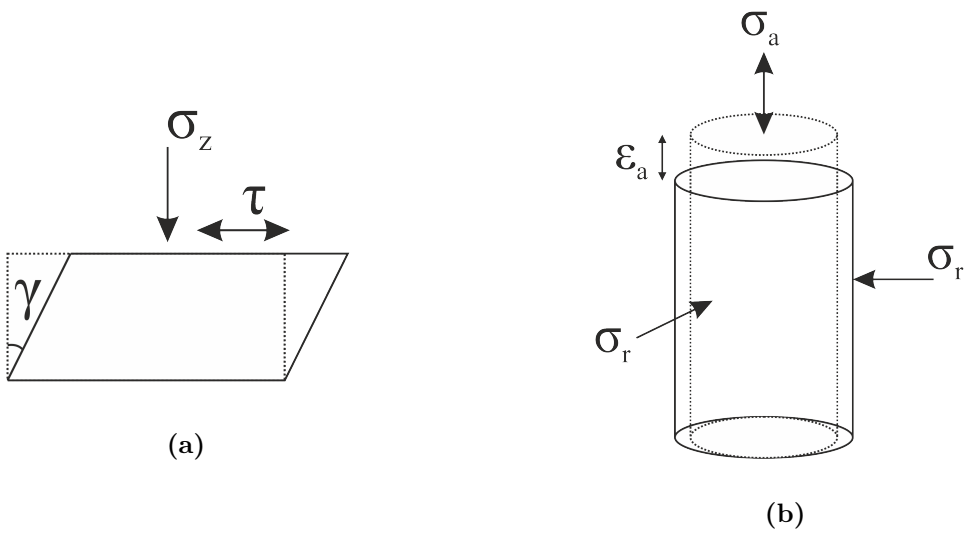

Figure 1.9: Stress conditions and notations in (a) 'NGI-type' *DSS* tests (b) CU tests

controlled tests, the shear stress τ is cycled whilst the shear strain γ is measured. If a device is such that the specimen cannot be saturated it is conventional to perform a drained test at a constant volume, by varying σ_v, such that undrained conditions apply (Dyvik et al., 1987).

Stress-strain distribution in the specimen is non-uniform and stress concentration can be experienced at the edges (Reyno and Airey, 2005). Lateral stresses are rarely measured and are assumed, whilst measurements of strain are averaged across the specimen. This creates the problem of an unknown inhomogeneous stress field.

Cyclic simple shear testing is, however, often preferred to tests which require larger samples for OWT design as numerous, rapid, tests can be undertaken with limited sample demands. The results of these tests facilitate the construction of cyclic contour diagrams (discussed in detail in Chapter 4.1).

In a triaxial test, Figure 1.9b, axial, σ_a, and radial stresses, σ_r, can be applied with mean effective and deviator stresses defined as:

$$p' = \frac{\sigma_a' + 2\sigma_r'}{3} \tag{1.3}$$

$$q = \sigma_a - \sigma_r \tag{1.4}$$

A cylindrical specimen (conventionally with a height/diameter ratio of 2 and diameter of 38mm, although offshore more commonly 76mm (Randolph and Gourvenec, 2011) is placed within a thin rubber membrane and two end-caps. The initial stress

Table 1.1: Advantages and limitations of DSS and CU testing

Test	Advantages	Limitations
DSS_{cyc}	Simple and quick to carry out. Small sample (multiple tests possible from single core).	Lateral stresses (due to the constraint of the rubber membrane) have to be estimated. Stress distribution along this surface is not uniform.
CU_{cyc}	Failure can occur on any surface. Applied stresses are principal stresses which are entirely controlled.	Stress concentrations caused by end restraint due to friction between the clay and the end plates. Large samples required.

state can be defined either isotropically or, more representative of in-situ conditions, anisotropically with respect to K_0 (σ'_r/σ'_a). A stress path can be defined, inducing compression or extension. In the majority of stress controlled undrained cyclic triaxial (CU_{cyc}) tests, q is varied sinusoidally by fixing σ_r and controlling σ_a. Axial strain ε_a is then recorded. Table 1.1 summarises key differences between the two tests.

1.3.2.1 Behaviour and relationships

Figure 1.10 shows a typical hysteresis loop of soil subject to constant amplitude cyclic loading defined by non-zero average (σ_{av}) and cyclic (σ_{cyc}) components. Stress variable σ refers to deviator stress q in CU_{cyc} tests and τ in DSS_{cyc} tests. Strain variable ε then refers to axial strain ε_a or shear strain γ respectively. Precise definitions of cycles, loads and response often differ between publications and between element and pile testing literature. This issue is reviewed in detail in Chapter 2 and is therefore not discussed here. Key components, related to section 1.2.3 are: accumulation of strain ε_n, here shown at the average load; change in loop secant stiffness k_n and hysteretic loop area E_H (indicative of energy dissipation); and any changes to the post-cyclic strength $\sigma_{u,pc}$ (covered in Section 3.4.1.5).

Cyclic element tests have been used for many years to investigate the response of soils to environmentally induced cyclic loads such as: wave loading on offshore oil and gas platforms, earthquake induced loads, and traffic-induced loading in pavement design. These primarily focus on accumulation of strain.

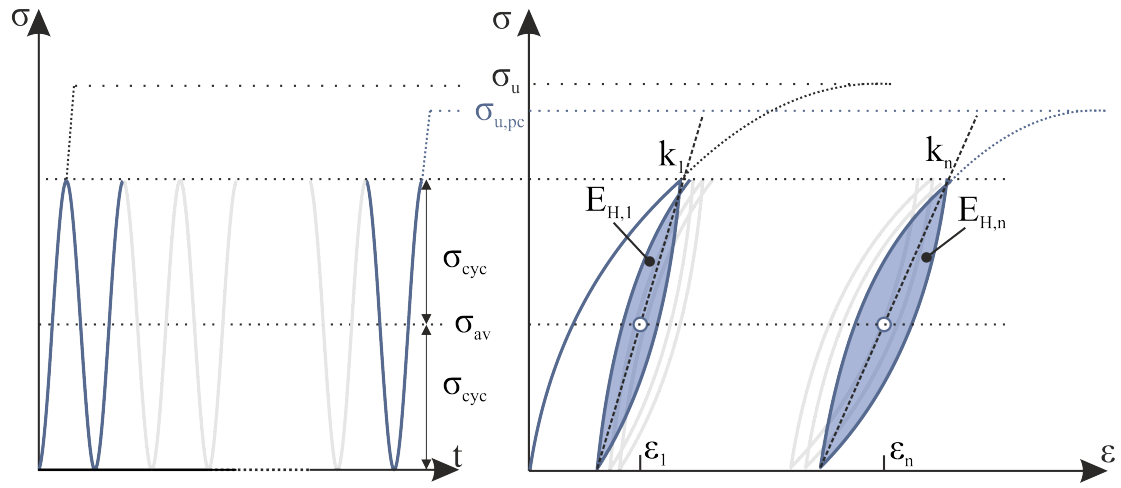

Figure 1.10: Typical hysteretic response of soil under one-way cycles of general stress σ and strain ε response.

In CU_{cyc} literature, Paute et al. (1993) state empirical relationships are often used of the form:

$$\varepsilon_n = f(n, \sigma) \tag{1.5}$$

Such that the accumulated strain, ε_n, can be estimated as a function of number of cycles, n, and some measure of stress magnitude, σ. Most relationships are based upon test results with one-way loading ($\sigma_{av} = \sigma_{cyc}$). In triaxial tests of fine-grained soils, logarithmic (e.g. Cheung, 1994) and exponential functions (e.g. Guo et al., 2018; Ushev, 2017) have been proposed; both predict a reducing rate of accumulation with number of cycles. Similar relationships have also been proposed in coarse-grained soils (e.g. Barksdale, 1971; Sweere, 1990). Exponential functions tend to be presented for larger numbers of cycles and stress magnitude is often employed as a multiplier. More extensive lists can be found in Arnold and Werkmeister (2010) and Lekarp et al. (2000).

Alongside accumulation of strain, a reduction on loop stiffness k with cycles (or inversely, an increase in cyclic/resilient strain $\varepsilon_{cyc} = \sigma_{cyc}/k$) is typically reported for undrained tests in clays. This occurs in tests with a considerable bias and in two-way testing ($\sigma_{av} = 0$), in DSS_{cyc} and CU_{cyc} tests. (e.g. Okur and Ansal, 2007; Wichtmann and Triantafyllidis, 2018; Guo et al., 2018). Loop area is less often reported, although Løvholt et al. (2020) showed that for selected DSS_{cyc} tests in high plasticity clays, loop area and with it 'damping factor' increased with reduction in loop stiffness (and

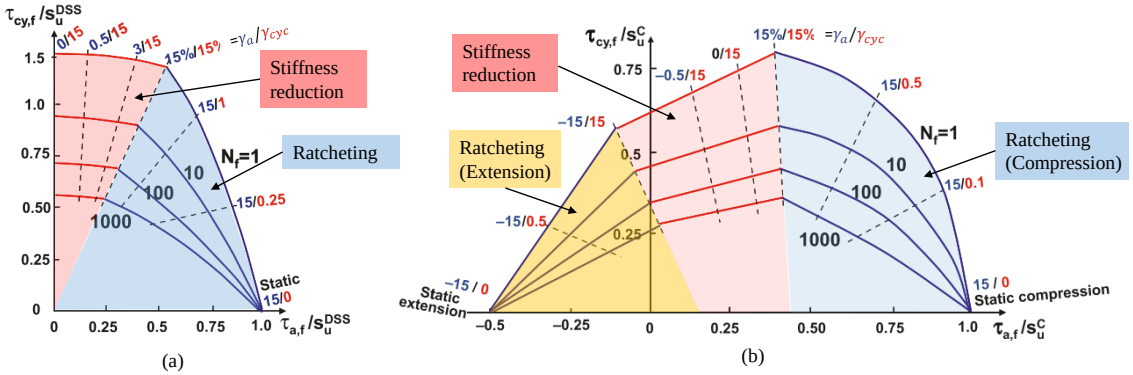

Figure 1.11: Contour diagram with number of cycles to failure as a function of normalised average $\tau_{a,f}$ and cyclic $\tau_{cyc,f}$ shear stresses. Built from tests in Drammen Clay, after Andersen, 2009. Accumulated shear strain γ_a and cyclic $\gamma_{cyc} = \tau_{cyc,f}/k$ shown. Failure is defined as either γ_a or $\gamma_{cyc} > 15\%$. Zones of dominant behaviour type are highlighted. (a) DSS_{cyc} (b) CU_{cyc}

thereby number of with cycles). This has also been reported in CU_{cyc} tests in soft clay by Guo et al. (2018). 'Damping' with regards to energy dissipation is discussed in more detail in Section 2.5.

The behaviour outlined above is known to depend upon load magnitude and type of cycles applied (i.e. relative magnitudes of σ_{av} and σ_{cyc}). Cyclic contour diagrams, which compile the measured data from a number of cyclic element tests (Andersen, 2015), are a common way of visualising behaviour across all possible applied cycles. Figure 1.11 shows two such contour diagrams, built from a series of DSS_{cyc} and CU_{cyc} tests on Drammen clay. Contours of numbers of cycles to failure N_f are drawn as a function of normalised average $\tau_{a,f}$ and cyclic $\tau_{cyc,f}$ shear stresses. In this case failure is defined as either average or cyclic strain exceeding 15% (γ_a or $\gamma_{cyc} > 15\%$). It is clear that tests with higher applied stresses (distance from the origin) fail in fewer cycles, but also that the 'type' of failure differs with loading type. These are drawn indicatively on Figure 1.11, as: 'stiffness reduction' or 'cyclic failure' where there is little accumulation of strain but high increase in cyclic strain (reduction of stiffness); and 'ratcheting' or 'mobility failure' in which the accumulation of average strain is larger than cyclic strain (and may occur in extension or in compression for cyclic triaxial tests). Examples of each can be seen in Figure 1.13a.

Pre-failure behaviour also varies with stress level. First developed to describe metals under repeated loading, 'Shakedown theory' has also been applied to piles and

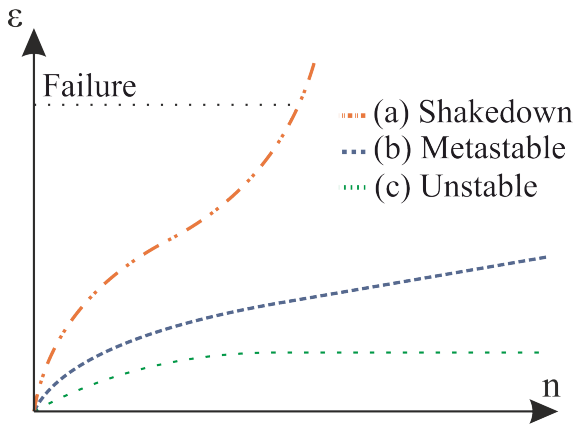

Figure 1.12: Shakedown Behaviour in which strain rates differ with applied stress amplitudes (a) Low stresses to (c) high stresses. Adapted from Qiao et al., 2015.

element tests in sands and clays (Jardine, 2014; Werkmeister, 2003; Wichtmann et al., 2005). Accumulation of strain with number of cycles has been reported to develop in three distinct ranges, Figure 1.12:

A Shakedown/Stable zone – Low stresses which lead to an initial deformation followed by complete reduction in accumulated strain rate to zero.

B Abation/Metastable zone – Accumulated strain rate decreases with each cycle until a relatively low and/or constant strain rate is reached.

C Stepwise failure/Unstable zone – Higher stress levels will initially cause the same response as (B) at a faster rate before a rapid 'unstable' accumulation of strain leads to failure.

In undrained testing the reduction in stiffness and accumulation of strain arises from a combination of destruction and effective stress reduction (Section 1.3.1), such that pore-pressure accumulation likely increases with cycles. This is shown in Figure 1.13 for CU_{cyc} tests in normally isotropically consolidated Kaolin clay. Both ratcheting-type and stiffness reduction-type failures can be seen and large shear strains occur as the effective stress reduces to meet the failure envelope.

1.3.3 Pile scale

Numerous tests on piles subject to cyclic lateral loads have been undertaken at centrifuge, model and full scale. There appears to be fewer experimental testing programs

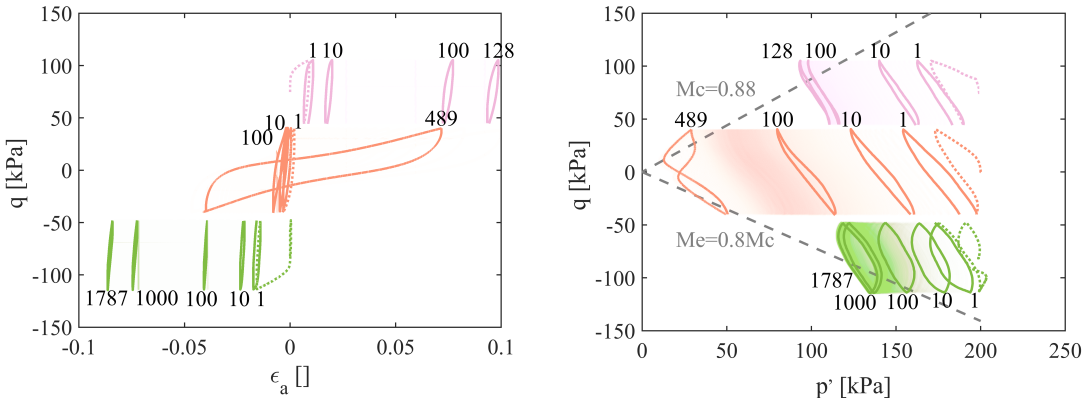

Figure 1.13: Behaviour of three CU tests in Kaolin with differing q_{av} with cycles shown (a) $q-\varepsilon_a$ (b) $q-p'$ with critical state line Mc from (Wichtmann and Triantafyllidis, 2018) alongside an estimated extensive line.

in clay than sands within the literature, possibly due to increased difficulties when handling clay. For a detailed review of pile testing in sands see Richards (2020).

Generally, pile response can be characterised in a similar way to Figure 1.10, where now $\sigma = M, H$ and $\varepsilon = \theta, u_G$ respectively. Full scale studies of piles in Cowden clay were undertaken as part of the PISA project (Byrne et al., 2017). The piles showed a hysteretic response during loading and unloading, accumulation of rotation in the direction of load bias (fitted to a power law by Beuckelaers, 2017) and some degradation of stiffness. Post-cycles the strength was not considerably degraded and the response returned to the original monotonic backbone. These tests are analysed in more detail in Chapter 6.

He et al. (2017) show similar results for a 0.8m diameter pile in soft clay with increased stiffness degradation under two-way loading. Centrifuge tests in Kaolin by Lau (2015) accumulated rotation and either softened or stiffened depending on loading type, Lau postulated 'work hardening' as the mechanism behind the stiffening tests. Zhu et al. (2017) and Garnier (2013) both found power laws to fit the accumulation of rotation in centrifugal tests. The former in studies of suction caissons (with a lower L/D) subject to 106 cycles founded in clay, sands and layered materials and the latter, of laterally loaded piles in Speswhite Kaolin.

Deformation mechanisms of piles subject to monotonic lateral loads are well defined. At ground level a conical passive wedge is pushed up by the moving pile, with an active wedge on the opposite side. This leads to a lower limiting resistance

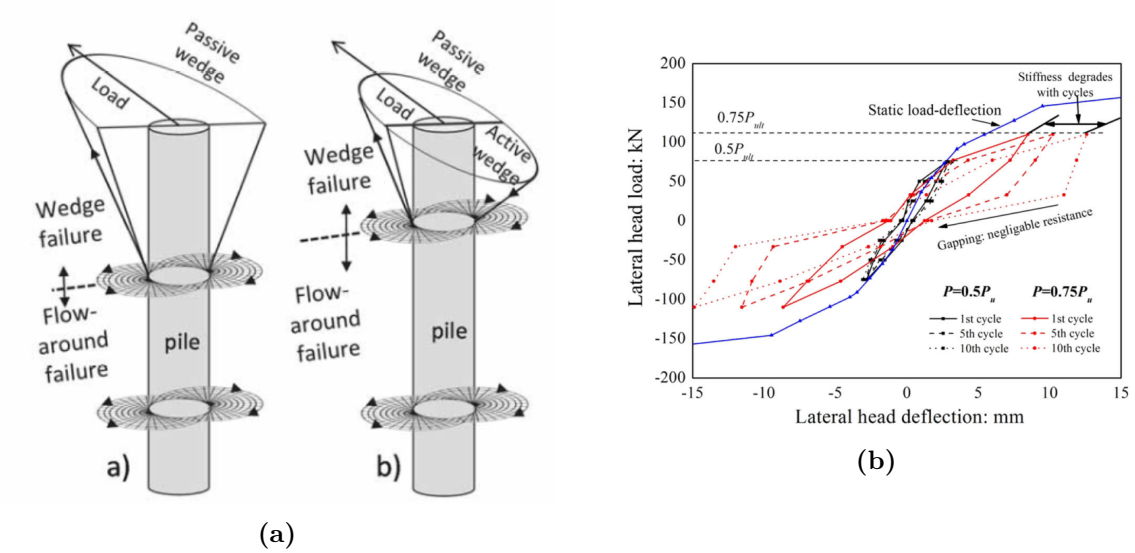

Figure 1.14: (a) Soil deformation mechanism of laterally loaded pile in fine-grained soil, (*a*) gapping (*b*) no gapping (Jeanjean et al., 2017) (b) Macro-response of a pile to two-way cyclic lateral load where gapping has been observed (He et al., 2017)

compared to that at depth. Below the wedge, clays flow horizontally around the pile in a 'flow around mechanism'. This mechanism can be found in numerous papers, (Jeanjean et al., 2017; Klar and Randolph, 2008; Murff and Hamilton, 1993; Yu et al., 2015), and is shown in Figure 1.14a. Shorter, stubby, piles (more similar to monopiles) rotate and 'kick out' near the pile toe, resulting in a rotational flow around mechanism with movement of soil depth-wise as well as laterally.

A gap between the pile and the surrounding soil (gapping) often develops in clays, in which the active wedge no longer fills the gap behind the translating pile head. This is observed in physical tests in clays (Byrne et al., 2017; He et al., 2017; Su et al., 2014) and recently chalk (Buckley et al., 2020), and can be seen in load-deflection curves as a soft response on unload, corresponding to a very low gradient, Figure 1.14b. This indicates gapping in which little resistance is offered in front of the moving pile, hence a large deflection for a small change in load.

The frequency of typical monopile loading is typically considered to result in undrained response in clays, and therefore accumulation of pore-pressures. However in the long term, as loading varies, pore pressure is likely to be dissipate.

1.3.4 Summary

Literature reviewed in this section shows, that for clays subject to cyclic shearing in element tests or to cyclic lateral loading at pile scale, generally:

- Strain accumulates with cycle number and magnitude for non-zero mean stress cycles
- Stiffness degrades in clays due to destruction and pore-pressure accumulation
- Energy dissipation largely increases as stiffness decreases

Empirical relationships for both element tests and laterally loaded model piles are exponential or logarithmic for accumulated strain or rotation, boding well for a link between the two. The response of soils subject to cyclic loading is dependent upon: loading (magnitude and shape), number of cycles, current stress state, drainage and stress history. In clays plasticity and loading rate affect the response.

1.3.5 Proposed design methods

Multiple methods for better predicting the response of monopile foundations under cyclic lateral loading have been proposed. A selection of these are discussed in this section and summarised in Table 1.2. Many focus on a single aspect of monopile response (typically ratcheting) and represent the monopile-soil interaction as a single-element (macro), 1D model (as in p-y or PISA method) or in a complete Finite Element Analysis (FEA). For application in the design office, speed of calculation and practical calibration is paramount.

The methods selected vary in complexity but can broadly be split into: 'Extrinsic methods', in which empirical relationships are used to predict displacement or degrade p-y type models (similar to Long and Vanneste (1994) and Rajashree and Sundaravadivelu (1996); or 'Intrinsic methods', in which the continuous loading history is predicted and behaviour is computed incrementally, such that hysteretic properties (stiffness and dissipation) are intrinsically computed.

Figure 1.15 depicts, generally, how each would compute single amplitude and more realistic pseudo-random loads. Only intrinsic methods can predict the latter.

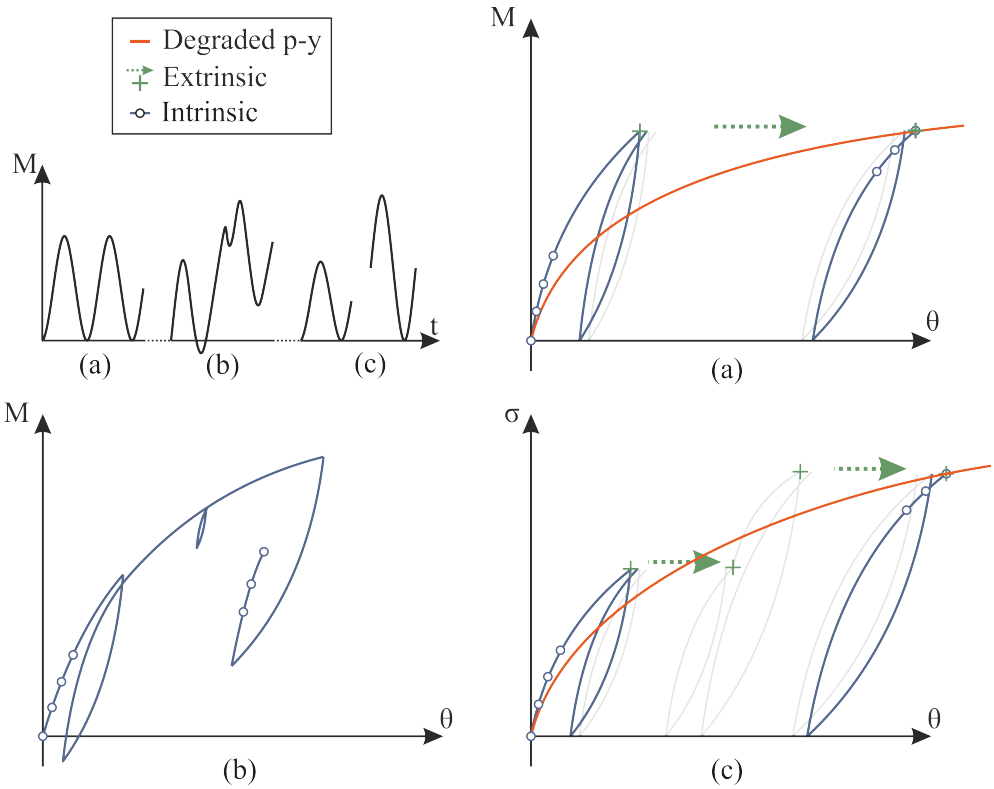

Figure 1.15: Illustration of cyclic modelling strategies for (a) Single Amplitude (b) Pseudo-Random and (c) Multi-amplitude batched loads.

For extrinsic and modified *p-y* type methods, pseudo-random loading must be discretised into a series of 'packets' of single-amplitude loads (e.g. following methods such as Noren-Cosgriff et al., 2015). Each packet may then be computed separately, adjusting for the change in amplitude between batches in some way. Leblanc et al. (2010a) showed that macro relationships of pile ratcheting in sand could predict multi-amplitude tests well with a strain-superposition method. It is unclear, however, if this discretisation is accurate representation of the effects of the true pseudo-random loading history on the soil.

As part of the the SOLCYP project, (Puech and Garnier, 2017) two cyclic design approaches were proposed; empirical 'macro' equations to predict pile displacement at a macro-scale and 'local' *p-y* modification multipliers. Both depend upon the number of cycles, load amplitude and specified coefficients for overconsolidated (OC) or normally consolidated (NC) clay. Whilst based upon experimental studies, the project focused primarily on the response of flexible piles (high L/D) and the methods are only capable of predicting ratcheting or final displacement at peak load.

Cyclic contour diagrams, based upon the measured responses from element tests Andersen (2015), have been used for cyclic design of offshore structures (predominantly large, gravity base, oil platforms in soft clays) since the 1970s (Andersen, 1976). Zhang et al. (2016) present a method in which post-cyclic *p-y* curves can be scaled from diagrams constructed from DSS_{cyc} tests. The UnDrained Cyclic Accumulation Model (UDCAM, see Jostad et al., 2014) performs a similar method in relation to FEA, in which the response is 'degraded' by tracking contour diagrams at each integration point. Initial stress-strain behaviour is calculated using total stress model such as NGI-ADP (Grimstad et al., 2012). Prediction of ratcheting is achieved by both the *p-y* and UDCAM methods but neither predicts changes to hysteresis loop shape and there appears to be no verification against medium or full-scale tests. Many element tests are needed to accurately construct the underlying contour diagrams (see Chapter 4.1), which can prove costly.

The Stiffness Degradation Model (SDM), was developed at the University of Hannover for cyclic loading of monopiles in sands (Achmus et al., 2007). In a 3-D FEA model (ABAQUS) an elasto-plastic constitutive model is used to apply realistic monotonic (lateral + axial) loads. The authors postulate that an increase in strain due to cyclic loading can also be interpreted as a decrease of stiffness in each element. The model is calibrated from CU_{cyc} tests (Kuo, 2008) and has been shown to predict the accumulated rotation of the model tests by Leblanc et al. (2010b) well (Achmus et al., 2011). Despite using a developing 'stiffness', this is really only a measure of permanent deformation and the model holds no information on development of the hysteresis loop with regards to stiffness or area. It is also unclear how this method might be extended for multi-amplitude loads.

In the High Cycle Accumulation (HCA) model, (Niemunis et al., 2005; Wichtmann and Triantafyllidis, 2016) the first couple of cycles are calculated implicitly (using, for instance, a hypoplastic model) before permanent strains are predicted using a constitutive formulation calibrated from CU_{cyc} tests. Intrinsic 'control cycles' allow for updated hysteretic response and extension to multi-amplitude loading. The model has been used in FEA predictions of a monopile in sand (Staubach and Wichtmann, 2020) but has not been validated against measured responses.

Table 1.2: A selection of proposed design methods for cyclic lateral loading of piles

Modelling Strategy	Method (Reference)	Type	Summary
Extrinsic	SOLCYP (Puech and Garnier, 2017)	Macro, 1D	+ Predicts macro pile-level response from experimental observations. - Focus on long, slender piles under relatively few cycles. Cannot predict hysteretic changes
	NGI (Zhang et al., 2016; Jostad et al., 2014)	1D, FEA	+ Informed by soil-specific contour diagrams from measured element testing. - Cannot predict dissipative behaviour. Requires numerous element tests for accurate calibration
	SDM (Achmus et al., 2007)	FEA	+ Distributes stress in soil. Parameters derived from element tests. Reasonable agreement with experimental results in sands. - Only one-way loading considered. Cannot predict hysteretic changes
	HCA (Wichtmann and Triantafyllidis, 2016)	FEA	+ Parameters derived from element tests. Intrinsic 'Control cycles' allow for updated hysteretic response and extension to multi-amplitude loading - Not validated against experimental results.
Intrinsic	REDWIN (Page et al., 2018)	Macro	+ Rapid. Captures hysteretic behaviour. Validated against PISA tests. - Does not capture cyclic behaviour. Calibration only applicable to geometry of 3DFEA
	PIMMS (Whyte et al., 2020)	FEA	+ Captures full response. Can predict pseudo-random loading. Calibrated from element tests. Validated against monotonic PISA tests. - Computationally expensive. Not validated against cyclic tests.
	HARM (Houlsby et al., 2017)	Macro, 1D	+ Captures full response. Can predict pseudo-random loading. Validated against experimental results at macro and 1-D level. - Calibration of parameters from element tests not yet defined

Intrinsic models developed for cyclic loading and implemented in FEA can suffer from instability and time-constraints when computing the response of a pile to many cycles. However Whyte et al. (2020) present a 'Parallel Iwan Multi-Surface' (PIMS) model, in which multiple elastic-perfectly-plastic micro models are overlayed with different weightings. A cyclic extension degrades the stiffness of each surface with respect to accumulation of strain. The model has been proven to robustly compute laterally loaded monopile tests to almost 100 cycles, predicting ratcheting and hysteretic stiffness changes. It is calibrated from element test data and has been validated against monotonic PISA pile data (Byrne et al., 2017) but not against cyclic tests.

Page et al. (2018) present a multi-surface kinematic hardening macro model which is able to rapidly compute the hysteretic response of monopiles, validated against the

PISA field tests at Cowden (Byrne et al., 2017). It does not, however, capture any changes to stiffness or ratcheting and is calibrated from FEA analyses. The macro model is only valid for the same geometry as the original FEA, which may be an issue for application to design.

Models derived in the hyperplasticity framework (Houlsby and Puzrin, 2006), offer a rigorous approach to modelling plastic behaviour which makes use of internal variables to describe the history of loading. Multi-surface kinematic-hardening models capture hysteretic response well. Extensions to capture the ratcheting and changes to hysteresis loop shape are well defined through empirical functions developing with incremental behaviour and the addition of a ratcheting element (plastic Accelerated Ratcheting Model, HARM see Houlsby et al., 2017). HARM models have been implemented as: macro models predicting model-scale tests in sand under unidirectional cyclic loading (Abadie, 2015) and complex, multi-directional and pseudo-random loading (Richards, 2020); and in 1D models predicting field-scale PISA in sand and clay (Beuckelaers, 2017). However, calibration of parameters for the models from element tests is not yet defined.

1.4 Research objectives

Section 1.1.2 described the important features of monopile design and outlined the increasing need for methods which are capable of more accurately predicting the response due to repeated loading, with particular focus on the accumulation of rotation (ratcheting), changes to strength and stiffness, and dissipative behaviour. Most current design methods are only able to capture ratcheting and are unable to accurately capture the response of more realistic loading (see. Section 1.3.5).

A new, intrinsic, approach to modelling of cyclic loading; 'Hyperplastic Accelerated Ratcheting Model' (HARM), can capture the key features of pile response to cyclic lateral loading on a cycle-by-cycle basis for many cycles. Previous research demonstrates that this approach to modelling compares well to experimental data. However, for design, it would be more appropriate for calibration parameters to be developed for site-specific conditions from laboratory element tests.

To facilitate this approach a database of cyclic laboratory tests in fine-grained soils has been acquired from the literature and private communication. This thesis explores calibration of each mechanism of the HARM model. The primary focus is an accurate reproduction of key behaviour observed (1.3.2) at element level when subject to a range of loading types. Whilst section 1.3 showed that similar behaviour is observed at pile and element level, in this thesis the same models are used at 1D scale to predict for pile tests at Cowden with potential mapping of parameters discussed.

The thesis forms a part of a wider effort by Oxford University to predict the response of monopiles to cyclic loading better, building upon previous experimental and numerical work (Richards, 2020 Beuckelaers, 2017 Abadie, 2015) and preceding a large-scale project PICASO (Pile Cyclic Analysis: Oxford and Ørsted, see Byrne et al., 2020) which aims to facilitate the use of new design methods with extensive laboratory testing, field testing and numerical work.

The structure of the thesis is outlined below.

1.4.1 Thesis structure

Chapter 1 describes current design practice and motivation for better understanding and methods for predicting the response of monopiles to cyclic lateral loading. Previous experimental work and proposed methods are summarised.

Chapter 2 presents a consistent framework for the interpretation of cyclic loading and response. The framework originated from a desire to compare cyclic element tests and cyclic pile tests using consistent and rigorous definitions. Possible definitions of cycles, strain, stiffness and damping are presented, concluding with reasoned suggested definitions for each.

Chapter 3 describes a database of cyclic element tests of fine-grained soils obtained from literature and private communication. Monotonic, rate-dependent and cyclic behaviour are summarised and presented to inform the formulation of multi-surface Kinematic Hardening hyperplasticity models. A best-fit model is then calibrated to each data set. The modelling framework is presented as a unified model with a discussion of required data, model parameters and default choices.

In **Chapter 4**, the 0D modelling framework is applied to two projects (both in conjunction with Norwegian Geotechnical Institute (NGI)) which aim to test the underlying mechanisms outside the calibrated range. Firstly, producing industry-standard 'contour diagrams' from synthetic tests. These provide an inter/extrapolated picture of development of strain with cycles across the full range of constant amplitude stress testing. By using mechanistic models, the diagrams can be described in terms of physical processes as well as validation tool for model formulation. The second application involves 'Class C' (Lambe, 1973) predictions of seven multi-amplitude, Direct Simple Shear (DSS) tests undertaken at NGI as part of the WAS-XL (Wave loads and soil support for extra-large monopiles) project. The model is calibrated from monotonic and constant-amplitude cyclic (DSS and DSS_{cyc}) tests in the same soil unit.

There are several possible ways of structuring such models. In **Chapter 5**, the implications of configuring units in series or in parallel is investigated. Comparisons of model behaviour are made by introducing the mechanisms presented in Chapter 3 in increasing complexity. Equivalence is met for some applications; where this is not the case evidence for a preferred choice is presented. This is particularly true when considering rate-dependency.

Chapter 6 extends total stress 0D models to 1D 'Winkler' type models for applications at pile scale. 'OxPile' soil models are extended to include kinematic hardening, rate dependent, ratcheting models which must be strain controlled. Model predictions are compared with PISA tests. Potential mapping of parameters from element to pile is discussed. Typical storm loading is applied and cyclic response is identified down the pile as mobilisation of lateral pressure. Comparisons between this and typical element tests leads to better assessment of required element testing, particularly for calibrating specific constitutive models.

The total stress models presented in Chapter 3 offer accurate predictions of the strains developed under repeated loading. However effective stress changes are not explicitly modelled, rather the effects on strain development are included via softening. Explicit prediction of effective stress has some benefits particularly with regards to triaxial tests. In **Chapter 7** rate-dependent, hyperplasticity models in triaxial effective stress space (q-p') are described. Although only at a development stage,

the approach is a step in the development of modified Cam-clay models to include changes due to repeated loading.

Appendix A presents derivation of incremental response in stress or strain control for any model configured in the hyperplasticity framework. Whilst not novel work, it is presented in full for reference and to facilitate the implementation of models described in this thesis.

Chapter 2

A consistent framework for cyclic loading

Definitions presented in this chapter were developed in collaboration with I.A. Richards. A summary can also be found in Richards (2020); here more information is given on the development and implications of choices made.

There is currently no consistency in definition of cyclic loading or the cyclic response between publications focused on pile testing and those focused on element testing. Definitions also vary within each field, from publication to publication.

A common framework for interpreting cyclic loading is necessary to facilitate comparison of test results from different institutions and, as this thesis aims to do, to compare behaviour observed at the pile system level with that observed at the soil element level. The latter is crucial for the practical calibration of design methods.

This chapter presents the development of a rigorous framework for characterisation of cyclic loading and definition of the cyclic response. In defining cyclic loading, consideration is given to the definition of a cycle and the characterisation of cyclic loading. In terms of the cyclic response; definitions of strain, stiffness and energy loss factor (a measure of energy dissipation) for a given cycle are described. The focus is on developing a consistent framework for unidirectional, constant amplitude cyclic loading, but some consideration is also given to unidirectional multi-amplitude loading.

The cyclic response is expressed generally in terms of stress σ and strain ε, however, σ and ε can represent a number of stress and strain parameters. In pile tests, σ may correspond to applied moment M or horizontal load H, while in element tests σ

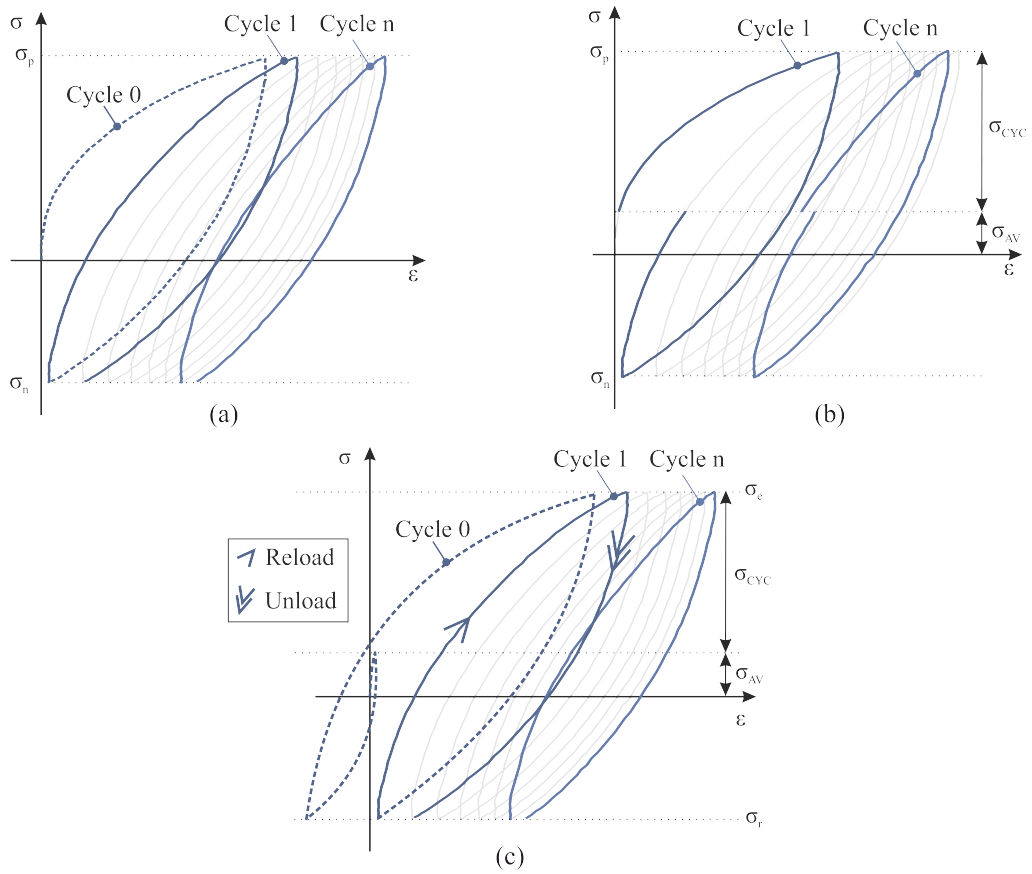

Figure 2.1: Typical cycle definitions in (a) pile testing literature (e.g. Abadie, 2015) (b) element testing literature (e.g. Andersen, 2015). (c) Consistent cycle definitions proposed

may correspond to deviator stress q or shear stress τ. In pile tests, ε may correspond to pile rotation θ or pile displacement u, while in element tests ε may correspond to shear strain γ or axial strain ε_a.

2.1 Cycle definitions

Figure 2.1 shows the cycle definitions typically found in (a) pile testing literature (e.g. Abadie, 2015) and (b) element testing literature (e.g. Andersen, 2015). For pile tests, a cycle is typically defined as a load-unload loop from the most negative stress, σ_n to the most positive stress σ_p and back to σ_n. Whilst cycle 0 is the first load-unload loop from zero load to σ_p and back to σ_n.

In element tests, a cycle is typically defined as starting and finishing at σ_{av}, where $\sigma_{av} = (\sigma_p + \sigma_n)/2$. The cycle starts at σ_{av}, loads to σ_p, unloads to σ_r and loads back to σ_{av}. Cycle 0 is not defined, although the initial consolidation to σ_{av} is typically

not considered as part of cycle 1. In element tests, the cyclic stress is defined as $\sigma_{cyc} = (\sigma_p - \sigma_n)/2$.

To allow both pile response and element tests to be presented in a consistent framework, the cycle definition presented in Figure 2.1(c) is recommended. This cycle definition follows the pile test approach and is considered to be more intuitive than the element test definition, and allows straightforward consideration of half-cycles, which is necessary for multi-amplitude loading. Rather than defining the cycle in terms of σ_p and σ_n, the cycle is defined in terms of the extreme load, σ_e, and reversal load, σ_r. The introduction of these terms allows the framework to consistently capture behaviour during extensive (element) tests, where $|\sigma_n| > |\sigma_p|$. In pile tests, the definition of a positive load direction is arbitrary.

For constant amplitude loading, σ_e is defined as the maximum absolute load at load reversals and σ_r as the minimum absolute load at load reversals. In terms of σ_{av}:

$$if \quad \sigma_{av} \geq 0 \rightarrow \begin{matrix} \sigma_e = \sigma_{av} + \sigma_{cyc} \\ \sigma_r = \sigma_{av} - \sigma_{cyc} \end{matrix} \tag{2.1}$$

$$if \quad \sigma_{av} < 0 \rightarrow \begin{matrix} \sigma_e = \sigma_{av} - \sigma_{cyc} \\ \sigma_r = \sigma_{av} + \sigma_{cyc} \end{matrix} \tag{2.2}$$

When $|\sigma_e| = |\sigma_r|$, σ_e is generally defined in compression or (for tests where direction is arbitrary) the direction of initial loading.

Cycle 1 begins and ends at reversal load σ_r and is defined as the second load-unload cycle to pass through σ_e. Cycle 0 is defined as all loading which occurs before cycle 1. Figure 2.2 shows examples for various types of loading; point e_0 will always be defined but r_0 only exists if initial loading occurs in the unloading direction, e.g. Figure 2.2a. This definition is necessary to account for pre-loading which typically occurs during cyclic triaxial extension tests. Cycle 0 begins at σ_0 which may be non-zero (e.g. Figure 2.2d, as is the case for anisotropically consolidated tests where $q_0 \neq 0$), and at $\varepsilon = 0$. Under multi-amplitude loading, cycle 0 is typically insignificant. This nomenclature is now used throughout this thesis.

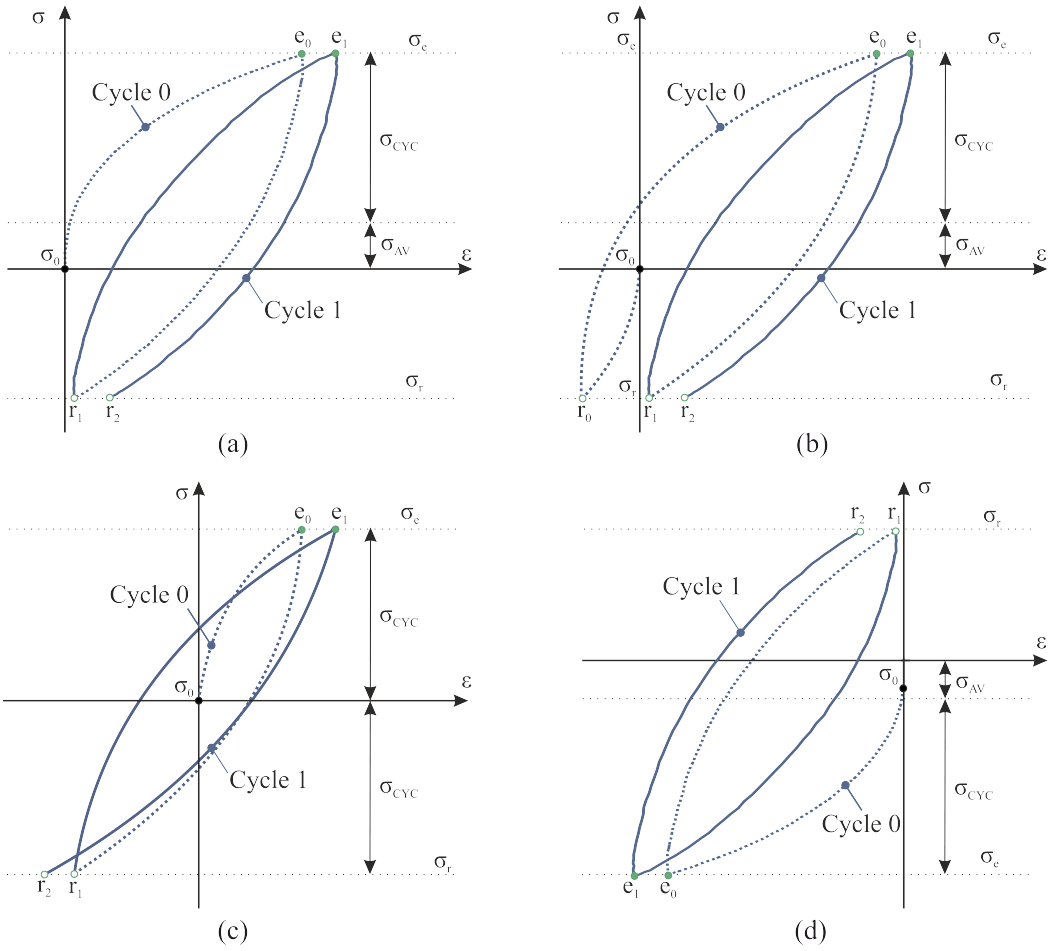

Figure 2.2: Definition of cycle 1 (and cycle 0) for (a) cycles with a positive bias $\sigma_{av} > 0$ (b) cycles with a positive bias $\sigma_{av} > 0$ but negative initial loading (c) cycles with a no bias $\sigma_{av} = 0$ (d) cycles with a negative bias $\sigma_{av} < 0$

2.2 Loading characterisation

Characterisation of cyclic loading is essential for interpretation of the cyclic response. For pile tests, cyclic load is typically characterised by (Leblanc et al., 2010b):

$$\zeta_b = \frac{\sigma_e}{\sigma_R} \qquad \zeta_c = \frac{\sigma_r}{\sigma_e} \tag{2.3}$$

The measure ζ_c describes the degree of load reversal or loading symmetry, and allows definition of loading categories: two-way, partial two-way, one-way and partial one-way. Examples are shown later in Figure 2.9 and Table 2.4. The parameter ζ_b describes the maximum load magnitude relative to an arbitrary reference stress σ_R. With σ_e and σ_r defined in previous section, ζ_c is well-defined ($-1 \leq \zeta_c \leq 1$), and is independent of load direction, i.e. extension or compression.

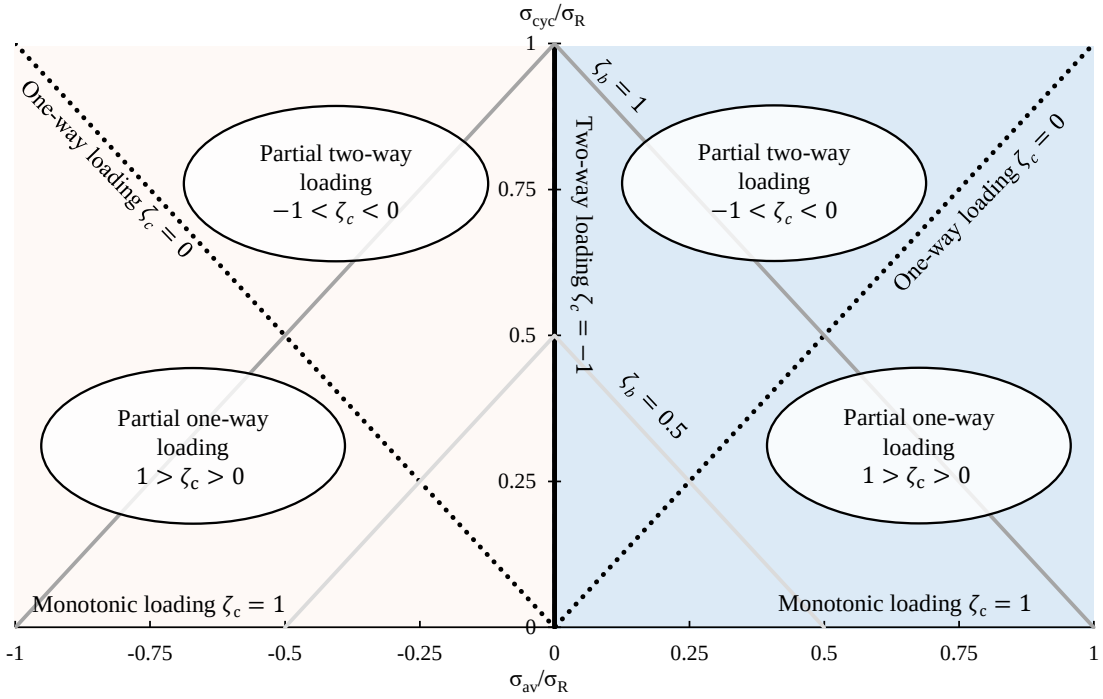

Figure 2.3: Relation between $\sigma_{av}, \sigma_{cyc}$ and ζ_b, ζ_c

In element testing, loading tends to be characterised by (Andersen, 2015):

$$\sigma_{cyc} = \frac{\sigma_e - \sigma_r}{2} \qquad \sigma_{av} = \frac{\sigma_e + \sigma_r}{2} \tag{2.4}$$

where σ_{cyc} defines the cyclic amplitude, while σ_{av} defines the degree of load bias. It not clear which pair of parameters (ζ_b, ζ_c) or $(\sigma_{cyc}, \sigma_{av})$ best characterise cyclic loading, but it is worth deriving the relationships between the two sets of parameters:

$$\zeta_b = \frac{1}{\sigma_R}(\sigma_{av} + \sigma_{cyc}) \qquad \zeta_c = 1 - \frac{2\sigma_{cyc}}{(\sigma_{av} + \sigma_{cyc})} \tag{2.5}$$

$$\sigma_{cyc} = \frac{\zeta_b}{2}(1 - \zeta_c)\sigma_R \quad \sigma_{av} = \frac{\zeta_b}{2}(1 + \zeta_c)\sigma_R \quad \frac{\sigma_{av}}{\sigma_{cyc}} = \frac{1 + \zeta_c}{1 - \zeta_c} \tag{2.6}$$

Figure 2.3 presents these relationships graphically. Charts similar to this are often used in element testing to define the loading regimes of a suite of cyclic tests, with individual tests represented by single points in normalised σ_{av} and σ_{cyc} coordinates. These form the framework for the NGI style contour diagrams, as detailed in Section 4.1. Loading type (defined by ζ_c and labelled in Figure 2.3) can be extracted by considering areas between limiting ζ_c values of -1 and 1. Contours of increasing ζ_b fan

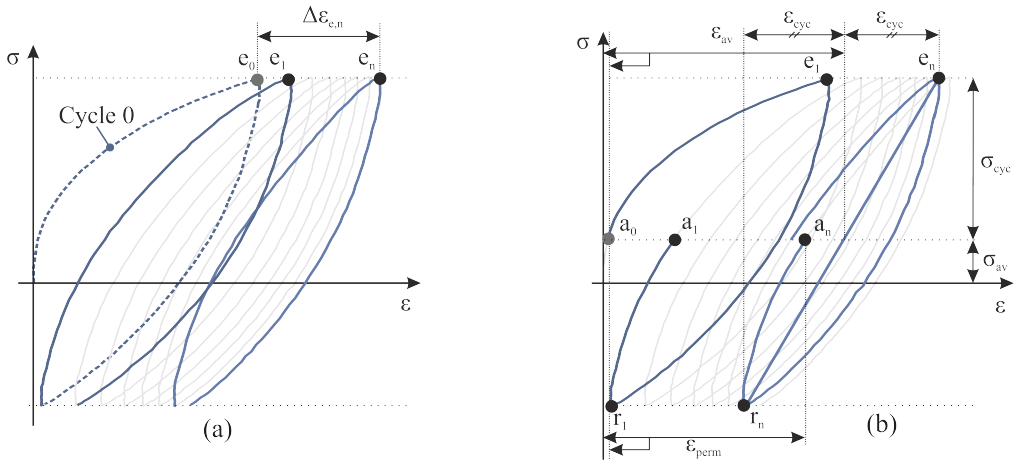

Figure 2.4: Typical strain per cycle definitions in: (a) pile testing literature (e.g. Abadie, 2015) (b) element testing literature (e.g. Andersen, 2015)

outwards from the origin. Considering cyclic triaxial CU_{cyc} tests, the right hand side of the plot ($\sigma_{av} > 0$) represents compression tests whilst the left hand side ($\sigma_{av} < 0$) represents extension tests. In pile tests and cyclic simple shear DSS_{cyc} tests, where the response is assumed isotropic with load direction, the plot may be reduced to $\sigma_{av} \geq 0$ only.

It should be noted there is no consistent method for defining σ_R. For pile tests this is often defined at some limiting rotation or pile head displacement (e.g. ULS conditions $\theta_R = 2°$ or $u_R = 0.1D$), whilst in element testing the initial consolidation pressure (σ_{vc} or p') or some measure of ultimate strength (e.g s_U or q_f) are typically used. Importantly, this means that ζ_b, and normalised values of σ_{av} and σ_{cyc} may not be directly comparable across sources.

2.3 Definition of strain per cycle

Ratcheting is defined as the permanent strain developed under cyclic loading, and requires the definition of a strain per cycle. However, this has been defined in numerous different ways by different authors. For pile tests, the accumulated rotation at peak load, $\Delta\varepsilon_{e_n}$ (often presented as $\Delta\theta$) is commonly used to measure strain per cycle, as shown in Figure 2.4a. Although commonly used, this definition couples permanent strain with stiffening or softening behaviour. Additionally, strain is defined at the point of maximum load, which is inconsistent with the idea of ratcheting being related to a permanent strain.

In element testing, cyclic strain ε_{cyc} (or sometimes resilient strain $\varepsilon_{res} = 2\varepsilon_{cyc}$) refers to the temporary strain generated within each load cycle. This is not pursued here as the same behaviour can be quantified by stiffness (see section 2.4). Average strain ε_{av} defines the strain mid-way between the cycle extrema e and reversal r and is commonly used to describe ratcheting. Permanent strain ε_{perm} is also occasionally used and is defined at σ_{av} on reloading, as shown in Figure 2.4b. Both ε_{av} and ε_{perm} are taken either from consolidated zero load or from the beginning of the first cycle. Although ε_{av} minimises coupling of ratcheting with stiffness change, accumulated strain is not well-defined. Accumulated rotation is commonly used in pile testing to consider the strain caused solely by cyclic loading (neglecting the monotonic response). However, this is not in common use in element testing literature.

Neither of the definitions used in pile and element tests avoids the coupling of ratcheting and stiffness change while also having a well-defined accumulated value. To help explore alternative definitions for ratcheting, Figure 2.5 presents various points which may be used to define strain at a given cycle number: at the extreme load σ_e (e), at the load reversal σ_r (r), at σ_{av} on reloading (a), at σ_{av} on unloading (b), at the minimum absolute value of stress on reloading (l), and at minimum absolute value of stress on unloading (u).

Nine potential definitions for strain at a given cycle number are then presented in Table 2.1. Of the nine potential definitions, ε_M is deemed to be the best definition. ε_M is the average of the strain developed at σ_{av} on unloading and reloading, and defined in terms of points a_n and b_n . This definition minimises conflation of stiffness change or change in hysteresis loop shape with ratcheting and also has a well-defined accumulated strain value $\Delta\varepsilon_M$.

2.4 Definition of stiffness per cycle

A number of authors have reported the evolution of secant stiffness across each cycle with cycle number. The loading stiffness k_{l_n} and unloading stiffness k_{u_n} are commonly used (e.g. Leblanc et al., 2010b; Abadie, 2015; Guo et al., 2018; Wichtmann and Triantafyllidis, 2018). However, these definitions couple stiffness change with ratcheting for open loops. Table 2.2 presents two alternative stiffness definitions: k_{f_n}

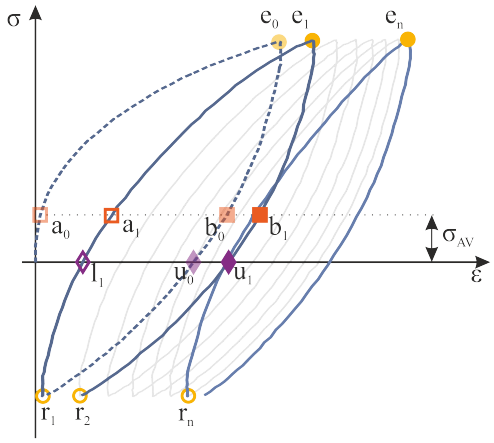

Figure 2.5: Key points for alternative definitions.

Table 2.1: Alternative definitions for ratcheting strain ε_{x_n} and accumulated strain $\Delta\varepsilon_{x_n}$. Definitions corresponds to cycle n

Definitions	Well-defined $\Delta\varepsilon$	Notes
$\varepsilon_{e_n} = \varepsilon(e_n)$ $\Delta\varepsilon_{e_n} = \varepsilon(e_n) - \varepsilon(e_0)$	✓	Couples stiffness change with ratcheting. Equivalent to ε_{p_n} as used in pile testing publications.
$\varepsilon_{r_n} = \varepsilon(r_n)$ $\Delta\varepsilon_{r_n} = \varepsilon(r_n) - \varepsilon(r_1)$	×	Couples stiffness change with ratcheting. Accumulated strain not well defined.
$\varepsilon_{l_n} = \varepsilon(l_n)$ $\Delta\varepsilon_{l_n} = \varepsilon(l_n) - \varepsilon(l_1)$	×	Couples hysteresis loop shape change with ratcheting. Accumulated strain not well defined.
$\varepsilon_{u_n} = \varepsilon(u_n)$ $\Delta\varepsilon_{u_n} = \varepsilon(u_n) - \varepsilon(u_0)$	✓	Couples hysteresis loop shape change with ratcheting.
$\varepsilon_{a_n} = \varepsilon(a_n)$ $\Delta\varepsilon_{a_n} = \varepsilon(a_n) - \varepsilon(a_0)$	✓	Couples hysteresis loop shape change with ratcheting. Equivalent to ε_{perm} for element tests.
$\varepsilon_{b_n} = \varepsilon(b_n)$ $\Delta\varepsilon_{b_n} = \varepsilon(b_n) - \varepsilon(b_0)$	✓	Couples hysteresis loop shape change with ratcheting.
$\varepsilon_{Q_n} = \frac{1}{2}(\varepsilon(l_n) + \varepsilon(u_n))$ $\Delta\varepsilon_{Q_n} = \varepsilon(Q_n) - \frac{1}{2}\varepsilon(u_0)$	×	Defined at most unloaded point. May couple stiffness change with ratcheting.
$\varepsilon_{av_n} = \frac{1}{2}(\varepsilon(e_n) + \varepsilon(r_n))$ $\Delta\varepsilon_{av_n} = \varepsilon(av_n) - \frac{1}{2}\varepsilon(e_0)$	×	Commonly used in element testing literature.
$\varepsilon_{M_n} = \frac{1}{2}(\varepsilon(a_n) + \varepsilon(b_n))$ $\Delta\varepsilon_{M_n} = \varepsilon(M_n) - \varepsilon(M_0)$	✓	Deemed to be the best definition.

the inverse of the average of loading and unloading flexibilities and k_{m_n} the mean of the unloading and reloading stiffness. Choosing either k_{f_n} or k_{m_n} minimises coupling of ratcheting and stiffness change. The definition k_{f_n} is preferred as, given that the displacement response is of concern, it seems sensible to average flexibilities. k_{f_n} is presented schematically in Figure 2.6, alongside the previous definitions.

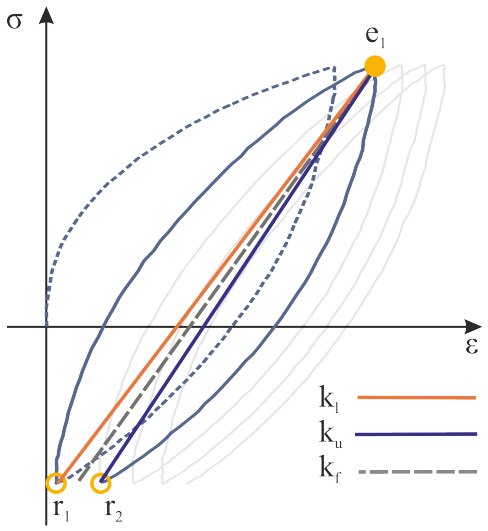

Figure 2.6: Alternative definitions for loop stiffness

Table 2.2: Options for stiffness definitions

Definition	Notes
$k_{l_n} = \frac{\sigma(e_n - \sigma(r_n)}{\varepsilon(e_n) - \varepsilon(r_n)}$	Loading stiffness as used by (e.g. Abadie, 2015). Couples stiffness with ratcheting behaviour.
$k_{u_n} = \frac{\sigma(e_n - \sigma(r_{n+1})}{\varepsilon(e_n) - \varepsilon(r_{n+1})}$	Unloading stiffness as used by (e.g. Leblanc et al., 2010b). Couples stiffness with ratcheting behaviour.
$k_{f_n} = 2\frac{k_{l_n} k_{u_n}}{k_{l_n} + k_{u_n}}$	Central cycle stiffness. Calculated as inverse of average of reloading and unloading flexibilities. Decouples stiffness from ratcheting behaviour. Proposed definition
$k_{m_n} = \frac{1}{2}(k_{l_n} + k_{u_n})$	Average of reloading and unloading stiffness. Decouples stiffness from ratcheting behaviour

2.5 Definition of energy loss factor per cycle

Cyclic energy dissipation is generally quantified for a closed hysteresis loop by a metric proportional to the ratio of hysteretic energy loss E_H to maximum 'stored elastic energy' E_E. E_H is represented by the area enclosed by the loop and E_E is defined at the maximum load, as indicated in Figure 2.7a and defined in terms of the extreme load σ_e , extreme strain ε_e and secant stiffness k :

$$E_E = \frac{1}{2}\sigma_e \varepsilon_e = \frac{\sigma_e^2}{2k} \tag{2.7}$$

$$E_H = \oint \sigma d\epsilon \tag{2.8}$$

In soil mechanics the 'damping ratio' ξ has been commonly used to characterise

soil dissipation (e.g. Kramer, 1996; Taborda et al., 2016; Abadie, 2015:

$$\xi = \frac{1}{4\pi}\left(\frac{E_H}{E_E}\right) \tag{2.9}$$

However, this definition is inconsistent with definitions in structural dynamics where the ratio of hysteretic energy loss to maximum stored elastic energy (or a proportional ratio) is instead called an 'energy loss factor' η. Whereas the 'damping ratio' specifically describes the ratio of viscous damping to critical damping for a SDOF (single degree of freedom) viscously damped system. The energy loss factor η is then typically defined as the energy lost per radian of the cycle divided by the maximum stored elastic energy (Inman, 2014). This is the reciprocal of the 'quality factor', Q , often used for describing resonant systems Green, 1955, such that:

$$\eta = \frac{1}{Q} = \frac{1}{2\pi}\left(\frac{E_H}{E_E}\right) \tag{2.10}$$

To avoid confusion with structural dynamics and be consistent with literature on dissipative systems, energy loss is characterised here using the energy loss factor η defined by Inman (2014). η is therefore equal to twice the 'damping ratio' proposed by Kramer (1996) and commonly used in soil mechanics, and is bound as $0 \leq \eta \leq 4/\pi$.

This energy loss factor is system-dependent and energy loss in the soil body is just one contributor to a system's overall energy loss. For pile tests, the boundary conditions (in the case of model tests) and pile roughness may impact the system's energy loss, while for element tests energy may be lost to friction at the end platens.

E_E and E_H are easily defined for closed loops, but adaptation is needed for non-closing loops which occur with ratcheting or when multi-amplitude loading is applied. Taborda et al. (2016) define E_E and E_H for multi-amplitude loading, where the energy loss is calculated incrementally from the previous loading increment to the current strain. Their method may be applied to either the reloading (η_{Tl}) or unloading (η_{Tu}) half cycles, or the average of η_{Tl} and η_{Tu} can be calculated (η_T) to estimate energy loss over the whole cycle. However, energy dissipation due to ratcheting is not considered. Abadie (2015) defines E_E and E_H to account for dissipation due to ratcheting (defined η_A here). However the definitions are only valid for constant amplitude, one-way loading. These definitions of E_E and E_H are presented schematically in Figure 2.7b and 2.7c, and the resulting energy loss factors are summarised in in Table 2.3.

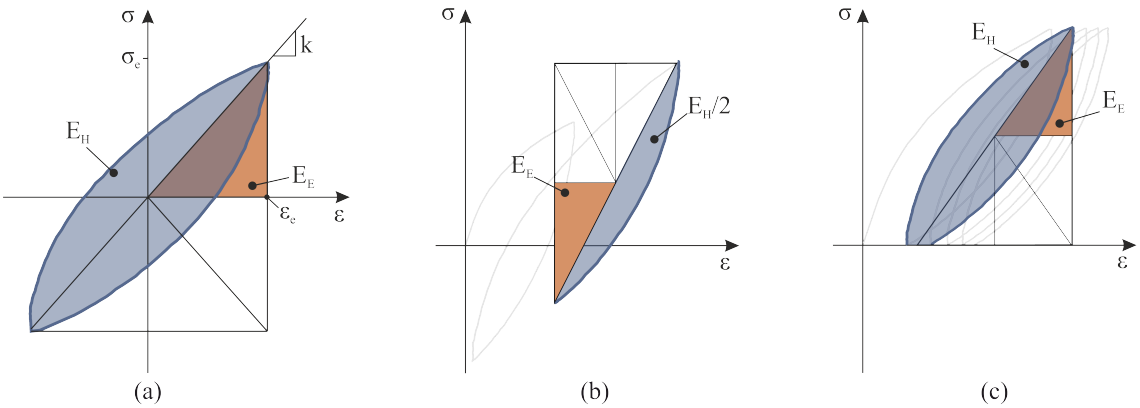

Figure 2.7: Definitions of E_H and E_H (a) for a closed hysteresis loop (b) following Taborda et al. (2016) on unloading (c) following Abadie (2015)

The hysteretic energy loss E_H may be more generally defined by integration of the response from r_i to r_{i+1} for cycle i as:

$$E_H = \int_{r_i}^{e_i} \sigma d\varepsilon + \int_{e_i}^{r_{i+1}} \sigma d\varepsilon \tag{2.11}$$

Figure 2.8 visualises the calculation of E_H for three different non-closing hysteretic responses: with open loops (e.g. positive ratcheting $\varepsilon_{r_{i+1}} - \varepsilon_{r_i} > 0$) and crossing loops (e.g. negative ratcheting $\varepsilon_{r_i+1} - \varepsilon_{r_i} < 0$); and with positive and negative values of σ_r . The sign of ζ_c and the direction of ratcheting relative to the direction of average load impact E_H . This definition of E_H remains robust for negative ratcheting (such as is seen in CU_{cyc} with a small compressive bias but much weaker extensive strength) or convex hysteresis loops (such as seen during gapping in a pile test).

A new energy loss factor, η_I is defined using the rigorous definition for hysteretic energy loss, where the central cycle stiffness k_f is used to define the maximum elastic energy E_E:

$$\eta_I = \frac{E_H}{2\pi E_E} = \frac{4k_f}{\pi(\sigma_e - \sigma_r)^2}\left(\int_{r_i}^{e_i} \sigma d\varepsilon + \int_{e_i}^{r_{i+1}} \sigma d\varepsilon\right) \tag{2.12}$$

For a closed loop η_I is equivalent to the definition of Inman (2014), and equivalent to the definition of Abadie (2015) for constant amplitude one-way loading. The definition is also equivalent to *Method 0* presented by Løvholt et al. (2020).

2.6 Impact of definitions on observed behaviour

Figure 2.9 presents the cyclic response of model piles and element tests in sand and clays, details of which can be found in Table 2.2. The cyclic response is presented

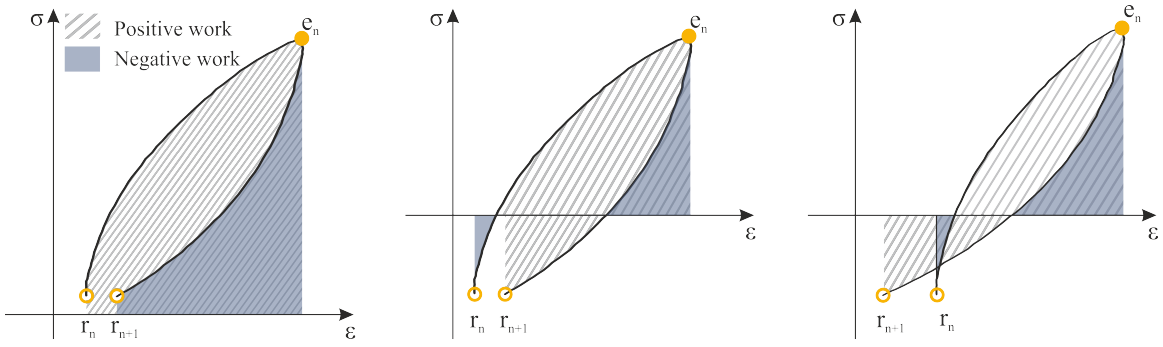

Figure 2.8: Visualisation of calculation of hysteretic energy loss E_H by integration: a) Positive ratcheting, $\zeta_c > 0$; b) $\zeta_c > 0$; c) Negative ratcheting, $\zeta_c > 0$

in terms of the stress-strain response (moment - rotation $(M - \theta)$ for the pile tests, deviator stress - axial strain $(q - \varepsilon_z)$ for the CU_{cyc} tests and shear stress – shear strain $(\tau - \gamma)$ for the DSS_{cyc} tests. Only the first 5 cycles are shown for clarity and are presented alongside: the strain per cycle ε , the secant stiffness per cycle k , and the energy loss factor per cycle η . Various definitions for ε , k and η (presented in Tables 2.1, 2.2 and 2.3) are used to highlight the impact of the choice of definitions. In general, ratcheting (increase in ε) is observed under 1-way and partial 1-way loading for both systems, secant stiffness k increases under cyclic loading for the monopile in sand while softening is generally observed in the clay element tests, and there is a general trend for reduction in η under cycling, at least for less than 100 cycles.

The apparent strain response differs significantly with the strain per cycle definition. Case (a) exemplifies the impact of stiffness change on the strain at load reversals and load extrema (ε_r , ε_e): despite symmetrical movement of the pile, the stiffening

Table 2.3: Options for energy loss factor definitions

Definition	Notes
$\eta_T = \frac{1}{2\pi}\left(\frac{E_H}{E_E}\right)$	Follows the method of Taborda et al. (2016) to determine E_E and E_H on either reloading (η_{Tl}) or unloading (η_{Tu}), or takes the mean across a load-unload cycle (η_T). Does not account for energy dissipation due to ratcheting.
$\eta_A = \frac{1}{2\pi}\left(\frac{E_H}{E_E}\right)$	Follows methods proposed by Abadie (2015) to determine E_E and E_H . Accounts for energy dissipation due to ratcheting. Not well-defined for multi-amplitude loading or non 1-way loading.
$\eta_I = \frac{4k_f}{\pi(\sigma_e - \sigma_r)^2}\left(\int_{r_i}^{e_i} \sigma d\varepsilon + \int_{e_i}^{r_{i+1}} \sigma d\varepsilon\right)$	Applicable to general non-closing loops

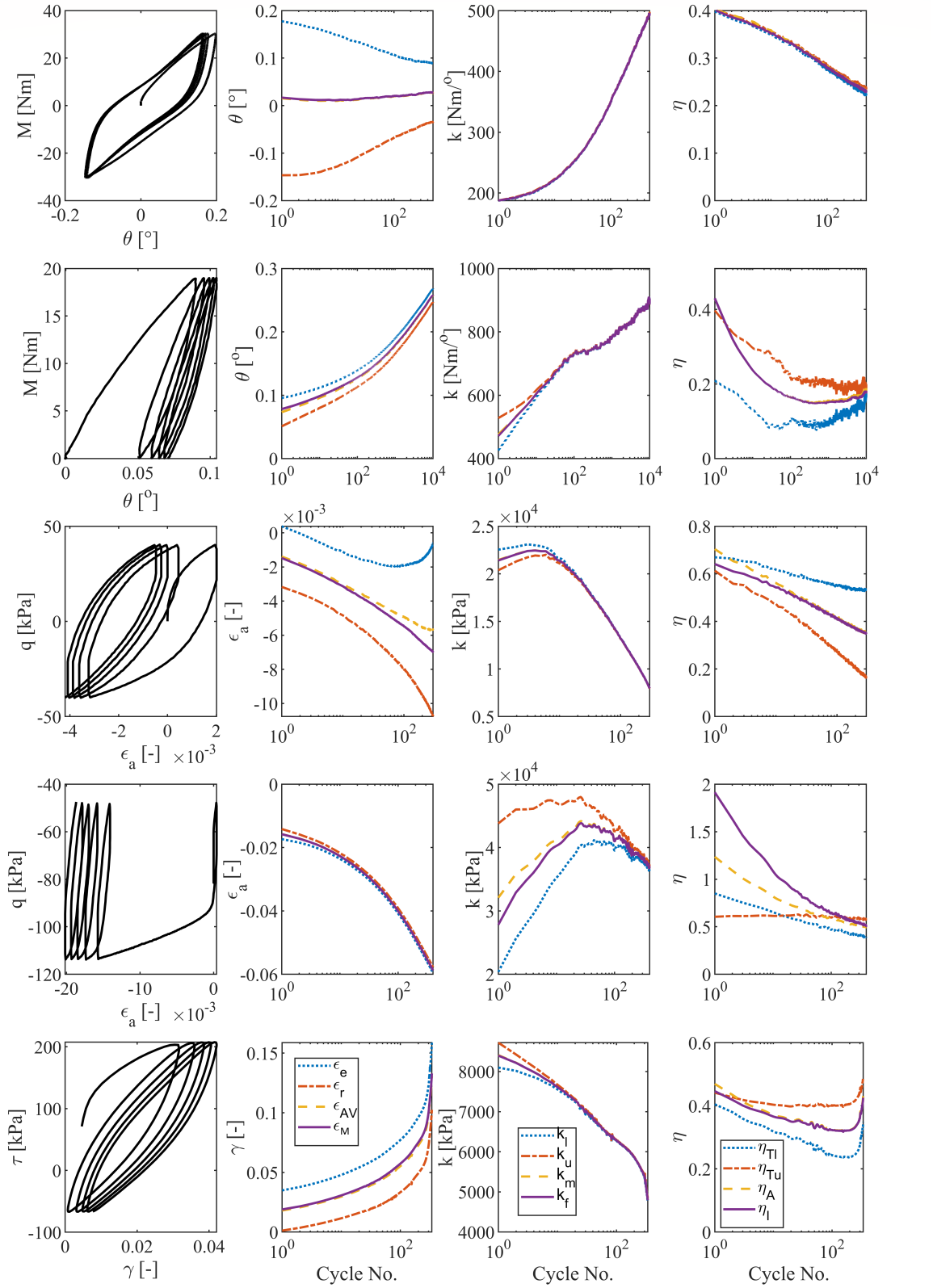

Figure 2.9: Impact of strain, stiffness and energy loss factor definitions for example pile, CU_{cyc} and DSS_{cyc} tests. See Table 2.4 for details.

behaviour causes changes in ε_r and ε_e which may be misinterpreted as ratcheting. In general, the average strain definition ε_{AV} as used in element testing and the proposed strain definition ε_M lead to similar results. The loading and unloading stiffness definitions k_l and k_u also differ significantly under some loading cases (particularly case (d)), due to asymmetry in the hysteretic response which may be related to ratcheting. The mean stiffness definitions lead to intermediate stiffness values, which better represent the stiffness across a cycle. There is no clear difference between the mean secant stiffness k_m and the proposed central secant stiffness k_f.

As expected, there is no clear variation in η for case (a) where the cycles are approximately closed and symmetric. However, the choice of definition for energy loss factor has a significant impact in other cases. The proposed definition for energy loss factor η_I generally leads to values between those obtained using the definitions of Taborda et al. (2016) on loading and unloading ($\eta_{Tl},\ \eta_{Tu}$), except in case (d) where partial 1-way loading is applied and only definition η_I accounts for the additional work due to the greater load magnitude.

2.7 Multi-amplitude

The consistent framework for defining cyclic loading and interpreting the cyclic response may be extended to multi-amplitude loading. This is focused on consistent presentation of the cyclic response and with the constant amplitude framework.The cyclic response is defined in terms of load and unload half-cycles, both starting and ending at load reversals. For each cycle (comprising a load and unload half-cycle) an extreme load σ_e , load-reversal load $\sigma_{r,l}$, unload-reversal load $\sigma_{r,u}$, load-average load $\sigma_{AV,l}$ and unload-average load $\sigma_{AV,u}$ may be defined, as shown in Figure 2.10.

Table 2.4: Test cases considered in Figure 2.9

	Description	Reference	ζ_c	Loading-type
a	Model monopile in dense, dry sand	Richards, 2020	-1	2-way
b			0	1-way
c	Cyclic triaxial (CU_{cyc}) test in NC Kaolin clay	Wichtmann and Triantafyllidis, 2018	-1	2-way
d			0.41	Partial 1-way
e	Cyclic Direct Simple Shear (DSS_{cyc}) test in OC North Sea clay	Private Communication See Table 3.1	-0.35	Partial 2-way

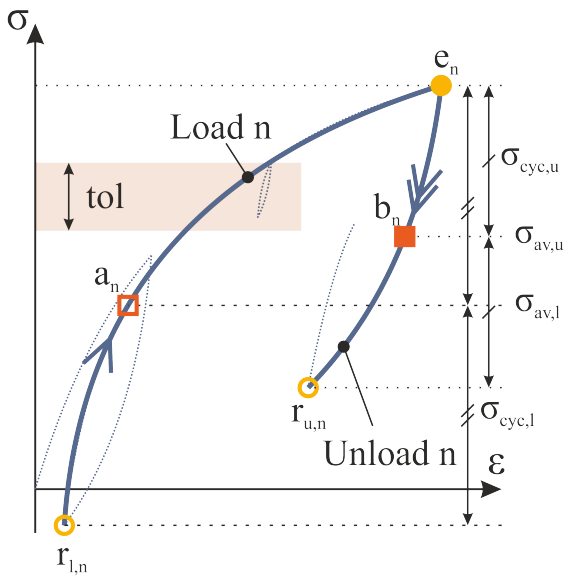

Figure 2.10: Multi-amplitude definitions

The extreme loads σ_e and reversal loads σ_r are defined at alternating load reversals. Across the data-set, $|\overline{\sigma_e}| \geq |\overline{\sigma_r}|$, and therefore ratcheting is generally expected in the direction of σ_e . It is also necessary to define a sensible cyclic threshold (labelled 'tol' in Figure 2.10) for multi-amplitude loading, to avoid counting noise as cycles.

The loading strain (ε_a) and unloading strain (ε_b) are defined (following Table 2.2) at the half-cycle average load σ_{AV} as shown in Figure 2.10. It is not appropriate to take the mean of these values for multi-amplitude loading, and plotting both ε_a and ε_b is recommended. The concept of accumulated strain becomes redundant for multi-amplitude loading, given that Cycle 0 is likely to be of arbitrary magnitude.

For stiffness, loading and unloading half-cycles are again considered, and the loading and unloading stiffness (k_l and k_u in Table 2.2) are calculated for each half-cycle. Again, it is not appropriate to take the mean value for multi-amplitude loading. The definitions for E_E and E_H presented by Taborda et al. (2016) are well-adapted for multi-amplitude loading. However, the resulting energy loss factors do not account for energy dissipation due to ratcheting.

2.7.1 Characterising realistic loading

In this section a realistic multi-amplitude load history is characterised and presented in a manner consistent with single-amplitude testing.

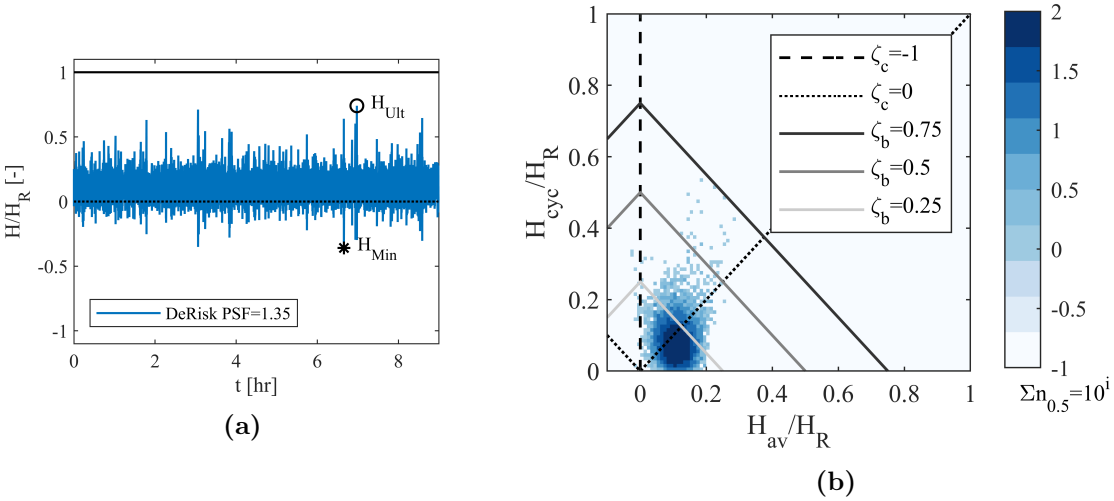

Figure 2.11: Normalised 100-year return storm (a) Continuous load history (b) Heat map of discretised half cycles $n_{0.5}$ indicates number of half cycles, colour intensity in logarithmic scale

The load history used is taken from Richards (2020) and originates from experimental readings of a prototype scale cylinder (representing a 7 m diameter monopile) subject to a 100-year return period storm in the North Sea (Bredmose et al., 2016). Further to the measured wave loading, Richards (2020) processed the data by: i) addition of constant wind loading, ii) application of a transfer function to model the structure's dynamic response, iii) projection of loads to constant eccentricity, iv) scaling to model-scale (for application to 1g model tests).

The resulting continuous load history, Figure 2.11a, is therefore representative of the combined horizontal load induced by a 9 hour storm. The maximum applied load, H_{Ult} is assumed to be equal to the maximum ULS design load. One may reasonably take the reference load, H_R as the maximum resistance of the structure. This has been back-calculated by following DNVGL-ST-0126 guidelines and using suggested safety factors specified as 1.35 for ULS (DNV-GL-ST-0437).

From the continuous load history in Figure 2.11a, individual half cycles may be derived as in Figure 2.10. Each load and unload represents a single half-cycle which can be characterised by a corresponding H_{av} and H_{cyc} and normalised by H_R. The full multi-amplitude loading may then be represented by counting the number of half-cycles corresponding to discrete packets of cyclic and average load. Figure 2.11b shows a heat map of a discretisation across the full range of the storm. The cyclic threshold is set to $H_{tol} = H_R/100$ such that extrema or minima which would result

in $2 * H_{cyc} < H_{tol}$ are not considered. This results in a total of 10500 half cycles which are counted in packets of width $H = H_R/100$ in H_{av} and H_{cyc}. The colours are representative of logarithmic values (base 10) such that 0 is indicative of $10^0 = 1$ half cycle.

The majority of half-cycles occur at ζ_b less than 0.25 or 0.35, and are either partial one-way, one-way or partial two-way. The higher magnitude half cycles tend to be partial two-way, $\zeta_c < 0$ ($H_{cyc} > H_{av}$). The most extreme load does not exceed $\zeta_b \approx 0.75$. This is sensible given the assumption of a total partial safety factor of 1.35, i.e. $\zeta_b = 1/1.35 = 0.74$, and shows how the choice of H_R is the main factor in mapping the magnitude of the loads. Importantly, presentation in this way this allows the appraisal and comparison of multi-amplitude loads against constant amplitude tests. This is valuable since fundamental understanding of the cyclic response is often derived from constant amplitude tests but would probably be validated against multi-amplitude tests.

Chapter 3

Modelling of element tests at 0D

3.1 Introduction

Unlike most engineering materials, soils are extremely variable. At any site, geotechnical properties vary laterally and with depth. This is especially true for an offshore wind farm where turbines are located hundreds of metres apart. Any practicable constitutive model must therefore be calibrated to site-specific conditions from practical tests.

Simple laboratory tests can be undertaken on soil samples retrieved offshore to ascertain monotonic and cyclic soil properties for design. Well established direct simple shear (DSS) and triaxial (CU and CD) tests impose shear stresses to a sample whilst controlling normal stresses (to varying degrees). Each has advantages and disadvantages (as discussed in Section 1.3.2) but both offer an example of soil response under controlled conditions. They are therefore useful guides for establishing key properties of geotechnical models.

Cyclic element tests are, however, time-consuming (often days per test, e.g. Ushev, 2017) and little value is added by repeating conventional testing in this work. Therefore, the focus has been on exploring literature and industry contacts for test data already compiled. This has been a successful exercise with hundreds of tests obtained across six clay units, which can be used to inform a constitutive model.

Constitutive models provide a relationship between stress σ and strain ε , and can be implemented at various scales. Continuum models (3D) typically used for FEA (Finite Element Analysis) are the most complex, such that for each force a corresponding strain may be found. Macro (0D) models are much less costly computationally,

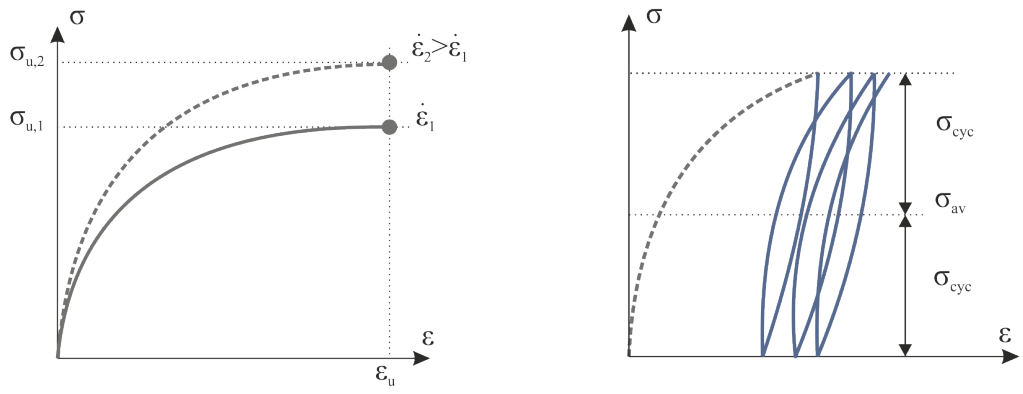

(a) **(b)**

Figure 3.1: (a) Monotonic loading and the effects of rate (b) Cyclic, stress controlled testing described by average σ_{av} and cyclic σ_{cyc} load with initial virgin loading shown in grey

isolating a single stress and conjugate strain component of the system, (e.g. shear stress τ and shear strain γ) and are useful for model development. In the hyperplasticity framework, extension to the continuum is straight-forward (e.g. Houlsby et al., 2017), allowing for much of the formulation to be studied at the simpler, faster, 0D scale.

In this chapter, the database of acquired tests are presented with the results summarised to establish important features of behaviour to be modelled. This is presented with a view to formulating kinematic-hardening, rate-dependent, 0D, hyperplasticity models in total stress space. Ultimately, this chapter aims to model clay behaviour at element test level by (in a similar manner to Whittle and Kavvadas, 1994):

(i) Establishing behaviour

(ii) Formulating the model

(iii) Establishing a procedure for determining input parameters

(iv) Evaluating predictions

These are presented progressively in terms of constitutive mechanisms: monotonic non-linearity, rate-dependency and cyclic behaviour.

Figure 3.1 shows examples of idealised response in general stress-strain space which broadly depicts each mechanism. A monotonic increase in stress at a fixed strain rate

Table 3.1: Available cyclic element tests data sets in clays. Properties and tests type of each unit is described alongside respective stress σ and strain ε like variable, reference stress σ_R, period of sinusoidal loading T, maximum number of cycles applied N_{max}, and if post-cyclic strength $s_{u,PC}$ was tested

Key	Soil Properties and Reference	Test Type	σ	ε	σ_R	T	N_{max}	$s_{u,PC}$
COW	Cowden Till $I_p = 17\%$, $K_0 = 1.5$, $s_{u,c} = 125kPa$ (Ushev, 2017)	$CAUcyc$	q	ε_a	$2s_{u,c}$	$5min$	3500	✓
DRAM	Drammen Clay $I_p = 27\%$, $OCR = 1, 4, 40$ (Andersen, 2015)	DSS_{cyc} CAU_{cyc} CIU_{cyc}	τ q	γ ε_a	$s_{u,DSS}$ $2s_{u,c}$	$10s$	1000	✓
KAO	Kaolin $I_p = 12.2\%$, $K_0 = 0.55 - 1$, $M_c = 0.88$ (Wichtmann and Triantafyllidis, 2018)	CAU_{cyc} CIU_{cyc}	q	ε_a	p'_0	$\dot{\varepsilon} = 0.02 - 1\%/min$	10000	×
KAO - UWA	NC Kaolin $I_p = 34\%$, $\sigma_{v,c} = 70kPA$, $M_c = 0.92$ (Zografou et al., 2019)	DSS_{cyc}	τ	γ	$s_{u,DSS}$	$10s$	1500	×
NSCA NSCB	Anonymised units of North Sea Clay $I_p = 20\%$, $OCR = 1 - 9$ Private Communication	DSS_{cyc} CAU_{cyc}	τ q	γ ε_a	$\sigma_{v,c}$ p'_0	$4s$	5000	✓
WEN	NC Wenzhou soft clay $I_p = 32\%$, $K_0 = 0.55$, $s_{u,c} = 26kPa$ (Guo et al., 2018)	CAU_{cyc}	q	ε_a	$2s_{u,c}$	$1s$	10000	×

is shown in grey in Figure 3.1a with a corresponding non-linear response; if the strain rate is changed (shown dashed) the response will vary. Figure 3.1b shows a typical constant stress amplitude cyclic test described by bias σ_{av} and amplitude σ_{cyc}. Initial loading is the same as a monotonic increase in Figure 3.1a and is hence shown dashed. Subsequent unloading and reloading produce a response which is dependent upon history and loading but which builds upon monotonic and rate behaviour.

3.1.1 Database of element tests in clay

Table 3.1 summarises data sets acquired through private communication or from open source. If not otherwise stated each set consists of sinusoidal stress-controlled cyclic tests alongside monotonic tests to failure at a constant strain rate. These consist of:

- COW - A laboratory investigation as part of the PISA project which explored the properties of a stiff over-consolidated glacial till sampled at the Cowden test site near Hull, UK (Zdravković et al., 2019). Data is acquired directly from plots in the thesis by Ushev (2017).

- DRM - A comprehensive testing program undertaken by NGI (Norwegian Geotechnical Institute) in the 1970s and 1980s, from which the acquired

measurements form the basis for the first 'contour diagrams' (Andersen, 1976; Andersen et al., 1980). Some data is freely available in publications by NGI (Andersen, 2015) with additional information acquired during a visit to NGI.

- KAO - Tests on Kaolin clay at Karlsruhe University. Continuous data is available for download from Wichtmann's personal website (Wichtmann, 2019). Cyclic tests are applied 'sawtooth' at constant displacement rate $\dot{\varepsilon}$ rather than period. All tests are cycled to some amplitude about the initial deviatoric stress (q_0) which is applied drained ($q_{av} = q_0$).

- KAO-UWA - Tests at the University of Western Australia (UWA) which aimed to inform the construction of cyclic contour diagrams. Data acquired directly from figures in the paper by Zografou et al. (2019). Staged DSS_{cyc} tests with varied orders of constant amplitude packets are also presented.

- NSC - A site investigation of two units of stiff glacial tills from an offshore wind farm site in the North Sea. Full stress strain data was obtained from Ørsted and is subject to a 'Non-funded personnel protocol' signed in January 2018, which requires anonymization before publication. Samples were taken from five boreholes 2-5km apart and at depths of 4-9m (NSCA) and 26-33m (NSCB). Information on initial stiffness has been found in the literature but references are omitted to preserve confidentiality of the data. Where required this is assumed to be similar to COW.

- WEN - *CU* tests undertaken by researchers at Wenzhou and Zhejiang Universities (Cai et al., 2017; Guo et al., 2018). Data has been obtained from the above papers with additional information, such as monotonic tests at varied rates and individual loop response, kindly shared by the authors.

Figure 3.2 shows a Casagrande diagram populated (where possible) with the clay units, indicating low to high plasticity clays. The North Sea Clay units (NSCA and NSCB) are assumed similar to Cowden till (COW) in this respect.

Figure 3.3 shows the locations of individual cyclic tests on an interaction diagram of average σ_{av} and cyclic stress σ_{cyc} where the stress quantity σ corresponds to either τ or q (as defined in eq. 1.4), see Table 3.1. Blue markers represent cyclic undrained

triaxial tests (CU_{cyc}), and the red markers either truly undrained or constant volume direct simple shear tests (DSS_{cyc}). It should be noted that the co-ordinates are highly dependent on the choice of reference stress σ_R defined in Table 3.1. This controls the distance from the origin of the plot (magnitude ζ_b), but does not change its polar coordinate angle (loading type ζ_c).

For CU_{cyc} tests, stress quantity q is normalised either by initial mean effective stress $p_0^{'}$ or by twice the undrained shear strength in compression, $s_{u,c}$. For DSS_{cyc} tests τ is normalised either by vertical stress $\sigma_{v,c}$ or by undrained shear strength $s_{u,DSS}$. An ultimate strength (s_u) would intuitively best represent a reference stress causing failure at $(\sigma_{av}+\sigma_{cyc})/\sigma_R = 1$ for a monotonic test. However, s_u is not always readily available for the consolidation conditions and is rate-dependent in magnitude. Those not normalised by the undrained shear strength are shown as filled solid markers.

The majority of the DSS_{cyc} tests are subject to two-way loading ($\sigma_{av}/\sigma_R = 0$), a product of current cyclic loading design methodology. CU_{cyc} tests are predominantly in compression ($\sigma_{av}/\sigma_R > 0$) with a few extension tests in each set. Generally, in cyclic laboratory testing, stress is applied at a faster rate than in monotonic tests; increased capacity due to rate-dependency means that in some tests $(\sigma_{av}+\sigma_{cyc})/\sigma_R > 1$ but $N > 1$ cycles are achieved before failure.

3.1.2 A note on modelling choices

Multi-surface kinematic hardening models formulated in the hyperplasticity framework can be constructed in series or parallel configurations, can be rate-dependent or

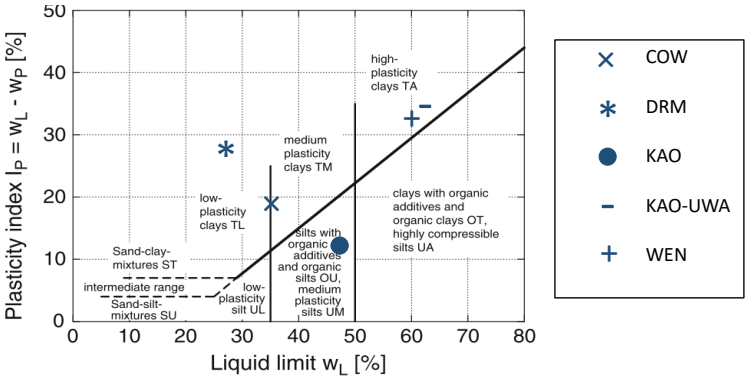

Figure 3.2: Casagrande diagram showing location of clays in database

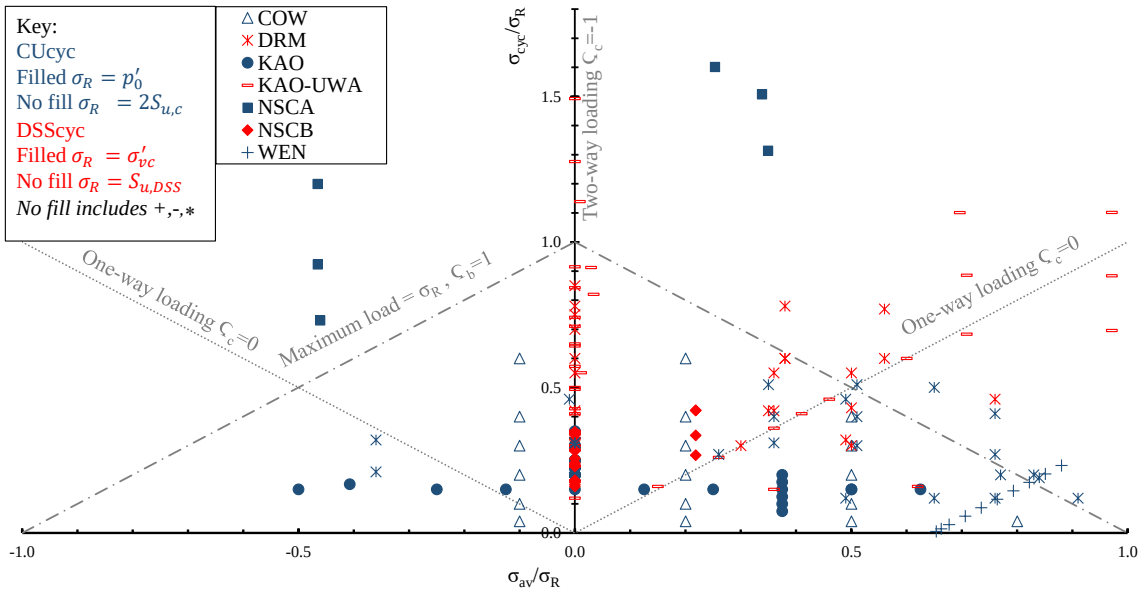

Figure 3.3: Location in cyclic stress space of available cyclic element tests in clays. Blue markers represent cyclic undrained triaxial tests (CU_{cyc}), and the red markers either truly undrained or constant volume direct simple shear tests (DSS_{cyc}). Fill indicates normalisation parameter, where markers $+, *, -$ are also considered 'no fill'.

rate-independent and may be applied at various scales.

Macro (0D) models are used in the following two chapters and here represent the integrated response of the soil element in terms of a stress σ and conjugate strain ε. Consequently, these are total stress models in which changes to effective stress are not explicitly included. Here, the σ and ε variables represent some shear stress and conjugate strain. The actual variables depend on the test conditions (and available data) and are shown for each data-set in Table 3.1.

Previous authors (e.g. Abadie, 2015) have rightly suggested that it is most intuitive to construct models in series when computing strains from a stress input (because strains are additive), and in parallel for strain input (where stresses are additive). Since the vast majority of cyclic element tests are stress-controlled, series models are used here.

Finite-element computations of pile response typically require strain-controlled constitutive models (and therefore parallel models are more easily implemented, Chapter 6). Consistency between element and pile scale is paramount for calibration. However, in series and parallel configuration, the internal variables have slightly different meanings and therefore equivalence is not guaranteed. A summary of work

investigating the implications of these differences is presented and discussed in Chapter 5 and therefore not discussed further here.

The 0-D, series models used are fully defined in the hyperplasticity framework by an energy and dissipation function. Incremental behaviour is derived. In this thesis, the Helmholtz free energy f is presented alongside the dissipation function d and yield function y or flow potential w. Stress and strain control is achieved by deriving the incremental forms as per standardised methods (e.g. Houlsby and Puzrin, 2006) outlined in Appendix A. Stress-time histories are used as model input such that constant period stress cycles, or constant strain rate tests such as those presented by Wichtmann and Triantafyllidis (2018) are easily computed (in practice these could also be computed using strain-time histories).

A single example of a model calibrated and applied to measured data is typically presented for each additional mechanism. Where inclusion of model complexity affects the previous mechanism, suitable re-calibration methods are explained. Calibrated parameters for each data-set are presented alongside a suitable goodness-of-fit measurement.

All tests included in this chapter are undrained (or constant volume). Whilst drained stress history (consolidation) before undrained testing is considered, total stress models are not capable of predicting consolidation. Each set of parameters is therefore applicable only for samples with the same initial stress conditions. Suitable normalisation can, however, make the monotonic response consistent at various initial consolidation pressures (Jeanjean et al., 2017; Whyte et al., 2020).

3.2 Monotonic non-linearity

In laboratory tests, application of an increasing shear stress produces a non-linear strain response typically characterised by an initial elastic stiffness G_0, an ultimate strength s_u, and an ultimate strain ε_u. Pre-failure, a curve of decreasing tangential stiffness G is observed. It is well reported that increasing confining stress, p'_0 (CU) or σ'_v (DSS), increases initial stiffness G_0 and strength s_u (e.g. Andersen et al., 1988).

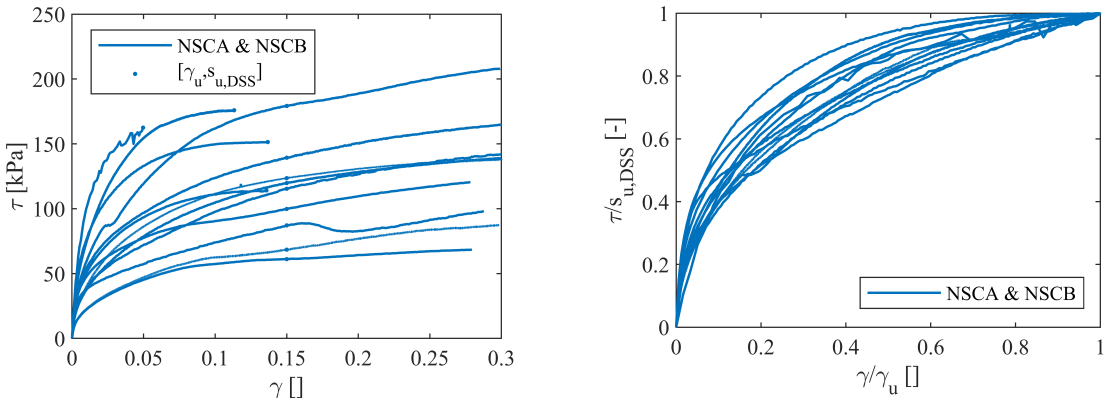

(a) **(b)**

Figure 3.4: 13 *DSS* tests on NSCA and NSCB (a) Original data (b) Normalised by ultimate stress s_u and strain γ_u

3.2.1 Isotropic response - DSS

Figure 3.4a shows examples of 13 *DSS* tests at various OCR and σ'_v, illustrative of a typical monotonic response in terms of shear stress τ and shear strain γ. γ_u is the ultimate strain corresponding to a peak in shear stress $s_{u,DSS}$ or a maximum of 15%. The same tests are shown normalised in Figure 3.4b in which non-linear pre-peak curves of decreasing stiffness are a common feature. In *DSS* conditions isotropy can be assumed such that the response is independent of loading direction. This no longer holds in triaxial conditions (*CUc* and *CUe*) adding complexities further discussed in section 3.2.2.

The non-linear response on loading can be captured by multiple linear surfaces of varying stiffness and yield strength. A multi-surface plasticity model with kinematic hardening in series configuration is depicted in Figure 3.5 and consists of an elastic element (H_0) in series with a number of units (i) each consisting of a spring (H_i) and slider (K_i). This is described globally by stress (σ) and strain (ε), alongside internal kinematic variables (α_i) identified with the plastic strain and conjugate stress (χ_i).

The model is defined in the hyperplasticity framework by the Helmholtz free energy f and dissipation d or yield functions y_i (See Appendix A for derivation of incremental behaviour):

$$f = \frac{H_0}{2}\left(\varepsilon - \sum_{i=1}^{Ns} \alpha_i\right)^2 + \sum_{i=1}^{Ns} \frac{H_i}{2}\alpha_i^2 \tag{3.1}$$

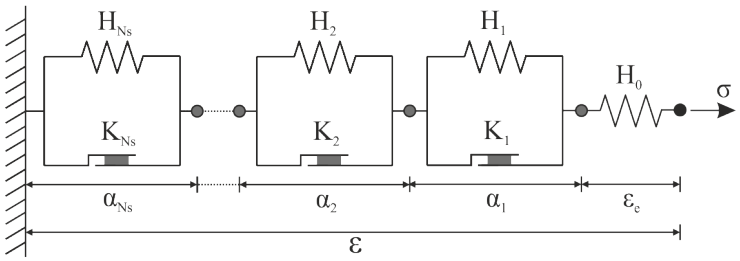

(a)

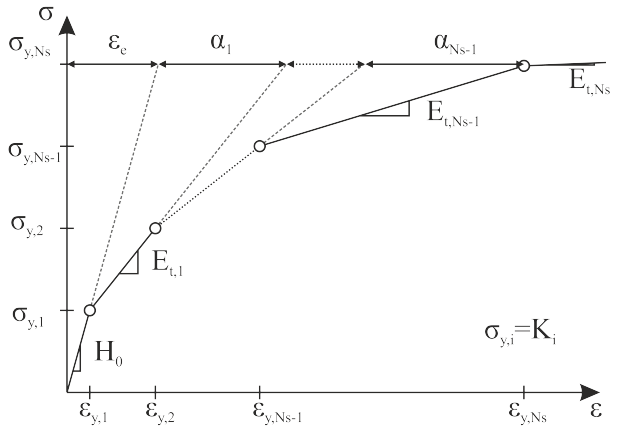

(b)

Figure 3.5: Rate-independent series kinematic hardening model with corresponding monotonic response

$$d = \sum_{i=1}^{Ns} K_i |\dot{\alpha}_i| \tag{3.2}$$

$$y_i = |\chi_i| - K_i \tag{3.3}$$

For a stress input, the incremental strains can be written (See Appendix A for full derivation):

$$d\varepsilon = \frac{d\sigma}{H_0} + \sum_{i=1}^{Ns} d\alpha_i \tag{3.4}$$

and if the surface is yielding :

$$d\alpha_i = \frac{d\sigma}{H_i} \tag{3.5}$$

The strengths of each slider range from first yield ($K_1 = \sigma_{y,1}$) to the ultimate strength of the system ($K_{Ns} = \sigma_{y,Ns}$), with the corresponding spring stiffness H_i ensuring that the tangent stiffness $E_{t,i}$ matches that of the material stress-strain response, Figure 3.5b. The larger the number of surfaces N_s, the smoother the curve. Upon unloading, Masing rules are observed as a natural consequence of the model.

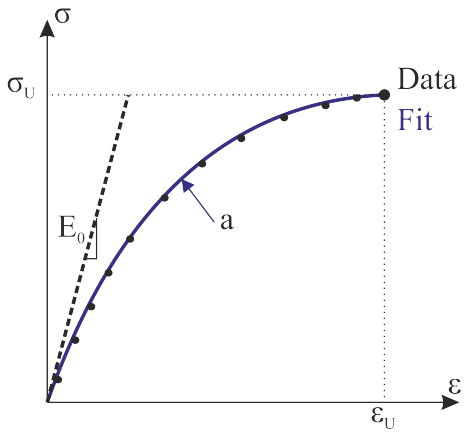

Figure 3.6: Example monotonic fit to data with Jeanjean curve parameters

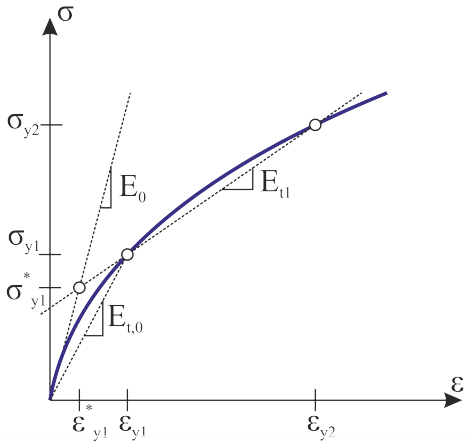

Figure 3.7: Correction of initial yield point to correct for true initial stiffness

H_i and K_i can be found by either directly deriving from the monotonic data (a 'data-driven' approach) or by fitting to an expression and then finding values at discrete points. With the latter: noise is eliminated; positive, reducing stiffness is guaranteed (such that $\partial\sigma/\partial\varepsilon > 0$); and normalised parameters between tests and sample types can be compared. This process is independent of the adopted function with much work already establishing suitable relationships of non-linear soil response.

Previous work at Oxford University investigating model pile tests in sands adopted a 'power law' (Abadie, 2015) for the stress-strain curve, though poor fit to small strain stiffness changes is found when applied to clay element tests. The PISA conical soil reaction curve (Byrne et al., 2019b), and the 'Jeanjean' hyperbolic tangent curve (Jeanjean et al., 2017) have little to differentiate them. Both require similar parameters G_0, s_u, ε_u, along with a curvature/fitting parameter named n or a for PISA and (Jeanjean et al., 2017) respectively.

In this chapter the Jeanjean equation is used, owing to a better-conditioned curvature parameter, a. To fit to the element tests included in this study, the PISA n parameter ($0 \leq n \leq 1$) is close to its upper limit of 1 and therefore sensitive to small changes, whilst the Jeanjean fitting parameter $a \approx 2$. The equation is described in general σ–ε as:

$$\frac{\sigma}{\sigma_u} = \frac{tanh\left(a\left(\frac{\varepsilon - \frac{\sigma}{E_0}}{\varepsilon_u - \frac{\sigma_u}{E_0}}\right)^{0.5}\right)}{tanh(a)} \tag{3.6}$$

To fit the relationship to element test data, E_0, σ_u and ε_u are fixed and a optimised. $\varepsilon_u = \gamma_u$ and $\sigma_u = s_u$ are defined as a pair at peak stress or 15% strain. $E_0 = G_0$ and

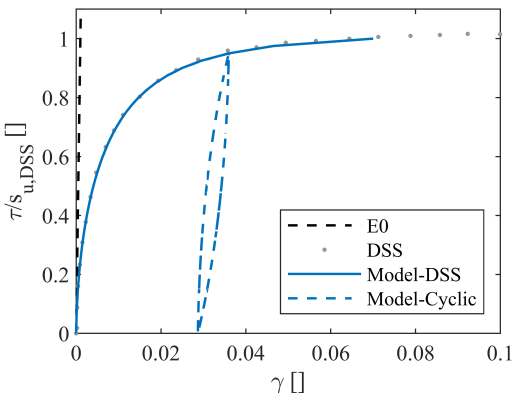

Figure 3.8: Parallel Kinematic Hardening Model prediction of *DSS* test in Drammen Clay with OCR=4

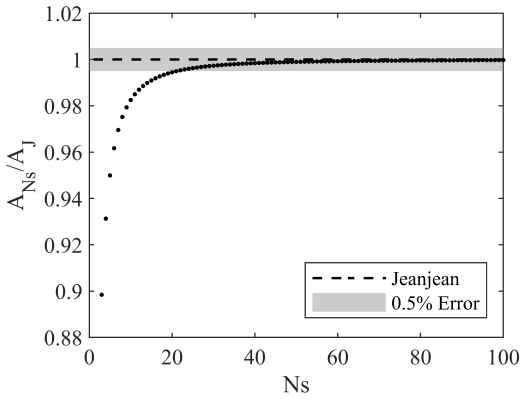

Figure 3.9: Area under monotonic test to failure with number of surfaces, normalised by analytical area (Model as in Figure 3.8)

can be found by bender element tests, or estimated via a known relationship with s_u (Andersen et al., 1988). The curvature parameter a is then derived by a proportional least-squares optimisation as shown schematically in Figure 3.6.

The small strain fit of the curve is important as this describes the initial loading and unloading stiffness. Typically, assuming constant sampling frequency and strain rate, there will be fewer data points in this zone and many data-points as the test reaches failure. Optimisation can be biased by only considering a percentage of the total data, for instance 80% would only consider data points in which $\sigma < 0.8\sigma_u$. Here the decision is made manually (but could be optimised) and is trade-off between accuracy at relatively small strains and as a whole. Typically 90% is found to be suitable.

K_i and H_i are then derived for an appropriate number of surfaces N_s following methods described by Houlsby et al. (2017). Firstly, surface yield strengths are defined at equally spaced stresses such that $\sigma_{y,i} = K_i = \sigma_u \frac{i}{N_s}$. Corresponding yield strains, $\varepsilon_{y,i}$ can then be found by rearranging Equation 3.6 and noting $\sigma = \sigma_{y,i}$:

$$\varepsilon_{y,i} = \left(\varepsilon_u - \frac{\sigma_u}{E_0}\right)\left(\frac{atanh\left(\left(\frac{\sigma_{y,i}}{\sigma_u}\right)tanh(a)\right)}{a}\right)^2 + \frac{\sigma_{y,i}}{E_0} \tag{3.7}$$

from which tangent stiffnesses $E_{t,i} = \frac{\sigma_{y,i+1}-\sigma_{y,i}}{\varepsilon_{y,i+1}-\varepsilon_{y,i}}$ and surface stiffnesses H_i are calculated knowing:

$$\frac{1}{E_{t,i}} = \frac{1}{H_0} + \sum_{i=1}^{Ns} H_i \tag{3.8}$$

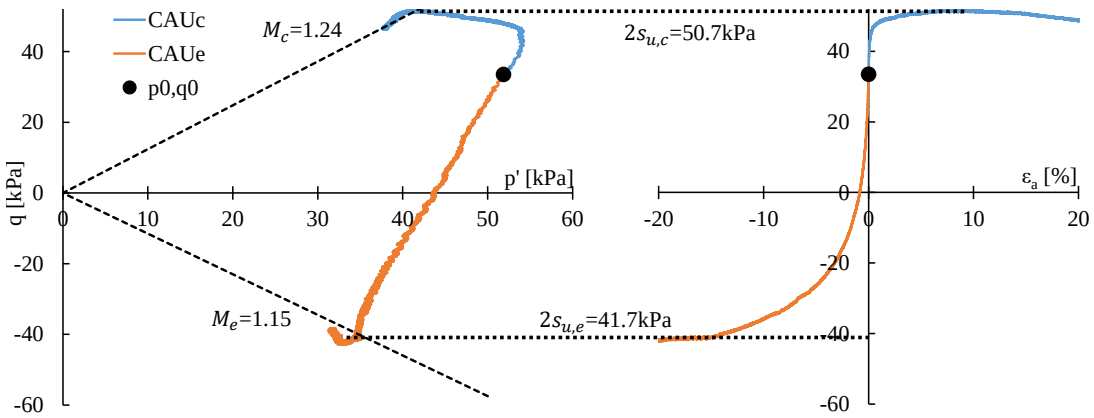

Figure 3.10: $CAUc$ and $CAUe$ tests on Wenzhou clay

In order to ensure the correct initial stiffness $H_0 = E_0$, the first yield point may be adjusted by changing the initial yield strain $\varepsilon_{y,1}$ by altering K_1 as depicted in Figure 3.7, such that:

$$\begin{aligned} \varepsilon^*_{y,1} &= \frac{\sigma_{y,1} - E_{t,1}\varepsilon_{y,1}}{E_0 - E_{t,1}} \\ \sigma^*_{y,1} &= K^*_1 = \frac{E_0}{\varepsilon^*_{y,1}} \end{aligned} \tag{3.9}$$

Figure 3.8 shows a model prediction of a DSS test in Drammen Clay. Upon unloading Masing rules are observed (shown dashed), such that fixed amplitude stress cycling traverses the same loop for N cycles. Comparison of calibrated parameters are discussed in section 3.2.3.

By fixing yield locations to points on the curve and assigning linear surfaces, the curved area (and therefore dissipative behaviour) is not conserved. However, the severity is reduced with increasing number of surfaces as the linear surfaces approach the curve. Figure 3.9 quantifies the sensitivity by calculating the area beneath a 'Jeanjean' curve with the same parameters as Figure 3.8, and that reproduced by a kinematic hardening model with N_s surfaces. Once 40 surfaces are employed (as is typically used in this thesis) the error is less than 0.1% and therefore considered negligible.

3.2.2 Anisotropic response - CUc and CUe

The previous section showed it is possible to capture non-linear isotropic behaviour using a multi-surface kinematic hardening model calibrated to backbone response

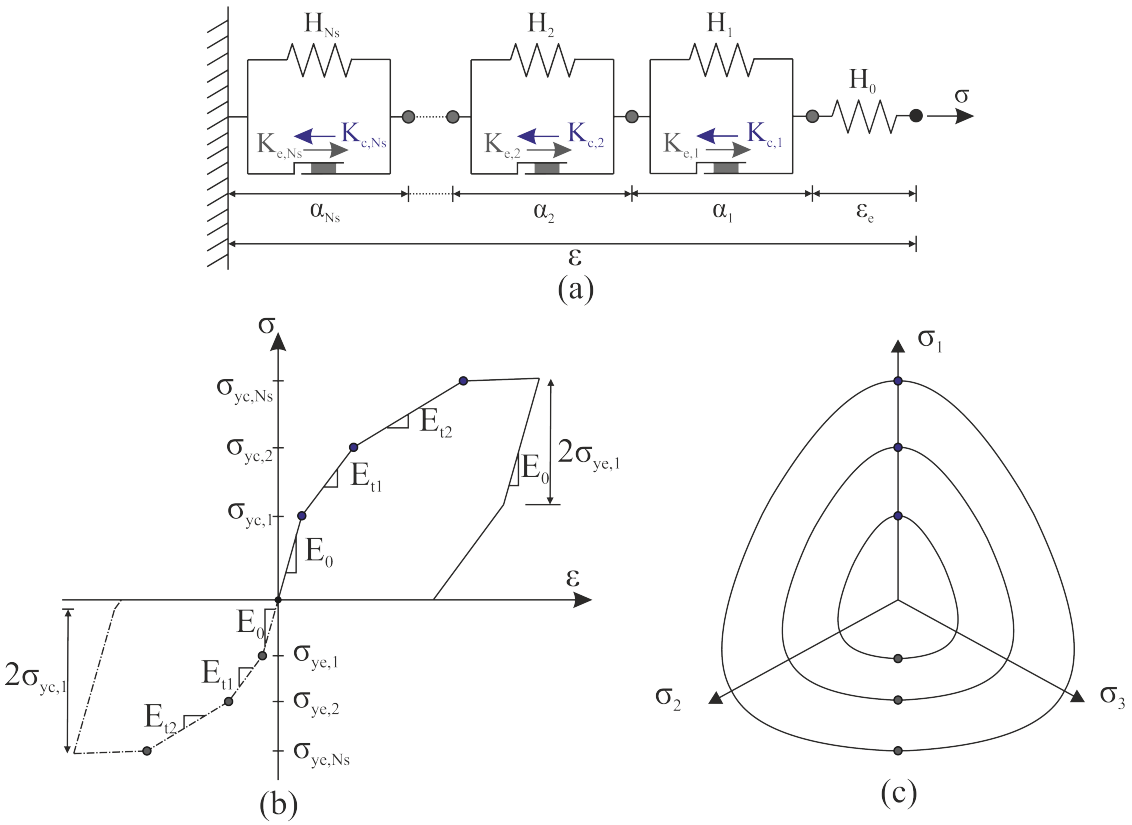

Figure 3.11: (a) Rate-independent series kinematic hardening model with asymmetrical yield strengths (b) corresponding monotonic response and (c) conceptual equivalent continuum yield surface diagram, based upon an anisotropic yield surface model proposed by Sheng et al., 2000

with examples given in *DSS* conditions. Two further complexities are introduced when considering *CU* tests such as that shown in Figure 3.10:

- Stress Anisotropy: The response of a sample will vary with loading direction. If this is limited to triaxial extension and compression it can be seen that shear strength s_u and pre-failure strain response differs. Typically $s_{u,c} > s_{u,e}$.

- Consolidation: The response will also differ depending upon sample consolidation and therefore stress history. In triaxial testing the sample may have been subject to anisotropic consolidation ($CAUc$) in which $q_0 \neq 0$, requiring careful consideration for total stress models.

Asymmetry can be introduced in the 0D model by changing the strengths (K) of each unit to incorporate compressive and extensive behaviour so that the plastic

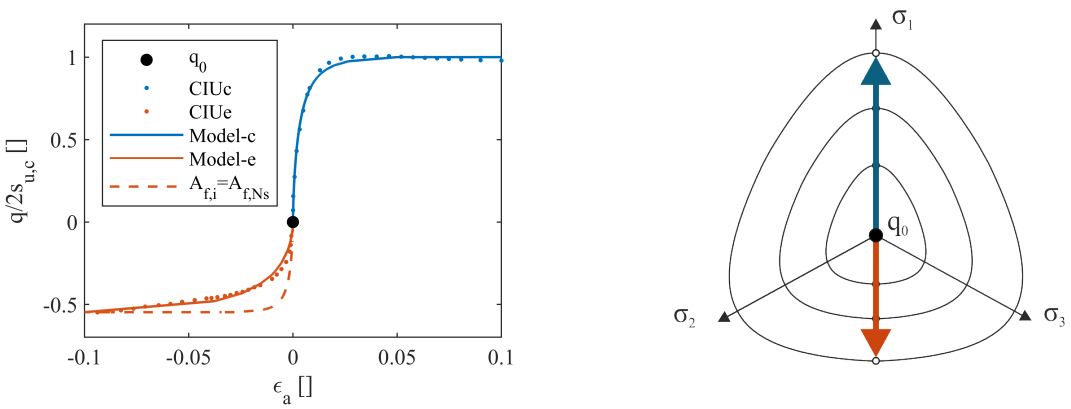

(a) (b)

Figure 3.12: Isotropically consolidated triaxial behaviour (a) Asymmetrical model calibrated to Drammen Clay OCR=4 CIUc and CIUe tests (b) Equivalent continuum yield surface diagram

dissipative and yield behaviour 3.2 changes to:

$$d = \sum_{i=1}^{Ns} K_{c,i}\langle\dot{\alpha}_i\rangle + K_{e,i}\langle-\dot{\alpha}_i\rangle \tag{3.10}$$

$$y_i = |\chi_i| - \mathcal{H}(\chi_i)K_{c,i} - \mathcal{H}(-\chi_i)K_{e,i} \tag{3.11}$$

where $\mathcal{H}(X)$ corresponds to the Heaviside step function. The model is shown schematically in Figure 3.11. The stiffnesses are equal $H_{c,i} = H_{e,i} = H_i$, such that the differential form of the energy function (Equation 3.1) remains constant. Initially constant scaling across all i surfaces is applied such that:

$$K_{e,i} = A_{f,i}.K_{c,i} \tag{3.12}$$

where $A_{f,i}$ is an asymmetry factor that can be estimated as $A_{f,i} = A_{f,Ns} = \frac{s_{u,e}}{s_{u,c}}$. It should be noted that the $A_{f,Ns}$ may not be equivalent to the ratio of the critical state line gradients (M_e/M_c), simply because the undrained strength may occur at different mean effective stress. This is the case in Figure 3.10 in which:

$$A_{f,i} = \frac{41.7}{50.7} = 0.82 \neq \frac{M_e}{M_c} = \frac{1.15}{1.24} = 0.9 \tag{3.13}$$

A truly anisotropic continuum model is shown schematically in Figure 3.11c, in which the asymmetrical yield strengths may be seen mapped in extensive and compressive directions.

An example of a model prediction of isotropically consolidated $CIUc$ and $CIUe$ tests on Drammen clay is shown in Figure 3.12a. A good prediction is achieved

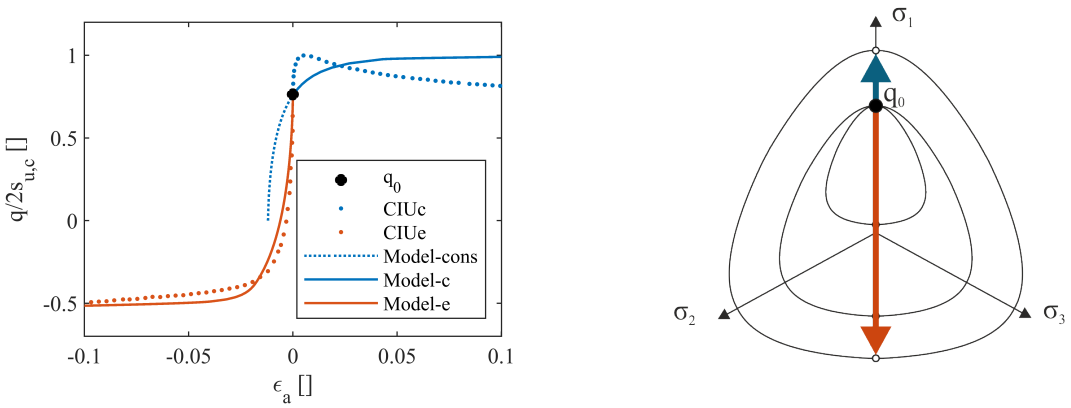

(a) **(b)**

Figure 3.13: Anisotropically consolidated triaxial behaviour (a) calibrated to Drammen Clay OCR=1 CAUc and CAUe tests (b) Equivalent Continuum yield surface diagram

with a final asymmetry factor $A_{f,Ns} = 0.55$. $A_{f,i}$ is allowed to differ with each surface provided the yield strengths continue to increase with surface number and ensuring that the final yield stress is equal to the ultimate extensive stress, giving the constraints to optimisation:

$$\sigma_{y,e,i+1} - \sigma_{y,e,i} = K_{e,i+1} - K_{e,i} > dK_{min} \tag{3.14}$$

$$K_{e,Ns} = \sigma_{e,u} \tag{3.15}$$

where $dK_{min} = \sigma_u/(3Ns)$ is used here. Figure 3.12a also shows a model in which $A_{f,i}$ is fixed, allowing less control of curvature. In Figure 3.12b each test tracks the yield surfaces along the σ_1 axis in triaxial compression (+ve) and extension (-ve) as shown by blue and orange arrows respectively.

Anisotropically consolidated triaxial tests are often undertaken to better recreate the assumed in-situ conditions (such as that shown in Figure 3.10). The sample is consolidated to a non-zero mean effective stress $p_0^{'}$ and deviator stress q_0, often termed K_0 consolidation (not to be confused with surface strength notation) where $K_0 = \frac{\sigma_{h,0}}{\sigma_{v,0}}$. If $K_0 < 1$, $\sigma_{h,0} < \sigma_{v,0} => q_0 > 0$ and vice versa if $K_0 > 1$, $q_0 < 0$.

The behaviour in both extension and compression now differs from an isotropically consolidated sample at the same $p_0^{'}$. Calibrating a total stress 0D model backbone-curve, which is capable of predicting both, is not trivial. The initial shearing to q_0 is drained such that p' changes will occur, not predicted by a total stress model. Prévost (1977) overcame this by applying q_0 undrained to a calibrated set of yield surfaces at

Table 3.2: Summary of evidence and modelling for monotonic shearing

Behaviour	Evidence	Modelling Technique	Calibration
Non-linear response with stifness reducing from an initial value G_0	Widely observed in all data-sets.	Multi-surface kinematic hardening.	Fit 'Jeanjean' relationship to data. From which strengths and stiffnesses of N_s surfaces may be calibrated.
Behaviour is stress-history dependent (OCR and consolidation conditions).	KAO DRM NSCA	Calibrated back-bone only applicable to consolidation conditions.	N/A
Anisotropy observed in CU tests. Weaker in extension than compression.	DRM COW WEN	Make yield strength direction dependent $K_{e,i} = A_{f,i}.K_{c,i}$ but keep stiffnesses the same.	Initially estimate constant $A_{f,i} = \frac{s_{u,e}}{s_{u,c}}$, if required vary $A_{f,i}$ may vary with surface.
Consolidation may be anisotropic such that $q_0 \neq 0$.	DRM COW WEN	Apply q_0 undrained to shift yield loci prior to true undrained shear tests.	Calibrate to either extension or compressive test post initial q_0. Accuracy decreases with magnitude of $\lvert q_0/2s_{u_c}\rvert$.

a known $p_0^{'}$. This is shown schematically in Figure 3.13b, where the anisotropic yield surfaces have been dragged to q_0, as before the blue and orange arrows show CAUc and CAUe tests respectively.

Figure 3.13a shows K_0 consolidated $CAUc$ and $CAUe$ tests in Drammen clay. The asymmetrical model has been calibrated to fit the extension test on unloading. The prediction shows initial undrained loading as a dotted line, representing consolidation to (p_0',q_0), followed by undrained shearing. Unsurprisingly the extension test (to which the yield strengths are calibrated) is predicted well. However, the compression test is too soft at initial shearing. This response is incorrect and importantly suggests that a total stress approximation of anisotropic consolidation works well only when K_0 values are close to 1.

3.2.3 Modelling summary and application to datasets

It is possible to predict the non-linear monotonic response of undrained laboratory shear tests for a sample at a known consolidation conditions using multi-surface kinematic hardening hyperplasticity models. Table 3.2 summarises the key observations, modelling techniques and calibration methods presented.

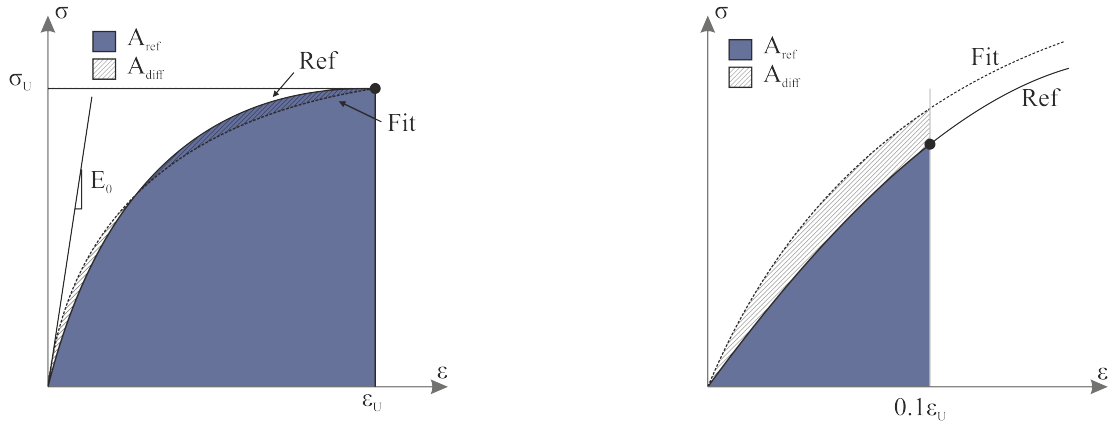

Figure 3.14: Quality of fit metric, edited from (Byrne et al., 2019b) (a) Ultimate fit, η_{ult} (b) small strain fit, $\eta_{s,d}$

In this section a model is calibrated, as previously presented, to each data set. This is evaluated in a similar way to Byrne et al. (2019b) by employing a quality of fit metric η. Ultimate η_{ult} and small strain η_{sd} (here as limited to $\varepsilon < 0.1\varepsilon_u$) quality of fit metrics are defined in σ-ε space in Figure 3.14 and are calculated by:

$$\eta = \frac{A_{ref} - A_{diff}}{A_{ref}} \tag{3.16}$$

where $0 \leq \eta \leq 1$. The closer to 1 the better the fit, here $\eta_{ult} > 0.9$ is assumed to represent a '*good*' fit.

Table 3.3 and Table 3.4 summarise the test conditions and calibrated parameters of the datasets used. Where more than one test is available an average is used for the function fitting. σ_u is taken as $s_{u,DSS}$ or $2s_{u,c}$ throughout but could be varied to allow focus on a specific area of the backbone (e.g. small strain applications), ε_u is then paired with σ_u. The curve fitting parameter a varies between 1 and 4 with a mean value of 2.35, closely following the results presented by Jeanjean et al. (2017).

For DSS and CIU tests the model matches measurements well. η_{sd} is typically lower than η_{ult} suggesting a worse fit at small strains, exaggerated by sparsity of data. In CAU conditions the Cowden ($q_0/2s_{u,c} = -0.1$) case is acceptable for all except the initial extension. However for Drammen OCR=1 the fit is poor (; the sample is highly anisotropically consolidated ($q_0/2s_{u,c} = 0.76$) and total stress anisotropic consolidation loses accuracy with magnitude of $|q_0/2s_{u,c}|$. Prediction of effective stress changes are, of course, not possible with a total stress model which limits the accuracy

Table 3.3: Summary of DSS data-sets, parameters fit to monotonic response, and goodness of fit values

KEY	σ_{vc} $[kPa]$	$s_{u,DSS}$ $[kPa]$	$\frac{E_0}{s_{u,DSS}}$	$\frac{\sigma_u}{s_{u,DSS}}$	ε_u	a	η_{ult}	η_{sd}
NSCA OCR1	70	61	750	1	0.15	1.36	0.98	0.95
NSCA OCR1	300	156	750	1	0.1	1.76	0.98	0.92
NSCB OCR3	325	176	750	1	0.11	1.47	0.97	0.84
DRM OCR1	392	84	1000	1	0.05	2.06	0.97	0.89
DRM OCR4	98	64	1000	1	0.09	2.74	0.97	0.95
KAO UWA	70	13	500	1	0.15	0.99	0.77	0.73
					Mean:	**1.73**	**0.94**	**0.88**

of predictions. Chapter 7 addresses development of models which might tackle this important issue.

Table 3.4: Summary of CU data-sets, parameters fit to monotonic response, and goodness of fit values

KEY	p_0 $[kPa]$	q_0 $[kPa]$	$s_{u,c}$ $(s_{u,e})$ $[kPa]$	$\frac{E_0}{2s_{u,c}}$	$\frac{\sigma_{u,c}}{s_{u,c}}$	$\varepsilon_{u,c}$ $(\varepsilon_{u,e})$	a	Af_{Ns}	$\eta_{ult,c}$ $(\eta_{ult,e})$	$\eta_{sd,c}$ $(\eta_{sd,e})$
DRM OCR1	264	193	127 (63)	1000	1	0.06 (0.1)	4.2	0.5	0.22 (0.96)	0.06 (0.80)
DRM OCR4	100	0	99 (52.5)	1000	1	0.07 (0.1)	3.19	0.53	0.98 (0.96)	0.98 (0.81)
COW	67	-25	125 (118)	1000	1	0.15 (0.07)	2.11	0.94	0.98 (0.90)	0.93 (0.61)
KAO	200	0	60 (-)	1000	1	0.15 (-)	2.05	(-)	0.97 (-)	0.91 (-)
						Mean:	**2.88**		**0.78 (0.94)**	**0.72 (0.74)**

3.3 Rate dependent response

3.3.1 Evidence

Fine-grained soils are viscous materials which exhibit creep when load is held and stress relaxation when strain is held (Vucetic, 2016). In DSS or CU conditions, a sample will typically behave as a stronger material if the rate of strain is higher, such that a higher undrained shear strength may be observed (See Figure 3.15). It is widely accepted that strength increases with the logarithm of strain rate (Yong and

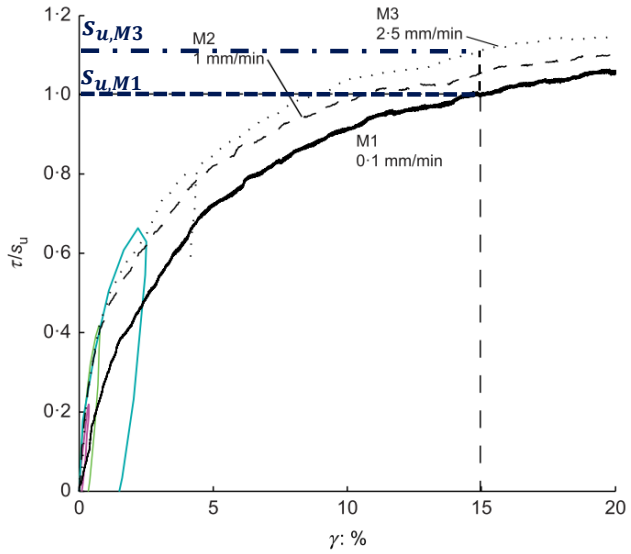

Figure 3.15: Varied rate monotonic *DSS* tests with initial cycles of cyclic tests (Edited from Zografou et al., 2019)

Japp, 1967; Vaid and Campanella, 1977; Lunne and Andersen, 2007) such that:

$$\sigma = \sigma_R + \alpha \ln\left(\frac{\dot{\varepsilon}}{\dot{\varepsilon}_R}\right) \tag{3.17}$$

where σ is the stress at rate $\dot{\varepsilon}$, along with a corresponding reference strain rate $\dot{\varepsilon}_R$ and stress σ_R measured at the same strain magnitude. α is a stress quantity which describes the rate of strength increase due to rate effects. Whilst σ may be measured at any strain value, typically undrained shear strengths are compared such that $\sigma = s_u$ ($\varepsilon \leq 15\%$). This can be rearranged to normalize α:

$$\frac{s_u}{s_{u,R}} = 1 + \eta \ln\left(\frac{\dot{\varepsilon}}{\dot{\varepsilon}_R}\right) \tag{3.18}$$

Such that $\eta = \alpha/\sigma_R$ is a dimensionless viscous parameter which follows similar notation to that used by Beuckelaers (2017). A typical value for clays is in the region of $\eta_{10} = \ln(10)\eta = 0.1$ representing a 10% increase in strength per order of magnitude increase in rate. Inversely, strength decreases logarithmically with reducing strain rate. However, reported tests (e.g. Vaid and Campanella, 1977; Lunne and Andersen, 2007) show that this trend is no longer true at very low rates, asymptotically slowing to some strength $s_{u,\dot{\varepsilon}\to 0}$ as the strain rate tends to zero (infinitely slow).

A more sophisticated approach to describe this type of behaviour is rate-process theory, in which the process is assumed to be thermally activated. Mitchell and Soga

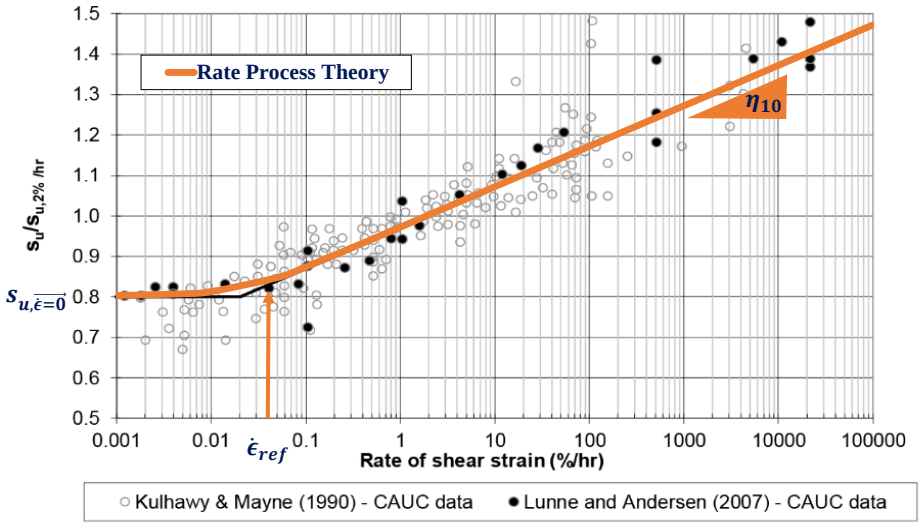

Figure 3.16: Strength increase due to strain-rate (Edited from Liedtke et al. (2019)

(2005) describe the basis of the theory and present its potential use in soil mechanics employing an inverse hyperbolic sine relationship (see also Houlsby and Puzrin, 2006). At low strain rates strength increases linearly, whilst at high strain rate the increase remains logarithmic. The point at which behaviour changes is indicated by a reference strain rate, ($\dot{\varepsilon}_{ref}$) such that the Equation 3.18 becomes:

$$\frac{s_u}{s_{u,\dot{\varepsilon}\to 0}} = 1 + \frac{\eta_{10}}{\ln(10)} \sinh^{-1}\left(\frac{\dot{\varepsilon}}{\dot{\varepsilon}_{ref}}\right) \tag{3.19}$$

Figure 3.16, shows normalised undrained shear strength ($s_u/s_{u,2\%/hr}$) against strain rate $\dot{\varepsilon}$ for two data sets (Liedtke et al., 2019); Equation 3.19 is shown in orange with values of $\dot{\varepsilon}_{ref} = 0.04\%/\text{hr}$, $\frac{s_{u,\dot{\varepsilon}\to 0}}{s_{u,2\%/hr}} = 0.8$ and $\eta_{10} = 0.1$. The relationship captures behaviour at high and low strain rates well.

As previously mentioned η_{10} typically takes a value of 0.05-0.1 for fine grained soils. $s_{u,\dot{\varepsilon}\to 0}$ is a strength value and is material and consolidation dependent. $\dot{\varepsilon}_{ref}$ is a slow rate and appears to be somewhere between 0.01-0.06%/hr (Vaid and Campanella (1977) suggest a value of $\dot{\varepsilon}_{ref} = 0.06\%/\text{hr}$). This can also be reported as test time to failure, $T_{u,ref} = \frac{\varepsilon_u}{\dot{\varepsilon}_{ref}}$ which for $\varepsilon_u = 10\% => 1month < T_{u,ref} < 1week$. For most typical laboratory tests, the strain rate will be larger than $\dot{\varepsilon}_{ref}$ and therefore on the logarithmic portion of the curve. Provided one takes $\dot{\varepsilon}_{ref}$ as some suitably small value and changes $s_{u,\dot{\varepsilon}\to 0}$ accordingly, the predicted s_u should be accurate.

Although typically reported as an increase in s_u (at failure strain), some authors have observed that rate-dependent strength changes appear to be strain dependent

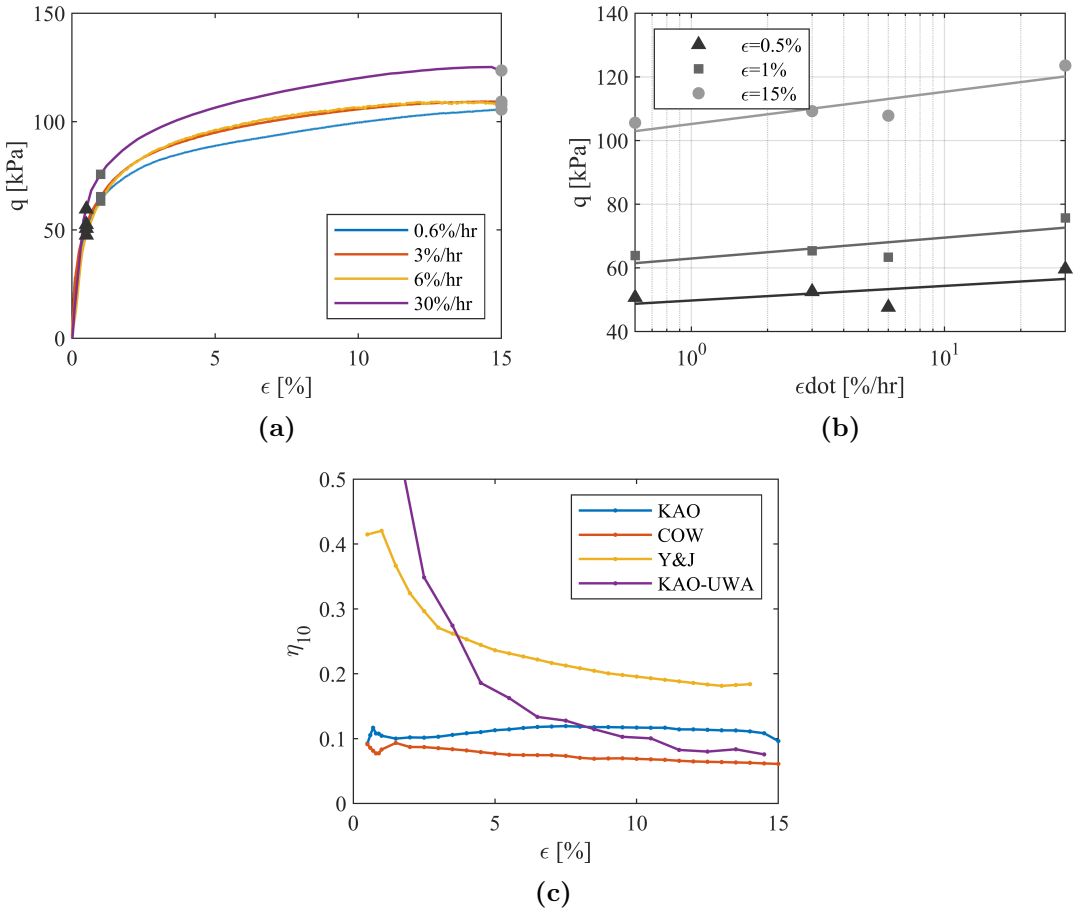

Figure 3.17: (a) Four CUc tests in Kaolin at differing rates (b) Deviatoric stress for each strain rate as a function of magnitude of strain (c) Strength increase per $\log_{10}$ increase in strain rate(η_{10}) as a function of strain magnitude

such that $\eta_{10} = f(\varepsilon)$ (e.g. Yong and Japp, 1967; Matešić and Vucetic, 2003). This is investigated by fitting Equation 3.19 to stress comparisons at various strain magnitudes. In Figure 3.17a: four CUc tests in Kaolin at differing rates are shown with markers at $0.5, 3$ and 15%, Figure 3.17b shows the increase in stress with strain rate for each. From this η_{10} may be calculated knowing $\eta = \ln(10)\alpha/\sigma_r$. Figure 3.17c shows this method applied to differing tests in the database and at various strain magnitudes, where:

- KAO – 4 $CIUc$ tests in Kaolin at $0.01, 0.05, 0.1$, and 0.5%/min
- COW – 3 $CIUc$ tests in Cowden clay at $5, 50$, and 500%/day
- YJ – 4 $CIUc$ tests in Kaolin at $1.67, 8.33, 15$, and 33.3%/min
- KAOUWA – 3 DSS tests in Kaolin at $0.1, 1$, and $2.5mm$/min

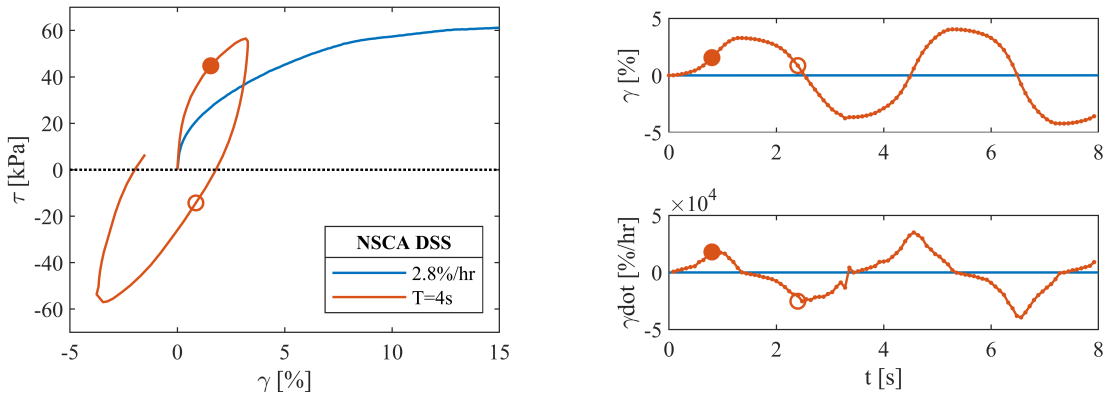

(a) **(b)**

Figure 3.18: Monotonic and Cyclic *DSS* tests on North Sea Clay A (a) Hysteretic Response (b) Strain and strain rate for the first 8 seconds

Data from Yong and Japp (1967) and UWA show a considerable increase in η_{10} at low strains, with the Cowden tests showing a similar, albeit less intense, trend. The dependency in Kaolin appears to be strain independent. This suggests that relative to the stress level, the viscous effects are larger at low strains and that rate dependency occurs even at very small strains. This is also presented by Vucetic (2016); in normalised secant stiffness plots, 'strongly increased' strain rate causes an increase of G_0 suggesting that initial stiffness is also rate-dependent.

Cyclic element tests are often defined in terms of sinusoidal load histories with a constant time period T which, combined with the non-linearity of the soil response, imparts varying strain rates on the soil throughout a cycle. Rate-effects are often described in terms of varying frequencies; Wichtmann and Triantafyllidis (2018) report deceleration of strain with increased loading frequency. In fact this problem may be re-framed in terms of strain-rates, such that higher frequency tests cause higher strain rates as the loading rate increases; higher magnitude tests will also cause higher strain rates as the tangential stiffness reduces.

Figure 3.18a shows the first load and unload of a DSS_{cyc} tests of NSCA clay with a period of $4s$, plotted alongside a slow $(2.8\%/hr)$ monotonic test of the same clay with the same consolidation conditions. Figure 3.18b shows the strain rate for the first 8 seconds (2 cycles). The rate changes considerably throughout each cycle and, as loading direction changes, passes through zero. Consequently, to accurately model cyclic tests one must be able to model constantly changing strain rates.

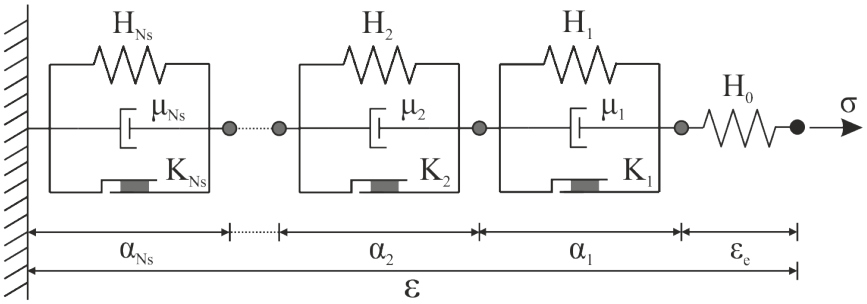

Figure 3.19: Rate-dependent, series, kinematic hardening model

3.3.2 Model

As described above, experimental results show significant viscous effects, which must be modelled continuously to accurately predict behaviour. Rate effects can be introduced into multi-surface hyperplasticity models by adding a viscous dissipation term, depicted as a dashpot in Figure 3.19. Following rate process theory this gives:

$$d = \overbrace{\sum_{i=1}^{Ns} K_i|\dot{\alpha}_i|}^{plastic} + \overbrace{\sum_{i=1}^{Ns} \frac{\mu_i}{t_{ref}}\dot{\alpha}_i \sinh^{-1}\left(|\dot{\alpha}_i| t_{ref}\right)}^{viscous} \tag{3.20}$$

or expressed in terms of the flow potential w, knowing $d = \chi\dot{\alpha}$, $dz/\dot{\alpha} = \chi$ and $w = d - z$:

$$w = \sum_{i=1}^{Ns} \frac{\mu_i}{{t_{ref}}^2}\left(\cosh\left(\frac{t_{ref}\langle|\chi_i| - K_i\rangle}{\mu_i}\right) - 1\right) \tag{3.21}$$

from which incremental behaviour can be derived for implementation following Appendix A (which also contains extension for asymmetrical strength):

$$d\alpha_i = \frac{\delta w}{\delta \chi_i}dt = \frac{S(\chi_i)}{t_{ref}}\sinh\left(\frac{t_{ref}\langle|\chi_i| - K_i\rangle}{\mu_i}\right) \tag{3.22}$$

where $\dot{\alpha}_i$ is the plastic strain rate and μ_i is a surface dependent viscous term (Houlsby and Puzrin, 2006). t_{ref} is a reference 'time', the inverse of the local reference strain rate $\dot{\alpha}_{ref}$ ($t_{ref} = 1/\dot{\alpha}_{ref}$), similar to the global reference strain rate described in Equation 3.19 where:

$$t_{ref,G} = \frac{1}{\dot{\varepsilon}_{ref}} = \frac{T_{u,ref}}{\varepsilon_u} \tag{3.23}$$

For a model configured in series, the magnitude of $\dot{\alpha}_i$ is dependent upon unit stiffness H_i, and the total number of surfaces N_s (see Equations 3.4 and 3.5). Therefore the local strain rates do not match the global strain rates, hence $\dot{\alpha}_{ref} \neq \dot{\varepsilon}_{ref}$

and $t_{ref} \neq t_{ref,G}$. To ensure model behaviour does not alter with number of surfaces $t_{ref} = N_s.t_{ref,G}$ (i.e. $\dot{\alpha}_{ref} = \dot{\varepsilon}_{ref}/N_s$) is specified in calibration. Further implications and comparison between series and parallel models are discussed in Chapter 5.

Beuckelaers (2017) rewrites Equation 3.20 with $\mu_i = K_i t_{ref} \eta$ in which $\eta = \frac{\eta_{10}}{\ln(10)}$ is the viscous constant. By including K_i, the viscosity scales directly with the strength of the surface, such that the viscous dissipation scales with plastic dissipation. Evidence presented in the previous section showed that one may wish to increase the contribution at lower strains.

Alternatively viscous contribution could be fixed such that $\mu_i = \mu = \sigma_u t_{ref} \eta$ (where typically $\sigma_u = K_{Ns}$). In this case the viscous dissipation is consistent across surfaces meaning that the relative contribution is larger at smaller strains ('constant viscosity'). This would have computational benefits reducing the model in Figure 3.19 to a single dashpot acting across the whole model rather than at each surface, thus only a function of the total of the plastic strains.

In fact, each of these is a limit for which a single dissipation function may be written by adding an additional parameter F_η, where $0 \leq F_\eta \leq 1$ and $\mu_i = \sigma_u (\frac{K_i}{\sigma_u})^{F_\eta} t_{ref} \eta$. This reduces to that presented by Beuckelaers (2017) at $F_\eta = 1$ and to constant viscosity at $F_\eta = 0$:

$$\begin{aligned} F_\eta = 0 \qquad & \mu_i = \mu = \sigma_u t_{ref} \eta \\ 0 < F_\eta < 1 \qquad & \mu_i = \sigma_u \left(\frac{K_i}{\sigma_u} \right)^{F_\eta} t_{ref} \eta \\ F_\eta = 1 \qquad & \mu_i = K_i t_{ref} \eta \end{aligned} \tag{3.24}$$

This formulation allows for control of viscous contribution with strain level, if required, by a single well defined parameter.

Figure 3.20a and Figure 3.20b show the effects of F_η for a typical monotonic backbone at two rates. Firstly, the development of pre-failure strain is subtly changed, which becomes more important as rates increase and for calibration to multiple rates. When focusing on small strain behaviour it is clear that for $F_\eta = 0$ the response 'sticks' to the elastic stiffness. Figure 3.20c shows a measure of the ratio of viscous to plastic dissipation (Equation 3.20), when $F_\eta = 0$ the viscous dissipation is much greater than plastic contribution at low stresses/strains. With greater F_η the effect is

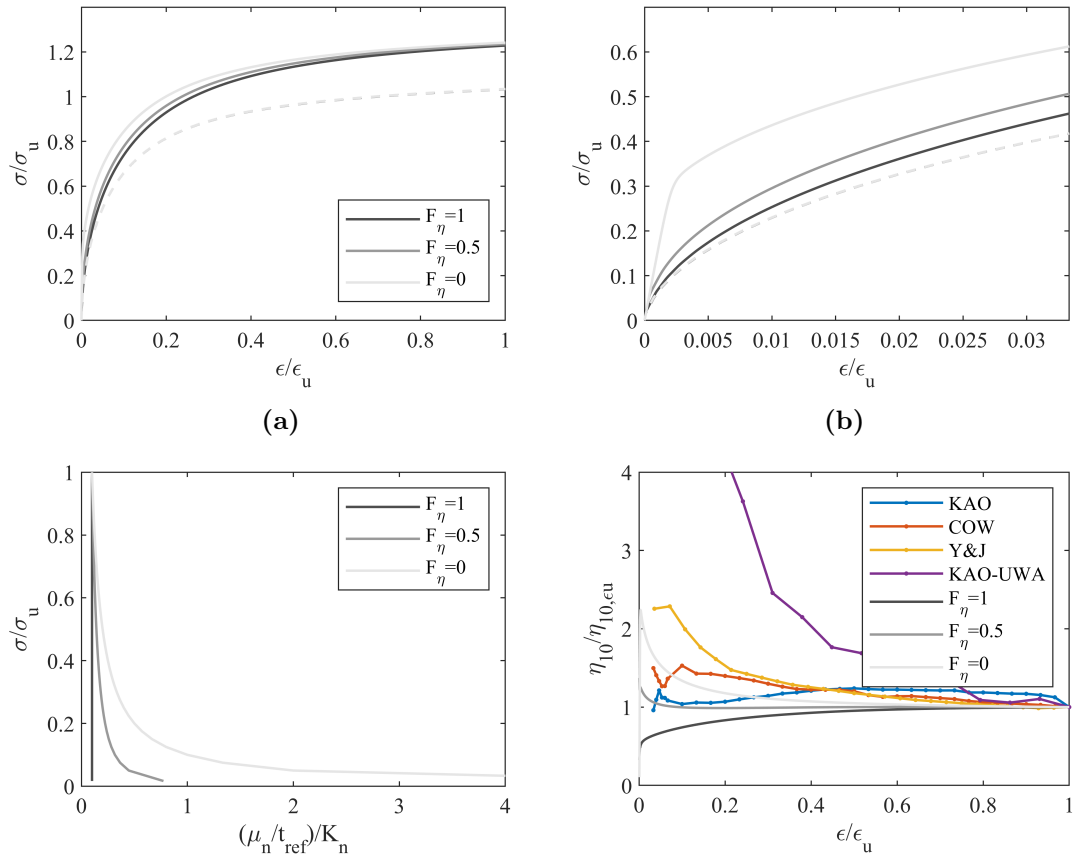

Figure 3.20: (a) and (b) Monotonic constant strain rate response at: (- -) Very slow $\dot{\varepsilon}_{ref} t_{ref,G} = 0.005$ and (–) Fast $\dot{\varepsilon}_{ref} t_{ref,G} = 50$ (c) Ratio of viscous to plastic dissipation with stress level (d) Effect of F_η on normalised strength increase due to rate, with strain level, compared to data presented in Section 3.3.1

reduced and increases with strain rate. The 'sticking' may be overcome by allowing the initial stiffness to vary with rate, although this is not pursued.

Figure 3.20d shows the normalised increase of strength due to rate η_{10} with respect to strain level, compared to the data presented in Section 3.3.1. At F_η=0.5 there is better agreement to the response in KAO and as $F_\eta \to 0$ a better agreement with YJ is seen. Generally the introduction of the parameter F_η allows for control of the viscous contribution with surface, independent of the rate.

3.3.3 Calibration

With the model developed a further three parameters must be calibrated; $\dot{\varepsilon}_{ref}$, η_{10} and F_η. Additionally, the backbone parameters presented in Section 3.2 must be revisited so that the surface strengths and stiffnesses correspond to $\dot{\varepsilon}_{BB} \to 0$. This is achieved

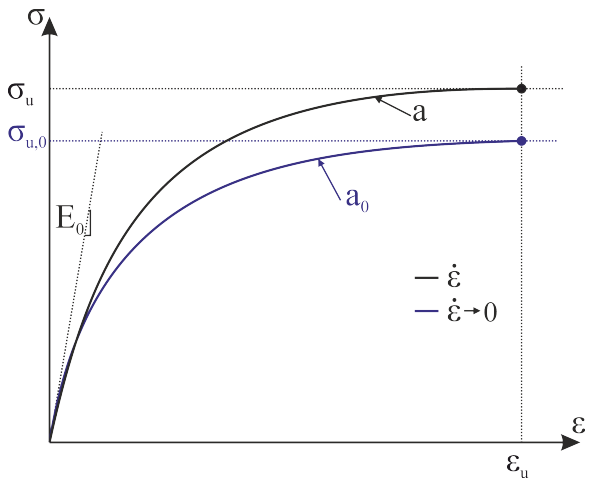

Figure 3.21: Recalibration of the monotonic response to that of a strain rate tending to zero

at the function-fit level (Figure 3.21 and Equation 3.6) by changing σ_u to $\sigma_{u,0}$ since strength is reduced at lower rates; and a to a_0 since the rate-dependent formulation chosen will affect each surface differently (and therefore the stiffness development). For calibration, tests at differing strain rates are required, typically this could be:

i Further monotonic tests at various $\dot{\varepsilon}$

ii The initial loading (and unloading) of a cyclic test at known frequency. Strain rates vary during the cycle and are typically higher than monotonic tests. If $\sigma_{av} \neq 0$, this may include an initial load and hold (with creep)

Considerable difficulty arises when attempting to calibrate rate dependency with a limited number of tests. Strength will vary between samples; this is particularly true for samples extracted from offshore Site Investigation (SI) and for DSS tests in which variability is high. It is therefore difficult to ascertain how much of the strength increase is due to rate and how much to sample variability.

Figure 3.22a shows 24 DSS and DSS_{cyc} tests in NSCA with OCR= 1, $\dot{\gamma} = 0.03hr^{-1}$ or T=4s. σ_{vc} varies between 50 and 300kPa with the shear stress normalised by a corresponding $s_{u,DSS}$. For the DSS tests this corresponds to the value at $\gamma = 0.15$, whilst for DSS_{cyc} a relationship of $s_{u,DSS} = m\sigma_{vc} + C$ is derived and used. The range and mean are plotted where only DSS_{cyc} tests in which the first peak $\gamma_{e,0} > 0.015$ are included (corresponding to an average strain rate $\dot{\gamma}_{av} = \frac{\gamma_{e,0}}{0.25T} =$

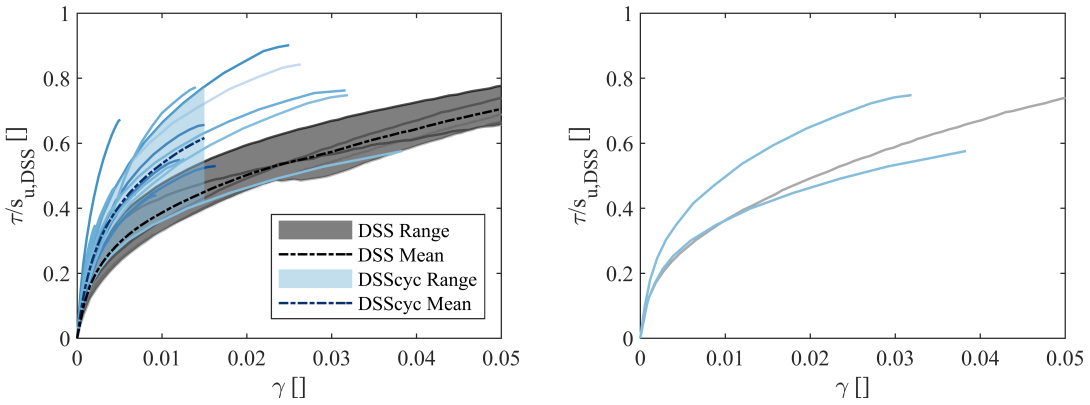

Figure 3.22: (a)DSS (Grey) and DSS_{cyc} (Blue) in NSCA with OCR=1. Stress is normalised by s_u at respective σ_{vc}, range and mean shown. (b) for OCR=1 and σ_{vc}=70kPa only

$50 - 100hr^{-1}$. It is clear that the mean DSS_{cyc} curve is stiffer and stronger than the DSS equivalent, although the range is large: an indicator of variability.

Figure 3.22b shows only the tests at σ_{vc}=70kPa. The two DSS_{cyc} tests differ considerably, and suggest a rate dependent decrease or increase of strength when compared to the DSS test. If repeatability of tests is low the best estimate for calibration can only be to take mean values (as is now shown); however, this affects the accuracy of further predictions.

In this thesis calibration of rate parameters is undertaken by least squares optimisation. Initial values are well defined given empirical experience. $\eta_{10} \approx 10\%$ in clays, $t_{ref,G}$ corresponds to a very slow test and is taken at 10^4hrs (equivalent to $\dot{\varepsilon}_{ref} = 0.01\%/hr$ and $T_{u,ref} = 1000$hrs). $\sigma_{u,0}$ is material dependent and will vary with choice of $\dot{\varepsilon}_{ref}$ but it is known that for practical calibration tests $\frac{\sigma_{u,0}}{\sigma_u} < 1$ and a_0 will be a value close to a. F_η may be material and data dependent but should start at 1.

An optimisation algorithm has been created which can either: minimise the proportional strain difference $\frac{|\gamma_{model} - \gamma_{measured}|}{|\gamma_{measured}|}$ or maximise the mean goodness of fit parameter η_{ult} (as defined in (Section 3.2.3). Data in Figure 3.22a is used as an example with a single mean DSS_{cyc} and mean DSS test. Optimisation of η_{ult} is chosen using the 'patternsearch' algorithm and applied over: DSS $(0 < \frac{\tau}{s_u} < 1)$ and $DSScyc$ $(0 < t < 0.25T)$ such that:

- Maximise ... $\eta_{ult,DSS} + \eta_{ult,DSScyc}$

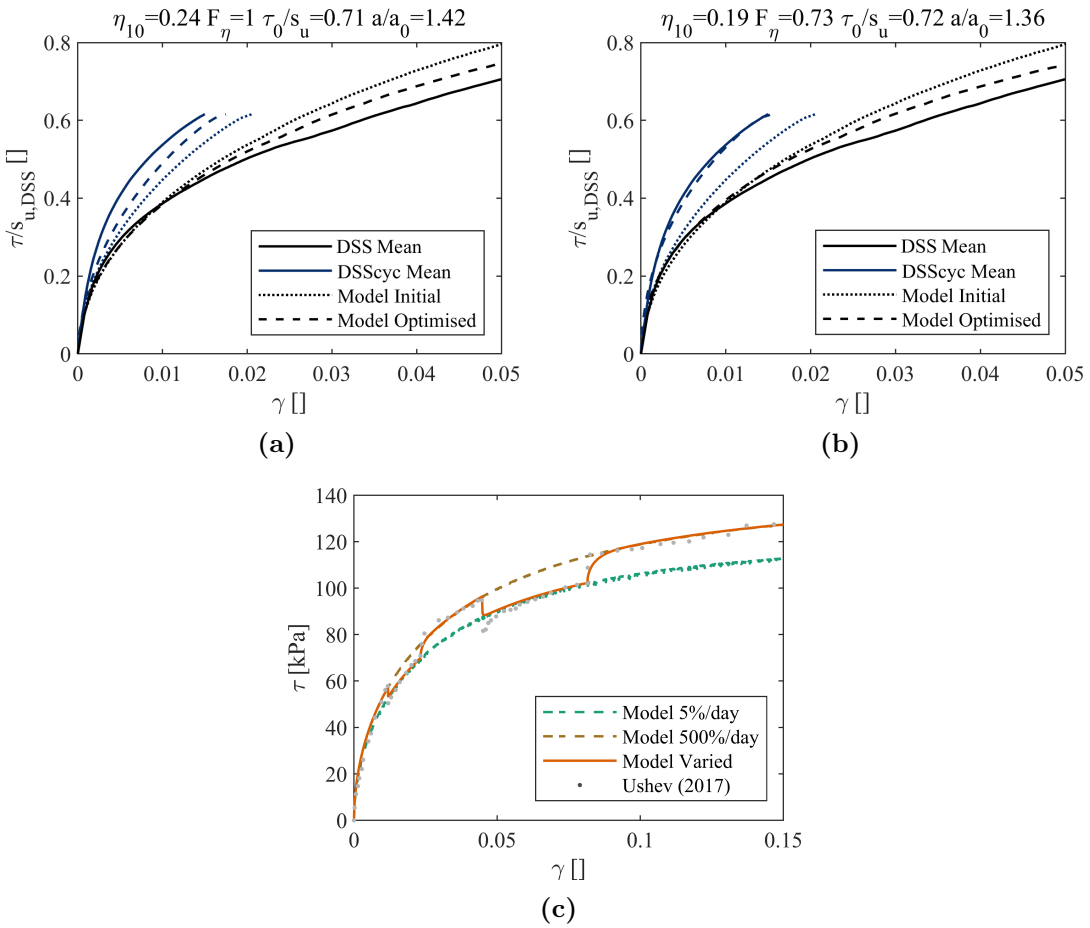

Figure 3.23: Rate process theory model calibrated to (a) mean DSS and DSS_{cyc} curves in NSCA (b) with a fixed F_η (c) Multi-rate test in Cowden after Ushev (2017)

- By varying ... $[\eta_{10}, \sigma_{u,\dot{\varepsilon}\to 0}, a_{\dot{\varepsilon}\to 0}, F_\eta]$
- Starting at ... $[0.1, 0.9\sigma_{u,0}, a_0, 1]$

Figure 3.23a shows initial and optimised model predictions when all parameters are allowed to vary. If data is sparse or less clear, subtle changes to development of rate dependency with strain may not be required. In this case $F_\eta = 1$. The optimised η_{10} therefore increases to cater for the higher strength at low strains, as shown in Figure 3.23b.

The parameters used are not decoupled (as shown in Figure 3.23a and Figure 3.23b). F_η increases viscous dissipation at low strain as does η_{10}; however, the high strain behaviour may differ greatly. Typically the data-sets obtained have a single rate monotonic test and a few cyclic tests to calibrate to; one slow test to high strains and some much faster tests at lower strains. In this case, by definition, an optimised

Table 3.5: Summary of evidence and modelling of rate-dependent response

Behaviour	Evidence	Modelling Technique	Calibration
Increased strain rate causes an increase in apparent strength. This is logarithmic until very low strain rates at which point it slows tending towards an asymptote at $\dot{\varepsilon} \to 0$.	COW DRM KAO	Viscous dissipative term added. Hyperbolic sinh relationship from rate process theory used to ensure linear increase at low rates and logarithmic at high rates.	Find $\dot{\varepsilon}_{ref}$ and η_{10} and from varied rate monotonic tests or more commonly optimise to the initial cycle of some fast cyclic tests.
Rate effects may be strain level dependent.	COW KAO (Yong and Japp, 1967)	Viscous dissipation can be scaled between surface-dependent and independent using F_η parameter.	Calibrate F_η to fine tune fit. Note default value of 1 (surface dependent viscosity).
In cyclic element tests where frequency is specified, strain rate changes throughout the cycle.	COW DRM NSC	Inherently captured by incremental model where stress and time are inputs.	N/A
G_0 is rate-dependent.	(Vucetic, 2016)	Not modelled at this stage.	N/A

fit takes no account of high rates at high strains, e.g. monotonic tests at high rates. This extends to a general point throughout the chapter that is important to know the limitations of calibration data with regards to the extrapolation of variables (rate and strain level in this case).

Since the introduction of rate effects is implemented during the incremental phase of the model, additional phenomena are intrinsically captured: creep, with load hold; curved, viscous peaks during sinusoidal loading; and interestingly, a high stiffness response immediately after the initial 'pseudo' q_0 consolidation shown in Figure 3.13a, this improves the prediction particularly for K_0 values close to 1. Figure 3.23c shows an example prediction of a varied rate CU test of Cowden Clay where computation of the response is accurately captured.

3.3.4 Modelling summary and application to datasets

This section has shown that rate-dependency of fine-grained soil response is well captured using a hyperplasticty model which follows rate-process theory. Table 3.5 summarises the key observations, modelling techniques and calibration methods.

Table 3.6: Summary of data-sets, parameters fitted to rate dependent response, and goodness of fit values where s_u refers to DSS or triaxial compression. Note that for NSCA OCR1 σ_{vc}=70kPa, parameters are calibrated to the mean of all tests Figure 3.23b but goodness of fit appraised against the three tests in Figure 3.22b. $t_{ref,g} = 10^4 hrs$

	KEY	Tests used	σ_{vc} or p_0 $[kPa]$	$s_{u,BB}$ $[kPa]$	$\dot{\varepsilon}_{BB}$ $[hr^{-1}]$	η_{10}	F_η	$s_{u,0}$ $[kPa]$	a_0	$\eta_{ult,av}$
DSS	NSCA OCR1	3	70	61	0.028	0.19	0.73	43.9	1.86	0.51
	NSCA OCR1	9	300	156	0.027	0.1	1	129	1.75	0.78
	NSCB OCR3	4	325	176	0.030	0.1	0.88	155	1.47	0.76
	DRM OCR1	3	392	84	0.045	0.2	0.91	60.4	2.51	0.72
	DRM OCR4	3	98	64	0.045	0.2	0.92	49.1	2.89	0.54
CU	DRM OCR4	5	100	99	0.02	0.26	0.91	65.8	4.19	0.6
	COW	5	67	125	0.002	0.1	0.7	101.2	2.76	0.82
	KAO	7	200	57.5	0.032	0.08	0.72	43.8	2.66	0.66
					Mean:	**0.15**	**0.85**			**0.67**

Table 3.6 summarises the test conditions and calibrated parameters of the datasets used. Two or three parameters are calibrated depending on quality and range of the calibration data, the focus is to best predict the initial quarter cycle of cyclic tests (important prior to the development of further mechanisms) whilst retaining a good monotonic prediction. An ultimate quality of fit metric (η_{ult}) is found in a similar manner to section 3.2.3, calculated for monotonic test to failure and cyclic tests to the first quarter cycle from which the average is taken $\eta_{ult,av}$. The values are lower than in the monotonic section due to the extra tests and variability in response. The viscous parameter η_{10} takes a value between 0.08 and 0.28, F_η between 0.7 and 1, with $s_{u,0}$ and a_0 recalibrated from the rate independent backbone.

3.4 Cyclic behaviour

Thus far only the response of single increase in load or of a few cycles has been introduced. The following section presents mechanisms which occur during repeated loading and unloading over numerous cycles. The mechanisms are described within the context of constant stress-amplitude cyclic tests in which the development of behaviour as a function of cycle number often proves a good starting point. Cycles are defined (where possible) following Chapter 2. In reality, loading conditions offshore are multi-amplitude. Application of a model based upon constant amplitude evidence to multi-amplitude problems is covered in Section 4.2.

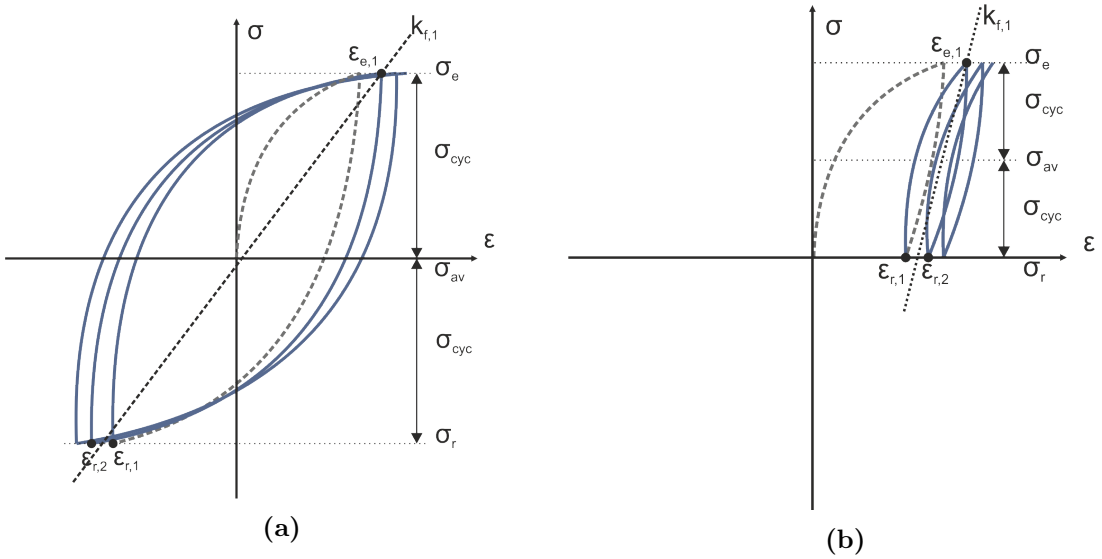

Figure 3.24: Idealised response of an element test in clay with the same maximum stress σ_e and therefore ζ_b subject to (a) Two way loading $\zeta_c = -1$(b) One way loading $\zeta_c = 0$

Figure 3.24 shows 3 cycles of idealised constant stress amplitude tests under one and two way loading. Load is initially increased to the same σ_e before unloading to different σ_r. Such that $\zeta_b = \sigma_e/\sigma_{ref}$ is equal but $\zeta_c = \sigma_r/\sigma_e = -1$ and 0 respectively.

The response with cycles now differs. In this example when $\sigma_{av} = 0$ (a), strain increases with cycles about zero such that $\varepsilon_{av,n} = 0$ and $\varepsilon_{cyc,i+1} > \varepsilon_{cyc,n}$, this can also be described as a reduction in secant stiffness (softening); $k_{f,n+1} < k_{f,n}$. It is also possible that stiffness increases with cycles (stiffening) $k_{f,n+1} > k_{f,n}$.

When $\sigma_{av} \neq 0$ (b) strains no longer develop about zero, accumulating strain (ratcheting) with cycles, such that $\varepsilon_{M,n+1} > \varepsilon_{M,n}$ (where M refers to recommended strain definition in Table 2.1) typically occurring alongside stiffness changes. For reasons described in Section 1.2.3, it is these two changes, along with that of the loop shape, which are predominately discussed in the following section.

3.4.1 Evidence

Firstly six *DSScyc* tests in NSCB are used as examples, Figure 3.25a (filled markers) shows the location of the tests in terms of normalised stress regime where $s_{u,DSS}$ is estimated from similarly consolidated monotonic tests. Tests in blue have an OCR=4, whilst for those in red, OCR=1 with a final σ_{vc}=325kPa and 308kPa respectively. Consistent colours are used in the following plots. The number of cycles to failure N_f (or test end) is shown and defined as the first cycle in which γ_{av} or $\gamma_{cyc} > 0.15$. N_f

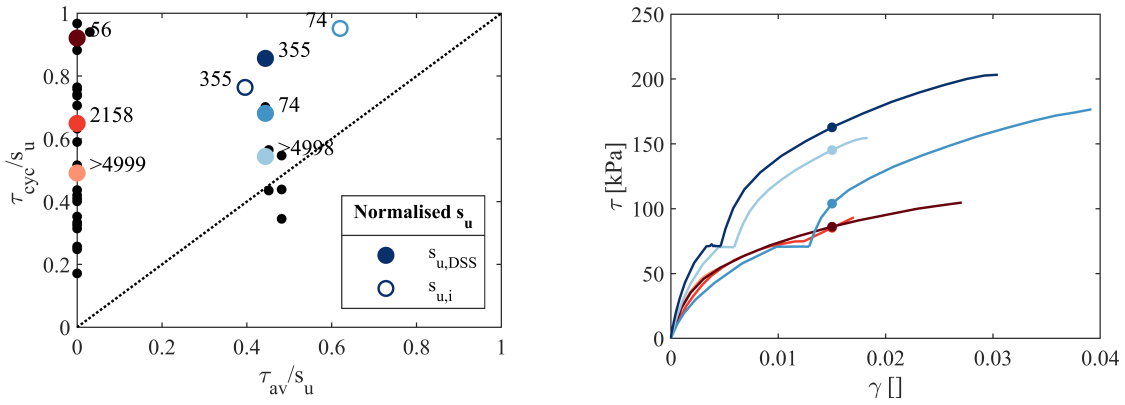

(a) (b)

Figure 3.25: (a) Interaction diagram with location of NSC *DSScyc* tests. 6 tests in NSCB highlighted in large colour markers with number of cycles to failure or end of test. Normalised by common $s_{u,DSS}$ or test specific $s_{u,i}$ edited to account for initial 1/4 cycle response. Small black markers indicate locations of all other NSC tests in the database (normalised by respective $s_{u,DSS}$). (b) Initial 1/4 cycle loading to first peak.

broadly decreases with increasing τ_{cyc} as would be expected although this does not follow for the tests in which N_f=74 and 355. The location is largely dependent upon the normalisation parameter s_u, assumed equal for each of the three samples. This assumption can be checked by interrogating the initial monotonic loading of each test.

Figure 3.25b shows the stress-strain response to first peak, $\tau_{e,0}$. If $\tau_{av} = 0$ this corresponds to a quarter cycle whilst if $\tau_{av} \neq 0$ there is an additional constant rate load and hold. The $\tau_{av} = 0$ tests track the same backbone; however, there is considerable variability in the $\tau_{av} \neq 0$ cases, this is to be expected in real-world materials, particularly in *DSS* conditions in which a small sample is used. With this in mind it may reasonably be assumed that s_u would also differ. This can be estimated by finding the percentage difference at a fixed strain (in this case $\gamma = 0.015$ shown as markers) and taking the mean value (in this case 2) as the previously assumed s_u, such that:

$$s_{u,i} = \frac{\tau_{\gamma=0.015,i}}{\tau_{\gamma=0.015,2}} s_{u,DSS} \tag{3.25}$$

The interaction diagram can then be replotted (Figure 3.25a non-filled markers) changing the location of the N_f=74 greatly due to a reduced s_u.This demonstrates the importance of normalisation values, and once recalibrated follows trends observed by Andersen (2015), Liedtke et al. (2019) and many others of reducing number of cycles to failure with increasing stress magnitude.

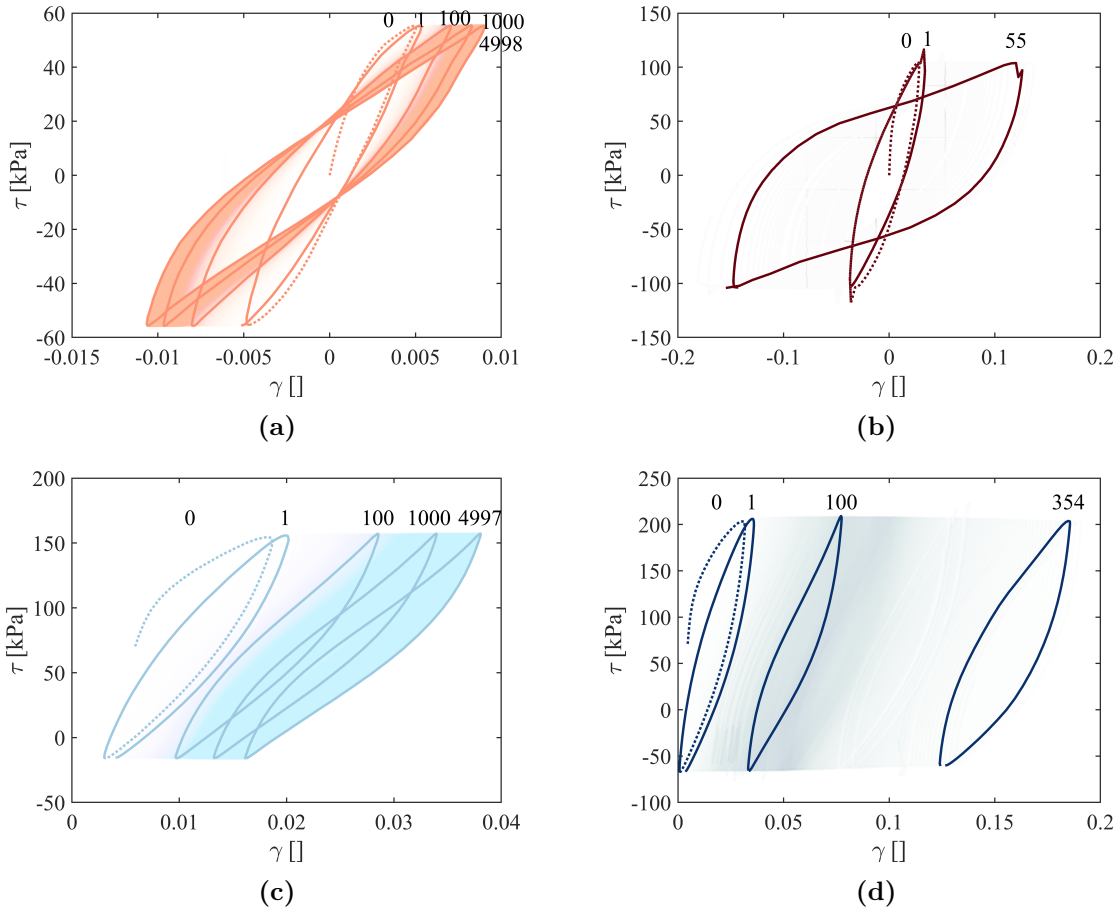

Figure 3.26: Stress - strain response of four NSCB tests, cycle numbers highlighted

Stress-strain responses at various cycle numbers are plotted in Figure 3.26 for four example cases, in which the 0th cycle (dashed) indicates the initial load and unload. Figure 3.26a shows a two-way test which does not fail; cycles develop around zero strain with a reducing secant stiffness, the loop shape remains largely consistent but rotated. Figure 3.26b shows a two-way test which fails after 55 cycles; the initial loop shape is a similar to (a) before large strains develop. The final loop shape differs greatly from cycle 1, with significantly lower secant stiffness and a more open and almost bi-linear hysteresis loop, with failure occurring at $\gamma_{cyc} = 0.015$. Figure 3.26c and 3.26d are partial two-way test responses; strain now ratchets in the direction of the average load, and both tests show decreasing secant stiffness and a similar loop shape throughout. This is true even at failure for (d) which occurs at $\gamma_{av} = 0.15$.

Similar behaviour is observed in undrained triaxial tests. Figure 3.27 shows the location (and number of cycles to failure N_f or end N_{max}) of 22 CUcyc tests in Kaolin. Failure here is defined at $\varepsilon_{a,u}$=0.01. $s_{u,c}$ is estimated based upon the initial

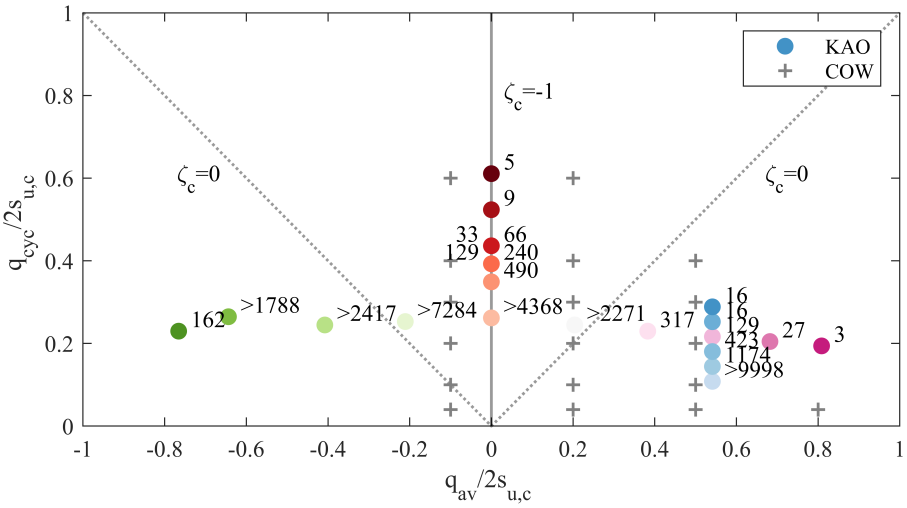

Figure 3.27: Interaction diagram of CUcyc tests in KAO showing location and number of cycles to failure N_f or end N_{max}, repeated tests show two values

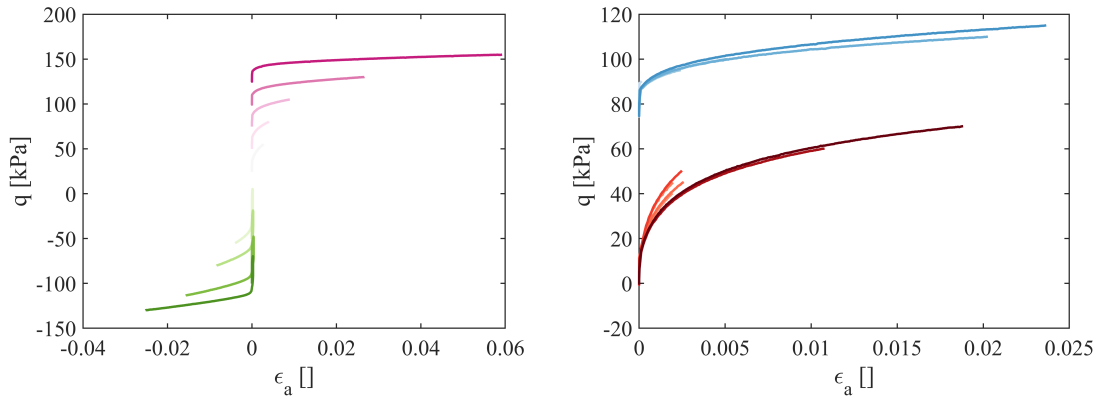

(a) **(b)**

Figure 3.28: CUcyc tests in KAO (a) Initial 1/4 cycle loading to first peak -100kPa $< q_0 <$125kPa (b) q_0=0 and q_0=75kPa

consolidation conditions $p_0^{'}$ and q_0. It is important to note that in this dataset q_{av} is applied drained prior to testing ($q_0 = q_{av}$) and therefore the tests will not all follow the same backbone, Figure 3.28a. However, those at similar q_0 do show a fairly consistent initial loading response, Figure 3.28b.

Deviatoric stress q versus axial strain ε_a responses at various cycle numbers are plotted in Figure 3.29a to 3.29d, where compression is positive. Figure 3.29a shows a two-way loaded test which does not fail; secant stiffness reduces and axial strain accumulates in a negative direction due to anisotropy. The loop shape remains convex but rotated until high cycle numbers when loops become concave. Figure 3.29b shows a two-way loaded test which fails after 239 cycles; the response is similar to 3.29a

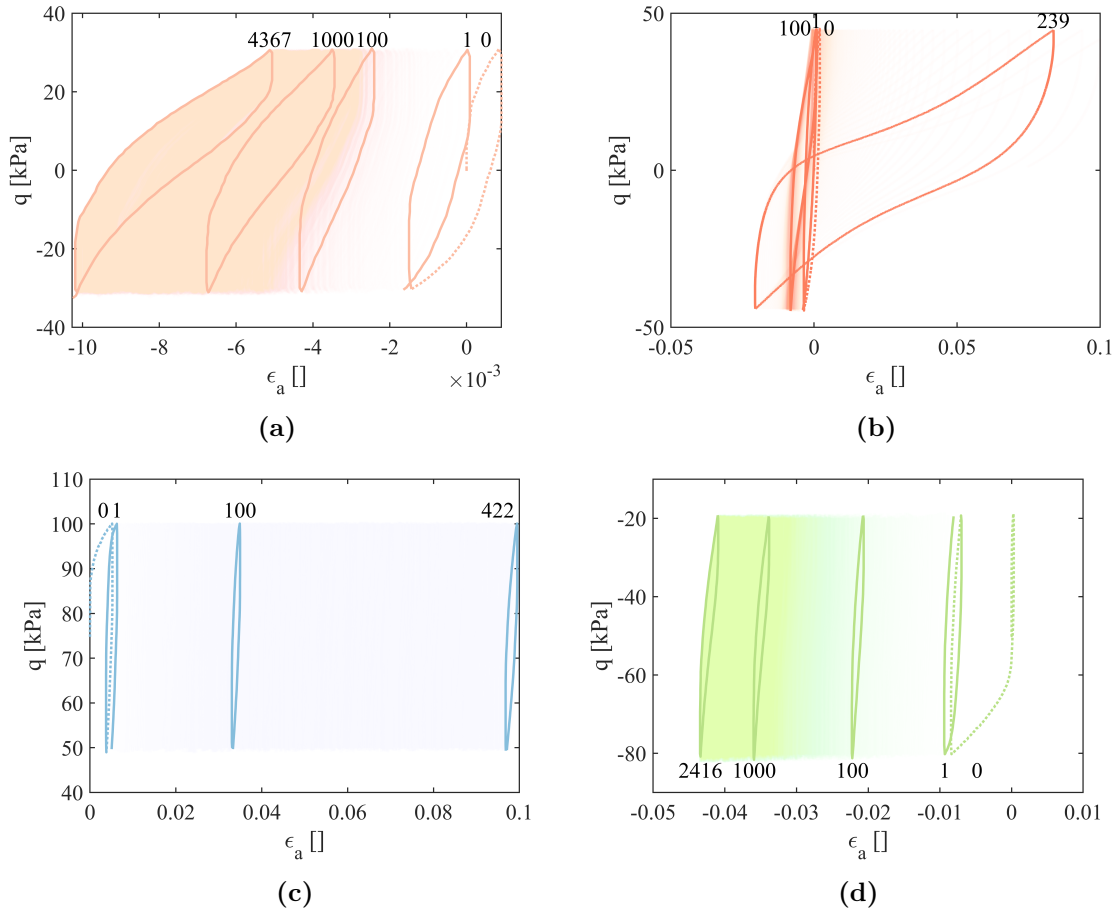

Figure 3.29: CUcyc tests in KAO - Deviatoric stress against axial strain of four tests

until cycle 100 but by failure the loop shape is concave and strains are predominantly compressive. Figure 3.29c and 3.29d are partial two-way test responses in compression and extension respectively; strain now ratchets in the direction of the average load. Both show decreasing secant stiffness with a similar loop shape throughout, even when close to failure. These tests are undertaken with constant strain rate applied between q_e and q_r rather than a fixed period T, removing effects of changing rate and causing less 'rounded' or viscous peaks than those shown in Figure 3.26.

As discussed in Section 1.3.1, in both *DSS* and *CU* conditions the increase in strain observed in softening and ratcheting may be attributed to combined destructuration and reduction of effective stress. The latter will be investigated further in Section 3.4.1.4.

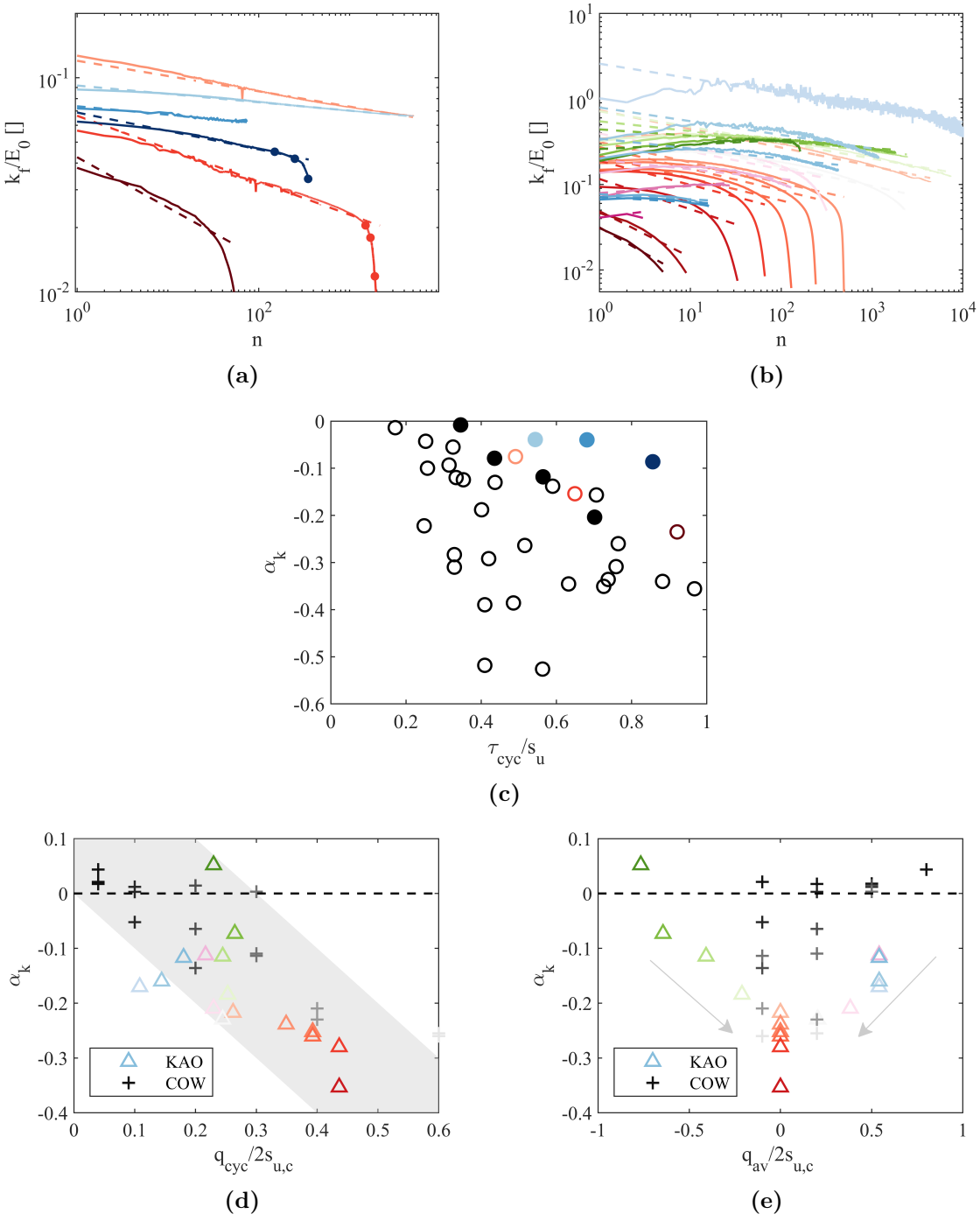

Figure 3.30: Normalised Secant stiffness against cycle number with power function (Equation 3.26) fit (a) for *DSS* tests in NSCA (b) *CU* tests in KAO (c) Exponent α_k with normalised cyclic stress for all NSC *DSS* tests in which $N_f > 20$ filled markers indicates tests in which $\tau_{av}/s_u > 0.1$ (d,e) α_k with normalised cyclic and average stress for all KAO *CU* tests in which $N_f > 20$ and for the COW dataset (shown as black crosses)

3.4.1.1 Softening

Figure 3.30a shows normalised secant stiffness (as defined in Table 2.2) development which reduces with cycles for all six DSS tests. The initial value is higher for tests with lower τ_{cyc} reflecting the non-linearity of the monotonic response. The reduction is linear in log-log space suggesting that the rate slows with increasing cycles. The rate of reduction is lower for the one-way tests, which is in agreement with Zografou et al., 2019, although in this case OCR also varies. Towards the end of most tests which finish before 1000 cycles, there is a sudden decrease as the sample nears failure.

Figure 3.30b shows normalised secant stiffness development for the triaxial tests, for most the stiffness is initially stable or increasing (to somewhere between $10 < n < 100$) before reducing until the test is stopped. This is true unless high cyclic strains are developed, in which case a sudden decrease towards failure is observed as in the DSS_{cyc} cases. This type of behaviour occurs predominately in $\tau_{av} = 0$ cases.

Leblanc et al. (2010b) suggested a logarithmic fit for stiffness development of piles in dry sand, although Richards (2020) showed that this was unsatisfactory for two-way loaded tests in a similar set-up. Achmus et al. (2007) suggest an exponential relationship in the 'Stiffness Degradation Method' (SDM), which was also followed by Richards (2020), and is applied to element tests in this thesis, such that:

$$\frac{k_{f,n}}{E_0} = A_k.n^{\alpha_k} \tag{3.26}$$

where E_0 is initial elastic stiffness (as defined in Tables 3.3 and 3.4), A_k gives the normalised stiffness of the initial cycle and α_k is an exponent which can be fitted to each data set. This is plotted in Figure 3.30c alongside all other NSC tests in the data-set in black. It can be seen that all tests show a negative exponent (softening) for which the absolute magnitude increases with τ_{cyc}. This exponent is generally smaller (closer to zero) for biased tests shown filled ($\tau_{av}/s_u > 0.1$), although OCR also varies.

Figure 3.30d and 3.30e show α_k in the KAO and COW (black crosses) triaxial tests against both τ_{cyc} and τ_{av}. Again the exponent is negative for most tests, apart from one case in KAO and a few very low τ_{cyc} cases in COW which show stiffening. α_k decreases with τ_{cyc} as in the DSS tests and increases with magnitude of τ_{av} in extension or compression. This is especially true for the KAO set where the exponents are generally smaller (closer to zero) for biased compressive and extensive

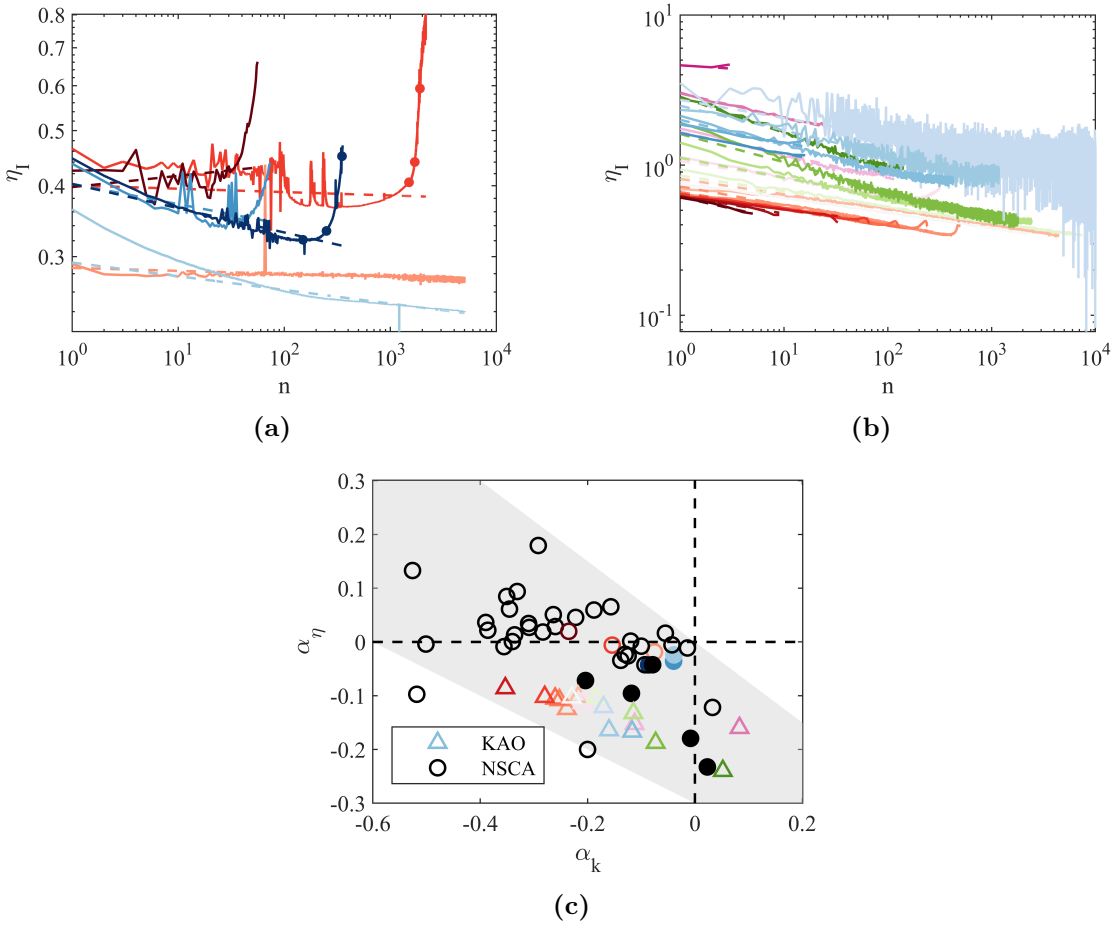

Figure 3.31: Energy loss factor against cycle number with power function (Equation 3.27) fit (a) for *DSS* tests in NSCA (b) *CU* tests in KAO (c) Softening exponent α_k against energy loss factor exponent α_η showing negative proportionality

tests (although consolidation is also changed), suggesting less softening occurs. At very high $|q_{av}|$, α_k is greatly increased; however, these tests have fewer cycles to a ratcheting type 'failure', therefore the secant stiffness no longer develops as a long term exponent.

In summary it seems that softening is more intense with increased cyclic stress and with proximity to two-way loading. Effective stress changes may explain some of these phenomena and are looked at more closely in Section 3.4.1.4.

3.4.1.2 Energy dissipation

Figure 3.31a shows development of the energy loss factor, η_I, an indication of the dissipation within each cycle found by a ratio of plastic and elastic work and defined in Equation 2.12.

The loops of the lower intensity tests are initially stiffer with correspondingly lower $\eta_{I,1}$. Tests with $\tau_{av} \neq 0$ show steadily decreasing η_I with cycles at a similar rate for all three tests, some of which is due to a reducing increment of ratcheting strain and therefore dissipation. When $\tau_{av} = 0$ the energy loss factor reduces at a slower rate. In the tests which fail a sudden increase in η_I occurs in the cycles leading up to failure, this is accompanied by a sudden reduction in secant stiffness. Figure 3.31b shows that the energy loss factor consistently reduces across all KAO *CU* tests regardless of cyclic stress, suggesting similar dissipative behaviour across all load types.

An exponential relationship has been fitted to energy loss factor development:

$$\eta_{I,n} = A_\eta . n^{\alpha_\eta} \tag{3.27}$$

Such that a negative exponent indicates a reducing energy loss factor with cycles and therefore less hysteretic energy dissipation. For the data-sets presented in this section it is found that α_η reduces with cyclic stress and increases with bias, such that it is largely inversely proportional to softening exponent α_k. This is shown in Figure 3.31c and means that if considerable softening occurs (large negative α_k) hysteretic energy dissipation will increase relative to the elastic energy (higher α_η and a more open loop). For the majority of the tests shown the energy loss factor decreases (negative α_η) and is more negative for triaxial tests (shown as triangle markers).

3.4.1.3 Ratcheting

Figure 3.32a shows development of cycle strain at average load in *DSS* tests (defined as ε_M in Table 2.1) normalised by failure strain $\gamma_u = 0.15$. Tests in which $\tau_{av} = 0$ show a small change which is probably due to inhomogeneity. Figure 3.32b shows accumulation of strain for only $\tau_{av} \neq 0$ which show considerable ratcheting. Similar plots of *CU* tests are shown in Figure 3.32c in terms of accumulated axial strain ε_a, where $\varepsilon_{a,u} = 0.1$ This is plotted in log-linear space to allow for negative strain to be plotted. Strain develops negatively (extensively) in $\tau_{av} <= 0$ cases.

An exponential function is often used when reporting ratcheting in pile and element tests, such that:

$$\frac{\Delta\gamma_{M,n}}{\gamma_u} \; or \; \frac{\Delta\varepsilon_{a,M,n}}{\varepsilon_u} = A_R n^{\alpha_R} \tag{3.28}$$

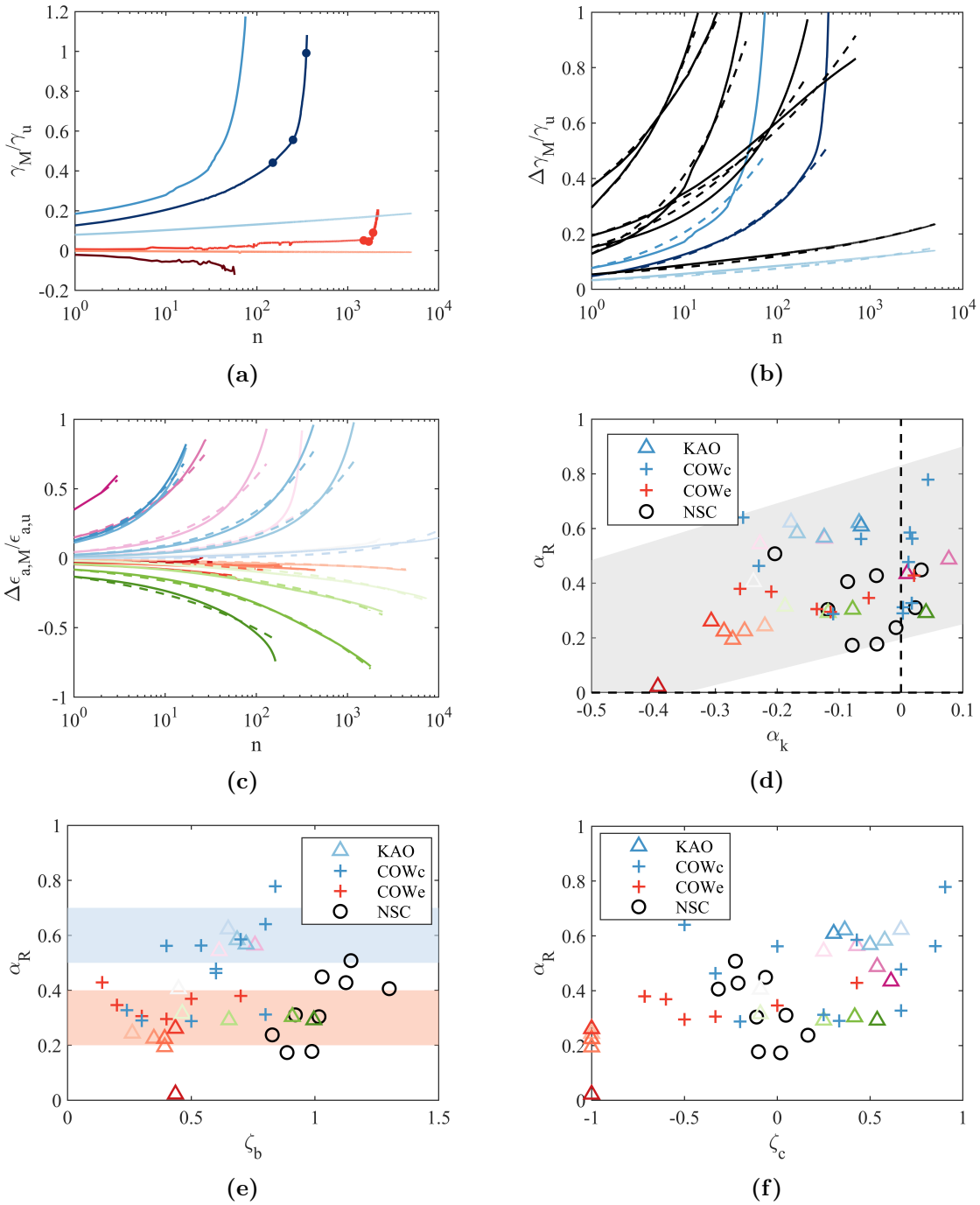

Figure 3.32: (a) Ratcheting response in *DSS* tests in NSCA normalised by $\gamma_u = 0.15$. (b) (c) Accumulation of ratcheting with with power-law fit (Equation 3.28) in *DSS* NSCA tests and *CU* KAO tests respectively. Grey band indicates general trend across all tests. (d) Ratcheting exponent α_R against softening exponent α_k. (e) Ratcheting exponent α_R against ζ_b. Blue and red bands show indicative trend of compressive and extensive tests respectively. (d) Ratcheting exponent α_R against ζ_c.

Leblanc et al. (2010b) assumed a constant exponent α_R and made $A_R = T_b(\zeta_b)T_c(\zeta_c)$ while Truong et al. (2019) let α_R vary and fixed $A_R = \Delta\varepsilon_1/\varepsilon_u$.

Initially α_R is allowed to vary (following Truong et al. (2019) and $A_R = \Delta\varepsilon_1/\varepsilon_u$) which fits well to the data in Figures 3.32b and 3.32c, indicating a slowing rate of accumulation; however, for highly stressed tests at cycles close to failure the rate increases abruptly until the failure strain of γ_u=0.15 which is not captured by the exponential relationship.

The resulting exponent is plotted against ζ_b and ζ_c in Figures 3.32e and 3.32f for all bias tests in KAO, NSC and COW. Note that in the Cowden data-set continuous data was not obtained such that in Equation 3.28 $\Delta\varepsilon_{a,M,n}$ becomes $\Delta\varepsilon_{a,av,n}$ (as defined in Table 2.1) and hence the magnitude of α_R and A_R will differ. In DSS conditions the exponent appears to increase with ζ_b and, since ζ_c is similar for all tests, cyclic amplitude τ_{cyc}, indicating a faster rate of ratcheting with larger amplitude cycles, albeit this is in competition with a typically reduced number of cycles to failure.

In the KAO triaxial tests α_R is largely constant for tests which accumulate strains compressively (blue markers) $0.5 < \alpha_{R,c} < 0.7$, and extensively (Red and Orange) $0.2 < \alpha_{R,e} < 0.4$. The reduced exponent in extension suggests a lower rate of strain accumulation in extension than in compression, despite a typically weaker response.

Fitting $A_R = T_b(\zeta_b)T_c(\zeta_c)$ for a constant exponent following Leblanc et al. (2010b) is not pursued as the testing programs were not undertaken with constant ζ_c or ζ_b in mind, and hence it is difficult to calibrate T_b or T_c. However, in triaxial conditions, A_R is initially negative for two-way or extensive tests and positive for compressive tests. A_R increases in magnitude with ζ_b, hence accumulation of strain is initially larger with larger bias and amplitude as would be expected. Leblanc et al. (2010b) and others have previously reported, with respect to pile tests, a relationship of $T_c = f(\zeta_c)$ which produces a maximum at $\zeta_c \approx -0.6$. Since $T_c = f(\zeta_c)$ cannot be accurately found with this data-set, no comparison is made.

In summary it is true that, as in pile testing, the rate of ratcheting decreases with cycles so that an exponential relationship of accumulated strain to cycles fits well, albeit this no longer applies when close to failure. Ratcheting occurs negatively in extension and for two-way tests in triaixal conditions and appears to occur at a slower rate (lower exponent) than equivalent compression tests.

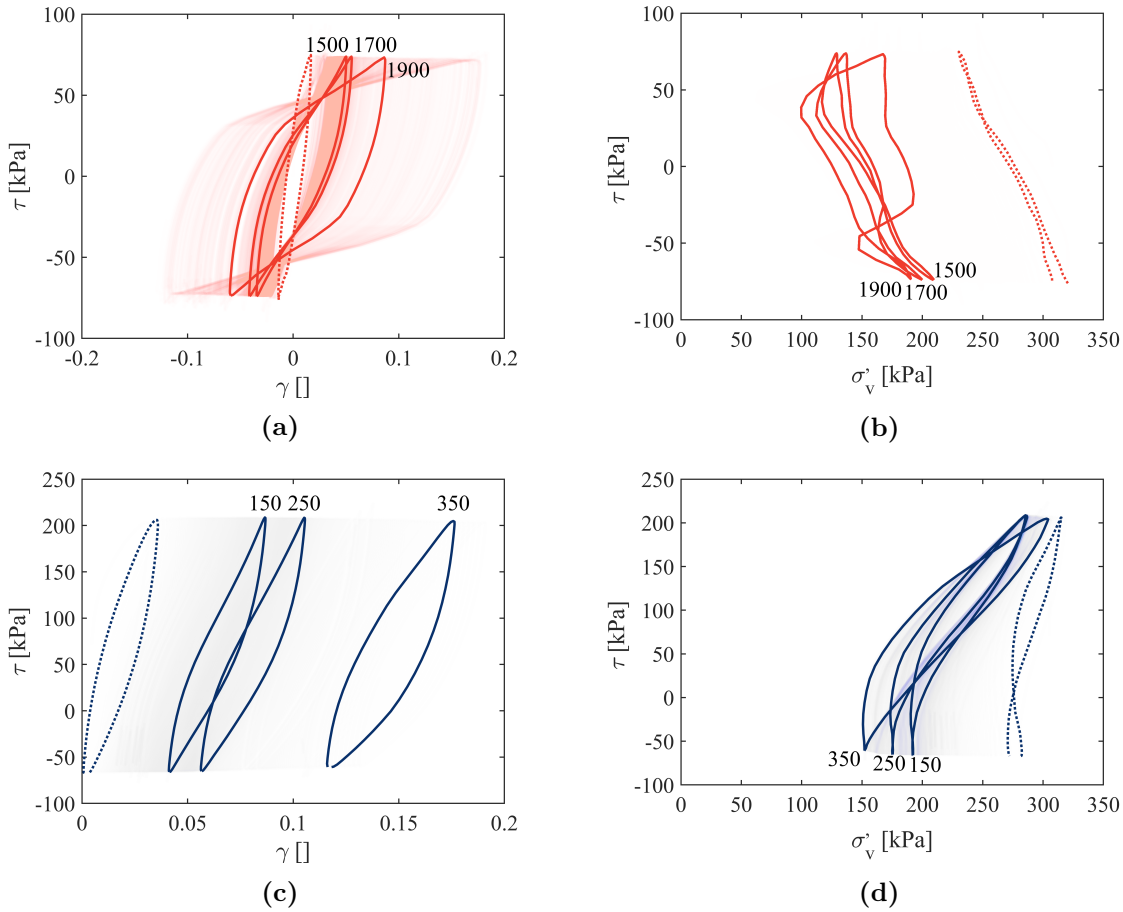

Figure 3.33: Response near failure of selected DSS_{cyc} tests in NSCA (a) Two-way test in stress-strain space (b) showing change in applied effective normal stress - reduction indicates contractive behaviour (c) and (d) for an equivalent one-way test

3.4.1.4 Near-failure behaviour and effective stress changes

Figure 3.33a and 3.33c show example tests with three cycles at equal spacing around the point where a sudden change in secant stiffness and strain accumulation is observed, corresponding to the points marked in Figure 3.30a and 3.32a. In both cases the loop shape is preserved for the first two cycles shown, but changes considerably between the second two; a greater decrease of secant stiffness alongside a more open and therefore dissipative loop. When $\tau_{av} = 0$ the response becomes almost bi-linear whilst in the $\tau_{av} \neq 0$ case there is a higher rate of ratcheting. When such large strains occur this may be indicative of the test no longer behaving as a single element but developing inhomogeneity with a significantly degraded shear-band.

More generally, the behaviour presented in this chapter, and described in total shear stress only, is in fact accompanied by a reduction in the applied normal stress.

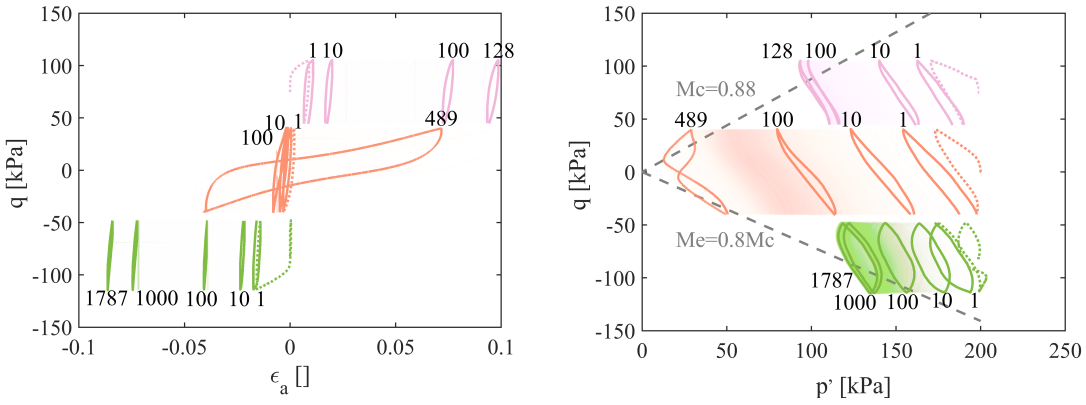

Figure 3.34: Behaviour of three *CU* tests in KAO with differing q_{av} with cycles shown (a) $q-\varepsilon_a$ (b) $q-p'$ with critical state line Mc from (Wichtmann and Triantafyllidis, 2018) alongside an estimated extensive line

This ensures constant volume, indicating contractive behaviour and a decrease in effective stress in undrained conditions, Figures 3.33b and 3.33d. As effective stress reduces, the applied stresses become close to critical state and the strains will be large. In the $\tau_{av} = 0$ case the loop begins to show a butterfly like response at n=1900, often associated with liquefaction.

Figure 3.34a and 3.34b show three KAO triaxial tests with similar τ_{cyc} but differing τ_{av} in $q-\varepsilon_a$ and $q-p'$ space. Again strain development and ultimately failure is dependent on τ_{av}. Various authors highlight that zones of differing behaviour may be illustrated using interaction diagrams (Wichtmann et al., 2013; Andersen, 2015; Ushev, 2017). These broadly fit into no-failure, extension, compressive and cyclic failures as shown in Figure 1.11.

In Figure 3.34b loading in q causes a reduction in p' (contraction) whilst unloading causes an increase in p' (dilation) which does not return to the previous point, reducing mean effective stress p' as excess pore-pressure develops. Failure occurs as the test gets close to the critical state line shown indicatively. As the effective stress nears critical state the rate of axial strain accumulation increases greatly, in two-way tests this produces a butterfly shaped curve of contraction and dilation.

In Figures 3.35a and 3.35b the change in effective stress with cycle number is plotted in DSS_{cyc} (σ_v') and CU_{cyc} (p') tests respectively. For each cycle the value is taken at the mean of values of average shear stress on unload and load (in a similar

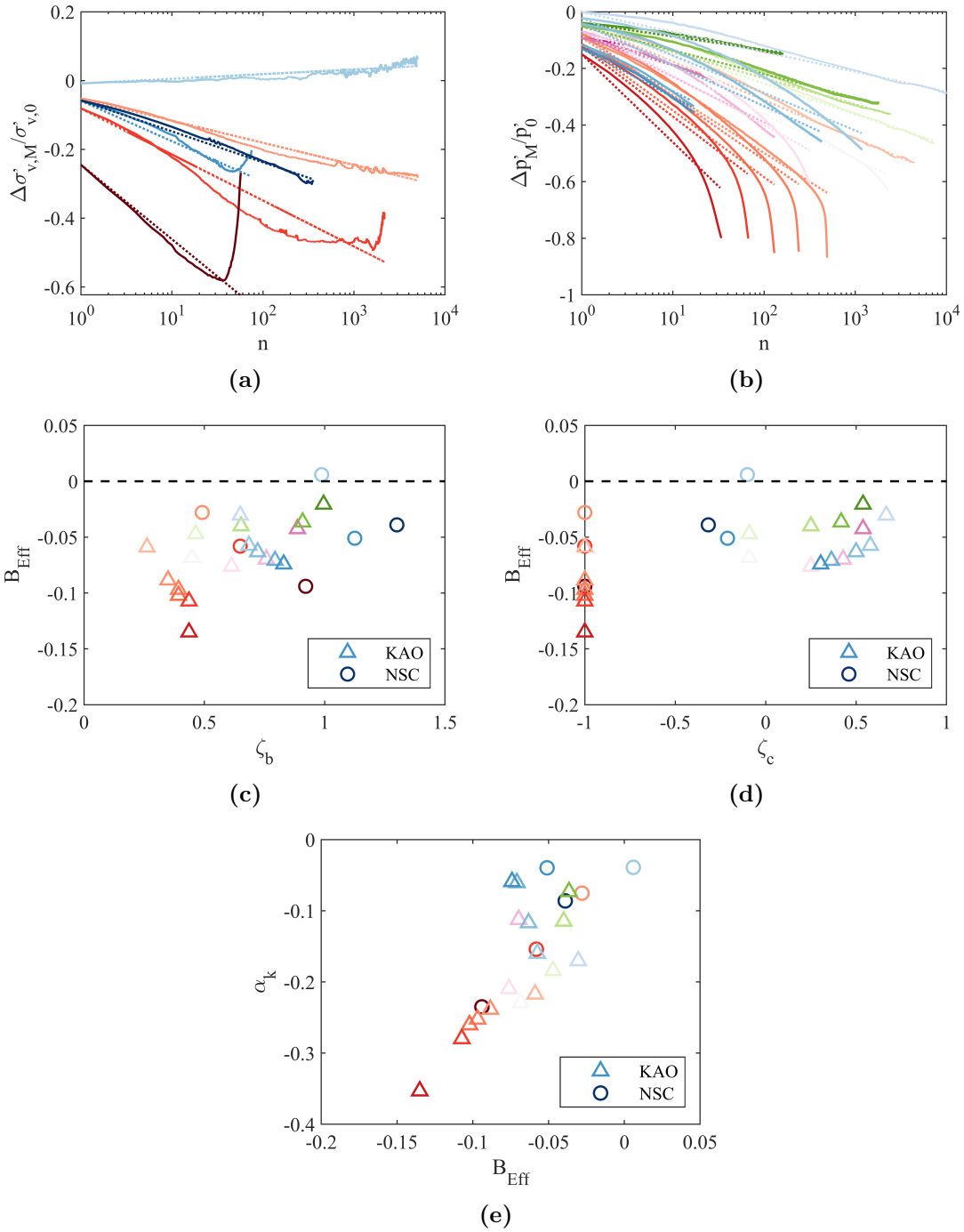

Figure 3.35: (a) Development of change in effective normal stress in selected *DSS* examples (b) change in mean effective stress in KAO with logarithmic fit (c,d) Intensity of effective stress change by logarithmic co-efficient B_{Eff} against load intensity and type ζ_b and ζ_c (e) Relationship of intensity of effective stress change to intensity of softening

manner to ε_M). Rather than fitting an exponent, a logarithmic law is found to produce a better fit, such that:

$$\begin{aligned} \frac{\Delta\sigma'_{v,M,n}}{\sigma'_{v,0}} &= \frac{\Delta\sigma'_{v,M,1}}{\sigma'_{v,0}} + B_{Eff}\ln(n) \\ \frac{\Delta p'_{v,M,n}}{p'_0} &= \frac{\Delta p'_{v,M,1}}{p'_0} + B_{Eff}\ln(n) \end{aligned} \tag{3.29}$$

Figures 3.35c and 3.35d plot the logarithmic co-efficient B_{Eff} against against load intensity and type ζ_b and ζ_c. A more negative B_{Eff} is indicative of a more rapid decrease in effective stress, which seems to be independent of ζ_b but heavily dependent on ζ_c. Two-way tests (at $\zeta_c = -1$) show the most negative and therefore intense exponent in both CU and DSS conditions, this reduces with increasing ζ_c and is lower in the extensive tests.

The intensity of effective stress reduction is closely related to the softening of secant stiffness observed. This can be seen by plotting the effective stress co-efficient derived in 3.29 against the softening exponent derived in 3.26. This is plotted in Figure 3.35e where there is a clear linear dependency; tests in which the most intense softening occurs in strain space (typically two way tests for this data-set) also show the most intense reduction in effective stress. It should be noted that in the KAO tests used here, the initial q_{av} is applied drained and therefore consolidation and strength properties vary.

Attempts to model explicitly the effective stress behaviour will be discussed in greater detail in Chapter 7, but here only the effects of this change (strength reduction) are considered.

3.4.1.5 Post-cyclic response

Until now, the mechanisms which occur during numerous stress cycles were considered. The cycling has a marked effect on the state, and therefore response, of the soil samples and by extension may affect their ability to withstand large stresses. Conventional element testing can be used to investigate this by assessing the sample's post-cyclic strength: applying a monotonically increasing strain to failure after cycling. Correctly modelling this strength is important, particularly when considering

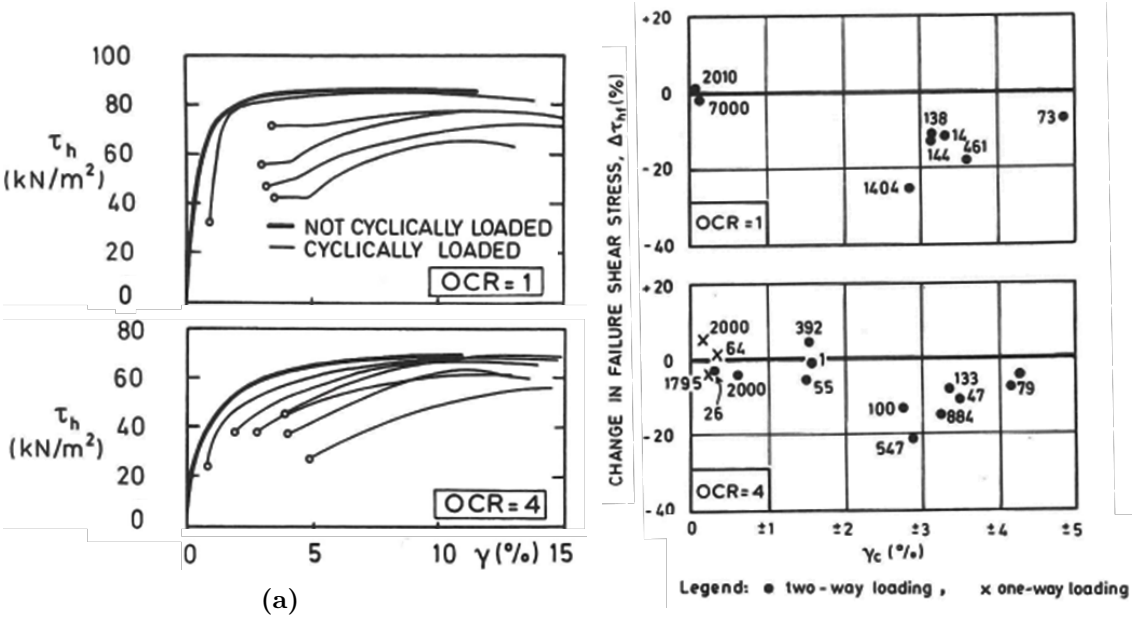

Figure 3.36: *DSScyc* tests on Drammen clay (Andersen et al., 1980) (a) Post-cyclic loading (b) Change in static shear strength against final cyclic shear strain (with Number of cycles to failure)

multi-amplitude (realistic) loading where loads which exceed the previous maximum are common after initial virgin loading (0th cycle).

Andersen et al. (1980) present further detail on Drammen clay element testing, Figure 3.36a shows post-cyclic shearing after DSS_{cyc} tests alongside a static test shown in bold. Andersen observed that if the cyclic shear strains are small, the post-cyclic test largely returns to the original static test curve whilst tests which undergo large cyclic strains show considerable reduction in shear strength. Figure 3.36b shows this plotted in terms of shear strength change, Δs_u, γ_{cyc}, and N_{max}. Tests below 2% cyclic strain show scatter about largely unchanged shear stress, while higher strained tests show a reduction in strength which appears to increase with cycles and is accompanied by large increases in pore-pressure (reduction in normal stress).

Tests are also presented in triaxial conditions with similar conclusions. Again pore pressure is increased during cycling, reducing the mean effective stress. Upon post-cyclic shearing the effective stress paths pass the failure line for similarly consolidated samples and approach an overconsolidated failure line. Andersen et al. (1980) propose that although drainage is prohibited, the reduction in effective stress during cycling

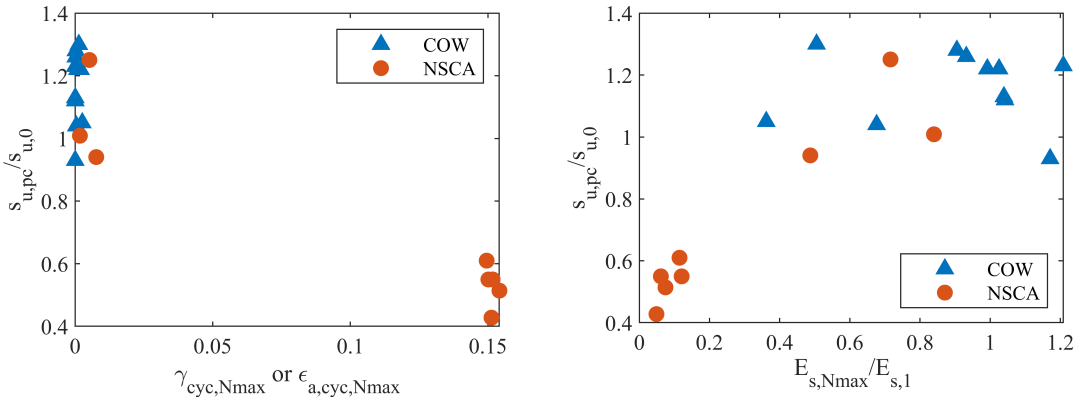

Figure 3.37: Normalised post-cyclic strength in Cowden (CU) and NSCA (DSS) OCR=1, $\sigma_{vc} = 300kPa$ plotted against (a) cyclic strain (b)change in secant stiffness

has the same effect as real unloading of the soil (over-consolidation).

Post-cyclic tests were undertaken on all NSCA and NSCB tests, inclusive of those which had already 'failed', γ_{cyc} or $\gamma_{av} > 15\%$. In Ushev (2017), CAU_{cyc} tests of Cowden till were sheared to failure, providing they had not failed during cycling. Figure 3.37a shows change in strength against cyclic strain (either shear or axial), two distinct zones can be seen: a large reduction in shear strength, corresponding to failed specimens; and a small decrease or increase for those with low strains. Figure 3.37b shows the same results plotted against normalised reduction in secant stiffness. This highlights that 'softening' is still occurring within cycles for many of the the tests in which no post-cyclic softening is observed.

Generally, post-cyclic capacity is heavily reduced if the preceding cyclic test has undergone excessive strains (close to failure). In the tests which do not fail, post-cyclic strength remains close to the static strength even if secant stiffness reduces. High stress cycling which induces high strains may not be of great interest when considering serviceability limit state for offshore wind-turbines founded on monopiles. It is relevant for the shallow soil and for soil elements close to the pile which may be relatively highly mobilised, but soil at increasing depth and distance from the pile will undergo cyclic shearing at a much lower level. For this, much greater volume of soil, the effects of numerous, relatively low stress cycles is of interest. Therefore a model which is capable of reducing secant stiffness whilst preserving, or separately

controlling, ultimate strength is useful. Post-cyclic monopile behaviour is discussed in greater detail in Section 6.3.

3.4.2 Model

The cyclic effects presented in the previous section can be modelled by a softening/stiffening relationship and an additional ratcheting element. In fast cyclic tests with a non-zero load bias, some ratcheting develops in the viscous model presented in 3.3.2. This occurs in the same way creep would for an average load held over a period of time. Secant stiffness and loop shape are, however, unaffected, assuming a constant period. In this section, softening is discussed first as, similar to rate dependency, it can have an effect on the accumulation of strains. Focus is given to correct modelling of stiffness and strength changes before 'topping up' the ratcheting for $\sigma_{av} \neq 0$ loads as required.

3.4.2.1 Softening

Abadie (2015) and Beuckelaers (2017) suggest a model for stiffening or softening in which the strength of each yield surface changes as a function of a hardening parameter β such that:

$$K_i = K_{i,0} f(\beta) \tag{3.30}$$

where K indicates both compressive and extensive strength in the asymmetrical model. For stiffening (as modelled by Richards (2020) and Abadie (2015) for piles in sand); $f(\beta) > 1$, which causes yield strengths to increase, loops to tighten and secant stiffness to increase. Whilst for softening; $f(\beta) < 1$, causing largely the opposite effects. Abadie notes that by changing the strengths rather than the stiffnesses, H_i remains independent of state variables, which preserves the form of the differentiation of energy functions. The softened yield strengths are implemented in the yield (Equation 3.11) or dissipation (Equation 3.21) functions and corresponding derivatives, as outlined in Appendix A. The definitions of β and $f(\beta)$, alongside some further model choices are now discussed.

Hardening parameter

The hardening parameter develops incrementally with model steps such that $\beta = \beta + \dot{\beta}\Delta t$. Abadie (2015) and Beuckelaers (2017) both suggest $\dot{\beta} = |\dot{\alpha}_r|$, where α_r

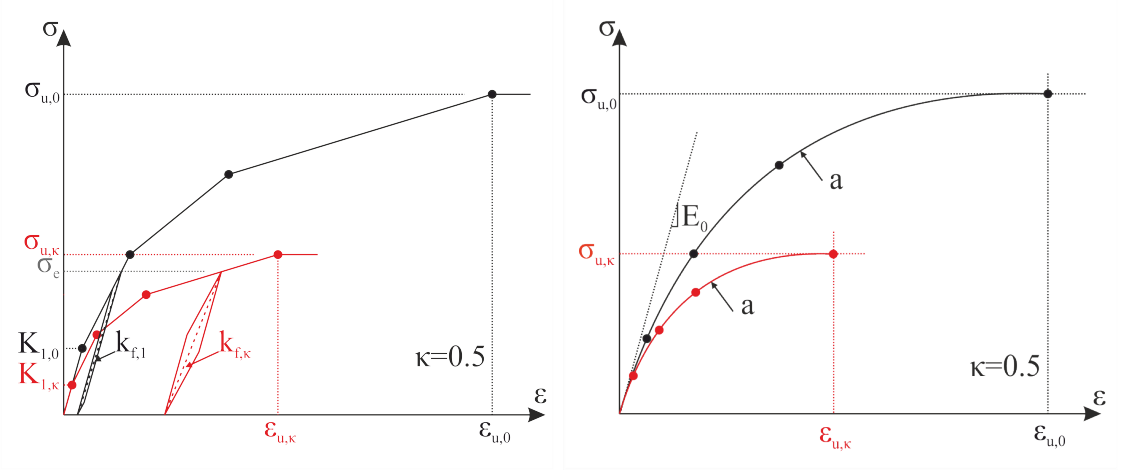

Figure 3.38: (a) Diagram of changes to backbone yield surfaces subject to softening of κ=0.5, indicative constant amplitude cyclic response for one way load with to σ_e shown. (b) Changes to idealised Jeanjean fit parameters

is a strain variable associated with an additional ratcheting unit (discussed in Section 3.4.2.2). Hence β is also a strain type variable. Using this definition couples softening and ratcheting, which causes some problems for calibration, particularly when modelling two-way tests.

β could instead take the form of other strain or work-type quantities, for instance: $\dot{\beta}_G = \sum |\dot{\alpha}_i|$ or $\dot{\beta}_G = \sum K_i |\dot{\alpha}_i|$. These formulations are synonymous with plastic-strain or plastic-work hardening and are independent of ratcheting strain α_r. It is unclear at this stage whether a work or strain-type quantity is most suitable, and this may be material dependent. Both are well used in plasticity theory. Plastic work hardening can ensure that some models are consistent in series and parallel as noted by Abadie (2015) and is therefore preferred, however strain hardening is also used (e.g. in section 4.2). Where choice of hardening parameter would change formulation this is highlighted.

By choosing to sum strains, the development follows the 'global' strain or work of the whole system. It is also possible to develop 'local' hardening parameters such that $\dot{\beta}_G = \sum \dot{\beta}_i$ where $\dot{\beta}_i = |\dot{\alpha}_i|$ or $\dot{\beta}_i = K_i |\dot{\alpha}_i|$; this proves to have useful consequences.

Function choice

As shown in Figures 3.30a and 3.30b, the secant stiffness $k_{f,n}$ reduces with cycle number and may be fitted with an exponential relationship. For high cycle tests the negative power tends to decrease with intensity of τ_{cyc}. The function choice in

Equation 3.30 is in terms of strength change $\kappa = K_i/K_{i,0}$, such that the surface stiffnesses remain the same whilst the yield strengths are reduced.

Figure 3.38a shows a model with four surfaces subject to softening of κ=0.5, the yield loci are halved in both the stress and strain direction. If a fixed stress amplitude is applied, the change in strain (or resulting secant stiffness of a cycle, $k_{f,\kappa}/k_{f,1}$) is not directly proportional to κ, as shown indicatively for a one-way cycle to σ_e. In multi-surface kinematic hardening models $k_{f,\kappa}$ varies depending on amplitude σ_{cyc}, but not bias σ_{av}, as Masing rules are observed. Therefore a relationship of $\kappa = f(\frac{k_{f,\kappa}}{k_{f,1}})$ is required for all possible σ_{cyc} before experimental derivation of κ development can be found.

Figure 3.38b shows softening of κ=0.5 for a smooth curve fit to the Jeanjean function 3.7 from which the backbone parameters are derived. The four constants are varied by a change in κ by: $\varepsilon_{u,\kappa} = \kappa\varepsilon_{u,0}$, $\sigma_{u,\kappa} = \kappa\sigma_{u,0}$, $E_{0,\kappa} = E_0$, and $a_\kappa = a_0$. The decrease in secant stiffness (for a fixed σ_{cyc}) for a given κ can therefore be approximated using the analytical Jeanjean expression as:

$$\frac{k_{f,\kappa}}{k_{f,1}} = \frac{\varepsilon_{cyc,1}}{\varepsilon_{cyc,\kappa}} = \frac{2\left(\varepsilon_u - \frac{\sigma_u}{E_0}\right)\left(\frac{atanh\left(\left(\frac{\sigma_{cyc}}{2\sigma_u}\right)tanh(a)\right)}{a}\right)^2 + \frac{\sigma_{cyc}}{E_0}}{2\kappa\left(\varepsilon_u - \frac{\sigma_u}{E_0}\right)\left(\frac{atanh\left(\left(\frac{\sigma_{cyc}}{2\kappa\sigma_u}\right)tanh(a)\right)}{a}\right)^2 + \frac{\sigma_{cyc}}{E_0}} \tag{3.31}$$

Using this equation and derived backbone parameters from Table 3.3 and 3.4, experimental development of κ with respect to number of cycles is found (such that $k_{f,\kappa} = k_{f,n}$). Although this analytical approximation does not account for anisotropy or rate, κ will affect both compressive and extensive strengths equally and rate effects can be assumed to be largely unchanged between cycles.

Figure 3.39 shows experimentally derived κ for the two datasets in the previous section. Instead of plotting against cycle numbers, absolute total strain at the peak stress of the cycle ($\sum_0^{t(\sigma_{e,N})} |d\varepsilon|dt$) is used which is indicative of cumulative plastic strain. Both are plotted in log-log space. A linear relationship is observed at high cycle numbers suggesting the suitability of a power-law fit. Richards (2020) showed this to be suitable for stiffening ($\kappa > 1$) of response of piles in dry sand. In Figure 3.39a a larger negative power is fitted to the two-way tests than the one-way tests

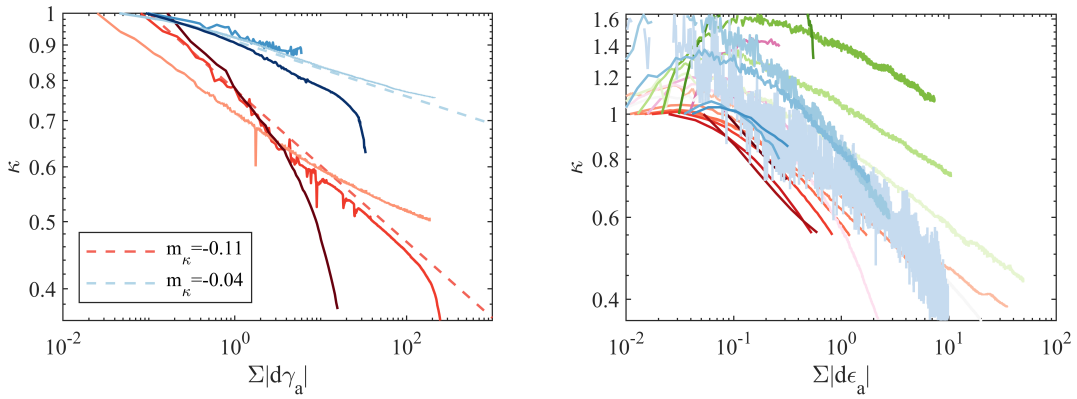

(a) **(b)**

Figure 3.39: Experimentally derived κ against absolute strain (a) *DSS* tests in NSCA (b) CUcyc test in KAO

although these also have have a different OCR ratio. In 3.39b initial stiffening over the first 1-50 cycles occurs before a consistent softening.

Assuming similarity of the development of total strain and plastic strain (and therefore hardening parameter β), a suitable function to describe $\kappa = f(\beta)$ is sought. Abadie (2015) previously suggested:

$$\kappa_G = \frac{K_i}{K_{i,0}} = \frac{\sum \beta_i}{\beta_0}^{-m_k} \tag{3.32}$$

where $m_k > 0$ controls the rate of softening and $\sum \beta_i$ indicates a global hardening parameter. β_0 is an initial value which must be defined as some small value. Calibration of β_0 is somewhat difficult and it does not have an obvious physical meaning. Instead a 'modified power law' as suggested by Richards (2020) may be used:

$$\kappa_G = \frac{K_i}{K_{i,0}} = \left(1 + \frac{\sum \beta_i}{\beta_{ref,G}}\left(\kappa_{ref}^{-\frac{1}{m_k}} - 1\right)\right)^{-m_k} \tag{3.33}$$

m_k remains the same, but now the hardening parameter is allowed to start at 0. $\beta_{ref,G}$ and κ_{ref} correspond to a co-ordinate which acts as a pin, translating the relationship in β or κ, aiding calibration.

With a global hardening function, all surfaces soften (or stiffen) equally with the development of a single hardening parameter $\sum \beta_i$. When cycling at any load amplitude, all surfaces will soften by a constant κ_G. Post-cycling, the whole backbone has degraded $K_{u,pc} < K_{u,0}$, such that subsequent monotonic shearing would fail at $s_{u,pc} = \kappa s_{u,0}$. However, as shown in Figure 3.37b there is evidence that in

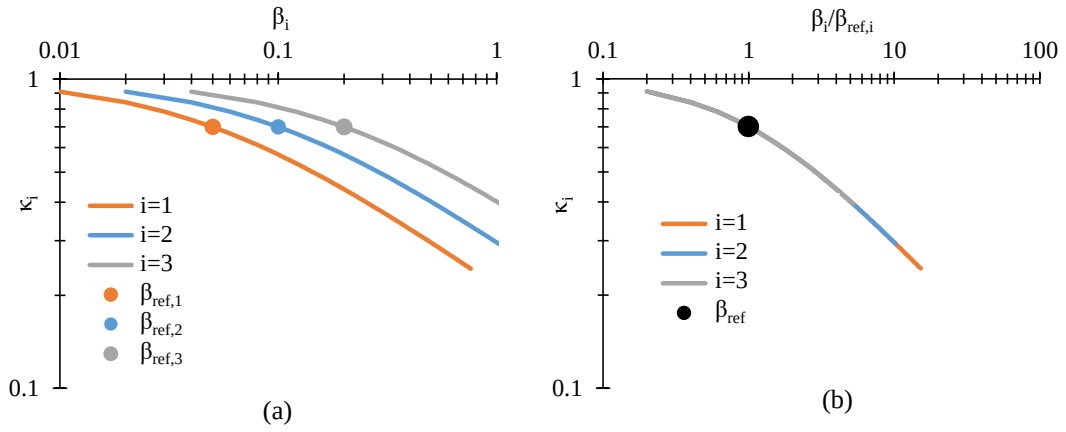

Figure 3.40: Development of surface specific softening (κ) for a three surface rate-independent model subject to monotonic loading to $\sigma = K_{Ns}$. m_k=-0.5, κ_{ref}=0.7, F_{β_l}=0.1 (a) with hardening parameter (β_i) (b) normalised against $\beta_{ref,n}$

some cases the post-cyclic strength either remains the same or increases $s_{u,pc} >= s_{u,0}$ despite a reducing secant stiffness ($\kappa < 1$).

Modelling both features is possible by only softening surfaces once they are active. A straightforward way of doing this would be to define a local hardening parameter for each surface, β_i. In this case the softening behaviour is dependent only on the plastic work in that unit. Equation 5.16 now becomes a local κ_l:

$$\kappa_l = \frac{K_i}{K_{i,0}} = \left(1 + \frac{\beta_i}{\beta_{ref,i}}\left(\kappa_{ref}^{-\frac{1}{m_k}} - 1\right)\right)^{-m_k} \tag{3.34}$$

where again $(\beta_{ref,i}, \kappa_{ref})$ defines a pin. Local and global softening models are limits for which a single function may be written and controlled by an additional parameter, F_κ. Where $0 \leq F_\kappa \leq 1$ and:

$$\kappa_i = \frac{K_i}{K_{i,0}} = \kappa_{l,i}^{F_\kappa} \kappa_G^{1-F_\kappa} \tag{3.35}$$

$$\begin{aligned} F_\kappa = 0 ... \kappa_i &= \kappa_G \\ 0 < F_\kappa < 1 ... \kappa_i &= \kappa_{l,i}^{F_\kappa} \kappa_G^{1-F_\kappa} \\ F_\kappa = 1 ... \kappa_i &= \kappa_{l,i} \end{aligned} \tag{3.36}$$

At the limits F_κ acts as a switch, reducing to constant softening at 0 and surface specific softening at 1. Values between the limits allow for 'combined' softening, offering further control of behaviour. κ_i is described by Equations 3.34, 3.33 and 3.35, and with $\dot{\beta}_i = K_i|\dot{\alpha}_i|$.

To ensure consistency of κ development, the choice of $\beta_{ref,i}$ must reflect the magnitude of work (or strain) expected on that surface (α_i and/or K_i). In the series model the units are arranged with slider and spring in parallel, this results in infinite stiffness until yield (K_i) after which the spring is activated with a stiffness (H_i). For consistency $\beta_{ref,G}$ may be formulated as a factor of expected β in a similar manner. Here the following expressions are used:

$$\begin{aligned} \beta_{ref,i} &= \overbrace{F_{\beta,l}\frac{K_{Ns}}{H_i}K_i}^{Work} \quad or \ \overbrace{F_{\beta,l}\frac{K_{Ns}}{H_i}}^{Strain} \\ \beta_{ref,G} &= F_{\beta,G}2A \qquad or\ F_{\beta,G}\frac{2A}{K_{Ns}} \end{aligned} \tag{3.37}$$

$F_{\beta,G}$ and $F_{\beta,l}$ are unitless factors. K_{Ns}/H_i is the plastic strain α_i expected on a surface upon local stress application K_{Ns}, K_i ensures a work quantity. A is the area beneath the backbone to K_{Ns} such that $A = \int_0^{K_{Ns}} \sigma d\varepsilon$. Hence $2A/K_{Ns}$ corresponds to a 'yield strain'.

The reference value is scaled by the expected plastic strain or work. Figure 3.40a shows the relationship for three arbitrary surfaces subject to a load to K_{Ns}. When normalised by $\beta_{ref,i}$, Figure 3.40b, these track the same curve. Importantly this ensures that $\kappa_i > \kappa_{i-1}$ for all i, since for a given surface to be active (and therefore developing β_i) the preceding surface must also be active. The lower surfaces therefore experience a higher normalised β and by extension κ.

In this thesis κ_{ref} is fixed at 0.7 from which β_{ref} may be calibrated. This corresponds to the cumulative, absolute plastic work done before the surface strengths are degraded by 30%.

Implications of local or global softening

Figure 3.41 shows how the choice of F_κ alters the model response. All other model parameters are consistent: the monotonic backbone uses the same (normalised stress) parameters as DSS tests DRM OCR=1; viscosity is removed by using a rate independent formulation; and work-softening parameters $\kappa_{ref} = 0.7$, $m_k = 0.1$, $F_{beta,l} = F_{beta,G} = 20$ are used alongside a reference case with no softening. 100 cycles of a one way load ($\sigma_{cyc} = \sigma_{av} = 0.25$) are applied followed by a monotonic application

of stress to failure. Cycles 1 and 100 are shown alongside the model backbone response without cycles. The development of yield strength K_i is shown against surface number i at approximately cycle n =0,25,50,75 and 100.

All model choices show a decreasing κ_n, resulting in a decreasing secant stiffness k_f the rate of which slows with cycle number following the power-law formulation. In the constant case the reduction happens over all surfaces equally. During cycling this manifests in ratcheting as well as softening; as the yield strengths of the softer surfaces are reduced they progressively become active, causing higher strains upon virgin loading in the same manner as a monotonic stress application (see the degraded backbone shown dotted). This is a secondary mechanism and cannot be controlled independently. Post-cyclic strength is much lower than the original backbone. With continued cycling, failure occurs once $K_{Ns} < \sigma$.

In the surface-specific case only the surfaces which are activated (where $K_{n,active} < \sigma_{cyc}$) degrade. Secant stiffness continues to reduce but the loop shape develops differently. This means that no ratcheting or changes to post-cyclic strength occurs. Eventually, with further cycles, the loop will become linear as $K_{n,active} \rightarrow 0$ and therefore limits secant stiffness development.

The combined case sits somewhere between the two. The linear change in yield strength K_i and sudden change at approximately surface 12 is a function of constant amplitude testing, for varied loading one could expect κ_n to vary much more smoothly with surface.

More subtly, the choice of F_κ changes the shape of loops. This is clearer for a two-way case as the accumulation of strains is removed. Figure 3.42 shows the same model (with consistent parameters) subject to 100 cycles of a two-way load in which $\sigma_{av} = 0$ and $\sigma_{cyc} = 0.45$. All three models show reducing secant stiffness. For the constant softening case the loop shape is preserved and rotated whilst for the surface specific case the shape becomes almost bi-linear. This is emphasized when considering energy loss factor η_I: increasing when F_κ=0, decreasing when F_κ=1 and remaining almost constant (for this case) when F_κ=0.5. The differing magnitude of $k_{f,n}/k_{f,1}$ with similar parameters means that $F_{\beta,l}$ and $F_{\beta,G}$ may take different values depending on F_κ and formulation of Equation 3.37.

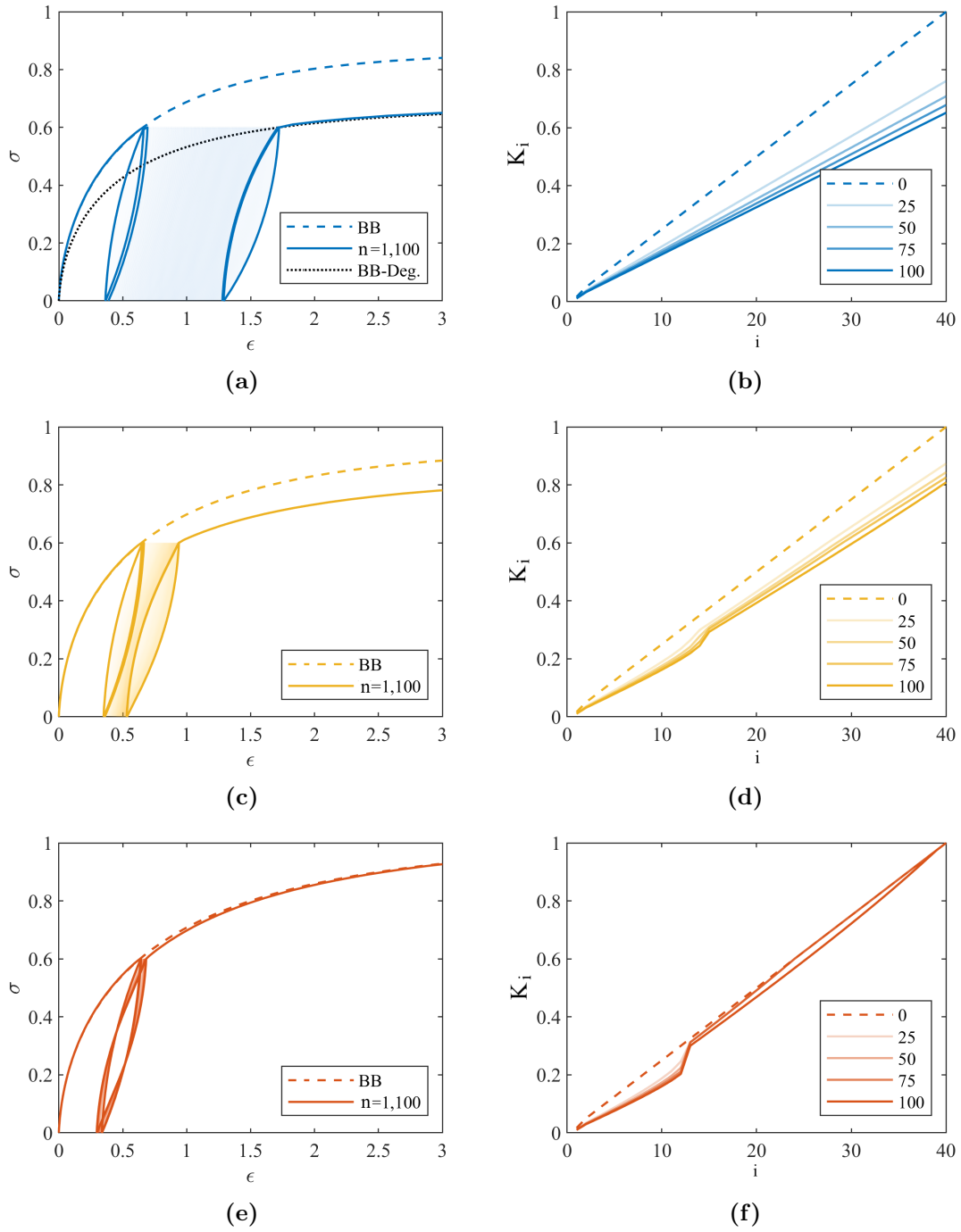

Figure 3.41: Softening model choice for a rate independent model with monotonic parameters similar to DRM OCR=1 and subject to 100 cycles of one-way loading. Left hand column – stress-strain response, Right hand column – surface strength degradation against surface number. (a)(b) Global softening, $F_\kappa = 0$ (c)(d) Mixed softening, $F_\kappa = 0.5$ (e)(f) Local softening, $F_\kappa = 1$

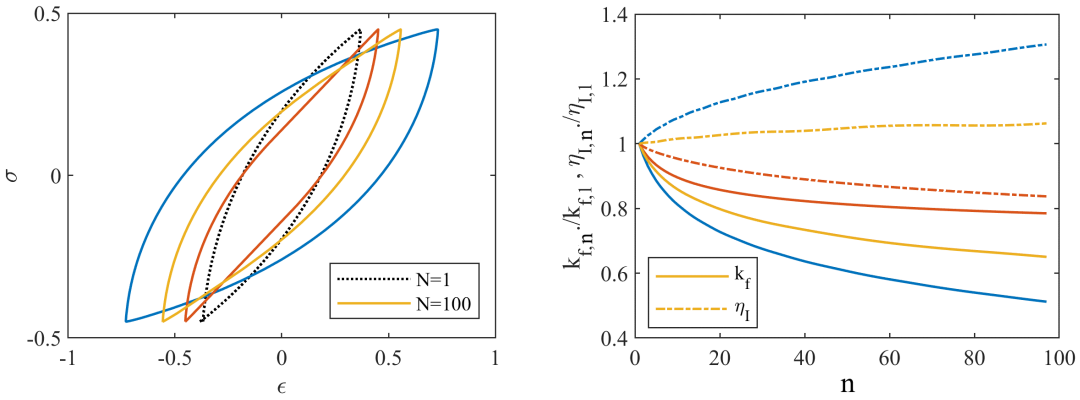

(a) **(b)**

Figure 3.42: Softening model choice as in Figure 3.41 with two-way load applied.

Given the evidence in the previous section in which the energy loss factor tended to reduce with cycles and post-cyclic strength did not reduce unless the sample was failed, it would provisionally seem that a value close F_κ=1 is the better option. This also allows for control of the development of ratcheting. The rapid degradation to failure sometimes seen when effective stresses become low may not be captured as well, and for constant amplitude tests secant stiffness reduction may be limited. It is noted that if higher softening is required, $F_\kappa < 1$.

Table 3.7 summarises the differences in behaviour between surface specific and

Table 3.7: Summary of model behaviour changes when employing constant or surface-specific softening for constant stress-amplitude loading. Mixed softening sits somewhere between the two

	Constant Softening $F_\kappa = 0$	Surface-specific Softening $F_\kappa = 1$
General	All surfaces are 'degraded' equally as a function of $\sum \beta_i$	Only activated surfaces degrade as a function of local parameter β_i
Secant Stiffness	Reduces in a similar manner to surface degradation	Reduces in a similar manner to surface degradation
Hysteresis Loop	Shape preserved, loop area and energy loss factor increase	Loop shape may become bi-linear as only lower surfaces degrade, energy loss factor decreases
Post-cyclic Response	Post cyclic ultimate strength is reduced by the same amount as surface degradation $s_{u,pc} << s_{u,0}$	Post cyclic ultimate strength is almost unchanged $s_{u,pc} \approx s_{u,0}$
Ratcheting	If $\tau_{av} \neq 0$ considerable ratcheting occurs as a by-product of global softening	If $\tau_{av} \neq 0$ no ratcheting occurs

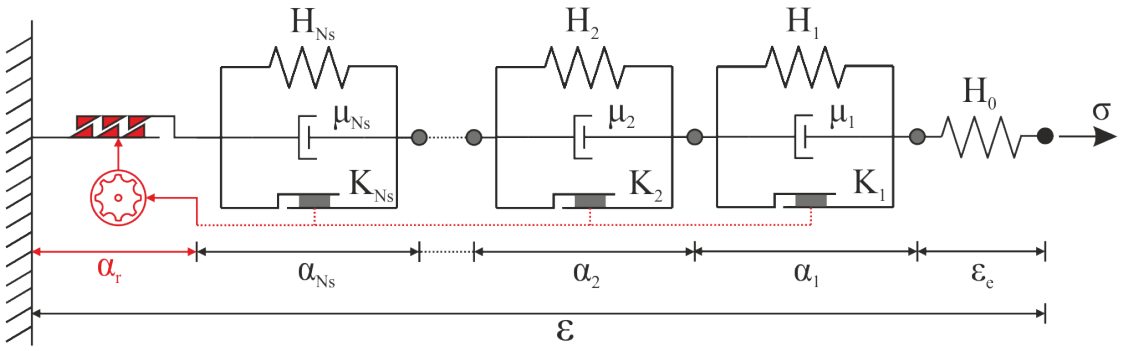

Figure 3.43: Rate-dependent series HARM model

constant softening. Large differences in behaviour are observed for a very subtle model change, in this case reduced to a single switch parameter, F_κ. Similar total-stress models exist which make use of softening or 'degradation' rules either degrading strength or stiffness subject to some quantity (Whyte et al., 2020; Vucetic and Dobry, 1988; Huang and Liu, 2015). Employing multi-surface, surface-specific degradation could give similar benefits to any similar constitutive model.

3.4.2.2 Ratcheting

Whilst some ratcheting already occurs in the model due to creep (rate-dependency) and softening, additional strain may be required. The HARM (Hyperplastic Accelerated Ratcheting Model) extension (Abadie, 2015; Beuckelaers, 2017; Houlsby et al., 2017) employs an additional ratcheting unit (shown in red) with associated internal strain parameter, α_r (shown schematically in Figure 3.43). The model is defined by energy and dissipation functions:

$$f = \sum_{i=1}^{Ns} \frac{H_i}{2}(\varepsilon - \alpha_i - \alpha_r)^2 + \frac{H_{Ns+1}}{2}(\varepsilon - \alpha_r)^2 \tag{3.38}$$

$$d = \left[\sum_{i=1}^{Ns} K_i|\dot{\alpha}_i| + \sum_{i=1}^{Ns} K_i\eta\dot{\alpha}_i \sinh^{-1}\left(\frac{\dot{\alpha}_i}{\dot{\alpha}_{ref}}\right)\right] + \sigma\dot{\alpha}_r \tag{3.39}$$

Incremental behaviour is derived as in Appendix A (which also includes extension to asymmetrical strength). α_r is controlled by a constraint function which can be written as:

$$\dot{\alpha}_r = S(\sigma)\sum_{i=1}^{N_s} R_i|\dot{\alpha}_i| \tag{3.40}$$

such that ratcheting develops with the sum of the increments of plastic strain. $S(\sigma)$ ensures that the increment of α_r is the same as the direction of current load, therefore developing in the direction of load bias (our cancelling out for symmetrical loading). R_i controls the rate of ratcheting which Houlsby et al. (2017) define as:

$$R_i = R_0 \frac{K_i}{\sigma_u} \left(\frac{\beta}{\beta_0} \right)^{-m_r} \left(\frac{|\sigma|}{\sigma_0} \right)^{m_s} \tag{3.41}$$

where m_r decreases R_i with hardening parameter, m_s increases R_i with current stress level and R_0 controls the magnitude of the function. K_i/σ_u (in combination with α_i in Equation 3.40) makes α_r dependent on work, particularly important for parallel models. In a similar manner to the softening relationship the simple power law means that at low β, $R > R_0$ and hence Richards (2020) proposed a modified power law:

$$R = R_0 \left(1 + \frac{\sum \beta_i}{\beta_{R,ref}} \left(\left(\frac{R_0}{R_{ref} \left(\frac{|\sigma|}{\sigma_u} \right)^{m_s}} \right)^{\frac{1}{m_r}} - 1 \right) \right)^{-m_r} \tag{3.42}$$

Parameters are similar to the previous relationship with the addition of $\beta_{R,ref}$ and R_{ref} which again act as a pin on the power relationship of R versus σ and β_i. K_i/σ_0 is no longer included since β becomes a work quantity. Implications of this are discussed in detail in Chapter 5). For consistency $\beta_{R,ref}$ may be formulated as a factor of expected β in a similar way to global softening (Equation 3.37) such that:

$$\beta_{ref,R} = \overbrace{F_{\beta,R}.2A}^{Work} \; or \; \overbrace{F_{\beta,R}.\frac{2A}{K_{Ns}}}^{Strain} \tag{3.43}$$

where A is the area beneath the backbone to K_{Ns} such that $A = \int_0^{K_{Ns}} \sigma d\varepsilon$ and $F_{\beta,R}$ is a unitless parameter. Work softening is advised such that $\dot{\beta}_i = |\dot{\alpha}_i| K_i$.The stress dependency may be turned off if $m_s = 0$. If strain dependency is required (rate of ratcheting only related to stress level) Equation 3.42 is rewritten as:

$$R = R_0 \frac{K_i}{\sigma_u} \left(\frac{|\sigma|}{\sigma_u} \right)^{m_s} \tag{3.44}$$

Some of the evidence presented previously shows that ratcheting increases with cycles despite cycling around the same stress magnitude. It should be noted that ratcheting is also dependent on plastic strain or work $\Sigma\beta_i$. As secant stiffness reduces with cycles so too plastic strain per cycle increases. In this case the reducing ratcheting rate would compete with the increasing plastic strain. Hence the two are intrinsically coupled.

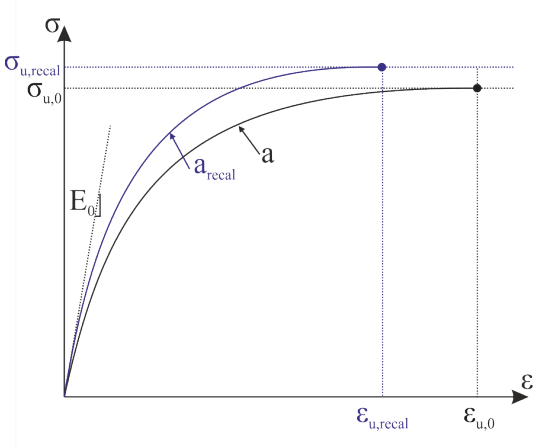

Figure 3.44: Original (0) and recalibrated (recal) '*Jeanjean*' function for softening

3.4.3 Calibration

The extended model may now be calibrated to cater for cyclic effects. As previously mentioned it is sensible first to ensure accurate softening before then extending the model for ratcheting. Optimisation or manual fit against the development of k_f (or ε_{cyc}) is therefore appropriate. If possible this can include η_I (which is only available with continuous data) and $s_{u,pc}$ to aid the choice between local and global softening.

There are now 5 parameters to calibrate which are well defined and limited by:

$$0 < \kappa_{ref} <= 1, 0 <= F_\kappa <= 1, 0 < m_k, 0 < F_{\beta,l}, 0 < F_{\beta,G}$$

Further limitation of variables is ensured by fixing one of the paired values (κ_{ref}, F_β), fixing global hardening parameter factor to be equal to the local $(F_{\beta,G} = F_\beta)$, beginning with surface-specific softening only, and setting sensible constraints for m_k and F_β. F_κ is only allowed to vary if a specific data-set requires it, e.g. higher levels of softening are required. Such that:

$$\kappa_{ref} = 0.7, F_\kappa = 1, F_{\beta,G} = F_\beta, 0 < m_k < 0.5, 0 < F_\beta < 50,$$

Whether optimising by eye or by routine, the aim is to minimise the difference in measured and modelled k_f (and η_I). Initial model values of $k_{f,1}$ and $\eta_{I,1}$ are dependent upon the accuracy of the rate and monotonic calibration, therefore $\Delta k_f = k_{f,n} - k_{f,1}$ is used to ensure the algorithm does not compensate for previous inaccuracy. Careful consideration of data is required to ensure each test is given an equal weighting (regardless of number of cycles and data points).

Accumulation of strain may be captured by decreasing F_κ (allowing further global softening), or including a ratcheting element. It is not clear which is most appropriate and may well be material or test dependent. Data regarding loop shape or post-cyclic strength may aid this choice by fixing F_κ, but this is not always available. Instead the choice is left open. If the former is chosen optimisation of softening parameters can simply include some measure of accumulated strain, ideally $\Delta\varepsilon_n$.

Instead the same metric may be used to calibrate ratcheting parameters; Fixing the value of R_{ref}/R_0 and optimising R_0, m_s, m_r and $F_{\beta,R}$. Richards (2020) suggests that m_s may be provisionally derived from experimental exponents, and proposes fixing $R_0 = 1$, whilst Abadie et al. (2019) describe an analytical method for parameter derivation, albeit for a different formulation. In this case R_0 is also allowed to vary but in future work it would seem sensible to fix $R_0 = 1$.

Softening and ratcheting will begin as soon as plastic strains develop which changes the calibrated, monotonic, 'backbone' response. A 'backbone recalibration' is therefore required as described in Section 3.3.3, achieved at the function fit level.

Figure 3.44 shows an idealisation of the original Jeanjean fit and the recalibrated ('recal') fit in which the ultimate stress,strain and curvature are optimised whilst the initial stiffness and strength is kept the same, such that typically for softening only:

$$E_{recal} = E_0, \sigma_{u,recal} > \sigma_{u,0}, \varepsilon_{u,recal} = \varepsilon_{u,0}, 0 < a_{recal}$$

ratcheting only:

$$E_{recal} = E_0, \sigma_{u,recal} = \sigma_{u,0}, \varepsilon_{u,recal} < \varepsilon_{u,0}, 0 < a_{recal}$$

and combined ratcheting and softening:

$$E_{recal} = E_0, \sigma_{u,recal} > \sigma_{u,0}, \varepsilon_{u,recal} < \varepsilon_{u,0}, 0 < a_{recal}$$

If the PISA conical function is used the curvature parameter n is limited by $0 < n_{recal} < 1$. Importantly this correction is undertaken using a rate-independent algorithm.

Table 3.8: Summary of evidence and modelling of rate-dependent response

Behaviour	Evidence	Modelling Technique	Calibration
Stiffness reduces with cycles in clay element tests. The rate of which increases with intensity of loading and reduces with number of cycles.	All	Introduce strain or work softening and reduce yield strengths of surfaces. Employ a modified power law.	Isolate softening by focusing on two-way tests.
Strain accumulation occurs when $\tau_{av} \neq 0$.	All	(1) Introduce ratcheting element. Stress dependency, and history dependency can be included. (2) Introduce mixed softening.	Calibrate to $\tau_{av} \neq 0$ to tests.
Post-cyclic shear strength differs depending on history: Highly strained samples tend to become weaker whilst samples with low strains remain the same or potentially increase.	DRM COW NSCA	Allow for control of this using a combination of surface-specific and constant softening. Implemented using parameter F_κ.	If post-cyclic shearing data is available (pre-failure only) this can aid calibration of F_κ. Default F_κ close to 1.
Behaviour remains consistent until close to failure. Change occurs due to large changes in effective stress and proximity to critical state line	KAO NSCA	Not explicitly modelled. May be possible to model with change to F_κ. But to genuinely model this a critical state model is required with effective stress capability.	*N/A*

3.4.4 Modelling summary and application to datasets

This section has shown that when subject to many constant amplitude cycles, strain response in clay element tests progressively changes. Table 3.8 summarises the key observations, modelling techniques and calibration methods. There is now the potential for two model choices which produce a similar response in the most commonly used metrics (γ_{av},γ_{cyc}) for constant stress amplitude tests. These are discussed further in 3.5.1 and applied in Chapter 4.

Table 3.9 shows the selected cyclic parameters. Drammen clay models are not calibrated for reproduction of the contour diagrams, which are discussed in section 4.1 and therefore not introduced here. NSCA OCR=1 cases have no ratcheting parameters as only two-way testing was undertaken, whilst in NSCB the ratcheting

Table 3.9: Parameters fit to cyclic tests in selected datasets. All employ work-hardening and $\kappa_{ref} = 0.7$

	KEY	Tests used	σ_{vc} or p_0 $[kPa]$	F_κ	F_β	m_k	R_0	m_s	m_r	$\frac{R_{ref}}{R_0}$	$F_{\beta,R}$
DSS	NSCA OCR1	2	70	0.9	0.5	0.3					
	NSCA OCR1	4	300	0.8	0.5	0.25					
	NSCB OCR3	5	325	0.9	1	0.1					
CU	KAO	8	200	0.7	0.3	0.25					
	COW	6	67	1	1	0.2	0.015	5	2	0.7	65
			Mean:	**0.86**	**0.66**	**0.22**					

was catered for by F_κ. In the KAO dataset q_{av} was applied drained, changing the backbone response ,therefore only symmetrical tests were used.

Figure 3.45a to 3.45d show an example fit to 6 tests within the Cowden data-set. Surface-specific softening is employed with ratcheting which reproduces measured strains well. The model fit is poorer at high cycle numbers of high intensity tests, which corresponds to an intensification of strain close to failure. Introducing a slightly reduced F_κ, e.g. F_κ=0.9, improves the prediction of 'progressive' failure but is not pursued for the Cowden set. This has been employed for some DSS_{cyc} tests, particularly those where the majority of the tests fail.

NSCA ($\sigma_{vc,0} = 300kPa$) is a good example of this. Figure 3.46a shows the change in cyclic strain, whilst Figure 3.46b shows modelled and measured hysteresis loops. Three of the four tests suddenly fail, with a steep increase in cyclic strain. By using a reduced F_κ value the computation of the sharp increase (and change in loop shape) is better predicted near failure although still not fully captured.

3.5 Model discussion

As mentioned throughout Chapter 3, hyperplasticity models are fully defined by two functions; energy and dissipation. The final model formulation including rate, asymmetry, softening and ratcheting is summarised in Appendix A. Each preceding model presented in this chapter can then be seen as a special case, easily switched off with the careful specification of parameters.

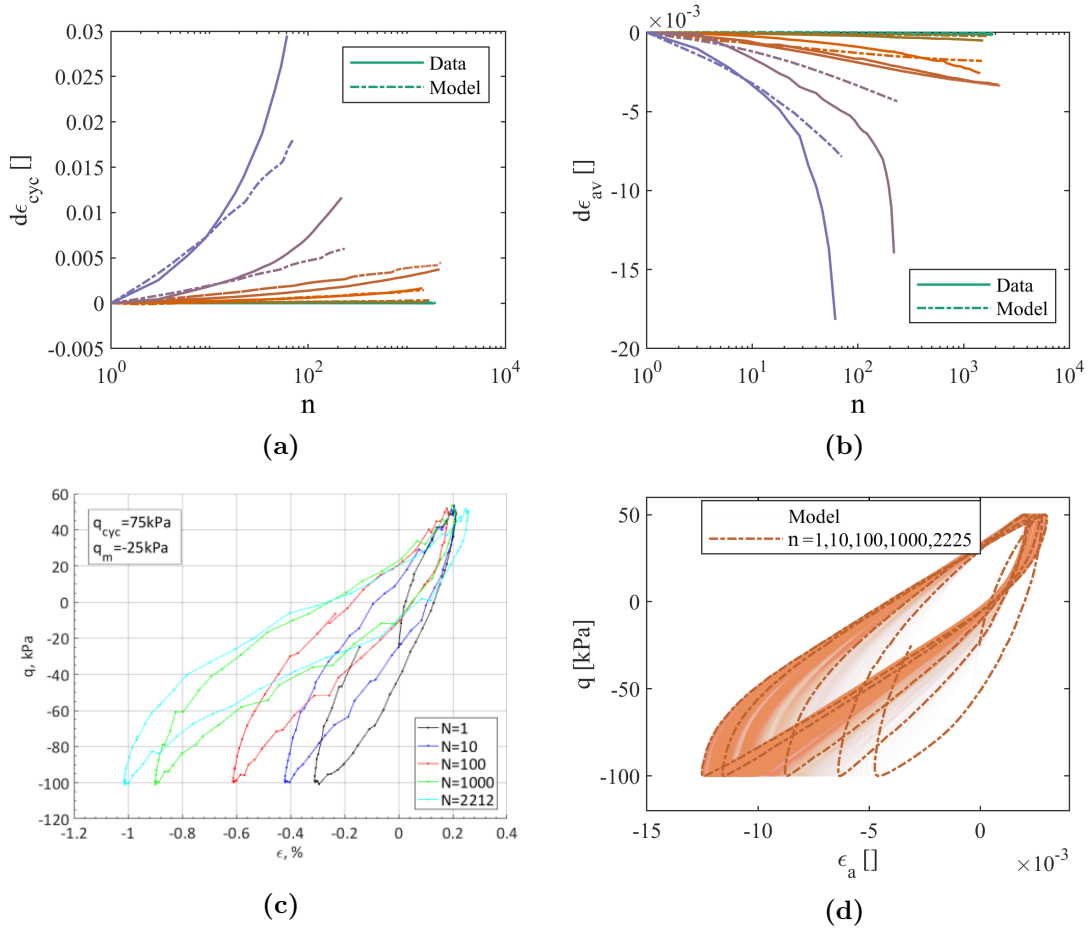

Figure 3.45: Calibrated series model compared to measured CU_{cyc} data from Cowden dataset (a) Change in secant stiffness with cycle number for tests in which q_{av}=-25kPa (b) Change in average strain with cycle number for tests in which q_{av}=-25kPa (c) Measured hysteresis loops, plot after Ushev, 2017 in which N refers to cycle number (d) Modelled hysteresis loops corresponding to test in (c)

3.5.1 Parameter choices

A total of 18 parameters could be used when calibrating the full hyperplasticity model presented, these are shown in Table 3.10. Some parameters are arbitrary, paired with other parameters to give a reference point (such as κ_{ref}), and are shown in blue. Those in grey take known values or control model precision. Within each mechanism complexity can be added at the cost of including another parameter (or more) which must then be calibrated, shown in green. The minimum number of parameters which must be calibrated (left in white), allowing for decoupled and fully defined behaviour, now reduces to 10 (3-Monotonic, 1-Rate, 2 Softening, 4-Ratcheting).

When modelling cyclic loading there appears to be a choice to be made between allowing ratcheting to be captured fully by softening behaviour (and therefore tuning

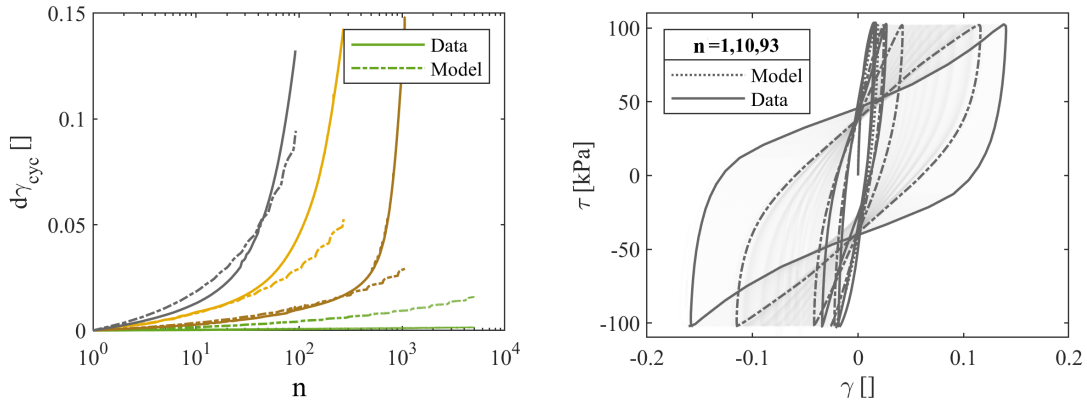

(a) **(b)**

Figure 3.46: Calibrated series model compared to measured DSS_{cyc} data from NSCA dataset (a) Change in secant stiffness with cycle number (b) Comparison of hysteresis loops

F_κ) or removing ratcheting from the softening behaviour and allowing this to be captured by a separate unit. So far this thesis has opted to use both, allowing more control and capturing the loop shape. With the experience of modelling constant amplitude stress tests it is not yet obvious which is the best choice.

3.5.2 Repeatability of tests

Hyperplasticity models are mechanistic and additive with each mechanism building upon the previous. The backbone calibration is therefore most important; small changes effect development of all metrics of monotonic and cyclic behaviour. Concurrently, variability is typically high in soil element testing. The response of a sample from the same unit subject to the same initial conditions and applied stress can vary considerably. This can be seen in Figure 3.22a for monotonic and initial 1/4 cycle of cyclic tests

It is therefore advantageous to have a number monotonic tests to base an average backbone upon, as well as repeated cyclic tests. This is particularly true for straight forward shear conditions where variability is higher owing to sample size and lack of lateral stress control.

3.5.3 Test location for calibration

In this chapter model accuracy is only measured against the calibration tests. In some cases only two-way tests were available, limiting the predictive ability to similar tests.

For those sets in which $\tau_{av} \neq 0$ tests are available, limitations of loading type and magnitude still hold. Interaction diagrams such as that shown in Figure 3.3 provide a useful pictorial view of these locations and therefore an idea of where the model will most likely be most accurate.

It would be useful to be able to test models outside of their calibrated range without further testing, as well as define what type and magnitude of cycles best represent that which the soil around a monopile may experience. The first point is addressed in the following chapter whilst the latter is addressed in Section 6.5.

Table 3.10: Summary of Parameters and nominal values

	Parameter	Description	Typ. Value	Range	Notes
Monotonic	$\boldsymbol{E_0}$	Initial Stiffness	$750s_u$	250-1000s_u	Estimated or found from bender element tests
	$\boldsymbol{\sigma_u}$	Ultimate yield strength	s_u	(50-200kPa)	Taken as s_u unless required focus at low stress levels
	$\boldsymbol{\varepsilon_u}$	Ultimate yield strain	0.1	0.05-0.15	Paired with k_u
	$\boldsymbol{a}$	Curvature parameter (Jeanjean)	2.2	1-3	Optimised fitting parameter
	$\boldsymbol{Ns}$	Number of surfaces	40	10-100	With more surfaces comes greater non-linearity at the cost of computational time
Rate	$\boldsymbol{t_{ref,G}}$	Reference time	$1000hrs$	1week – 2 months	Controls point at which rate dependency changes from linear to log
	$\boldsymbol{\eta_{10}}$	Viscous constant	0.2	0.05-0.3	Can be estimated as increase in strength per log strain rate
	$\boldsymbol{F_\eta}$	Rate surface factor	1	0.5-1	Controls viscous development with surface
Softening	$\boldsymbol{F_\kappa}$	Softening type factor	1	0-1	Controls how softening occurs. 1 = surface specific, 0 = constant.
	$\boldsymbol{\kappa_{ref}}$	Reference strength reduction	0.7	0-1	Paired with F_β
	$\boldsymbol{F_{\beta,l}}$	Softening development factor	1	0.1-5	Controls how quickly local softening reduces to k_{ref} (as factor of expected strain)
	$\boldsymbol{m_k}$	Softening exponent	0.2	0-0.4	Controls rate of reduction of κ
	$\boldsymbol{F_{\beta,G}}$	Global softening development factor	F_β	F_β	Can independently control when global softening occurs
Ratcheting	$\boldsymbol{R_0}$	Ratcheting constant	0.1	0.01-10	Initial rate of ratcheting (Magnitude changes depending on m_r and m_s)
	$\boldsymbol{m_s}$	Stress dependency exponent	2	1-5	Ensures ratcheting increases with stress magnitude
	$\boldsymbol{m_r}$	History dependency exponent	5	2-10	Ensures ratcheting decreases with stress magnitude
	$\boldsymbol{\frac{R_{ref}}{R_0}}$	Reference ratcheting rate reduction	0.7	0-1	Paired with $F_{\beta,R}$
	$\boldsymbol{F_{\beta,R}}$	Ratcheting development factor	30	5-60	Controls how quickly local softening reduces to k_{ref} (as factor of yield)

Chapter 4

Application of 0D models

In Chapter 3, a stress controlled model was developed with a view to capturing behaviour observed in constant stress amplitude tests. This was then applied to a variety of data-sets, each with a small number of cyclic tests subject to a variety of loading regimes. In this chapter the same model is applied to more extensive tests of the underlying mechanisms.

Calibrating to typical cyclic element tests is a useful exercise, but is limited as a true test of model formulation. Each calibration is based solely upon the types of loading of the tests in the given set. One may reasonably assume that for similar stress conditions the model will perform equally well. This conclusion is less clear, however, when interpolating between tests which are relatively far apart, or indeed extrapolating behaviour. This is shown indicatively in the interaction diagram and example tests of Figure 4.1

To truly test the model, calibration and comparison could be undertaken on all possible locations of the interaction diagram (or discrete points at a certain distance apart), thereby testing all loading conditions and magnitudes for a sample at known consolidation conditions. Data-sets of this kind would be unjustifiably time consuming to obtain, but work by the Norwegian Geotechnical Institute (NGI) has aimed to summarise behaviour across all loading conditions by interpolation (Andersen et al., 1980; Andersen, 2015). The results take the form of 'contour diagrams' which are well established in offshore geotechnics. Section 4.1 aims to reproduce these plots synthetically using hyperplasticity models.

However, perfect prediction of response across a full range of constant amplitude cyclic testing is not necessarily indicative of a model capable of accurately predicting

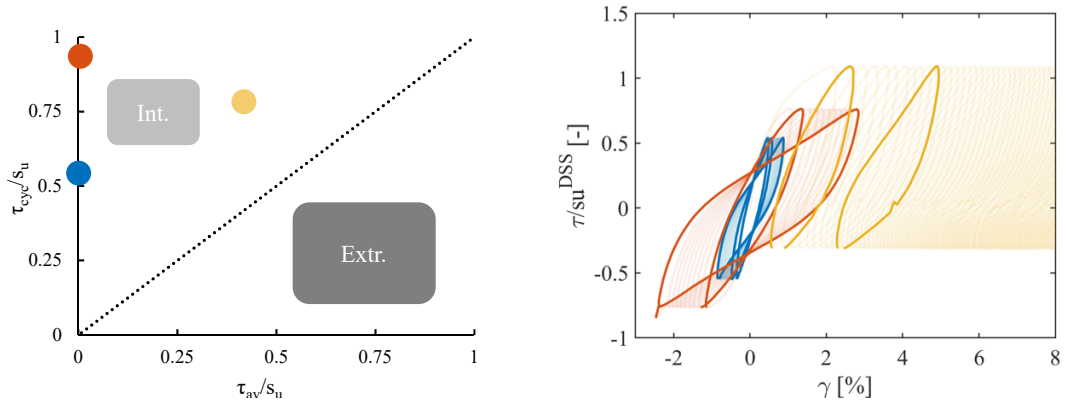

(a) (b)

Figure 4.1: Example stress-controlled DSS_{cyc} testing regime of a clay showing locations on an interaction diagram (a) and measured response (b). Indicative positions of interpolated or extrapolated tests shown.

the response of more realistic offshore loads. These will probably be pseudo-random (i.e. loads changing magnitude with time). As discussed in the previous chapter, the behaviour of soil is often dictated by the previous stresses which have been applied (history), constant amplitude tests hide the fact that the history will develop in a less orderly manner. Given that the models developed can apply any increment of load (intrinsic, as introduced in Section 1.3.5) it seems sensible to test against truly multi-amplitude loading. Fortunately these have also been undertaken at NGI as part of the WAS-XL (WAve Loads and Soil support for eXtra-Large monopiles) project. Section 4.2 compares the predictions of a model calibrated to constant amplitude tests against measured irregular loading response in DSS_{cyc} conditions.

4.1 Synthesising contour diagrams

Strain contour diagrams, developed at NGI, are representations of cyclic element test results across a coordinate system of applied stress and cycle number. These are commonplace in the design of offshore foundations to cyclic loads. The method was initially developed for Drammen clay (Andersen et al., 1980) and has since been applied to many other soil units (e.g. Wichtmann et al., 2013). It offers a quantitative, albeit heavily smoothed, view of strain development in a material subject to various cyclic stress regimes.

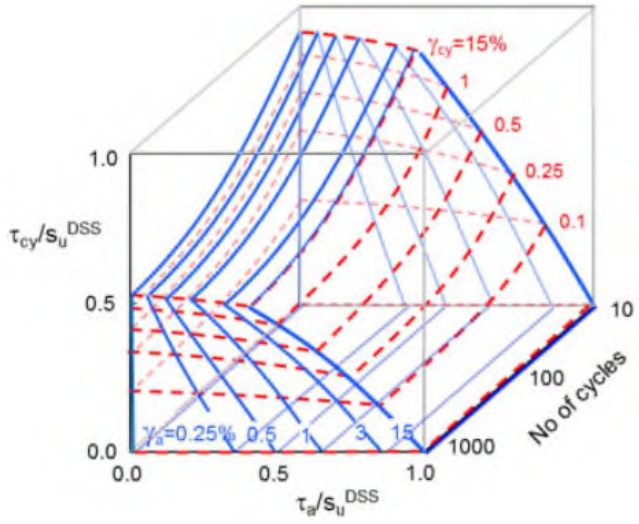

Figure 4.2: 3D Contour Diagram of cyclic (red) and average (blue) shear strains as a function of cyclic and average shear stress and number of cycles for normally consolidated Drammen clay in DSS conditions (Andersen, 2015).

Andersen (2015) writes with regards to contour diagrams: 'Since the contour diagrams represent a compilation of directly measured data without modification they can also be used to develop other soil models and to provide data to such models.'; this chapter aims to do just that by recreating the NGI plots synthetically using the hyperplasticity models presented in Chapter 3. Using a mechanistic model sheds light on the physical processes at play across the stress and cycle space and is a crucial step in validation of model choices.

4.1.1 Introduction

Cyclic element tests with similar initial conditions and frequency of loading are required to build a contour diagram. Each test can be identified by τ_{av} and τ_{cyc}, the response is then measured at each cycle until failure and presented as γ_{av} and γ_{cyc}. Figure 4.2 shows a 3D representation of the resulting diagram for DSS_{cyc} conditions (τ and γ represent shear stress and strain), from which planes of fixed N or τ_{av} are often extracted. Similar plots are also constructed for tests in CU_{cyc} conditions where $\tau = q/2$ and $\gamma = 1.5\varepsilon_a$.

Here, contour plots are reproduced by simulating, using a hyperplasticity model, multiple synthetic tests in a grid of possible stress conditions (τ_{av},τ_{cyc}). The model input is a sinusoidal stress-time history which, to be a genuine comparison, must be

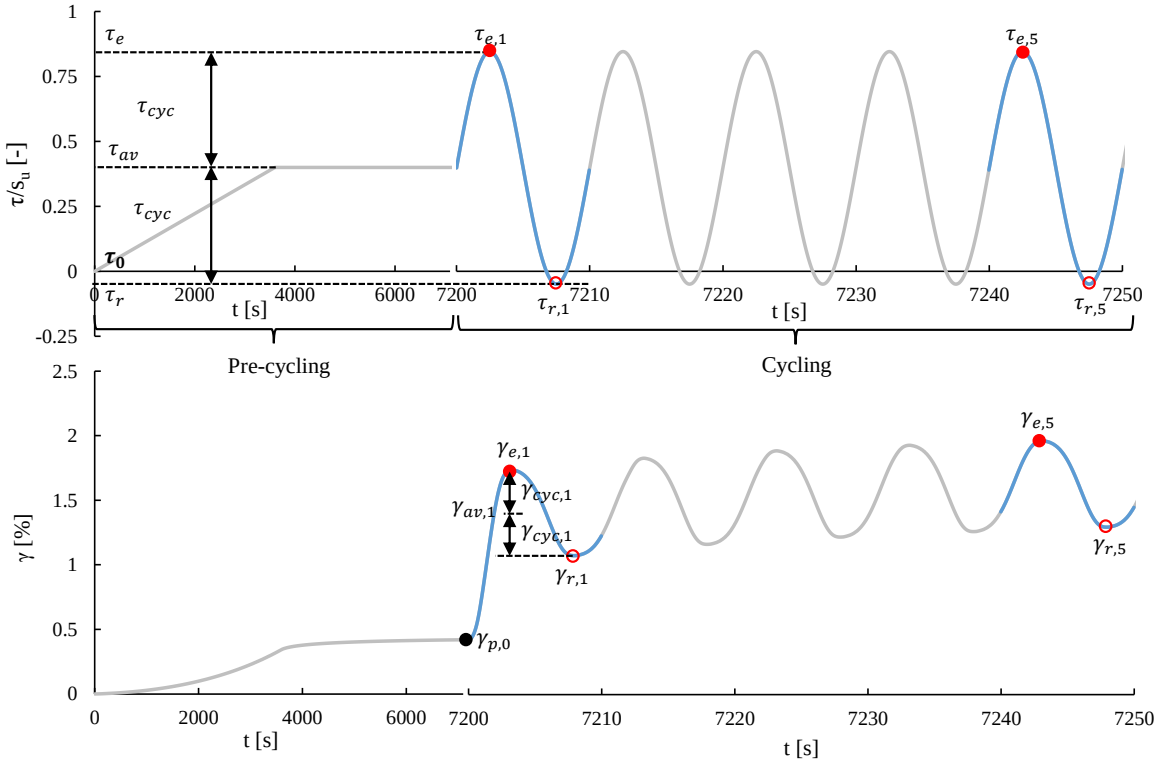

Figure 4.3: Load and strain history of typical DSS_{cyc} or $CUIcyc$ test. Left-hand side shows slow increase to average stress, Right-hand side shows $T = 10s$ cycles. First and fifth cycle shown in blue. Note difference in time scales.

equivalent to that of a real test at the corresponding coordinate. It is therefore crucial that cycle and response definitions are met closely.

Figure 4.3 shows idealised time histories of stress and strain for a typical simulated DSS_{cyc} or CUI_{cyc} test, Figure 4.4 shows the resulting hysteresis loop. The loading conditions are described by τ_{av} and τ_{cyc} which are normalised by the respective s_u, in this case $\tau_{av}/s_u = 0.4$,$\tau_{cyc}/s_u = 0.45$. The loading shown is post-consolidation and undrained, it may be split into pre-cycling and cycling.

Pre-cycling behaviour is shown on the left-hand side of Figure 4.3 ($t < 7200s$) and includes ramping of the shear stress from τ_0 to τ_{av} at a slow rate (say 1 hour) before holding the stress at τ_{av} for a further hour to allow for creep. τ_0=0 for DSS_{cyc} and CIU_{cyc} tests and corresponds to $q_0/2$ for CAU_{cyc}. The strain response observed is typically a non-linear increase with stress followed by further increase due to creep during the load hold. All further quantities of γ are measured inclusive of pre-cycling such that γ_0=0 at τ=τ_0 directly after the consolidation and before pre-cycling ($t = 0s$).

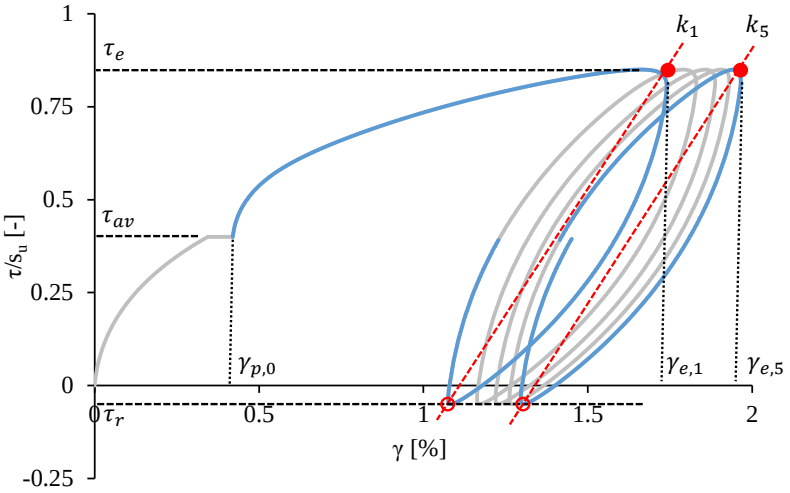

Figure 4.4: Stress strain diagram of a typical *DSScyc* or *CUIcyc* test. Corresponds to Figure 4.3.

Cyclic loading is shown on the right hand side of Figure 4.3 ($t > 7200s$). Cycle 1 begins immediately after pre-cycling, loading to the extremum $\tau_e = \tau_{av} + \tau_{cyc}$, unloading to the reversal stress $\tau_r = \tau_{av} + \tau_{cyc}$, before reloading to τ_{av}. Further cycles are defined in the same way, beginning and ending at τ_{av}. The loading is applied sinusoidally with a loading period $T = 10s$.

Extremum (τ_e, γ_e) and reversal (τ_r, γ_r) points may be found for each cycle (n) as the peak and trough in the time domain and may occur at different times due to viscous behaviour, $t(\tau_e) \neq t(\gamma_e)$. This can be seen for $\gamma_{e,1}$ in Figure 4.4, where the strain increases after the peak shear stress is applied, an effect which is more pronounced with higher strain rates (highly stressed tests). Average strain, $\gamma_{av,n} = (\gamma_{e,n} + \gamma_{r,n})/2$, cyclic strain, $\gamma_{cyc,n} = (\gamma_{e,n} - \gamma_{r,n})/2$ and secant stiffness $k_n = (\gamma_{e,n} - \gamma_{r,n})/(\tau_{e,n} - \tau_{r,n}) = \gamma_{cyc,n}/\tau_{cyc}$ may then be computed.

For consistency with NGI practice, the cycle definitions above are used throughout this Chapter in both the 'original' and 'synthetic' contours. They differ from those advised in Chapter 2, most notably in that virgin loading still occurs during cycle one. The hysteresis loop of the initial cycle therefore differs somewhat from further cycles (Figure 4.4). Similarly, strain is presented in units of % and number of cycles referred to as N (or n when used for subscripts).

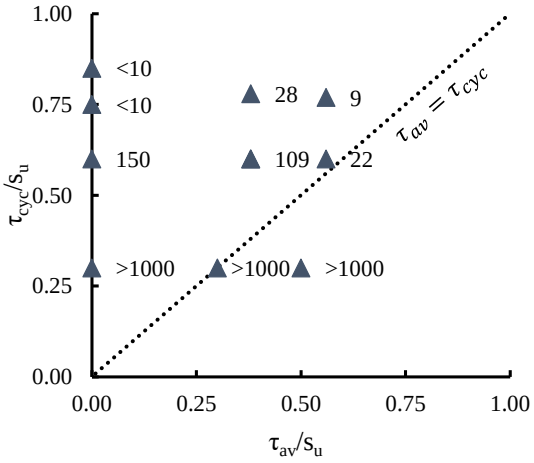

Figure 4.5: Location of DSS_{cyc} tests at OCR=1 with numbers of cycles to failure, N_f (defined as γ_{av} or γ_{cyc} >15%)

4.1.2 Cyclic simple shear OCR=1

4.1.2.1 Calibration

In this exercise the original direct simple shear tests used to create the contour plots are employed for calibration. 10 DSS_{cyc} tests were normally consolidated to σ'_{vc}=392kPa before being subject to stress controlled cycles. Applied stress conditions are shown in Figure 4.5, alongside numbers of cycles to failure, N_f (defined as γ_{av} or $\gamma_{cyc} > 15\%$). At each location $\gamma_{av,n}$ and $\gamma_{cyc,n}$ are known at cycles N=1,10, 100 and 1000 (Andersen, 1976; Andersen et al., 1980), unless $N_f < N$ in which case one can only infer that $\gamma_{av,N}$ or $\gamma_{cyc,N} > 15\%$. Additionally, two monotonic Direct Simple Shear (DSS) were undertaken at a strain rate $\dot{\gamma} = 4.5\%/hr$ with the same initial stress conditions.

A multi-surface, rate-dependent model configured in series is used. The model formulation and calibration follows that presented in Chapter 3. In Figure 4.6, a normalised rate-independent backbone curve is calibrated to the two DSS tests by fitting a hyperbolic tangent curve (Equation 3.6, Jeanjean et al., 2017). Surface strength and stiffnesses, K_n and H_n are then derived (see Section 3.2.1) for 40 surfaces.

Viscosity is calibrated against tests of differing strain rate; the 'slow' DSS tests and the initial cycles of the much faster DSS_{cyc} tests for which continuous data is available (Figure 4.7). Calibration follows Section 3.3.3, in which the same reference 'time' $t_{ref} = 10^4 hrs$ ($T_{u,ref} \approx 1$ month) is used. Viscous constant, η_{10} and surface

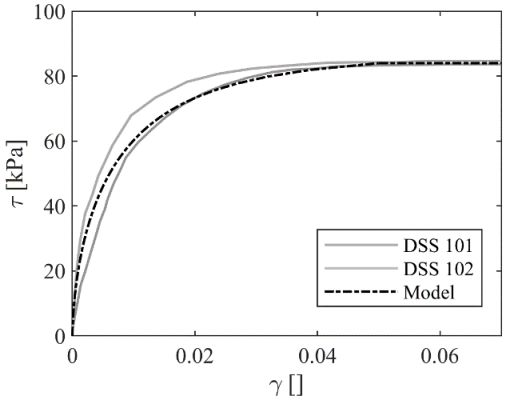

Figure 4.6: Monotonic fit to DSS data

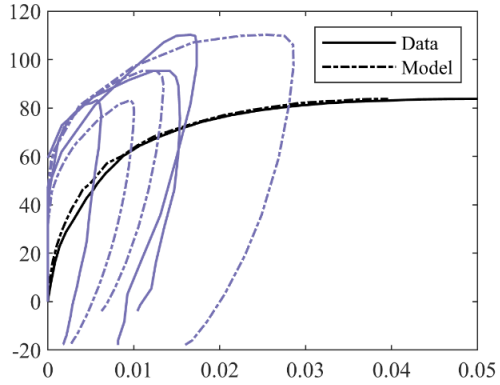

Figure 4.7: Model prediction of initial 3/4 cycle of selected DSS_{cyc} tests and one monotonic DSS test

Table 4.1: Monotonic and Rate-dependent parameters for Drammen Clay in DSS Conditions (OCR=1)

σ_{vc}	$s_{u,DSS}$	$\dot{\varepsilon_{BB}}$	$\frac{E_0}{s_{u,DSS}}$	$\frac{\sigma_u}{s_{u,DSS}}$	ε_u	a	t_{ref}	η_{10}	F_η	$\frac{\sigma_{u,0}}{s_{u,DSS}}$	a_0
$[kPa]$	$[kPa]$	$[kPa]$	[ ]	[ ]	[ ]	[ ]	$[hr]$	[ ]	[ ]	[]	[ ]
392	84	0.045	1000	1	0.07	2.06	10^4	0.2	0.91	0.77	2.51

factor F_η are then optimised alongside a recalibration of backbone parameters σ_u and a such that surface properties correspond to a test of time $t_u >> t_{ref}$ (as in Figure 3.21). Figure 4.7 shows that by adding viscosity, a good prediction of the increased strength with rate is achieved. A summary of monotonic and rate parameters is shown in Table 4.1.

Cyclic parameters are chosen to fit best the average and cyclic strain (γ_{av} and γ_{cyc}) values for each of the ten original tests at the known numbers of cycles N=1,10,100,1000 resulting in a total of 80 (=2*4*10) strain values. If $N_f < N$ then $\gamma_{av} = \gamma_{cyc}$=FAIL, and careful consideration is therefore required ensure the model predicts 'failure' after a similar number of cycles to the observations.

Figure 4.8 shows the model predictions (parameters shown in Table 4.2) of the biased ($\tau_{av} \neq 0$) tests with measured values shown as crosses. As in Section 3.4.3 work-hardening is employed, κ_{ref} is fixed at 0.7 whilst F_κ , m_k and $F_{\beta,l} = F_{\beta,G}$ were varied (along with a further backbone recalibration following Figure 3.44). No additional ratcheting element was employed because sufficient prediction of average strains was achieved with suitably calibrated softening behaviour. F_κ=0.8 implies

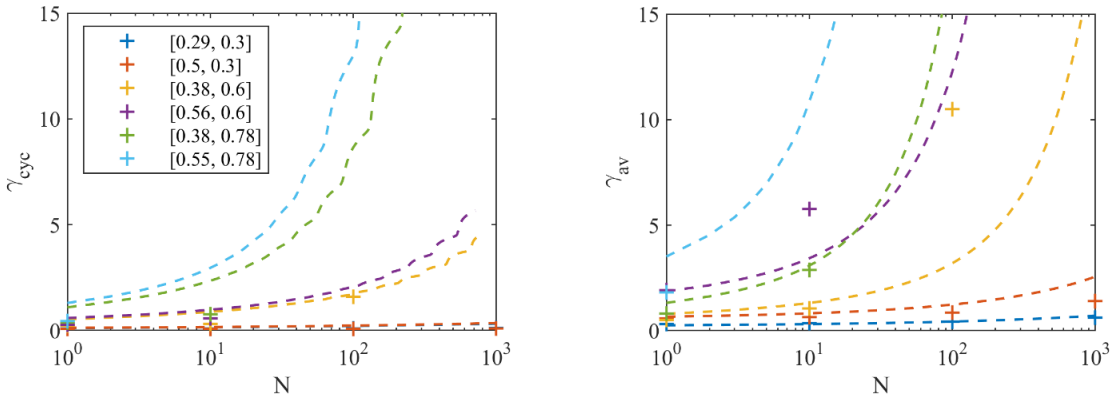

(a) **(b)**

Figure 4.8: Model fit (–) to measured data (+) for all biased tests, $\tau_{av} \neq 0$ (a) Cyclic strain γ_{cyc} (b) Average strain γ_{av}

Table 4.2: Unitless cyclic Parameters for Drammen Clay in *DSS* Conditions (OCR=1)

F_κ	κ_{ref}	F_β	m_κ
0.8	0.7	0.2	0.3

predominantly surface specific softening with some global softening. This allows for large changes to γ_{cyc} which whilst controlling the corresponding γ_{av} in $\tau_{av} \neq 0$ cases.

4.1.2.2 Contour diagrams

The left-hand column of Figure 4.9 shows cyclic and average shear strain contour diagrams derived by NGI (γ_{av} and γ_{cyc}) as a function of τ_{av} and τ_{cyc} after a fixed number of cycles N. Each row represents a different N from 1 to 1000. The original tests (shown as triangles) correspond to single points with associated strain values from which contours are drawn by inter/extrapolation. The contours use the measured data as markers but also involve some 'common sense' interpretation, drawn from the many years of experience of Knut Andersen and others at NGI. The x-axis ($\tau_{cyc} = 0$) does not correspond to a monotonic test but rather the strain after pre-cyclic stress application of a test at the same τ_{av}, labelled $\gamma_{p,0}$ in Figures 4.3 and 4.4.

The right-hand column shows the same plots produced by running synthetic tests at a grid of locations with spacings indicatively shown by black markers. The underlying model uses parameters in Tables 4.1 and 4.2. As discussed in Section 3.4.4, near failure behaviour (such as that shown in Section 3.4.1.4) is not well-modelled. This level of strain is not particularly important for OWT design. Here too, the

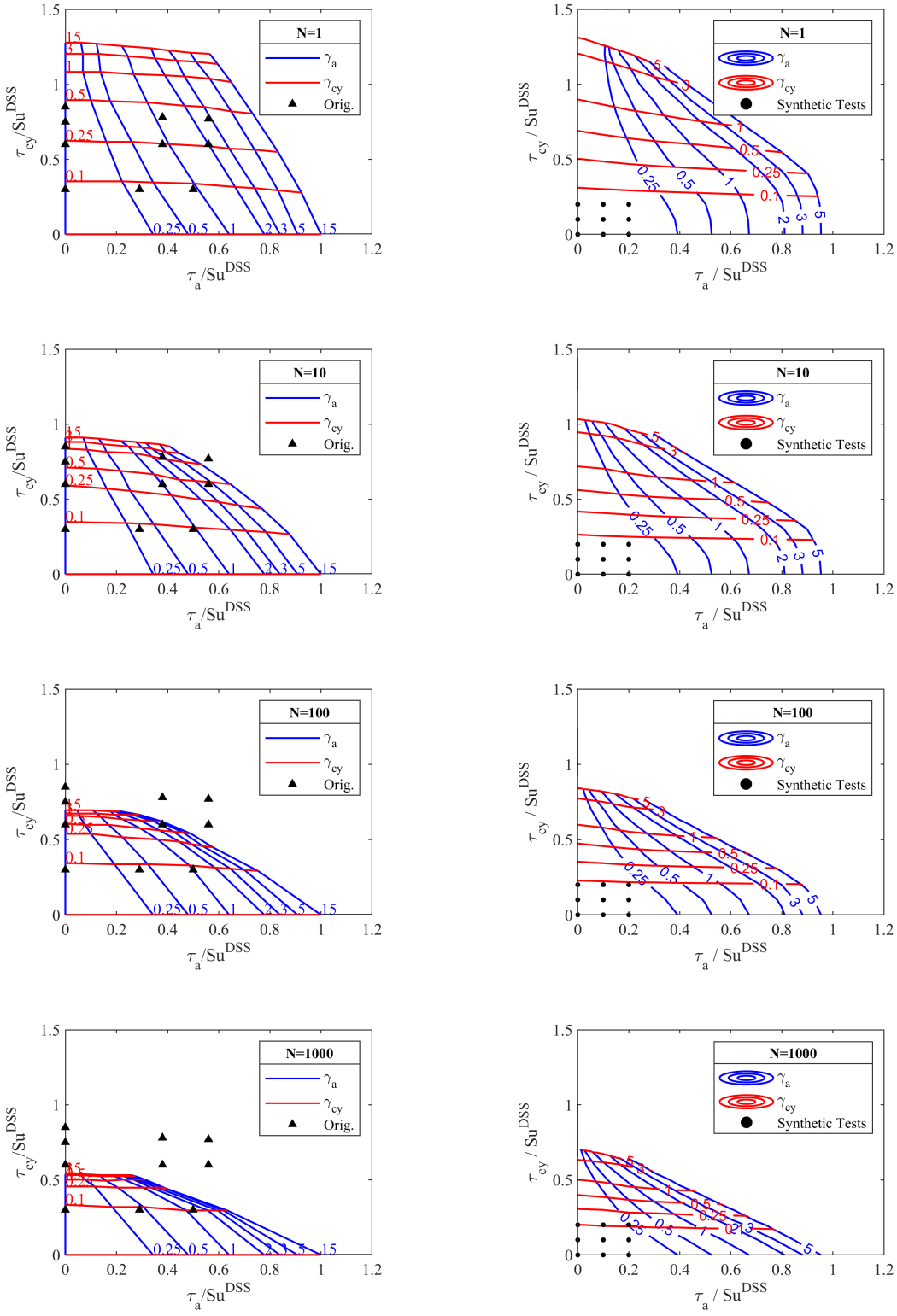

Figure 4.9: Drammen contour plots of DSS conditions $OCR = 1$ (a) Original Data, (b) Synthetic hyperplasticity predictions. Spacing of the test locations is only shown for 9 tests, although the grid extends across the full stress space.

development from 3% strain to 15% strain occurs rapidly (as seen by proximity of contours). For this reason final synthetic contours are chosen at 5% rather than at 15% in the original.

Qualitatively the synthetic contours are an excellent reproduction of the original plots and reproduce much of the original well. At $N = 1$ the γ_{av} contours meet the x-axis at similar intersections (pre-cyclic creep strain $\gamma_{p,0}$) suggesting a well calibrated $\dot{\gamma} \to 0$ backbone. The γ_{cyc} contours meet the y-axis at similar intersections too, albeit less accurately, this could be fine-tuned by slightly recalibrating rate-dependency but is considered adequate.

As cycles develop, both sets of contours close in towards the origin. This broadly occurs at a similar rate for both cyclic and average strains. In the original plots the higher magnitude strains progressively converge, suggesting an increasing rate of strain to failure which is not captured to the same extent by the model.

The γ_{cyc} cyclic contours have a negative gradient which is captured by the synthetic model as a product of: Masing rules, which would predict similar strain response for a given τ_{cyc} regardless of τ_{av} (producing horizontal contours); and work-softening, in which more softening and therefore higher γ_{cyc} is expected at higher stresses (higher τ_{av}).

The γ_{av} contours tilt inwards with stress amplitude and bias, consistently reproduced by the model. At low τ_{cyc} and N the γ_{av} contours are almost vertical, indicating reduced development of ratcheting for a given τ_{av}. This is not observed in the original diagrams, but this area is considerably extrapolated from the original measured data.

It is possible to isolate the softening behaviour by focusing on the plane of the contour diagram in which $\tau_{av} = 0$ (two-way tests), such that $\gamma_{av,n} = 0$ and $\gamma_{cyc,n}$ is a function of number of cycles (Figure 4.10a). In this case, element tests at fixed τ_{cyc} form horizontal lines from which contours of γ_{cyc} are plotted. The same diagram is synthetically reproduced and shown in Figure 4.10b, running multiple tests at increments of τ_{cyc} (as shown by black markers) to 10000 cycles.

With increasing cycles the secant stiffness reduces causing contours to progressively drop with N. This occurs at a faster rate with increasing strain magnitude. The synthetic plot reproduces much of the behaviour of the original with some exceptions: the predicted distance between the contours at high ($> 1\%$) strains is too large,

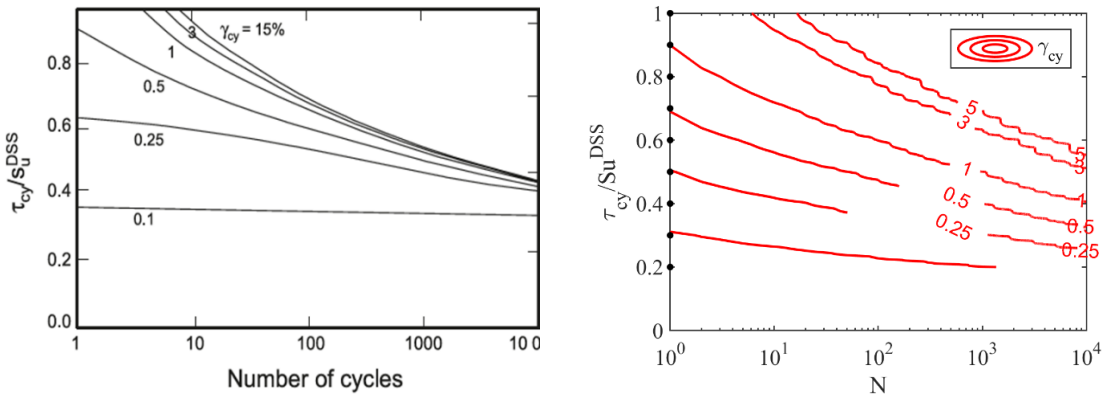

(a) **(b)**

Figure 4.10: Drammen contour plots of DSS conditions OCR=1 and $\tau_{av} = 0$. (a) Original (Andersen, 2015), (b) Synthetic hyperplasticity predictions

further indication that for a given test the rapid increase to failure is not captured; the contours meet the y-axis (which is the same as N=1 in Figure 4.9) at slightly different points; the synthetic reduction in secant stiffness is lower at high strains and steeper at low strains than in the original.

The model could, instead, have been optimised to fit the contour diagrams rather than the measured data. This has not been pursued. Modelling conclusions and quantitative comparison are discussed in the following sections.

4.1.2.3 Quantification of prediction

Further comparison can now be made between three data-sets of tests: 'Measured', which corresponds to the values measured in original DSS tests; 'Contours', where values are taken by interpolation between drawn 'Original' contours from NGI at the known test locations; and 'Synthetic', in which the model has been used to run the original tests. Table 4.3 summarises the 240 data-points, where the values in each cell correspond to γ_{av},γ_{cyc}. Those indicated 'Fail' are such that either γ_{av} or γ_{cyc} exceeds 15% such that the point lies outside of the corresponding contour diagram.

The same data are shown in Figure 4.11 by plotting the predictive 'contour' and 'synthetic' against the 'measured' strain values. All cycle numbers are included and split into γ_{av} (a and b) and γ_{cyc} (c and d). If a data-point is indicated by 'Fail', 15% is used. The figure is plotted at two scales for clarity, with the second focusing on the smaller strain values. In both, the dashed line indicates a perfect prediction of the measured data.

Table 4.3: Strain comparison for all original tests, values in each cell correspond to γ_{av},γ_{cyc} and are presented in %

	I.D	**1**	**2**	**3**	**4**	**5**	**6**	**7**	**8**	**9**	**10**
Test	τ_{av}/s_u^{DSS}	0	0.29	0.5	0	0.38	0.56	0	0.38	0.56	0
	τ_{cy}/s_u^{DSS}	0.3	0.3	0.3	0.6	0.6	0.6	0.75	0.78	0.77	0.85
Measured	N=1	0.02,0.05	0.31,0.09	0.57,0.07	0.06,0.21	0.52,0.22	1.93,0.27	0,0.35	0.81,0.37	1.82,0.45	0,0.45
	10	0.03,0.05	0.35,0.1	0.64,0.08	0.06,0.25	1.05,0.32	5.76,0.58	Fail	2.87,0.78	Fail	Fail
	100	0.04,0.06	0.43,0.11	0.86,0.08	-0.15,0.65	10.5,1.6	Fail	Fail	Fail	Fail	Fail
	1000	0.04,0.06	0.61,0.11	1.39,0.1	Fail	Fail	Fail	Fail	Fail	Fail	Fail
Contours	N=1	0,0.08	0.35,0.09	0.94,0.09	0,0.24	0.91,0.25	2,0.26	0,0.36	1.21,0.42	2.77,0.44	0,0.46
	10	0,0.09	0.34,0.09	0.96,0.1	0,0.29	1.01,0.39	4.33,0.47	0,0.61	2.88,1.4	Fail	0,1.58
	100	0,0.09	0.41,0.09	1.02,0.09	0,0.54	3.85,0.84	Fail	Fail	Fail	Fail	Fail
	1000	0,0.09	0.45,0.09	1.46,0.1	Fail	Fail	Fail	Fail	Fail	Fail	Fail
Synthetic	N=1	0,0.09	0.23,0.11	0.59,0.12	-0.02,0.38	0.72,0.48	1.69,0.53	-0.05,0.59	1.19,0.99	3.29,1.18	-0.08,0.85
	10	0,0.12	0.28,0.14	0.74,0.15	0,0.61	1.2,0.8	3.2,0.89	-0.01,1.07	2.91,2.16	Fail	-0.01,1.77
	100	0,0.17	0.39,0.2	1.12,0.21	0,1.04	3.02,1.59	Fail	-0.01,2.29	Fail	Fail	-0.01,5.07
	1000	0,0.23	0.65,0.29	2.38,0.32	0,2.38	Fail	Fail	0,8.23	Fail	Fail	Fail

γ_{av} predictions are broadly similar for both the 'contours' and 'synthetic' model. At smaller strains ($< 1\%$) there is little to choose between the two, whilst the 'contour' plot reproduces strain values slightly better in the medium range (1-10%). Failures due to high average strain are suitably predicted by both. Data points at (15,0) indicate failed two-way tests which were not predicted to do so, and thus predict a 0% average strain in line with symmetrical loading.

It is clear from Figure 4.11c that measured cyclic strains $\gamma_{cyc,n}$ are bi-modal (either $< 2\%$ or at failure 15%), evidence of the rapid increase to failure often observed in tests and reproduced by the proximity of 3% and 15% contours (Figure 4.9a). Predictions are similar, with the 'contour' tests reproducing the measured tests better than the synthetic model which slightly over-predicts values. At failure, both under predict strains for some tests, with more occurrences for the synthetic model. This can be seen more clearly in Table 4.3, for example Test 10.

4.1.2.4 Loop comparison

For some tests, the mechanically recorded stress and strain history of the first few cycles has been digitised, these offer continuous data which gives more information on the loop shape and development between log increments of cycles. Figure 4.12 shows comparison of the model with continuous data available; approximately 20, 3 and 8 cycles of tests 5, 6 and 9 respectively. Test 6 [0.56,0.6] is reproduced most closely

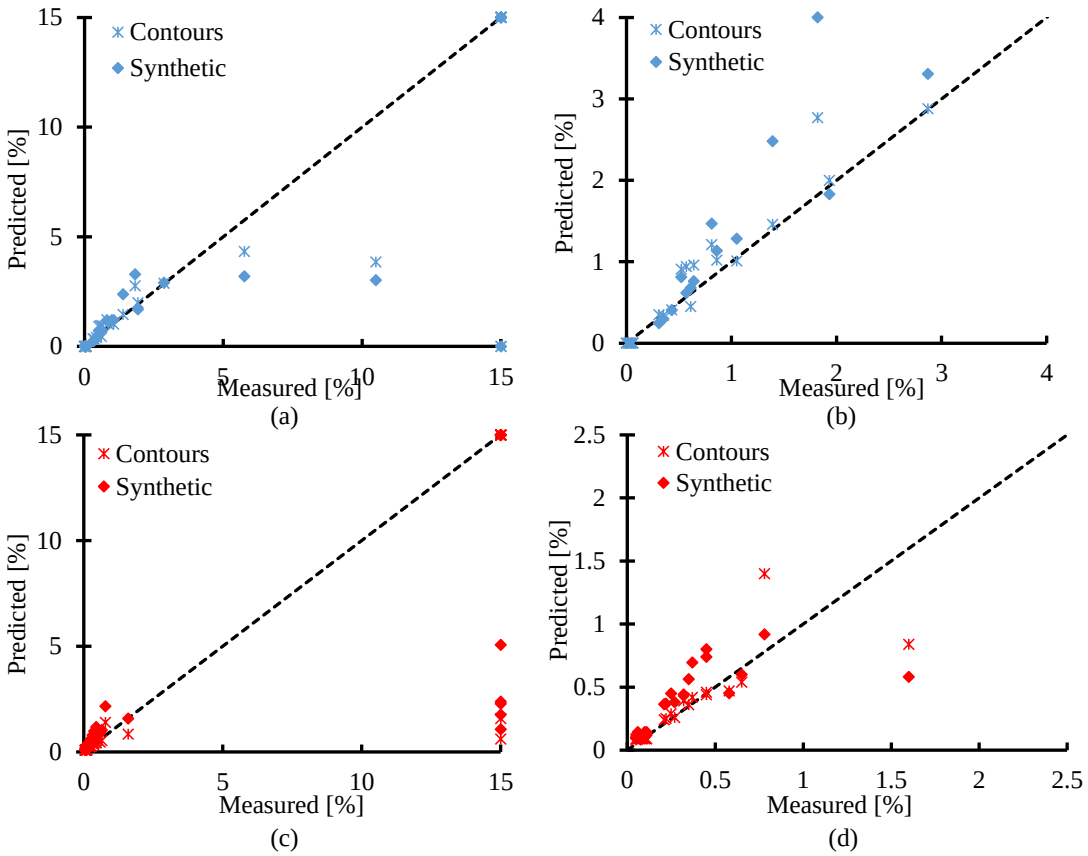

Figure 4.11: Comparison of predicted strains (contours/synthetic) against measured strains for the original 10 DSS tests. Shown at two scales for clarity. a) and b) γ_{cyc}. c) and c) γ_{av}

with a similar wide loop showing highly dissipative behaviour. In test 5 [0.38,0.6], the loop secant stiffness (τ_{cyc}/γ_{cy}) is under predicted, with a tighter more elastic loop measured. In test 9 [0.56,0.77], load and unload tangent stiffnesses are almost linear whereas the model observes Masing rules and thus largely overpredicts the loop area, average strain accumulation rate increases with cycles which is not predicted as well by the model.

4.1.2.5 Mechanisms

'Switching on' the model mechanisms piecewise allows for further understanding of the importance of each with regards to the full contour diagram. Figure 4.13a shows the original contour diagram at N=100 with the $\gamma = 15\%$ contours also shown for $N = 1$ and $N = 10$, giving an indication of the development with cycles. Figure 4.13(b-d) shows synthetically produced equivalents using models of increasing complexity

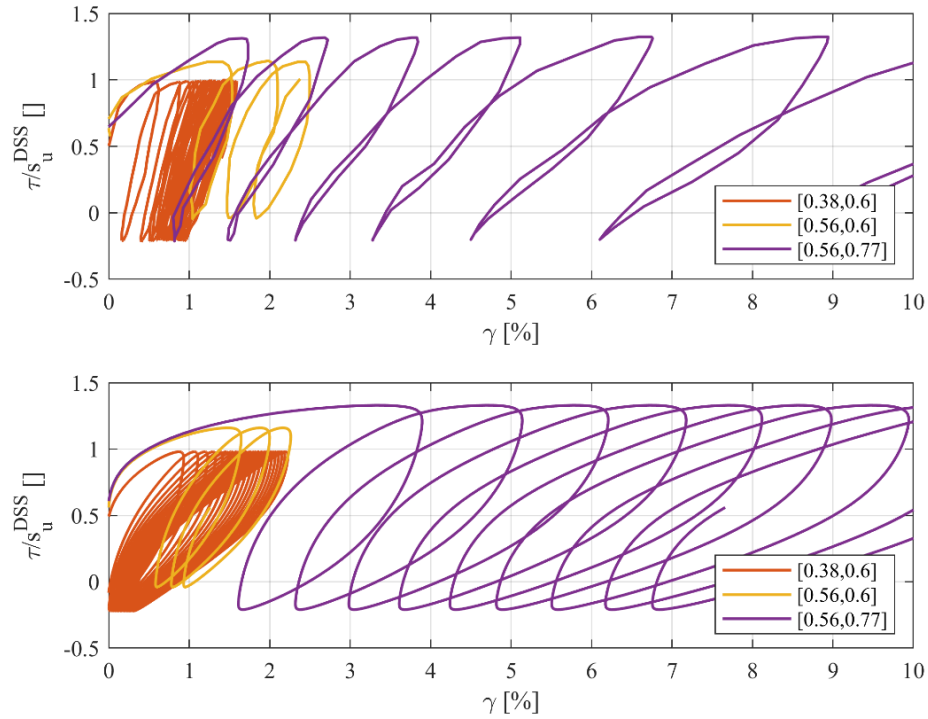

Figure 4.12: Comparison of measured (top) and synthetically produced (bottom) hysteresis loops. Legend indicates τ_{av} and τ_{cyc}

($\gamma_u = 5\%$).

In Figure 4.13b the underlying tests are produced using a Kinematic Hardening model. There are no changes with cycle number as the same loop is traversed repeatedly. The failure strain occurs at $\tau_{av} + \tau_{cyc} = s_u^{DSS}$. γ_{cyc} contours are linear as Masing rules are observed.

In Figure 4.13c rate is introduced. The intersection with the x-axis is largely unchanged as this corresponds to the 'low-rate' pre-cyclic load and hold. The intersections with the y-axis, however, occur at higher magnitudes as rate dependent strength changes cause lower strains within cycle, these remain horizontal and do not develop with cycles. Each test has a fixed cyclic period, such that more highly stressed tests impart a higher strain rate and therefore rate dependent strength. γ_{av} contours are more 'open' than in the kinematic hardening case owing to a stiffer initial response, this closes over time with creep. Failure only occurs at average strain ($\gamma_{av} = 5\%$).

The addition of softening in Figure 4.13d causes the cyclic contours to draw downwards with cycles as secant stiffness reduces. Work softening causes a negative gra-

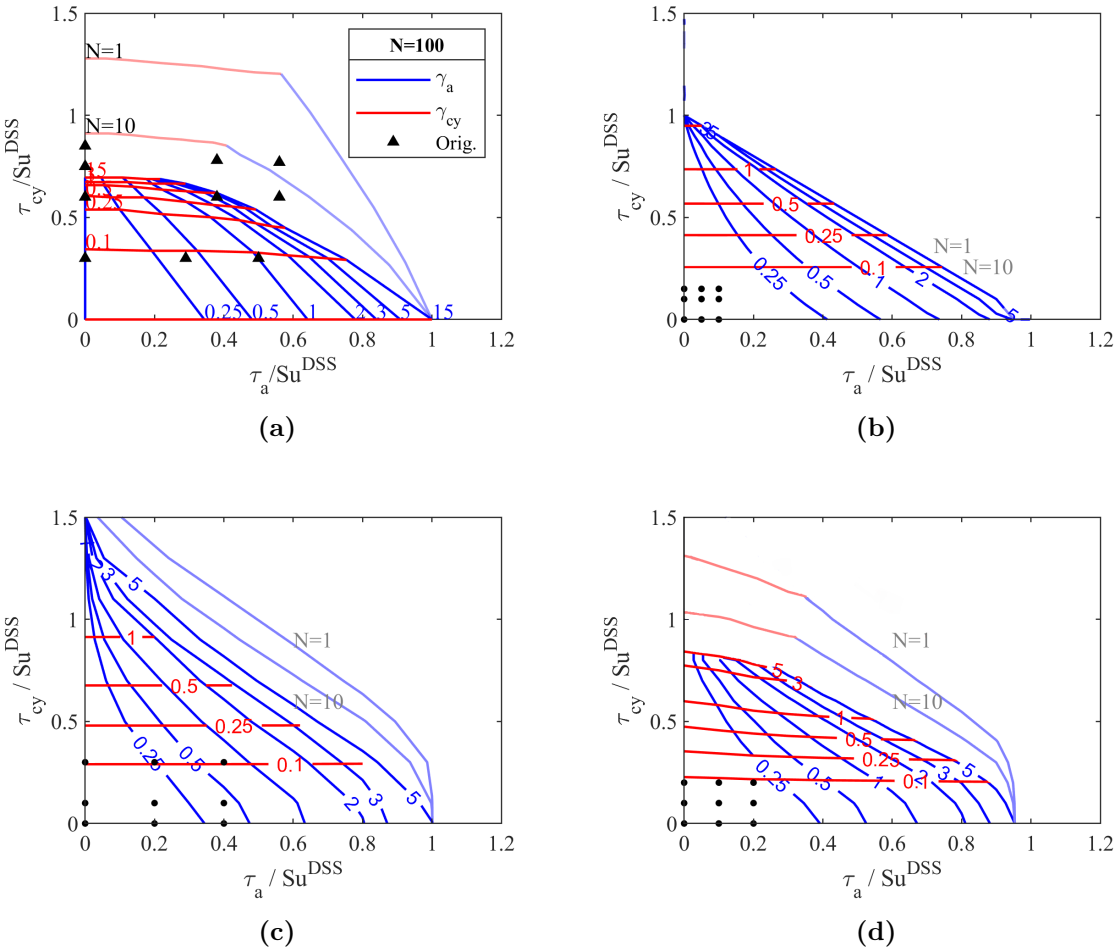

Figure 4.13: Development of contour diagram with cycles , $\gamma = 5\%$ shown for N=1 and N=10 above N=100 diagram. (a) Original Data, (b) Kinematic hardening only (c) KH + Rate Process Theory (d) KH + RPT + Softening.

dient of γ_{cyc}. The secondary effect of additional ratcheting (as $F_\kappa \neq 1$) causes the average contours to draw in further too, with some changes to the intersection of γ_{av} assumed to be due to an imperfect backbone recalibration. Interestingly this also aids in deciding upon softening model choices, as discussed in the following section . Cyclic failure $\gamma_{cyc} = 5\%$ is now part of the envelope even from cycle 1; as softening occurs the cyclic strains increase greatly, particularly at high stresses.

4.1.2.6 Model choice

As discussed in Chapter 3, modelling of cyclic behaviour when limited to just the cyclic strains (with no consideration of post-cyclic behaviour or loop shape) can be achieved with multiple model choices (via F_κ). Contour diagrams (which give no 'in-loop' information) are good examples of this issue.

In the above model, combined softening was employed which catered for both softening and ratcheting behaviour by specifying $F_\kappa = 0.8$. At the limits this parameter allows surface-specific or constant softening. Applying each to the synthesis of contour diagrams gives further ideas on suitability. Figure 4.14 (top) shows two way contour diagrams for a surface specific and constant softening model. The preceding monotonic and rate parameters follow those shown in Table 4.1 and the softening parameters in Table 4.4. The values of F_β and m_κ were chosen in an attempt to predict the original two-way contour diagram shown in Figure 4.10a. This is difficult to achieve in the surface-specific case as the intensity of secant-stiffness reduction is limited during constant-amplitude stress.

Figure 4.14 (middle) shows a synthetic two-way test produced by each model; the effect of model choice on loop shape is clear. Figure 4.14 (bottom) shows the development of γ_{av} and γ_{cyc} with cycle. Surface specific softening creates a similar diagram to Figure 4.10b with less development of γ_{av} and γ_{cyc}. The former could be 'topped up' with a ratcheting element. In the constant softening case (which more accurately reproduced the τ_{av}=0 plot), the cyclic contours at higher strains are removed from the plot. This is caused by high levels of uncontrolled and coupled ratcheting which push the average strains across and allows for only 'ratcheting type' failure unless $\tau_{av} < 0.1$.

In summary, surface specific softening does not model constant amplitude testing well and cannot predict the intensity of change to cyclic strains observed at high magnitudes or cycle numbers. Constant softening, on the other hand, is able to predict cyclic strains (at higher magnitudes), but greatly over predicts the average strains, completely removing the 'cyclic failure' from the diagram. In this case it is clear that a mixed softening model is required to allow for cyclic strain development but not over-predict average strains.

Table 4.4: Cyclic Parameters of softening limits

	F_κ	κ_{ref}	F_β	m_κ
Surface-specific	1	0.7	0.1	0.4
Constant	0	0.7	0.2	0.15

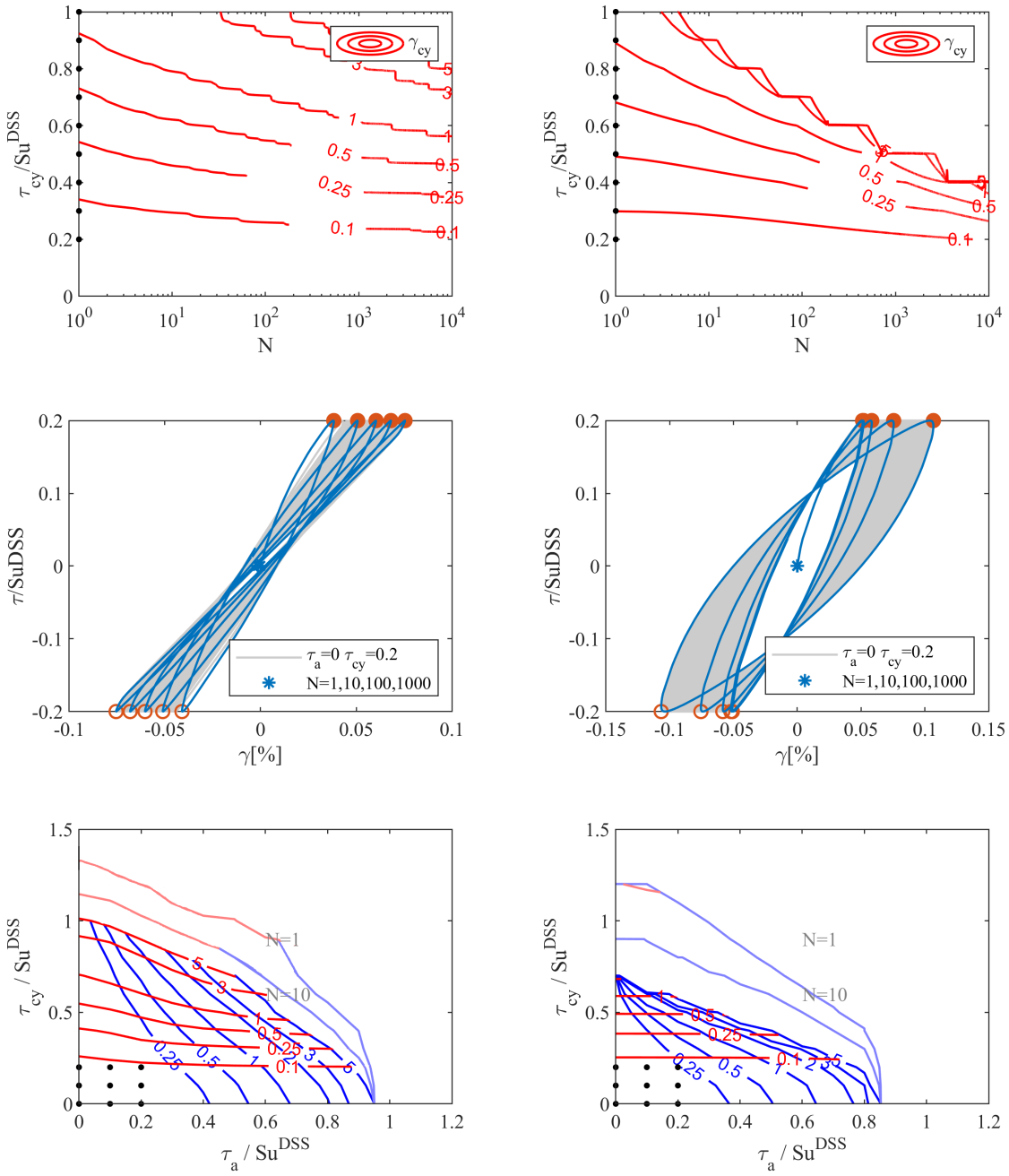

(a) Surface specific **(b)** Constant

Figure 4.14: Two way contours, indicative two way test, and development of full contour diagram with cycles. Shown for a model with: Left (a) - 'surface specific softening' F_κ=1 and Right (b) – 'Constant softening' F_κ=0. In the middle plots the red dots correspond to locations of peak and reversal points for cycles N=1,10,100,1000.

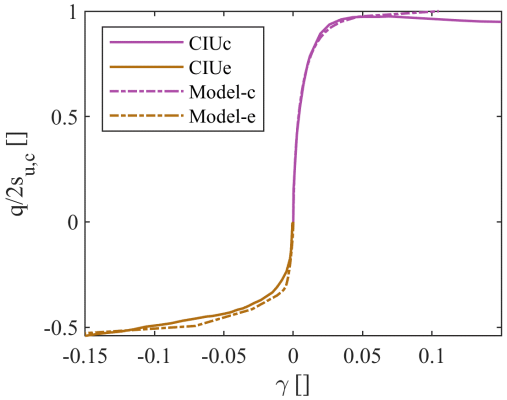

Figure 4.15: Monotonic fit to $CIUc$ and $CIUe$ data

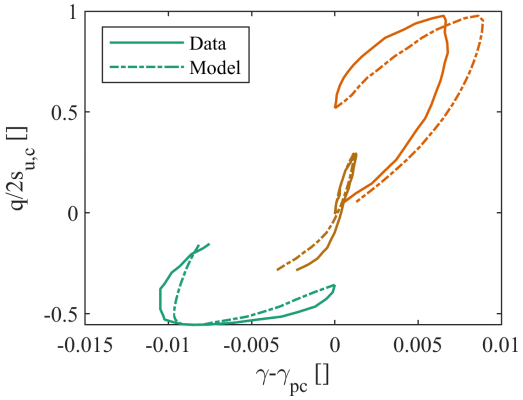

Figure 4.16: Model prediction of initial 3/4 cycles of selected CU_{cyc} tests

Table 4.5: Monotonic and Rate-dependent parameters for Drammen Clay in CU Conditions ($OCR = 4$)

p_0	$s_{u,c}$	$s_{u,e}$	$\dot{\varepsilon_{BB}}$	$\frac{E_0}{s_{u,DSS}}$	$\varepsilon_{u,c}$	$\varepsilon_{u,e}$	$A_{f,Ns}$	t_{ref}	η_{10}	F_η	$\frac{\sigma_{u,0}}{s_u}$	a_0
$[kPa]$	$[kPa]$	$[kPa]$	$[hr^{-1}]$	[ ]	[ ]	[ ]	[ ]	$[hr]$	[ ]	[ ]	[ ]	[ ]
100	99	52.5	0.03	750	0.11	0.15	0.53	1000	0.26	0.91	0.66	4.19

4.1.3 Cyclic triaxial OCR=4

Similar plots are created for cyclic triaxial tests. In this section the model is used to synthetically reproduce the diagrams created for isotropically consolidated triaxial (CUI_{cyc}) tests on overconsolidated (OCR=4) Drammen clay. Here, $\tau = q/2$, shear strain is calculated from the axial strain such that $\gamma = 1.5\varepsilon_a$ and loading conditions following Section 4.1.1.

In DSS tests the strain response is similar regardless of the loading direction. This no longer holds in triaxial tests where anisotropy of the sample becomes important. Asymmetry can be introduced in the 0D model following Section 3.2.2.

Firstly, the compressive backbone is calibrated to an undrained triaxial test ($CIUc$), before local anisotropy factor $A_{f,i}$ is optimised to fit an extensive test ($CIUe$), Figure 4.15. Rate parameters are recalibrated to ensure a good fit to initial quarter cycles of available cyclic tests Figure 4.16, but remain similar to those used in Table 4.1 (see summary in Table 4.5). Cyclic parameters used in Section 4.1.2 are retained and used here instead of recalibrating, following Table 4.2.

Figure 4.17 shows the original contour diagrams on the left and model predictions on the right. The synthetic contours are limited to approximately $2/3\varepsilon_u$ and $2/3\varepsilon_{u,e}$.

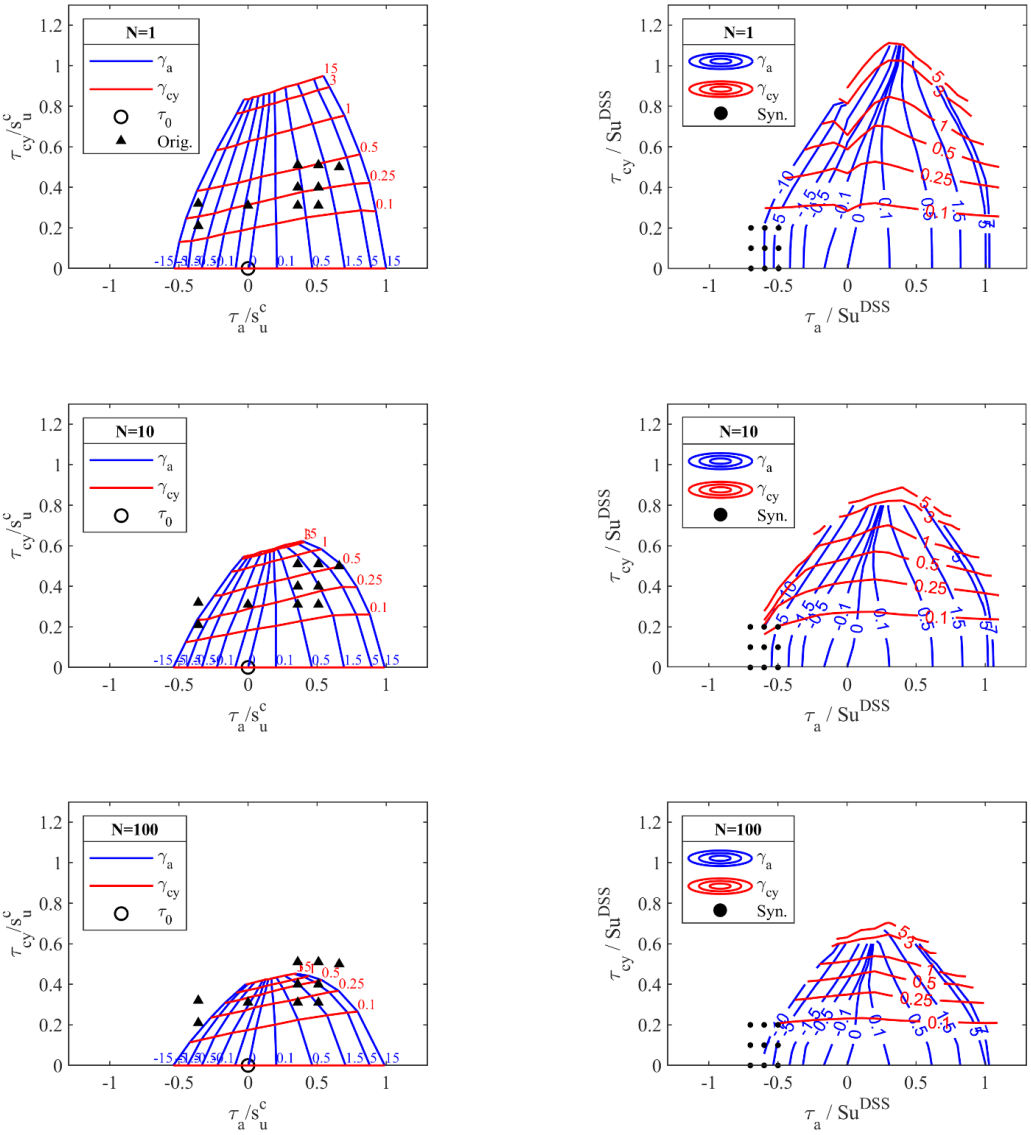

Figure 4.17: Hyperplasticity predictions of CU_{cyc} contour plots. Left – Original Contour Plots, Right – Synthetic predictions. Spacing of the synthetic test locations is only shown for 9 tests, although the grid extends across the full stress space.

The γ_{av} contours develop in a similar manner to the DSS contour diagrams; however, anisotropy causes asymmetry about $\tau_{av} = 0$. $\gamma_{av} = 0$ moves towards the positive τ_{av} with increasing τ_{cyc} as ratcheting occurs in the extensive direction. This, along with the x-axis intersections points are well predicted, suggesting a good monotonic and asymmetrical parameter choice. From cycle one, higher average (and cyclic) strains are seen in extension due to anisotropy. There is a trough in the cyclic strains at zero stress which disappears by the 10th cycle.

With increasing cycles, predicted average strains accurately close in towards $\gamma_{av} =$

0. In the original plots cyclic strains do the same, remaining higher with extensive bias. This is not shown in the synthetic diagrams where a peak occurs at approximately zero average strain. Without softening, Masing rules would be observed producing horizontal contours, although with softening a peak is to be expected at zero average strain as historically there will have been less strain.

Overall, given that only monotonic and cyclic parameters have been calibrated the synthetic plot matches well. These results may also suggest that the softening parameters are transferable across test type.

4.1.4 Conclusions

This section presented the synthesizing of contour diagrams, by running multiple model tests across a grid of stress co-ordinates. The synthetic diagrams match well in simple shear and triaxial space. As a method, this technique could be used to test any constitutive model across the full range of cyclic type and magnitude. The precision of the contours depends upon the coarseness of the grid, with a finer grid comes more synthetic tests and therefore computational effort. The DSS_{cyc} contour plots shown typically required 165 analyses of 1000 cycles, each taking approximately 2 minutes to run on a laptop computer. Computation time can be reduced by only running 100 cycles (15 seconds per analysis) or using a coarser mesh. This results in full contour plots in less than half an hour, and can therefore be a useful test of formulation or parameters.

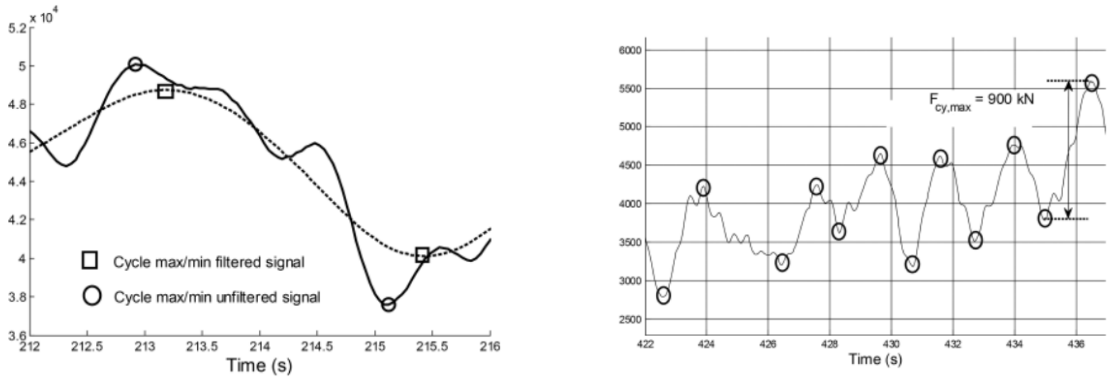

(a) **(b)**

Figure 4.18: NGI rainflow counting method (a) Determination of local maxima/minima using a low-pass filtered signal (b) Example load case. (Noren-Cosgriff et al., 2015)

4.2 Irregular test predictions - WAS-XL

The models presented in this thesis appear to be able to reproduce the response of clays to constant amplitude laboratory testing to a reasonable degree of accuracy. This section moves to more realistic, pseudo-random loading. It does so by reporting model predictions of strain development in multi-amplitude DSS_{cyc} tests undertaken at NGI as part of the WAS-XL (WAve loads and Soil support for eXtra-Large monopiles) project (Skau et al., 2020).

A multi-surface, kinematic hardening, rate-dependent, hyperplasticity model configured in series was calibrated using monotonic and constant-amplitude DSS_{cyc} tests in the same soil unit. Predictions are compared to measured strains and improvements suggested. The original predictions are 'Class C' (Lambe, 1973), such that whilst the testing had already been undertaken, the results were not known to Oxford University prior to predictions being made in May 2019.

4.2.1 Introduction

Idealisations of truly irregular loads are often required for 'extrinsic' models (see Section 1.3.5) which predict strain to many, constant amplitude cycles without consideration of 'in-loop' behaviour (Achmus et al., 2007; Wichtmann et al., 2009; Grimstad et al., 2012). As part of the WAS-XL project, work undertaken at NGI examined the differences of soil response to irregular and idealised loads, thereby appraising the idealisation process.

Two irregular load histories were created, based upon time domain integrated analyses of a 10MW wind turbine. Equivalent 'idealised' load histories were then derived, before both were scaled and applied in DSS conditions to samples of an over-consolidated North Sea clay.

The idealisation process is described by Noren-Cosgriff et al. (2015). It differs from the more conventional rain-flow counting (e.g. Downing and Socie, 1982), in that the amplitude of each half-cycle is determined only from adjacent extrema and reversals. In order to avoid counting small amplitude cycles the extrema and reversals are first found from a low-pass filtered signal, the unfiltered signal is then searched again to ensure true magnitudes, Figure 4.18a. Figure 4.18b depicts the method applied over many peaks.

Table 4.6 describes the nine applied stress histories provided by NGI, seven of which are shown in Figure 4.19. Test 3A and 3G directly apply load history 1 (Irregular) but at two different magnitudes to investigate stress level effects. Test 4C and 4E both apply load history 2 (with a high bias). The load magnitude is scaled by s_u at the corresponding sample depth, z, based upon an assumed profile, hence the same history will have a slightly different applied stress. Tests 3E, 3F, 4D and 4B are idealised tests where packets are applied in increasing order, Test 3H applies the packets in a 'pyramid' to investigate order of application. Each idealised cycle has a frequency $f = 0.25Hz$ which, along with an initial average load hold of about 1 hour, causes the total time T_u to differ between the tests.

After each test, three reference cycles matching the corresponding final load packet were applied such that average strain, $\gamma_{av,u}$ and cyclic strain, $\gamma_{cyc,u}$ could be compared

Table 4.6: Load-cases applied in simple shear apparatus as part of WAS-XL Project

Test	Load History	Load Type	Depth z [m]	Amplitude $\tau_{cyc,u}$[kPa]	Bias τ_{av}[kPa]
3A	1	Irr.	15.85	92.9	8.5
3E	1	Pac.	15.85	92.9	4.7
3F	1	Pac.	15.85	97.6	5.1
3G	1	Irr.	15.6	96.5	8.9
3H	1	Irr. Pyramid	15.72	97.1	4.9
4C [4E]	2	Irr.	16.9 [16.94]	66.1 [66.6]	46.7 [46.9]
4D [4B]	2	Pac.	16.9 [16.86]	65.3 [65.2]	50 [50]

for the same final cycle. $\tau_{cyc,u}$ indicates the maximum cyclic amplitude, which corresponds to the final applied control cycles. τ_{av} is the average applied load over the whole time history, found by integrating the stress and dividing by the total time, $\tau_{av} = (\int_{t=0}^{t=T} \tau dt)/T$.

This section aims to complement the experiments and demonstrate the predictive ability of hyperplasticity models under irregular loading when calibrated to simpler tests. A 0-D model applicable to DSS conditions only is used. Hyperplasticity models are 'intrinsic', so that both irregular and idealised tests can be run with the model without the need for cycle counting, offering a test of the formulation outside the constant amplitude tests of Chapter 3 and 4.1.

4.2.2 Calibration

In order to generate class C predictions of the above loads, a model was calibrated to single amplitude tests. The multi-amplitude loads were applied to an over consolidated North-Sea clay in 2018. This unit was characterised in late 2015 by DSS and constant amplitude DSS_{cyc} testing. Samples from two boreholes between 15 – 19m depth with a plasticity index $I_p = 18\%$ and OCR=2-3 were tested. The same boreholes were used in the later tests with further characterisation tests undertaken to investigate any effect of ageing from lab storage over the 2+ years. The two sets of testing are referred to as: 'WXL', tests circa November 2015; 'WXLAGED', tests circa August 2018.

Table 4.7 summarises the monotonic DSS tests each shown in Figure 4.20. σ'_{vc} indicates the final vertical consolidation stress before undrained, 'constant volume', shearing. A much higher ($\approx 30\%$) undrained shear strength s_u was observed in WXL.103 than in the other tests. This perhaps indicates that age effects are less

Table 4.7: Monotonic DSS tests on WXL clay. Three tests performed in late 2015, one in 2018.

Test ID	Borehole	Depth z [m]	σ_{vc}[kPa]	OCR	$\dot{\gamma}$ [%/hr]	s_u [kPa]	γ_u [%]
DSS.WXL.101	4001A	17.17	176	2.9	4.4	114	12.0
DSS.WXL.102	4003A	18.88	193	2.9	4.4	117	10.4
DSS.WXL.103	4003A	18.92	190	2.9	4.1	153	9.3
DSS.WXLAGED.101	4001A	15.85	164	2.1	4.6	114	10.0

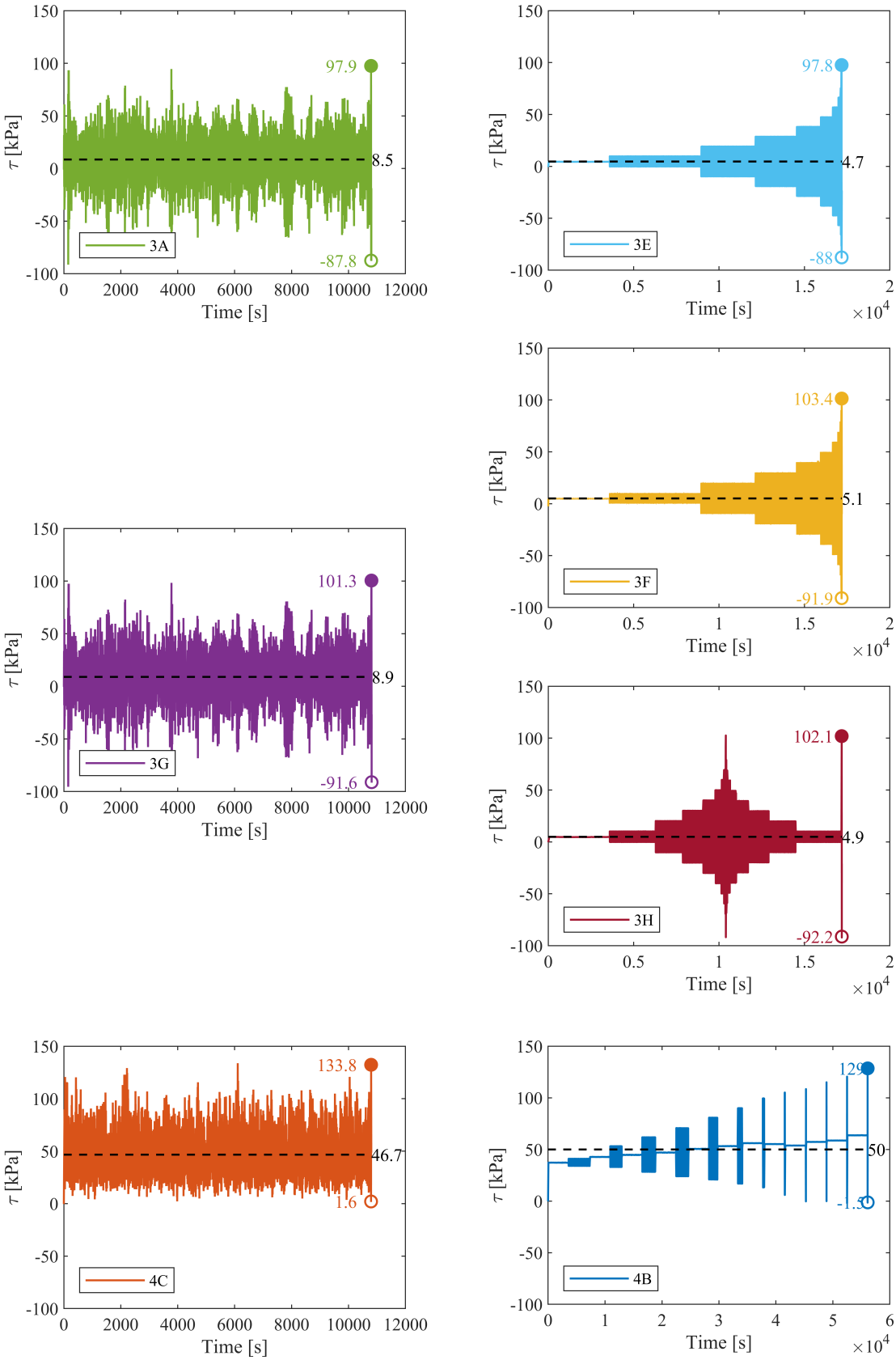

Figure 4.19: Stress histories as applied in DSS_{cyc} conditions. Left hand side – Irregular, Right hand side – corresponding idealised

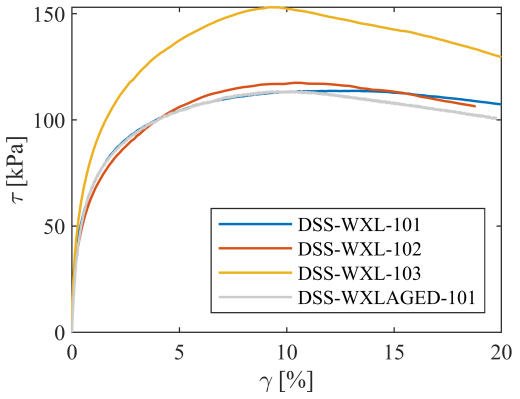

Figure 4.20: Monotonic tests on WXL clay before and after storage

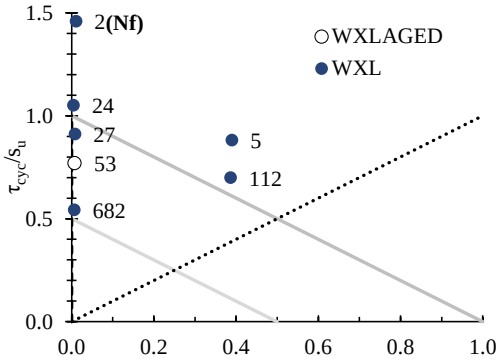

Figure 4.21: Interaction diagram of DSS_{cyc} tests

important than sample variability. Normalisation with s_u gives a consistent pre-failure response as shown in Figure 4.22a. Bender element measurements on a sample close to WXLAGED.101 showed an initial shear modulus $G_0 = 101.6MPa$ such that $G_0/s_u \approx 900$.

Table 4.8 summarises the seven cyclic DSS_{cyc} tests, plotted in an interaction diagram in Figure 4.21 alongside number of cycles to failure N_f (defined as γ_{av} or $\gamma_{cyc} > 15\%$). N_f decreases with increasing τ_{av} and τ_{cyc}, indicating consistent results. A consistent s_u=115kPa is assumed for normalisation of all DSS_{cyc} tests, found by taking the average of the consistent DSS tests WXL-101,WXL-102 and WXLAGED-101 (i.e. ignoring the outlier WXL-103).

Figure 4.22 shows the calibration process which follows a similar route to that presented in Chapter 4.1. Figure 4.22a shows rate-independent backbone calibration to the four DSS tests calibrated to normalised response (τ/s_u) before rate-dependency is introduced based upon initial cycles of DSS_{cyc} tests in Figure 4.22b). Cyclic effects

Table 4.8: DSS_{cyc} tests on WXL clay. Eight Tests performed in late 2015, one in 2018.

Test ID	Borehole	z $[m]$	σ_{vc} $[kPa]$	OCR	f $[Hz]$	τ_{av} $[kPa]$	τ_{cyc} $[kPa]$	N_f
CSS.WXL.102	4001A	17.21	174	2.9	0.1	44.4	80.5	112
CSS.WXL.103	4001A	17.25	174	2.9	0.1	-0.7	62.4	682
CSS.WXL.104	4001A	17.29	175	2.88	0.1	44.8	101.4	5
CSS.WXL.106	4003A	18.96	192	2.9	0.1	0.5	120.9	24
CSS.WXL.107	4003A	19.00	193	2.9	0.1	-1.2	167.8	2
CSS.WXL.108	4003A	19.04	193	2.9	0.1	-0.9	104.8	27
CSS.WXLAGED.101	4001A	15.68	163	Unknown	0.25	-0.8	88.5	53

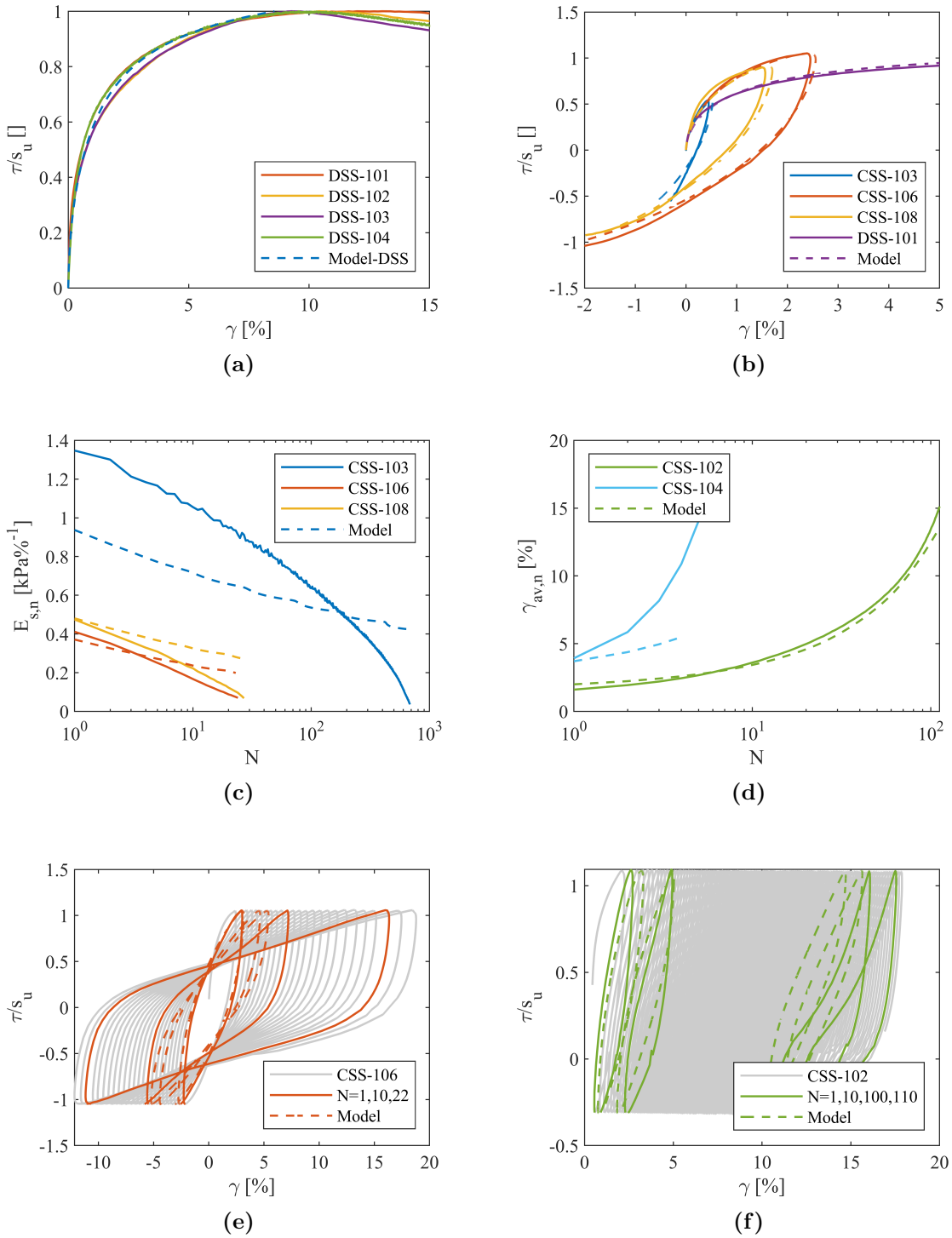

Figure 4.22: Calibration tests and calibrated model prediction. (a) DSS – Monotonic (b) Initial cycles – Rate Dependency (c) Secant Stiffness Development (d) Average strain development (e) Example hysteresis loops - $\tau_{av} = 0$ (f) Example hysteresis loops - $\tau_{av} \neq 0$

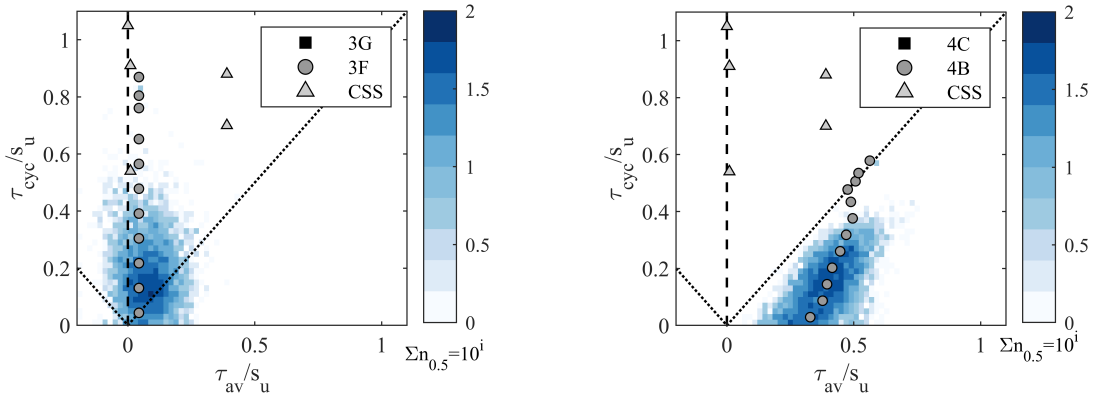

Figure 4.23: Heatmap of (a) 3G (b) 4C, showing cyclic properties of half cycles in the irregular tests. Tests 3F and 4B and corresponding CSS calibration also shown.

are calibrated to the development of secant stiffness (Figure 4.22c) and average strain (Figure 4.22d). Figures 4.22e and f show two examples of stress-strain hysteresis loops.

In this case strain-dependent viscosity change was not required ($F_\eta = 1$). Surface-specific strain softening was chosen, such that $F_\kappa = 1$ and $\dot{\beta}_i = \dot{\alpha}_i$, with an additional ratcheting component catering for accumulation of average strains. Note that $\beta_{ref,i} = F_{\beta,l}.K_i/H_i$ here rather than $\beta_{ref,i} = F_{\beta,l}.K_u/H_i$ as used previously in this thesis. In practice this has little effect on the response but means that, combined with strain hardening parameter, $F_{\beta,l}$ is not directly comparable with previous work presented thus far. The reduction of secant stiffness is not particularly well fitted in this calibration (Figure 4.22c) under-predicting the incremental softening with cycles.

The limited evidence in Figure 4.22d shows no slowing of strain accumulation with cycles, therefore a simple ratcheting formulation function was used (Equation 3.44) with ratcheting constant R_0 and stress dependency exponent m_s. Eight key parameters are required (Table 4.9) with a further five 'arbitrary' parameters highlighted in grey.

Table 4.9: Hyperplasticity parameters used for model predictions shown in Figure 4.22

	Monotonic			Rate			Softening				Ratcheting	
ε_u	$\frac{E_0}{s_{u,DSS}}$	$\frac{\sigma_{u,0}}{s_{u,DSS}}$	a_0	F_η	t_{ref}	η_{10}	F_κ	κ_{ref}	$F_{\beta,l}$	m_k	R_0	m_s
[−]	[−]	[−]	[−]	[−]	[hr]	[−]	[−]	[−]	[−]	[−]	[−]	[−]
0.1	900	0.65	2.68	1	10^4	0.29	1	0.6	10.0	0.18	0.1	3.0

Figure 4.23 show heat maps of the two irregular tests (3G and 4C) alongside the corresponding idealised tests (3F and 4B) and constant amplitude calibration tests (as in Figure 4.21). The heatmap scale is logarithmic such that the darkest blues correspond to 10^2 cycles. This figure shows that the DSS_{cyc} tests are typically of higher stress magnitude and more focused on 'two-way' loading than the cycles which will be predicted. The implications of this are considered during class C.1 predictions in Section 4.2.5.

4.2.3 Class C predictions and comparisons

In order to generate class C predictions, the load histories described in the introduction were applied incrementally to the model, each taking approximately 20 minutes on a laptop computer. Example measured time histories are shown in Figures 4.24 to 4.28 alongside model predictions in grey. Importantly, it is clear that as well as the final secant stiffness, instantaneous tangential stiffness is predicted throughout, as well as changes to the loop shape (hysteretic damping).

Table 4.10 summarises final average $\gamma_{av,u}$ and cyclic strains $\gamma_{cyc,u}$ for the nine tests along with predicted values. Initially considering only the measured strains; cyclic strains were higher for 'Load History 1' and measured average strains higher for 'Load History 2', reflecting the stress amplitudes and bias respectively. Higher strains were consistently observed in irregularly loaded tests compared to the respective idealised packet tests, although the difference varies between tests. In the idealised tests, higher γ_{cyc} was observed when the largest loads were applied later in the stress history (during test 3F in comparison to test 3H).

Table 4.10: Comparison of predicted ultimate average and cyclic strains against measured data. Irr.=Irregular loads, Pac. = Idealised Packets, Alt. Pac. = Idealised packets applied in different order

Test	Load Type	Amplitude $\tau_{cyc,u}/s_u$	Bias τ_{av}/s_u	$\gamma_{av,u}$[%]		$\gamma_{cyc,u}$[%]	
				Measured	Predicted	Measured	Predicted
3A	Irr.	0.84	0.07	0.7	0.6	3.0	2.0
3E	Pac.		0.04	0.1	0.3	2.9	1.9
3F	Pac.	0.88	0.04	1.0	0.5	5.0	2.3
3G	Irr.		0.08	2.0	0.8	6.1	2.5
3H	Alt. Pac.		0.04	0.0	0.5	4.0	2.3
4C [4E]	Irr.	0.56	0.41	10.7 [11.9]	7.4	1.1 [1.0]	1.1
4D [4B]	Pac.		0.43	6.7 [7.6]	5.8	0.9 [1.1]	1.0

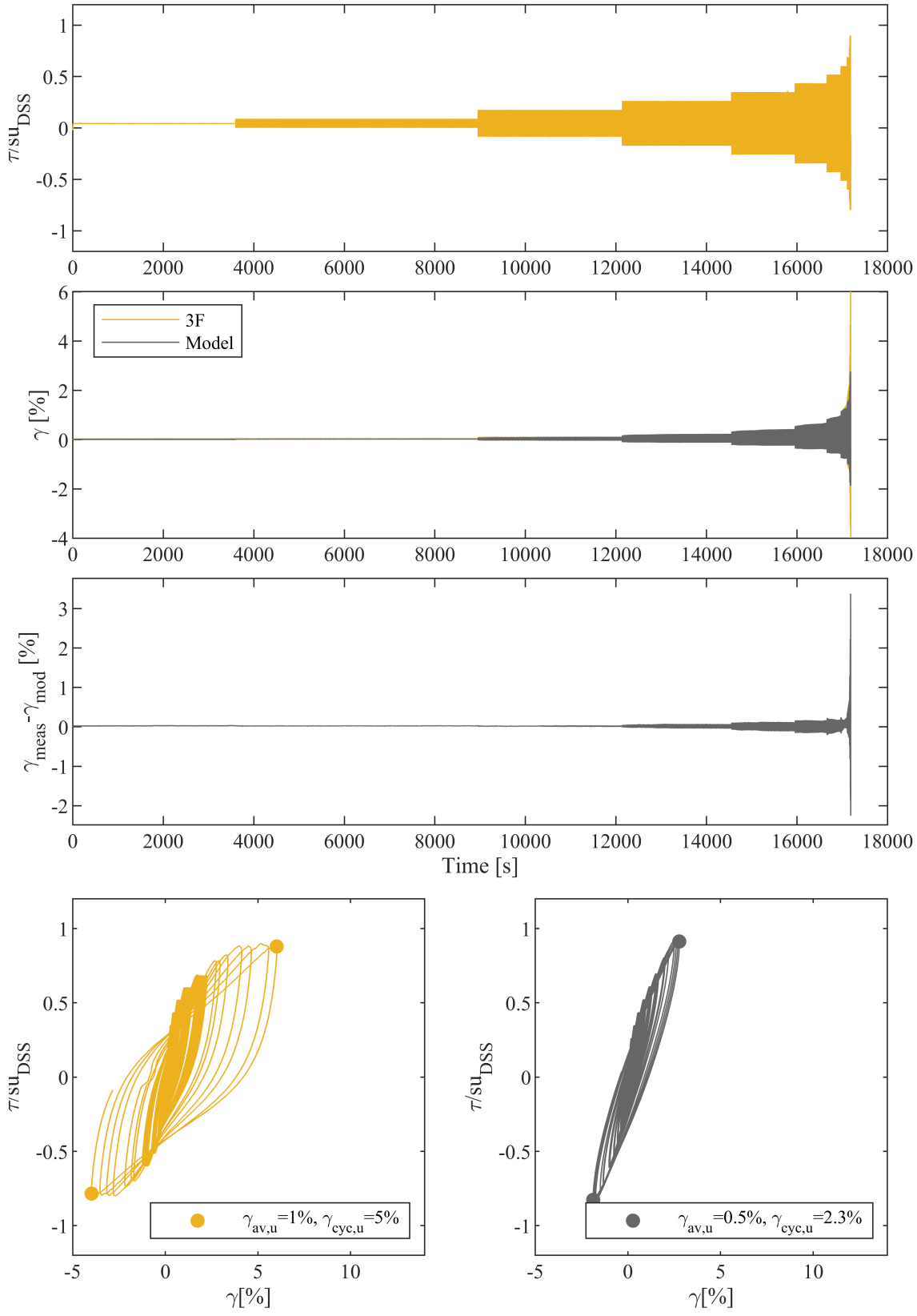

Figure 4.24: Model prediction of two-way, idealised loading history 3F.

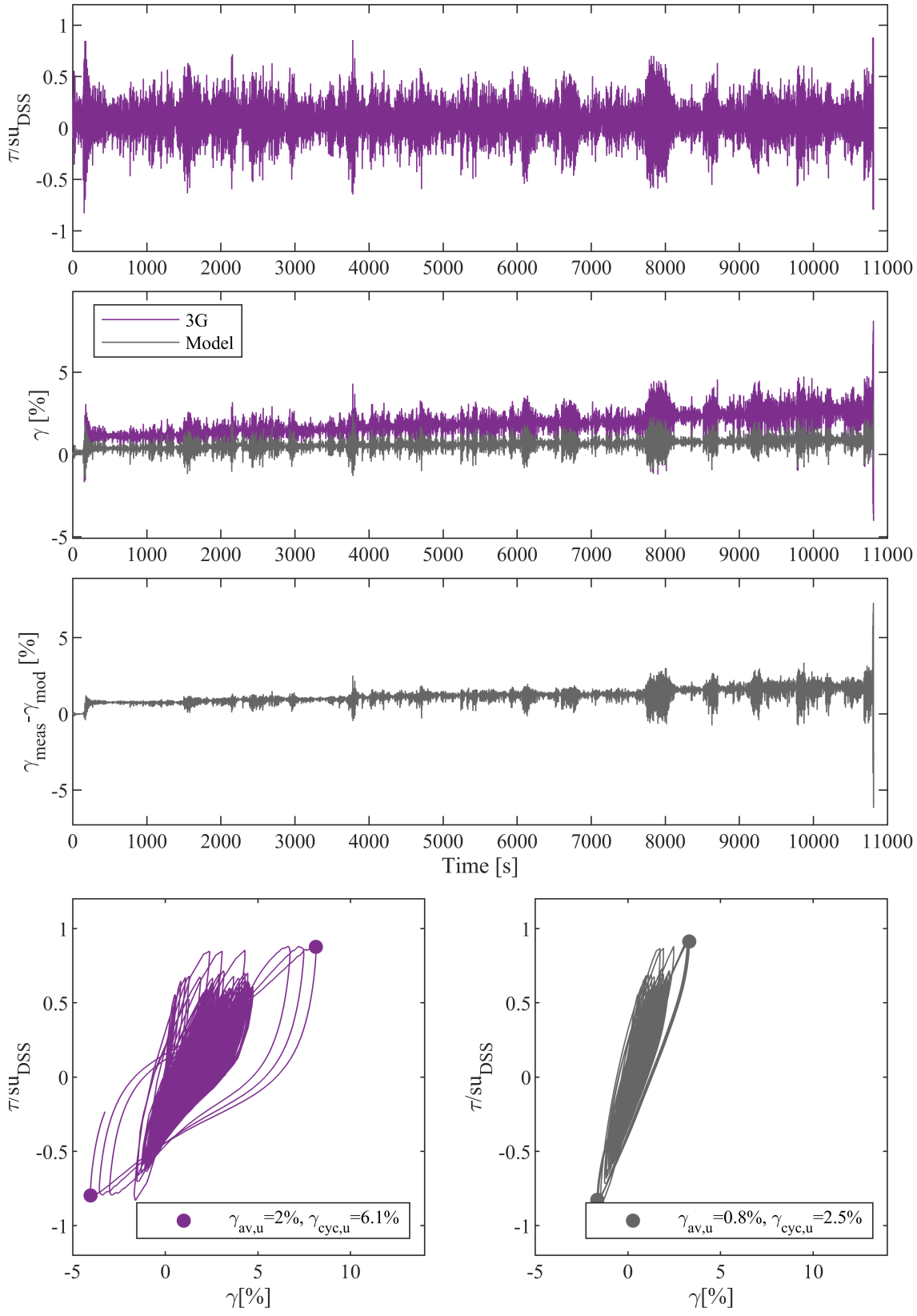

Figure 4.25: Model prediction of two-way, irregular loading history 3G.

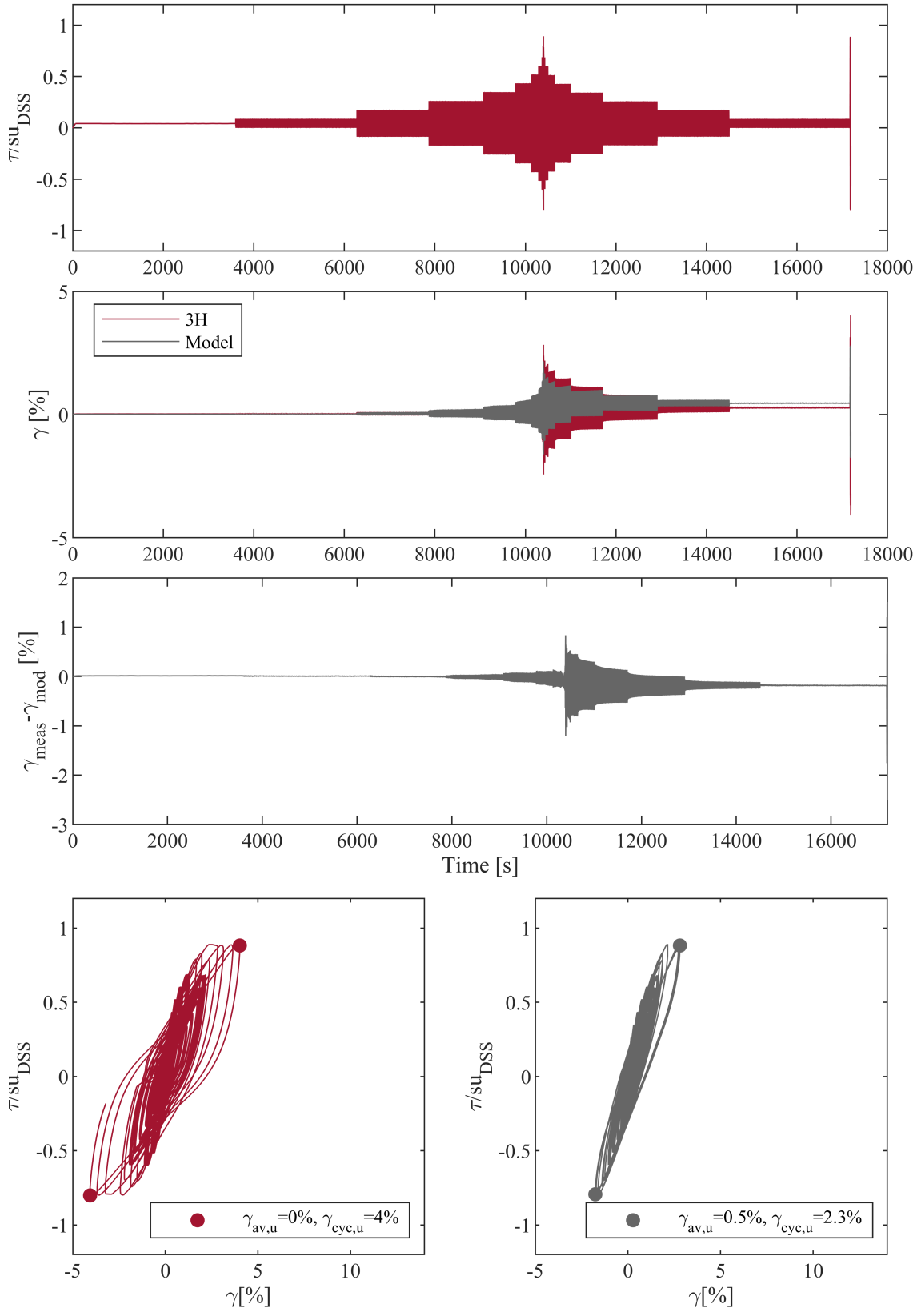

Figure 4.26: Model prediction of two-way, idealised loading history 3H.

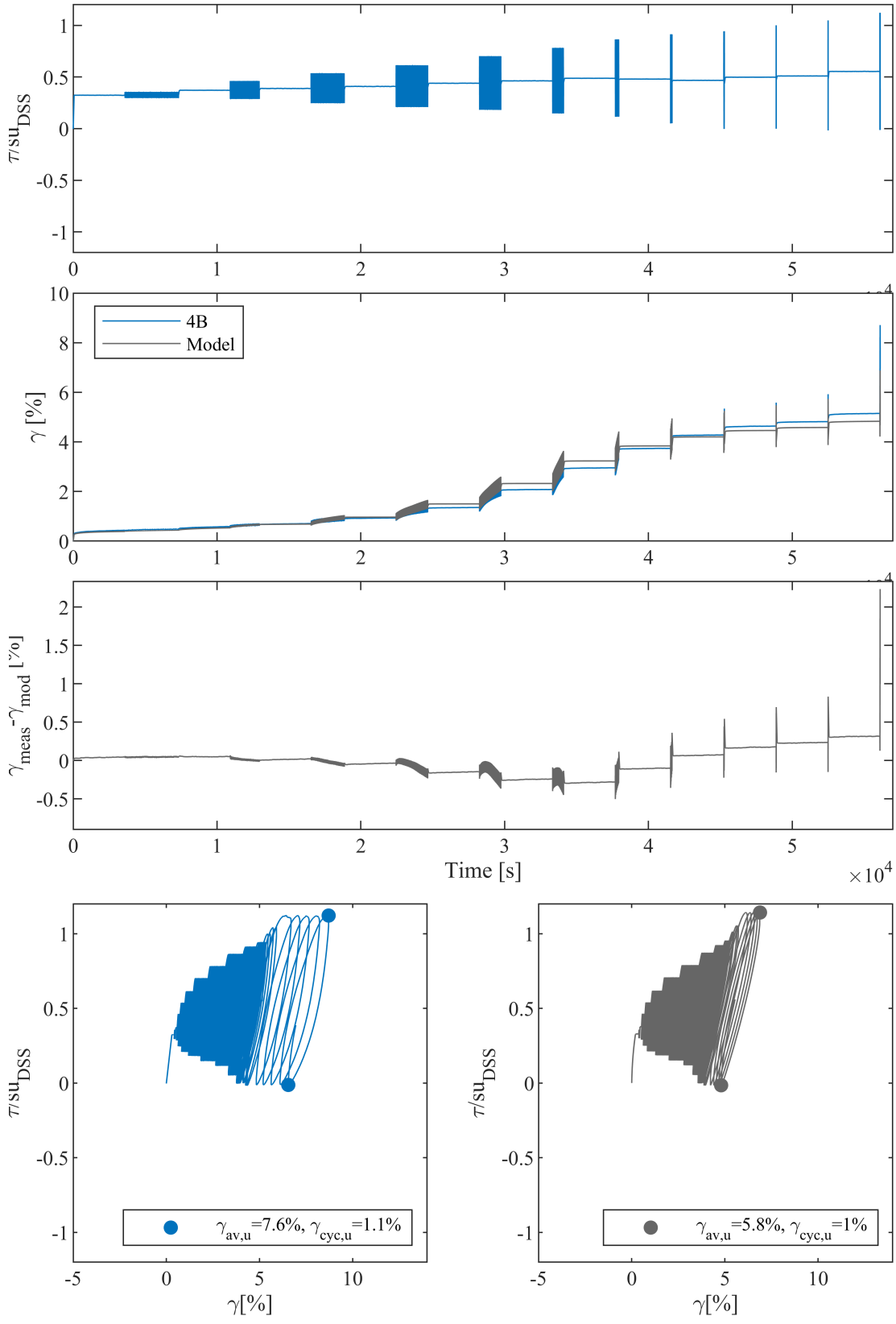

Figure 4.27: Model prediction of one-way, idealised loading history 4B.

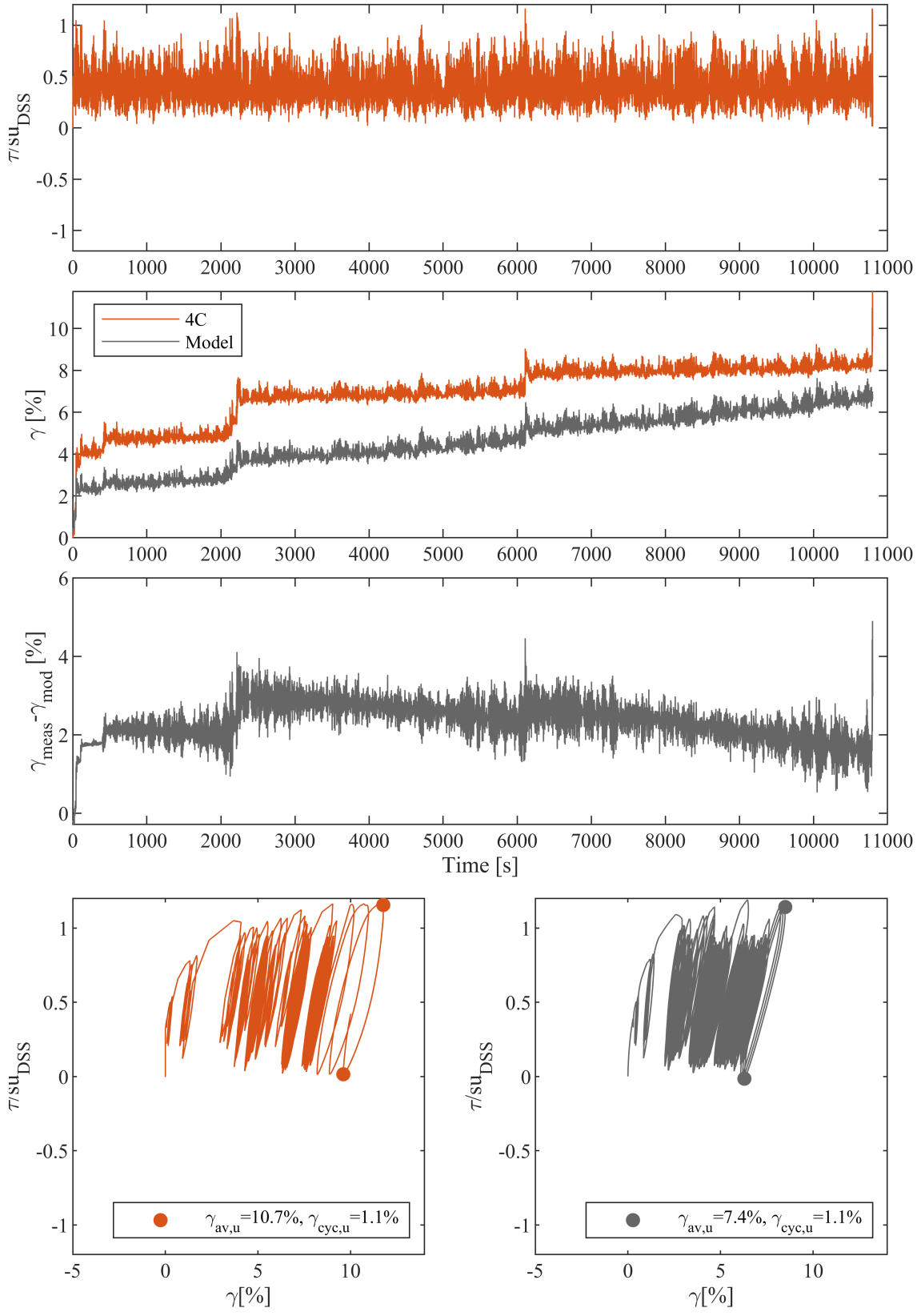

Figure 4.28: Model prediction of one-way, irregular loading history 4C.

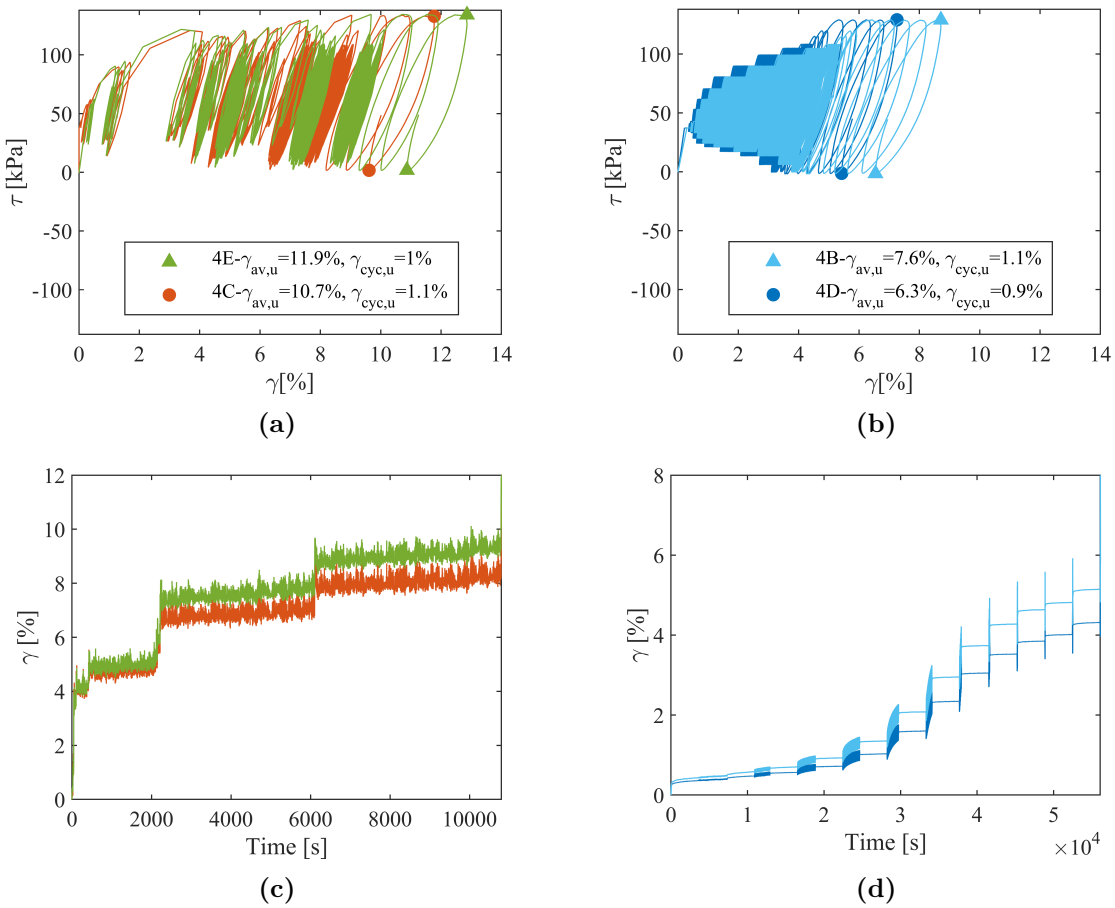

Figure 4.29: Comparison of measured strains for (a,c) Tests 4B and 4D (b,d) Tests 4B and 4D

Tests 4B and 4E are repeat tests of 4C and 4D with results compared in Figure 4.29. Considering potential sample variability, the measured strains match well. Loop shape and virgin loading curves are broadly similar along with final predicted, $\gamma_{cyc,u}$. Final average strain $\gamma_{av,u}$ differs more, diverging gradually during the idealised tests and at peak loads during the irregular tests.

Considering Figures 4.24 to 4.28, there is good agreement between predicted and measured strains. The predicted trends of strain development and resulting loop shapes indicate that key mechanisms are captured. In the two-way tests (3F and 3G) secant stiffness reduces with time and the largest, most open, loops occur at the end of the history, albeit strain magnitude is somewhat under-predicted by the model.

The reduction of stiffness is predicted less well with increasing stress magnitude (e.g. in test 3H, Figure 4.26). Figure 4.30 depicts the difference for irregular tests 3F, 4C and 4E. The heatmap shows the mean difference in cyclic strain $\gamma_{diff,cyc} =$

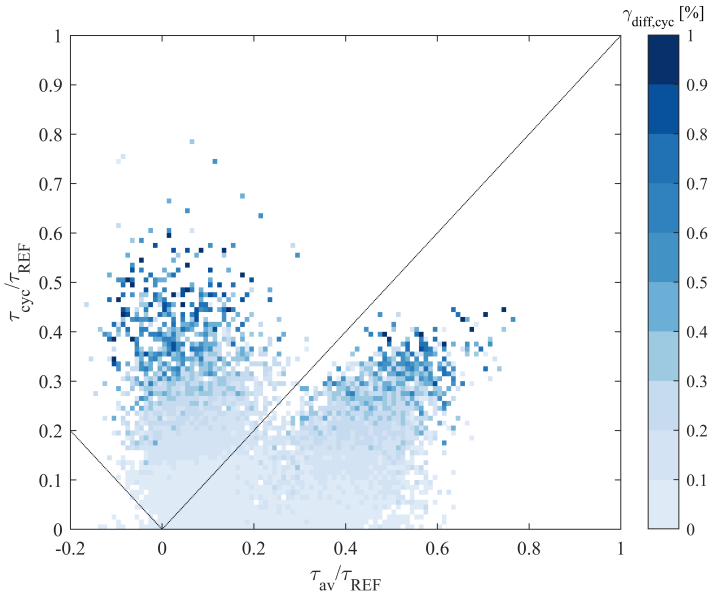

Figure 4.30: Mean difference between measured and modelled cyclic strain for irregular tests 3F, 4C and 4E $\gamma_{diff,cyc} = |\gamma_{meas,cyc} - \gamma_{pred,cyc}|$. Calculated for each half-cycle, averaged and plotted in corresponding co-ordinate of average and cyclic stress

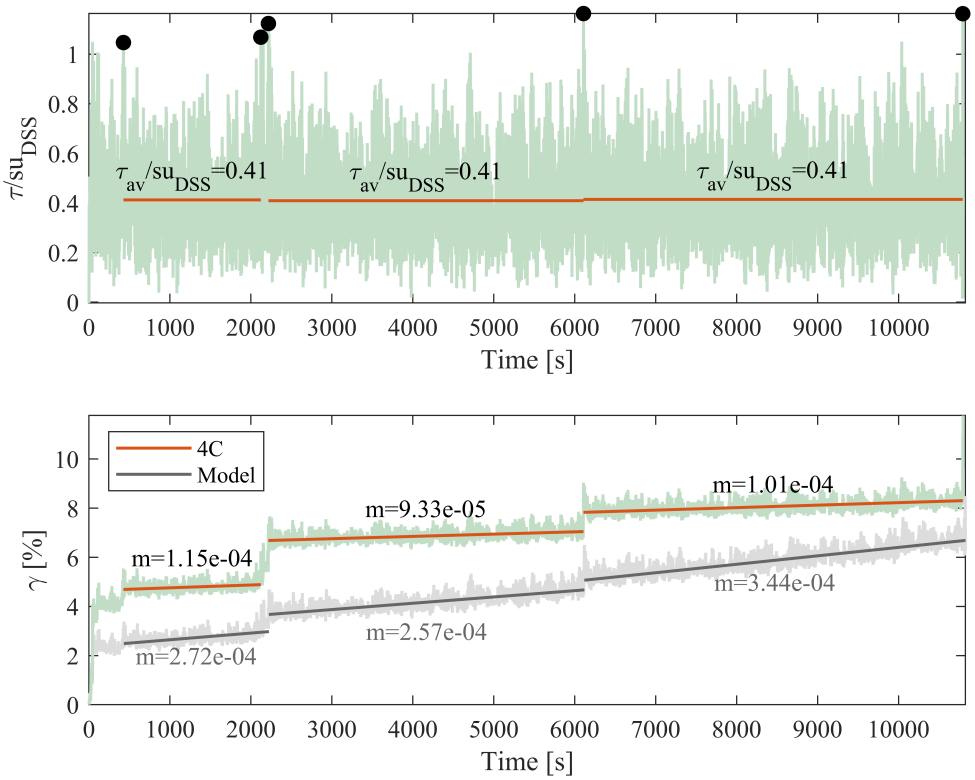

Figure 4.31: Measured and model response for test 4C with gradient of strain accumulation (m) shown for three sections between large loading peaks. Black dots indicate the chosen peaks and therefore time of the start and end of the computed gradients.

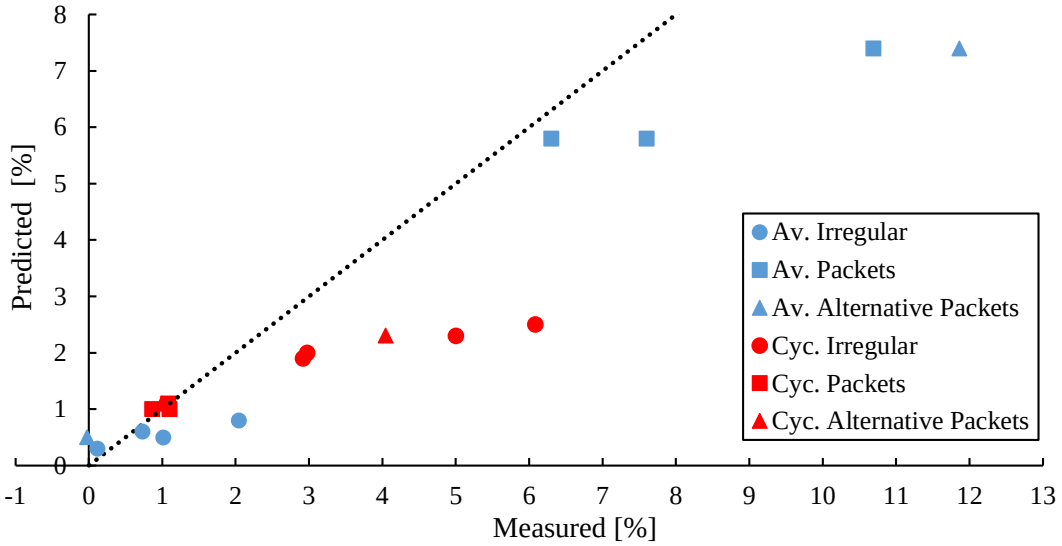

Figure 4.32: Comparison of ultimate strain predictions against measurements. Sorted into γ_{av} (blue) andγ_{cyc} (red). Marker type indicates load type: Irregular – ∘, Packets - □, Pyramid packets - △

$|\gamma_{meas,cyc} - \gamma_{pred,cyc}|$ for all half-cycles. This clearly increases with load amplitude τ_{cyc} but is independent of bias τ_{av}.

Accumulated strain γ_{av} can be seen most clearly in strain-time histories. In both measured and predicted response large 'jumps' of strain accumulation occur when the previous maximum stress is exceeded (virgin loading), as can be seen after $\approx 200s$ in test 3G. In test 4C three 'jumps' of strain are seen in measured and modelled response, accumulation between jumps occurs gradually with loading and unloading. The accumulation is over-predicted whilst the jumps under-predicted by the model. This is highlighted in Figure 4.31 where the gradient of accumulation (found by a linear least squares fit) is much higher across all three defined sections. The time-average load is the same in each section although the cyclic stresses may be of different intensities in each.

Generally the development of strain is predicted less well with increasing magnitude. This can be seen more clearly in Figure 4.32 where the measured and predicted ultimate average and cyclic strains, $\gamma_{cyc,u}$ and $\gamma_{av,u}$, are plotted against each other. The majority of the points are to the right of the $\gamma_{pred} = \gamma_{meas}$ line (indicating under prediction similar to Figure 4.22c) and deviate more with strain magnitude.

At high load magnitudes, small changes to stress level cause large changes in strain due to the non-linearity of the backbone response (see Figure 4.22a). This makes

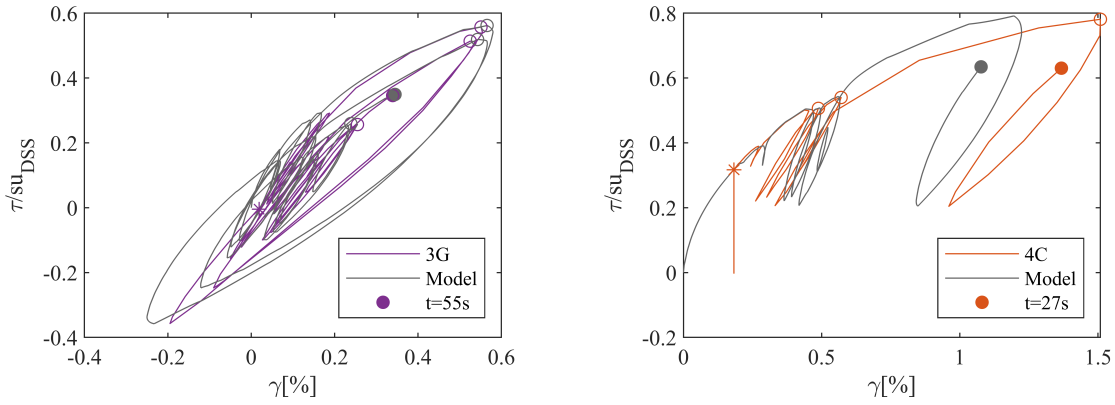

(a) **(b)**

Figure 4.33: Initial hysteresis loop to some large peak (a) 55s of Test 3G (b) Initial 27s of test 4C

predictions sensitive and, given the results in Figure 4.22c, may suggest that the calibrated backbone is stiffer than required at high stresses. Moreover, predictions of tests with high stress magnitudes are more sensitive to any disparity between assumed and real $s_{u,DSS}$ used in normalisation.

Figure 4.33 shows the early stages of response for two irregular tests for the first t seconds, alongside a model prediction in grey. The prediction fits the measured response well ,broadly following a similar 'backbone'. However the response begins to diverge at high stress magnitude in test 4C.

Given that the class C predictions are based upon a model which has only been calibrated to single amplitude tests, the results are promising. Development of strain with time is broadly captured, with much the same accuracy as with constant-amplitude cycles. This suggests the underlying model mechanisms still capture key behaviour under more complex loads.

4.2.4 Model improvement and sensitivity

Improvements to the model predictions can be achieved by slight variation of the model based upon the evidence of the multi-amplitude tests. This can inform new model choices and identify areas where the model is sensitive to calibration data. The revised model is termed Class C.1 in alignment with Lambe (1973). Areas of improvement are identified in Table 4.11, described by mechanism, potential improvement and proposed data for calibration.

Table 4.11: Proposed model improvements

Mechanism	Evidence	Improvement	Method of Calibration
1.Mono	Too stiff at high stresses - Figures 4.32 and 4.33b.	Softer backbone curve at high stress.	Optimise irregular tests to first large peak.
2.Rate	As above. Prediction of curvature at load reversal points is good indicating accurate viscous parameters.	Compare creep prediction at load holds for possible improvement	Tests 4B and 4D initial ramp and hold.
3.Softening	(1) Global/surface specific softening modelling choice not well defined. (2) Slight over-prediction of softening at low magnitudes, under-prediction at high magnitudes - Figures 4.26 and 4.30 .	(1) Introducing global softening may improve prediction (2) Recalibration of softening parameters	(1) Interrogate tests 3F, 3G and 3H for significant signs of post-cyclic softening. (2) Additional calibration tests using low magnitude packets of load in 3F.
4.Ratcheting	(1) Not enough accumulation at virgin loading. Test 3A, 3G, 4C. (2) Too much accumulation at high stress between peaks - Test 4C	(1) Slightly softer backbone curve. (2) Reduced ratcheting rate may be required.	(1) See monotonic calibration (2) Use initial packet of test 4B and 4D as extra test.

4.2.4.1 Monotonic

The backbone is a crucial part of hyperplasticity models with all further mechanisms depending upon the strengths and stiffness; small changes can alter the predictions greatly. It was observed that the predicted strains at high stress magnitude were consistently less than the measured strains.

The measured data allows a recalibration. Figure 4.34a shows the initial 174s of test 3G and Figure 4.34b the initial 54s of test 4C. Both are plotted alongside the 'Class C' model prediction in which a reducing accuracy with stress level can be seen.

The model prediction has been optimised by allowing a change to backbone parameters ε_u,k_u and a, using a proportional least-squares optimisation in a similar manner to the backbone recalibration presented in Chapter 3. The changes are termed 'Class C.1', in which an increased yield strain and curvature parameter and reduced k_u compute a more accurate response (for a summary of all parameters changed see Table 4.12). This change reduces the accuracy of the DSS prediction, but as shown later in Figure 4.38a not considerably.

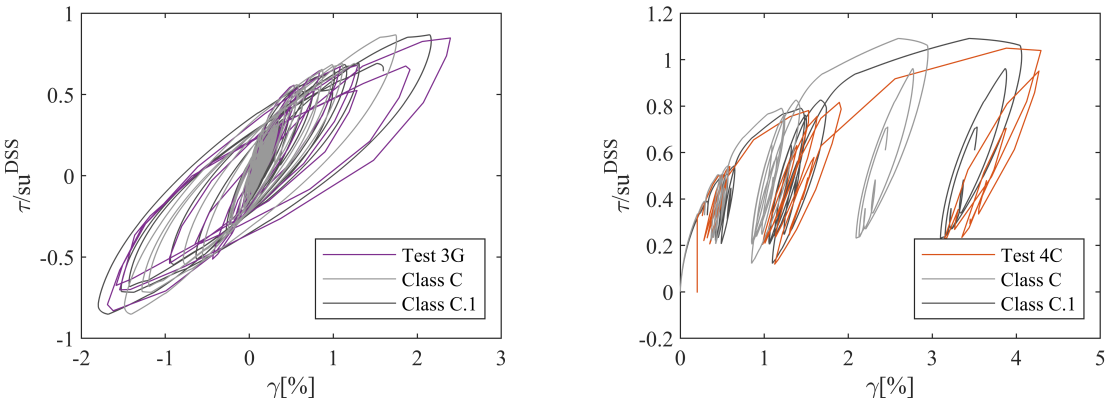

(a) (b)

Figure 4.34: Model prediction of initial hysteresis loop to some large peak (a) 174s of Test 3G (b) Initial 54s of test 4C

4.2.4.2 Rate dependency

Figure 4.35 shows the initial load and hold for the two idealised load cases with a high bias alongside the original 'Class C' and new 'Class C.1' model predictions. In the two tests, ramp time differs but load hold time is similar. It is clear from Figure 4.35b that both models capture the initial loading and creep to an acceptable level. On initial loading (hysteresis at $\tau/s_u \approx 0.32$) the model is stiffer than the measured response. This could be changed by reducing the initial stiffness, reducing rate dependency and/or adding more surfaces to facilitate plastic strain at lower magnitudes. This is not considered critical and thus not pursued.

4.2.4.3 Softening

When modelling softening behaviour as in Section 3.4.2.1, a key choice is the formulation (surface-specific, constant or mixed) controlled by parameter F_κ .Evidence for this choice may be found in the 'post-cyclic' response; by determining if degradation

Table 4.12: Hyperplasticity parameters used for model predictions

Model	Monotonic				Rate			Softening				Ratcheting	
	ε_u [%]	$k_{u,0}$ [kPa]	E_0 [$kPa/\%$]	a [–]	F_η [–]	$\dot{\alpha_{ref}}$ [$\%/hr$]	η_{10} [–]	F_κ [–]	κ_{ref} [–]	F_{MP} [–]	m_k [–]	R_0 [–]	m_s [–]
C	8.5	0.65 x $s_{u,DSS}$	9 x $s_{u,DSS}$	2.68	1	0.01	0.29	1	0.6	10.0	0.18	0.1	3
C.1	**15**	0.58 x $s_{u,DSS}$	9 x $s_{u,DSS}$	**3.95**	1	0.01	0.29	**0.9**	0.6	10.0	0.18	**0.03**	**2**

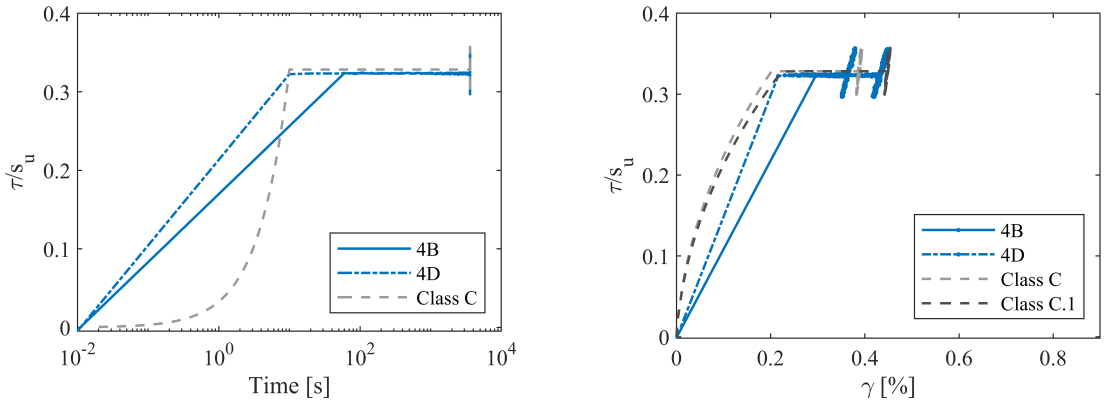

Figure 4.35: Initial ramp and hold from tests 4B and 4D alongside class C and C.1 model prediction (a) Stress-time history (b) Stress-strain response

in virgin response due to lower magnitude load reversals occurs. Given that the calibration tests were constant amplitude (without post-cyclic shearing) a surface-specific (F_η=1) model was chosen, this choice can now be appraised. Figure 4.36a shows the three two-way loaded tests 3F, 3G and 3H. The corresponding markers track points of the 'virgin load peaks' (points where stress level exceeds the previous maximum).

The 2-way tests are chosen so that additional strain due to ratcheting is removed. The three tests consist of: 3G - irregular, in which a large peak (at τ/s_u=0.85) occurs after 200 seconds; 3F - idealised, with the largest loads occurring at the end (τ/s_u=0.85 at $t \approx 17800s$); 3H, idealised with the largest loads in the centre of loading history (τ/s_u at $t \approx 10500s$).Figure 4.36b shows the virgin load peaks plotted without the history for clarity. Cumulative absolute strain values ($\Sigma|d\varepsilon|$) are shown at approximately $\tau/s_u \approx 0.85$ as a measure of strain history.

At the large virgin load jumps, 3G and 3H track broadly the same curve despite large differences in history. However, the equivalent curve for test 3F is clearly softer. The latter may suggest post-cyclic softening is occurring, but is not conclusive, particularly given likely sample variability. The shaded area shows the difference in results for tests 4B and 4D (same loading) as an indication.

Given that generally the Class C ultimate strain predictions were lower than the measured data a small amount of constant softening (F_κ=0.9) is allowed in the Class C.1 predictions. Figure 4.36c shows virgin load peaks as predicted by the models C and C.1, which also includes changes to ratcheting as discussed in the next section.

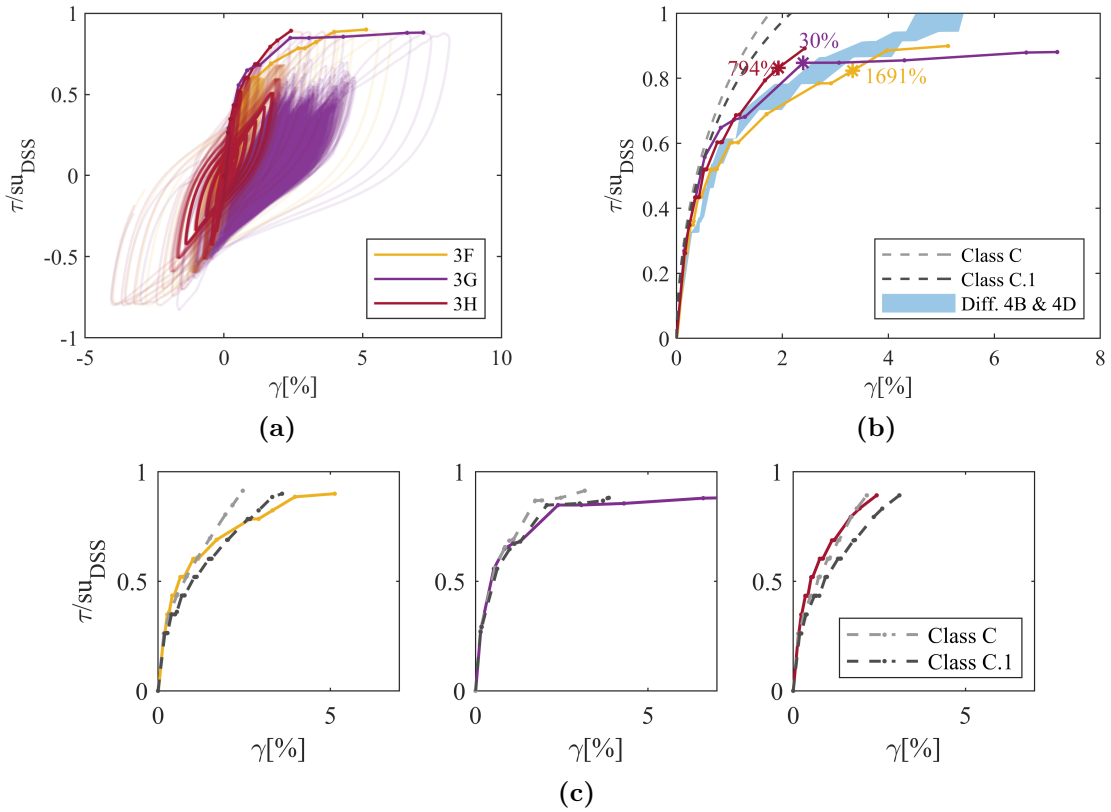

Figure 4.36: (a) High magnitude two-way tests 3F, 3G and 3H with virgin-load peaks tracked (b) 'Virgin load peaks' of two-way tests alongside model monotonic backbone prediction (T=1s to mimic T=4s loading) (c) 'Virgin load peaks' of two-way tests alongside model monotonic predictions

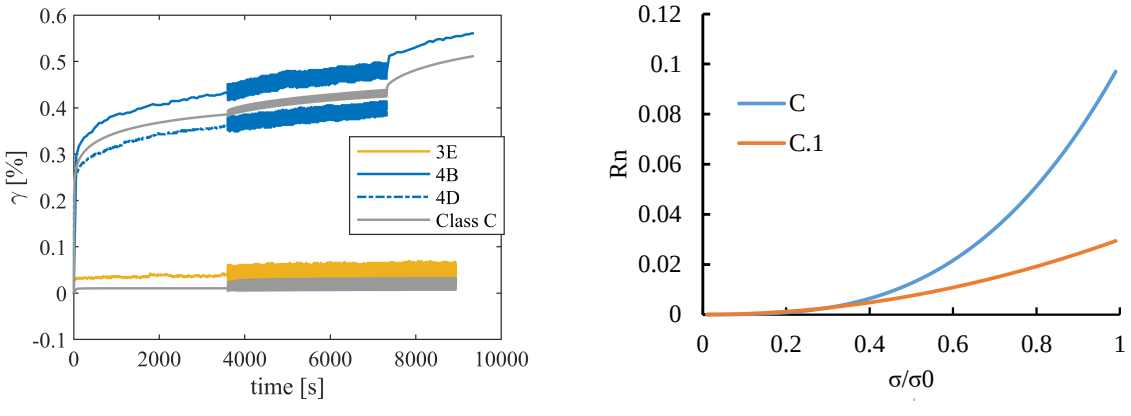

Figure 4.37: (a) Strain development for first packets of idealised loads.(b) Ratcheting rate parameter with stress level

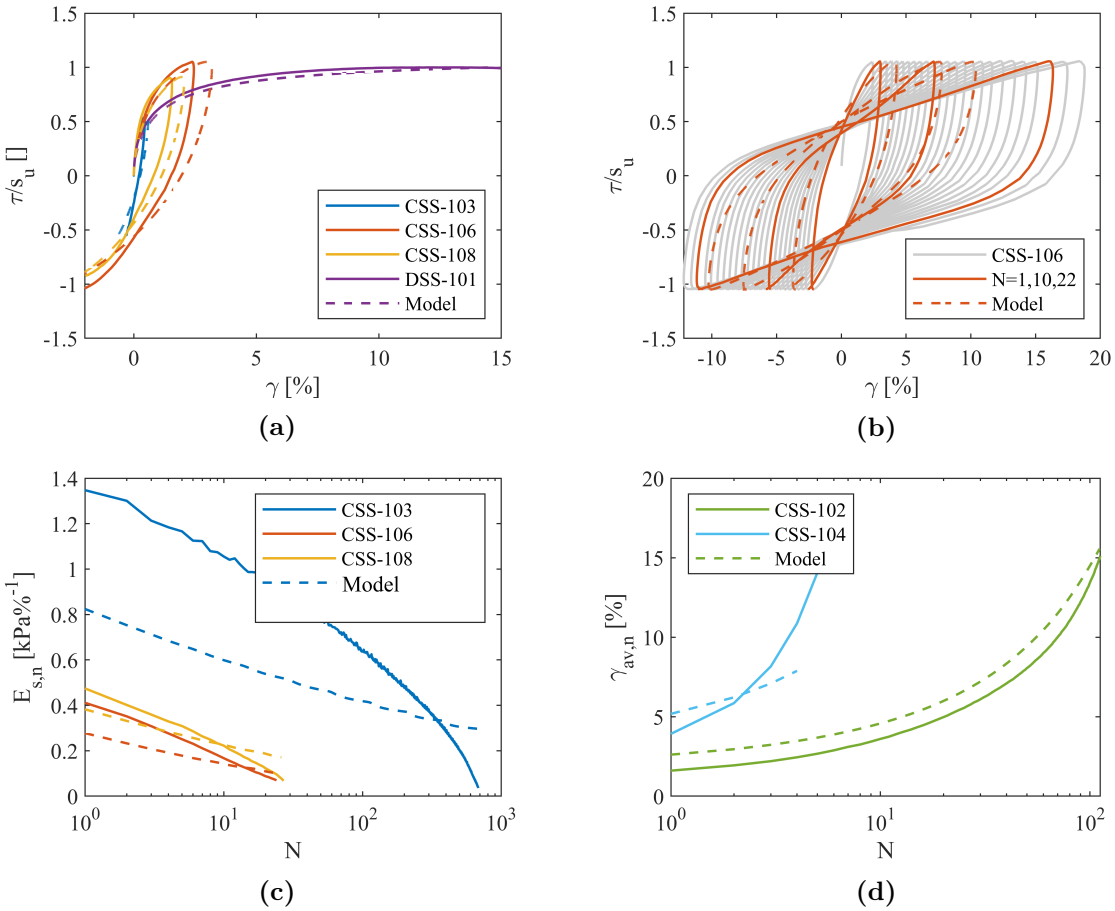

Figure 4.38: Calibration tests and Class C.1 model prediction. (a) Initial cycles – Rate Dependency (b) Example hysteresis loops - $\tau_{av} = 0$ (c) Secant Stiffness Development (d) Average strain development (e)

4.2.4.4 Ratcheting

The heat-map in Figure 4.23b demonstrates that the DSS_{cyc} tests to which the model is calibrated are of a much lower stress magnitude than that applied in test 4C. A lower magnitude test may have better informed the calibration of ratcheting parameters across the stress space. Figure 4.37a shows development of strain for the first packets of the idealised loads alongside the Class C prediction. In fact it seems that ratcheting is predicted well at low level.

When viewed together, Figure 4.31 and 4.37a suggest that the ratcheting is less accurately predicted when the average stress is large but correct when small; evidence that the stress magnitude effect (m_s) is too high. Therefore, for the Class C.1 predictions m_s is reduced. Reasons for this possible error are discussed in section 4.2.6.

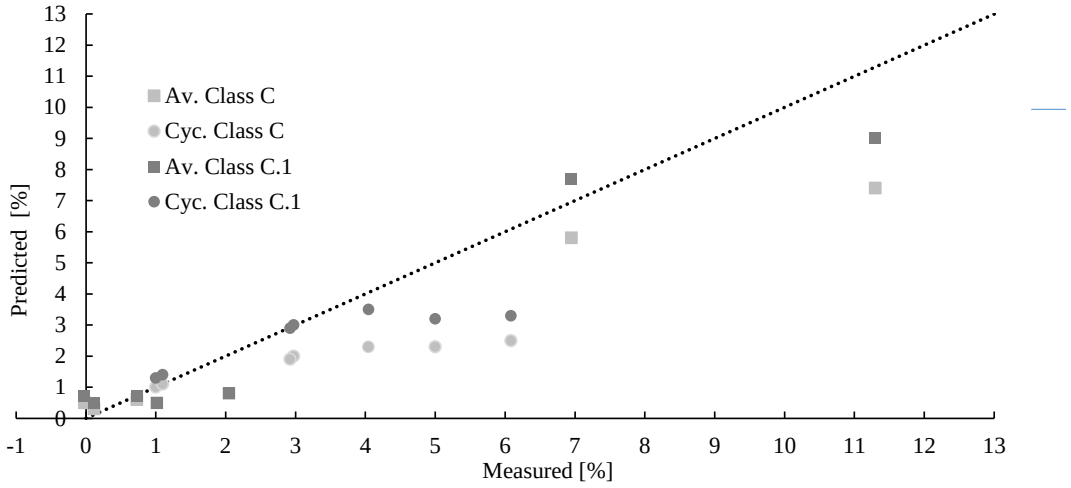

Figure 4.39: Comparison of ultimate strain class C and C.1 predictions against measurements. Marker type indicates strain type: γ_{av} – ∘, γ_{cyc} - □

Table 4.13: Comparison of predicted ultimate average and cyclic strains against measured data. Class C (Original) and Class C.1 (optimised) predictions. Irr.=Irregular loads, Pac. = Idealised Packets, Alt. Pac. = Idealised packets applied in different order

Test	Load Type	$\gamma_{av,u}$[%]			$\gamma_{cyc,u}$[%]		
		Measured	Class C	Class C.1	Measured	Class C	Class C.1
3A	Irr.	0.7	0.6	0.7	3.0	2.0	3.0
3E	Pac.	0.1	0.3	0.5	2.9	1.9	2.9
3F	Pac.	1.0	0.5	0.5	5.0	2.3	3.2
3G	Irr.	2.0	0.8	0.8	6.1	2.5	3.3
3H	Alt. Pac.	0.0	0.5	0.7	4.0	2.3	3.5
4C [4E]	Irr.	10.7 [11.9]	7.4	9.0	1.1 [1.0]	1.1	1.3
4D [4B]	Pac.	6.7 [7.6]	5.8	7.7	0.9 [1.1]	1.0	1.4

Figure 4.37b shows the ratcheting rate R_n with stress level, $R_n = R_0(\frac{|\sigma|}{\sigma_0})^{m_s}$, for the Class C and C.1 predictions with a reduced m_s=2. At low stresses ($\sigma/\sigma_0 < 0.4$) R_n is maintained, but it is greatly reduced at high stresses. This is combined with a softer backbone at high magnitudes (and therefore higher plastic strains) so the effect will be less pronounced.

4.2.5 Class C.1 predictions

In this section the suggested 'Class C.1' changes are used to re-predict the WAS-XL tests. Table 4.12 shows the changes in bold to Monotonic, Softening and Ratcheting parameters.

The original calibration tests were computed throughout each of the Class C.1

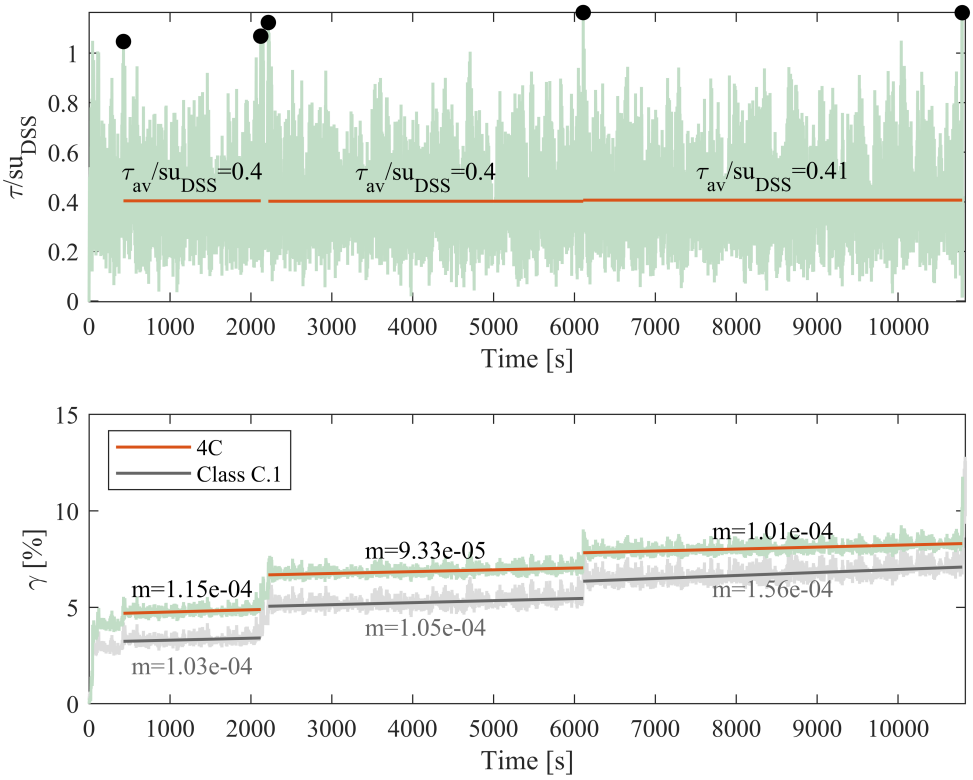

Figure 4.40: Measured and Class C.1 model response for test 4C with gradient of strain accumulation (m) shown for three section between 'virgin loading' peaks

changes to ensure any change did not greatly affect the comparison with the original results. Figure 4.38 shows examples in which the resulting predictions are very similar to Class C (Figure 4.22).

Table 4.13 and Figure 4.39 show the new predictions of the WAS-XL tests, compared to the previous. Cyclic strains are increased with the allowance of some global softening (F_κ=0.9) and the softer backbone. This improves the fit, particularly the final, much larger amplitude cycles. The order of ultimate cyclic strain for tests 3F,3G and 3H is not preserved, predicting highest cyclic strains in the pyramid case. This is presumably due to more plastic strains, and therefore changes in hardening parameter, occurring earlier in the history, thus degrading (globally) the yield strengths earlier and in turn causing a softer response with more strain. This is limited if only local softening is permitted.

Average strain predictions for the low bias tests remain fairly similar but increase somewhat for tests 4C and 4D. This is despite a reduction of ratcheting parameter

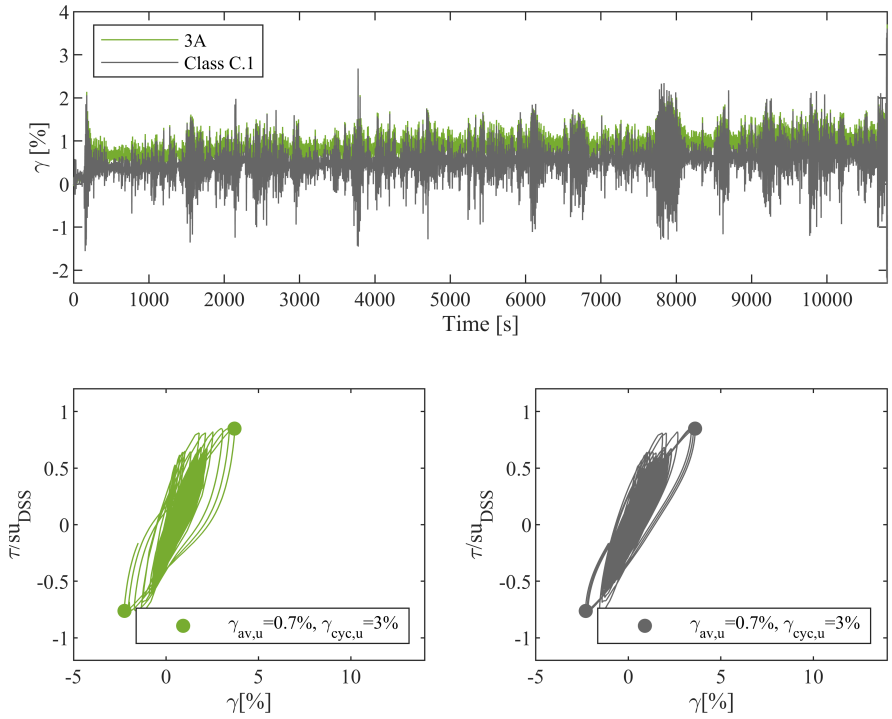

Figure 4.41: Measured and Class C.1 model response for test 3A

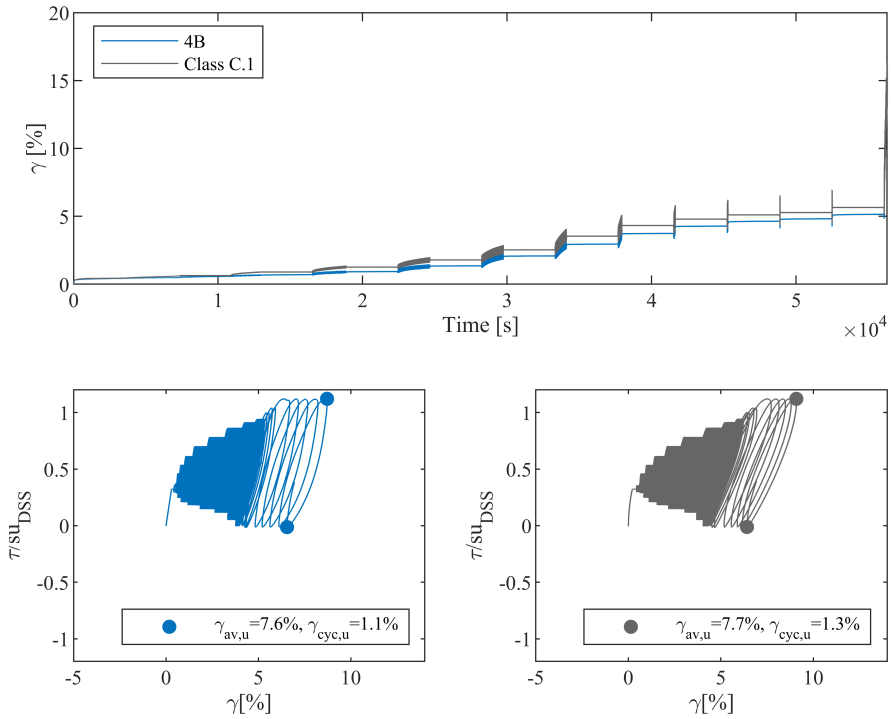

Figure 4.42: Measured and Class C.1 model response for test 4B

with high stress value. The reduction is offset by a reduced stiffness of the backbone at high stress and an allowance for some global softening which will in turn yield higher plastic strains per cycle. More importantly the development of average strain is now much more accurate. Figure 4.40 shows the irregular test 4C with the gradients of accumulation again shown (as per Figure 4.31), the virgin load accumulations are larger and the gradients between jumps much smaller following that of the data more closely. Figures 4.41 and 4.42 shows two examples predictions of tests 3A and 4B.

4.2.6 Conclusions

Given that the class C predictions are based upon a model which has only been calibrated to single amplitude tests, the results are promising. Development of strain with time is broadly captured, with much the same accuracy as with constant-amplitude cycles. This suggests the underlying model mechanisms still capture key behaviour under more complex loads.

Hyperplasticity models are able to predict long, multi-amplitude tests quickly and accurately. The initial Class C predictions, using a typical suite of constant-amplitude tests, were a true test of model calibration. The resulting predictions were promising, capturing broadly the development of strain with time with much the same accuracy as with constant-amplitude cycles.

This suggests a robust model which works well with default (or straight forward to calibrate) parameters. The predictions were improved by using additional data from the WAS-XL tests (Class C.1), highlighting sensitive areas of modelling and calibration. Table 4.14 describes the changes made and a comment on the reasons for each.

Generally, the calibration tests were of high quality and with low variability. Initial quarter cycles matched and numbers of cycles to failure increased with magnitude. However, as can be seen in Figure 4.23, the stress conditions were at much higher magnitudes than the following WAS-XL tests. This should be considered when specifying laboratory testing and will be discussed further in Chapter 6.

The idealised cycle tests (particularly $\tau_{av} \neq 0$) proved a useful source for second calibration. By having two of the same test, variability could be estimated. Perhaps

Table 4.14: Changes made between Class C and C.1 predictions and comments

Parameter Change	Comments
Softer Backbone at high stress (γ_u,k_u,a)	The backbone calibration is crucial to an accurate prediction. At high stress magnitudes, strains are very sensitive to small changes in stiffness which appeared too high. This is easily re-calibrated by optimisation of irregular test which have a large peak early in the history.
Introduction of some global softening (F_κ)	Post-cyclic tests may have informed this choice, but not clear. Mainly allows for greater increase in strain amplitude after numerous cycles.
Reduction in ratcheting rate and stress magnitude exponent (R_0, m_s)	Only two $\tau_{av} \neq 0$ calibration tests, both with high τ_{cyc}, low N_f and an increasing average strain to failure. Therefore difficult to 'pin' stress dependency.
General	Calibration tests were at much higher stress magnitude than those predicted. It is perhaps fortunate that model parameters worked well at a lower magnitude stresses too.

stepped tests could be an efficient solution for model calibration, since each load packet provides a higher level of strain development to calibrate to.

4.3 Summary of 0D modelling

Chapters 3 and 4 of this thesis are concerned with the application of 0D total-stress hyperplasticity models to laboratory tests in clays. Chapter 3 presented experimental data, model choices and applied these to individual datasets. Chapter 4 attempted to probe the model further by: testing it across all cyclic stress regimes with the synthesising of contour diagrams; testing the predictive ability by computing multi-amplitude tests. Both exercises have proven useful.

It is concluded that it is possible for extended hyperplasticity models to:

- reproduce key behaviour of clays subject to DSS_{cyc} and CU_{cyc} testing
- reproduce this behaviour across varied cyclic magnitudes and degree of reversals
- predict multi-amplitude tests (both truly irregular and idealised)

The model predictions are satisfactory, but of course could be improved. Importantly they have shed light on model performance, presented as before, by mechanism.

Predicting the backbone response well is crucial. The equation presented by Jeanjean et al. (2017) seems adequate for this application but the model is not dependent on the choice of this form; any equation or stress-strain curve is acceptable. A fundamental difficulty is sample variability, which can be high. All proceeding mechanisms build upon the assumed backbone and therefore it would be good practice to use an average of multiple tests.

Rate-dependent behaviour is accurately reproduced by a model based upon rate process theory. The magnitude of strain rate changes considerably throughout constant period cycles. Therefore incremental implementation of viscous models is key to accurate prediction of cyclic loads. In doing so, effects such as creep, relaxation and the rounded peaks of sinusoidal tests are inherently reproduced.

To accurately capture the effects of load applications and reversals a model must be in place which captures softening and ratcheting. Subtle changes to the softening of yield strengths produces differing secondary effects. It is clear from the data in this thesis that 'global' softening, in which all yield strengths are degraded, over-predicts the accumulation of strain for biased tests and causes unrealistic levels of 'post-cyclic softening' for most cyclic stress applications. Instead a model with some combination of surface specific and global softening alongside a ratcheting element was presented. There are now two options which produce similar results for some tests, and it is not clear which is correct:

A) Mixed softening only. This causes post-cyclic softening and couples secant stiffness reduction with ratcheting, thereby removing control of strain accumulation from the user. This is successfully applied to the contour plot reproduction exercise (Section 4.1) and to NSCA datasets in Chapter 3.

B) Surface specific softening with additional ratcheting element. This removes post-cyclic softening and allows full control of ratcheting behaviour. This approach was successfully employed in the WAS-XL work (Section 4.2) and applied to the COW data-set in Chapter 3. In this case, secant stiffness reduction is limited and can therefore be inaccurate near failure. A small amount of mixed softening removes some of issues with highly strained tests (as introduced in WAS-XL Class C.1). With further reduction this may reduce to (A).

The above choice may be material and test dependent and is therefore left open here. It is important to consider 'zones' of calibration when finding model parameters and be aware of possible limitations. This is true for rate parameters where accuracy may well be limited at extrapolated strain rates and strain magnitudes. It is also the case for cyclic parameters in terms of stress level and numbers of cycles.

Chapter 5

Equivalence of series and parallel models

5.1 Introduction

In Chapter 3, models were developed in the hyperplasticity framework to describe the key behaviour observed when clays were subject to shear stresses in undrained laboratory tests. Multiple surfaces with differing strengths and stiffnesses were employed to capture the non-linearity of typical soil response when subject to stress. There are, however, several ways in which the individual surfaces can be arranged, with implications on the meaning of internal parameters and subtle differences in model behaviour.

The surfaces were configured in series, such that each surface is subject to the same individual stress and the strains are additive (Figure 5.1b). The same individual surfaces could be arranged in parallel form, such that multiple individual surfaces are subject to the same strain and the stresses become additive (Figure 5.1a). A third possibility is a 'nested' configuration (Houlsby, 2020b) (connecting surfaces in a chain) but this is not pursued here.

Previous authors have rightly suggested that it is most obvious, and possibly computationally beneficial, to construct models in series when computing strains from a stress input since strains are additive (Richards, 2020; Abadie, 2015), and in parallel (where stresses are additive) for strain input such as in FEA implementation (Beuckelaers, 2017). In deriving incremental behaviour using a compliance matrix as described in Appendix A, either configuration may be implemented for stress or strain control.

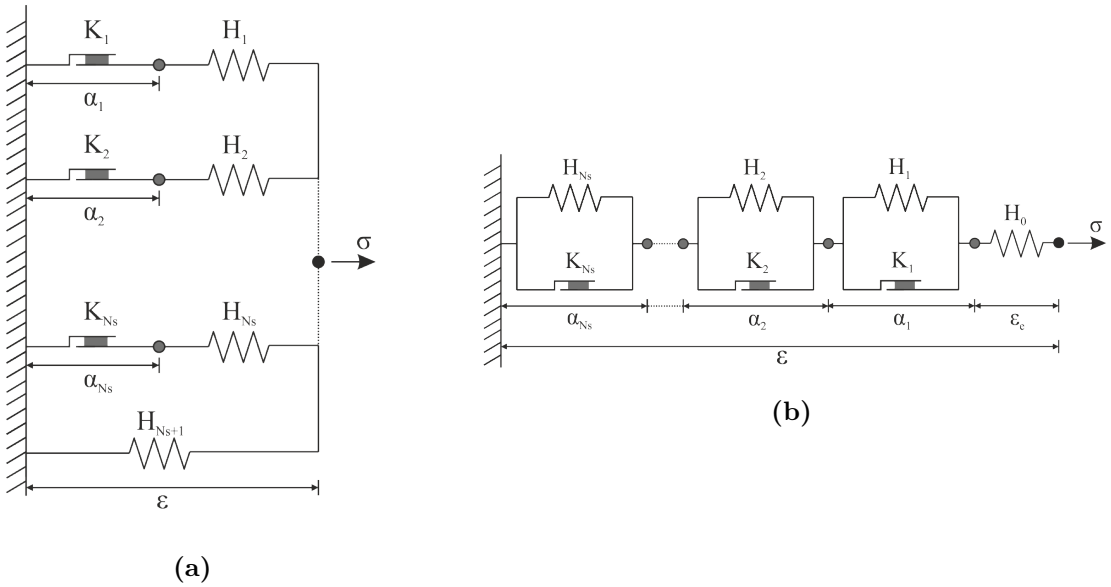

Figure 5.1: Conceptual diagrams of multi-surface kinematic hardening models in (a) parallel configuration and (b) series configuration

In this section the equivalence between series and parallel models is investigated for each of the mechanisms presented in Chapter 3, alongside a summary of similar work done by previous authors. Ultimately, this aims to summarise the differences between the model structures, appraise the implications, advise parameter choices which can produce equivalence or near-equivalence, and present reasons for preference of one or the other.

Consistency is paramount if the possibility of calibrating pile-scale models from element testing is to be achieved. Either one must decide upon a configuration to use or prove that parameters map between the two.

5.2 Kinematic hardening

Figures 5.1a and 5.1b show multi-surface kinematic hardening models configured in parallel and series. Both models can be calibrated to ensure similar yield locations ε_y, σ_y following methods presented by Houlsby et al. (2017). In this case the role and magnitude of surface strengths K_i and stiffnesses H_i differ. In a series configuration, surface behaviour is governed by a yield stress criterion $\sigma_{y,i} = K_i$ after which the local spring is activated. By contrast in parallel, the yield strain criterion $\varepsilon_{y,i} = K_i/H_i$ causes the local slider to activate, deactivating the spring.

The models can be described by energy functions and a common dissipation (and therefore yield) function from which incremental behaviour can be derived (following methods described in Appendix A):

$$f_{par} = \sum_{i=1}^{Ns} \frac{H_i}{2}(\varepsilon - \alpha_i)^2 + \frac{H_{Ns+1}}{2}\varepsilon^2 \tag{5.1}$$

$$f_{ser} = \frac{H_0}{2}\left(\varepsilon - \sum_{i=1}^{Ns} \alpha_i\right)^2 + \sum_{i=1}^{Ns} \frac{H_i}{2}\alpha_i^2 \tag{5.2}$$

$$d = \sum_{i=1}^{Ns} K_i|\dot{\alpha}_i| \tag{5.3}$$

Note, however interpretation of α_i, K_i and H_i differs between the models. Figure 5.2a shows computations of strain ε from 1000 equal increments of stress σ for a series and parallel model. Both models were calibrated to a backbone described by the 'Jeanjean' function (equation 3.7) with parameters following those fit to normally consolidated DSS tests in Drammen Clay in Table 3.3. A total of 40 surfaces are used for which the derivation of strengths K_i and stiffnesses H_i differ (following Houlsby et al., 2019).

The final computed global responses are identical despite local differences, and match the calibration function well. Beuckelaers (2017) also showed that uni-directional rate-independent kinematic hardening models produce identical responses. However, this is no longer true for bi-directional (σ_x, σ_y) models. Richards (2020) compared multi-directional calculations with experimental results of a model pile in sand, concluding that once experimental variability is considered the model responses overlap. She was unable to detect which of the two was best suited on the basis of data alone.

Figure 5.2b and 5.2c show the development of local internal variables α_i at surfaces $i = 1, 10, 20$ and 30. In series, Figure 5.2b, $\alpha_i = 0$ until the corresponding yield stress is exceeded, after which it increases linearly with applied stress. The gradient differs between surfaces and is a function of the surface stiffness H_i. In parallel, Figure 5.2c, $\alpha_i = 0$ until the corresponding yield strain is exceeded, after which it consistently increases at the same rate as global strain ε across all surfaces, $d\alpha_i = d\varepsilon$. This behaviour is derived from the constitutive energy and dissipation function as shown in Appendix A.

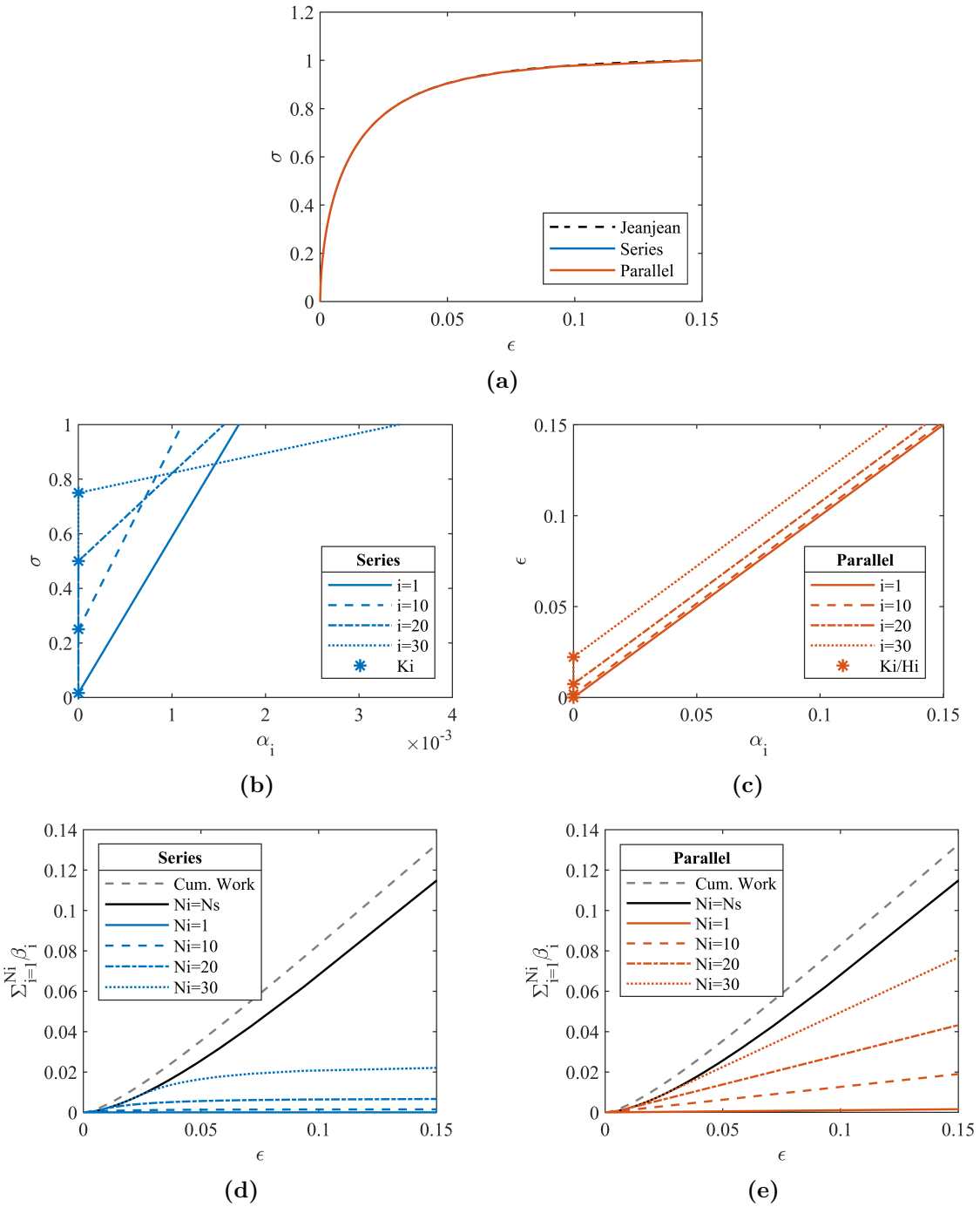

Figure 5.2: Comparison of series and parallel rate-independent kinematic hardening models. 40 surfaces calibrated to a backbone described by the 'Jeanjean' function (equation 3.7) with parameters equivalent to those of *DSS* tests of normally consolidated Drammen Clay (Table 3.3); (a) model computations of strain ε from 1000 equal increments of stress σ and comparison with original 'Jeanjean' curve; (b) series - development of local α_i with σ; (c) parallel - development of local α_i with ε; (d) and (e) cumulative work with strain level, where plastic work $\dot{\beta}_i = K_i|\dot{\alpha}_i|$

.

Figure 5.2d and 5.2e show a measure of work against strain level. The total cumulative work is found by integration (from 0 to ε) of the 'Jeanjean' function shown in Figure 5.2a. β_i is a measure of plastic work at surface i where:

$$\dot{\beta}_i = K_i|\dot{\alpha}_i| \tag{5.4}$$

Such that $\Sigma_{i=1}^{Ni}\beta_i$ is the cumulative plastic work from the 1^{st} to the N_i^{th} surface. It is clear that the global ($N_i = N_s$) plastic work is the same for both models. However, locally work develops at differing rates throughout the computation. In series, the higher surfaces (with a higher K_i and α_i) contribute much more than in the parallel models where the distribution of K_i and α_i is more uniform.

These local differences play an important role as further mechanisms are considered.

5.2.1 Asymmetry

Section 3.2.2 described a kinematic hardening model with strength asymmetry, useful in describing the behaviour due to soil anisotropy in extension and compression as observed in triaxial testing. Figure 5.3a and 5.3b shows the model in series and parallel which can be described by energy functions 5.1 and 5.2 and a common dissipation function:

$$d = \sum_{i=1}^{Ns} K_{n,c}\langle\dot{\alpha}_i\rangle + K_{n,e}\langle-\dot{\alpha}_i\rangle \tag{5.5}$$

Surface stiffnesses H_i are kept constant whilst local strengths differ depending on direction of loading, such that:

$$K_{i,e} = A_{f,i}.K_{i,c} \tag{5.6}$$

where $A_{f,i}$ is a local asymmetry factor. Requirements for increasing strengths must still be met as outlined in 3.2.2. Effectively, the locations of yield points are altered (typically reduced) in extension by fitting to respective data. This is shown schematically in Figure 5.3c, where for clarity absolute stresses and strains are plotted. Since in parallel, yield strains $\varepsilon_{y,i} = K_i/H_i$ and in series, yield stresses $\sigma_{y,i} = K_i$:

$$A_{f,i,par} = \frac{\varepsilon_{ye,i}}{\varepsilon_{yc,i}} \tag{5.7}$$

$$A_{f,i,ser} = \frac{\sigma_{ye,i}}{\sigma_{yc,i}} \tag{5.8}$$

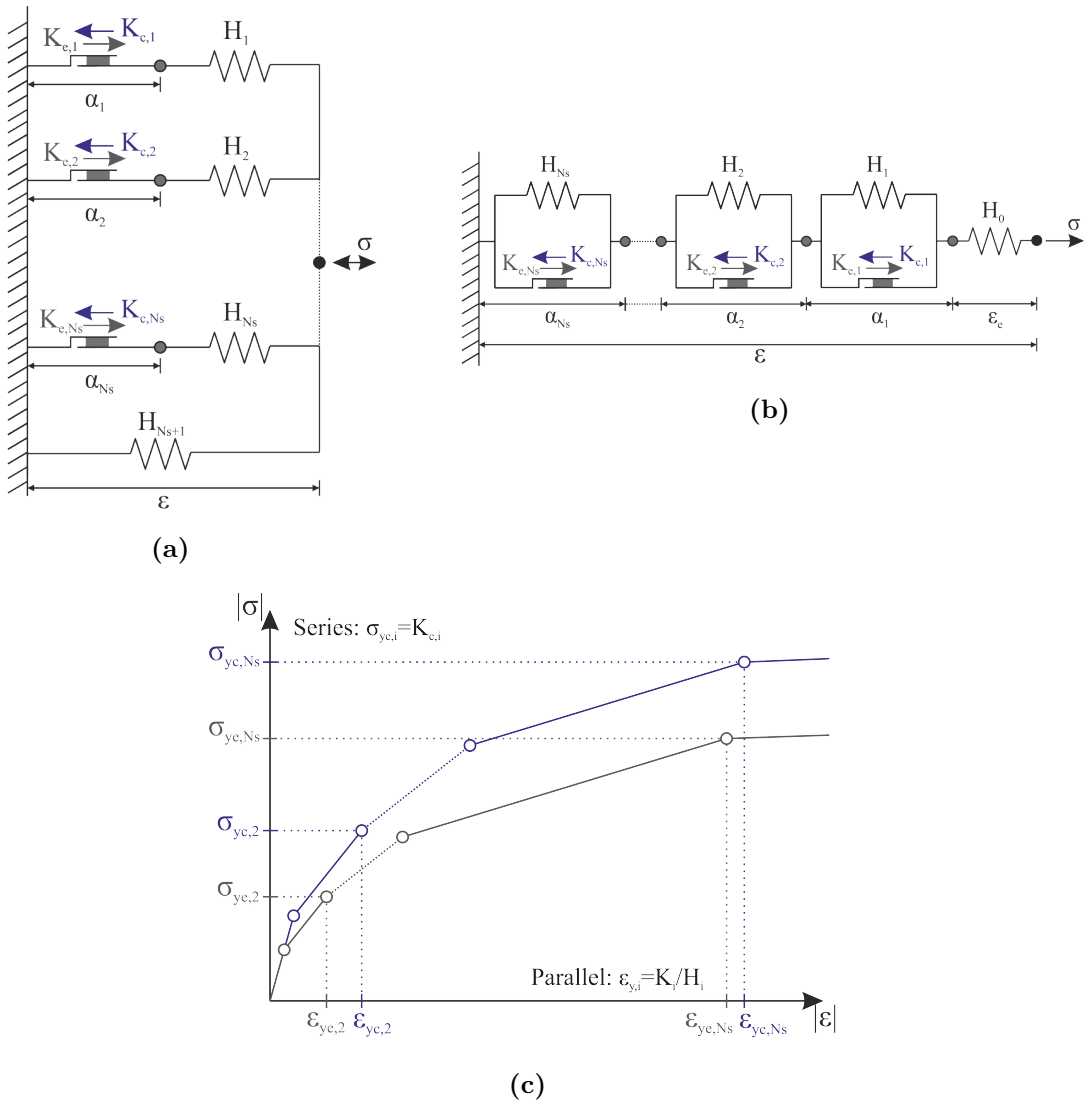

Figure 5.3: Conceptual diagrams of multi-surface kinematic hardening models with strength asymmetry in (a) parallel configuration and (b) series configuration; (c) example yield points in $|\sigma|$,$|\varepsilon|$ space for a weaker extensive backbone

$A_{f,i,par} \neq A_{f,i,ser}$ if the ratio of local yield stresses and strains differ. In the case where a single 'global' anisotropy factor is used for each surface, $A_{f,i,par} = A_{f,i,ser} = A_{f,G}$ for all i. As in the previous section exact equivalence can be achieved, but the parameters may differ at a local level.

5.3 Rate process theory

Figure 5.4a and 5.4b show rate-dependent multi-surface kinematic hardening models configured in parallel and series. Viscous dissipation is included conceptually with a dashpot at each surface, such that each internal variable has an associated local

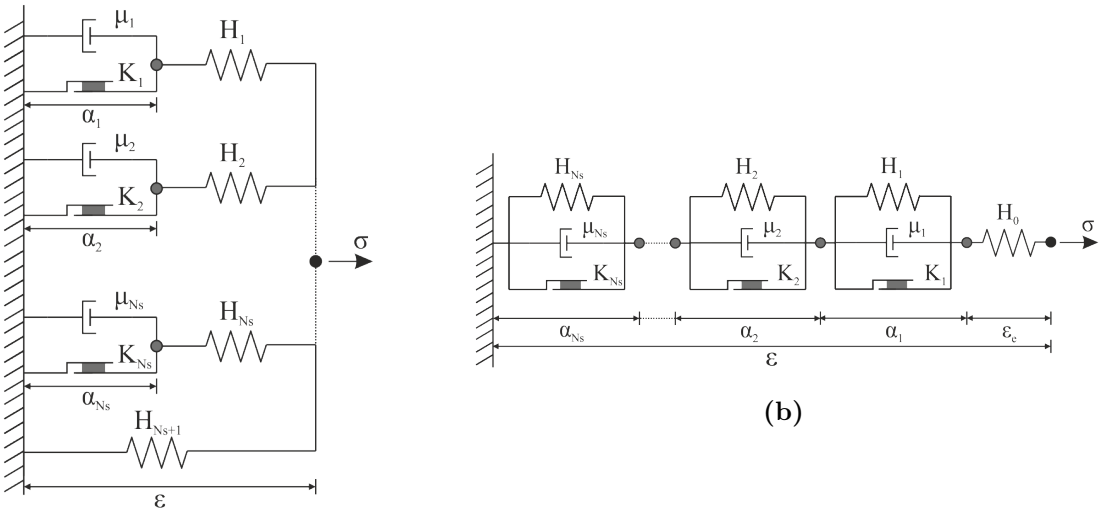

Figure 5.4: Conceptual diagrams of rate-dependent, multi-surface, kinematic hardening models in (a) parallel configuration and (b) series configuration.

viscosity μ_n. In Section 3.3.2 more realistic modelling of rate-effects was achieved by using an inverse hyperbolic sinusoid relationship which fits the underlying physics of rate-process theory. The model can be defined in series or parallel with energy functions 5.1 or 5.2 and a common dissipation function:

$$d = \sum_{i=1}^{Ns} K_i|\dot{\alpha}_i| + \sum_{i=1}^{Ns} \frac{\mu_i}{t_{ref,i}}\dot{\alpha}_i \sinh^{-1}\left(|\dot{\alpha}_i|t_{ref,i}\right) \tag{5.9}$$

where μ_i is the surface viscosity and $t_{ref,i}$ is a reference time to failure (the inverse of the reference strain rate $\dot{\alpha}_{i,ref}$). The $\sinh^{-1}$ function results in approximately linear viscosity at low strain rates $|\dot{\alpha}_i|t_{ref,i} << 1$ and approximately logarithmic viscosity at high rates $|\dot{\alpha}_i|t_{ref,i} >> 1$.

In Section 3.3.2, μ_i and therefore relative viscous contribution was allowed to vary with rate surface factor F_η (Equation 3.24). This allowed viscosity to be scaled between surface strength (as above) and ultimate system strength, thus facilitating strain-level dependent rate effects. This is not investigated here, rather local viscosity is assigned proportional to the strength parameter K_i, ($F_\eta = 1$) such that:

$$\mu_i = K_i \eta t_{ref,i} \tag{5.10}$$

Incremental behaviour can be derived from standardised form in Appendix A. It is clear from the second term in Equation 5.9 that the dissipative behaviour now

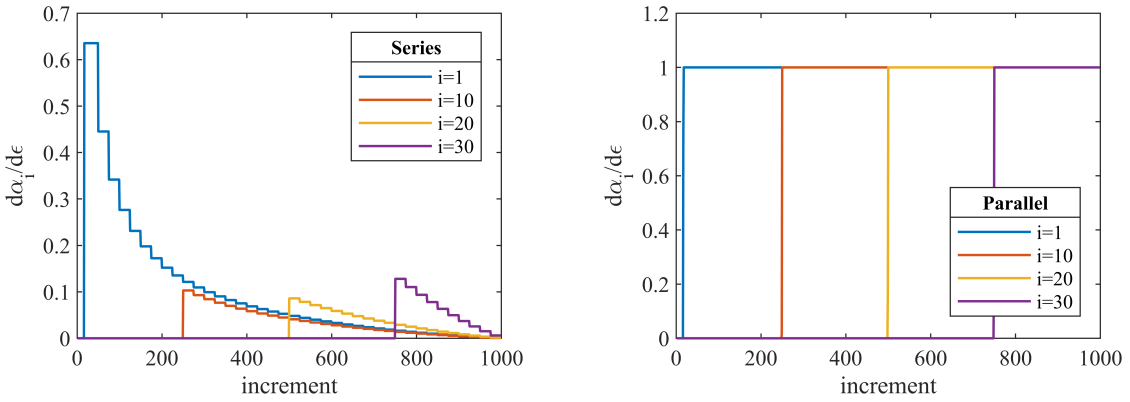

(a) **(b)**

Figure 5.5: Development of local strain $d\alpha_i$ with respect to global strain $d\epsilon$ for the Rate-independent model presented in Figure 5.2a. Increment is associated with equal stress application from $\sigma = 0$to $\sigma = 1$

depends on a normalised local strain rate $|\dot{\alpha}_i|t_{ref,i}$. As shown in the previous section (Figure 5.2b and c), $\dot{\alpha}_i$ takes on different values in the series and parallel models, therefore $t_{ref,i}$ may be expected to differ to ensure consistent normalised local strain rates and therefore response.

To equate local strain rates to experiments in which global strain values are measured, define $t_{ref,i}$ by:

$$|\dot{\varepsilon}|t_{ref,G} = |\dot{\alpha}_i|t_{ref,i} \rightarrow t_{ref,i} = t_{ref,G}\frac{d\varepsilon}{d\alpha_i} \tag{5.11}$$

Figures 5.5a and 5.5b show $\frac{d\alpha_i}{d\varepsilon}$ with each increment of stress application for the rate-independent model presented in Figure 5.2a. Figure 5.5a shows that in parallel, once a surface yields, $d\alpha_i = d\varepsilon$ (observable in Figure 5.2c too). Importantly, this means that strain rates are consistent locally and globally and therefore $t_{ref,i} = t_{ref,G}$.

Conversely, in series (Figure 5.5b) it is clear that local strain rates differ between surfaces and are dependent upon the number of active surfaces. This seems sensible given that strains are additive in series. However, it means that estimating the magnitude of strain is more involved and $t_{ref,i} \neq t_{ref,G}$. In fact:

$$d\alpha_i = \frac{d\sigma}{H_i}, d\varepsilon = \frac{d\sigma}{E_{t,y}} \rightarrow \frac{d\varepsilon}{d\alpha_i} = \frac{H_i}{E_{t,y}} \tag{5.12}$$

where E_t is the tangent stiffness and subscript y indicated the highest yielding surface. Therefore for consistency with the parallel model:

$$t^*_{ref,i} = t_{ref,G}\frac{H_i}{E_{t,y}} \tag{5.13}$$

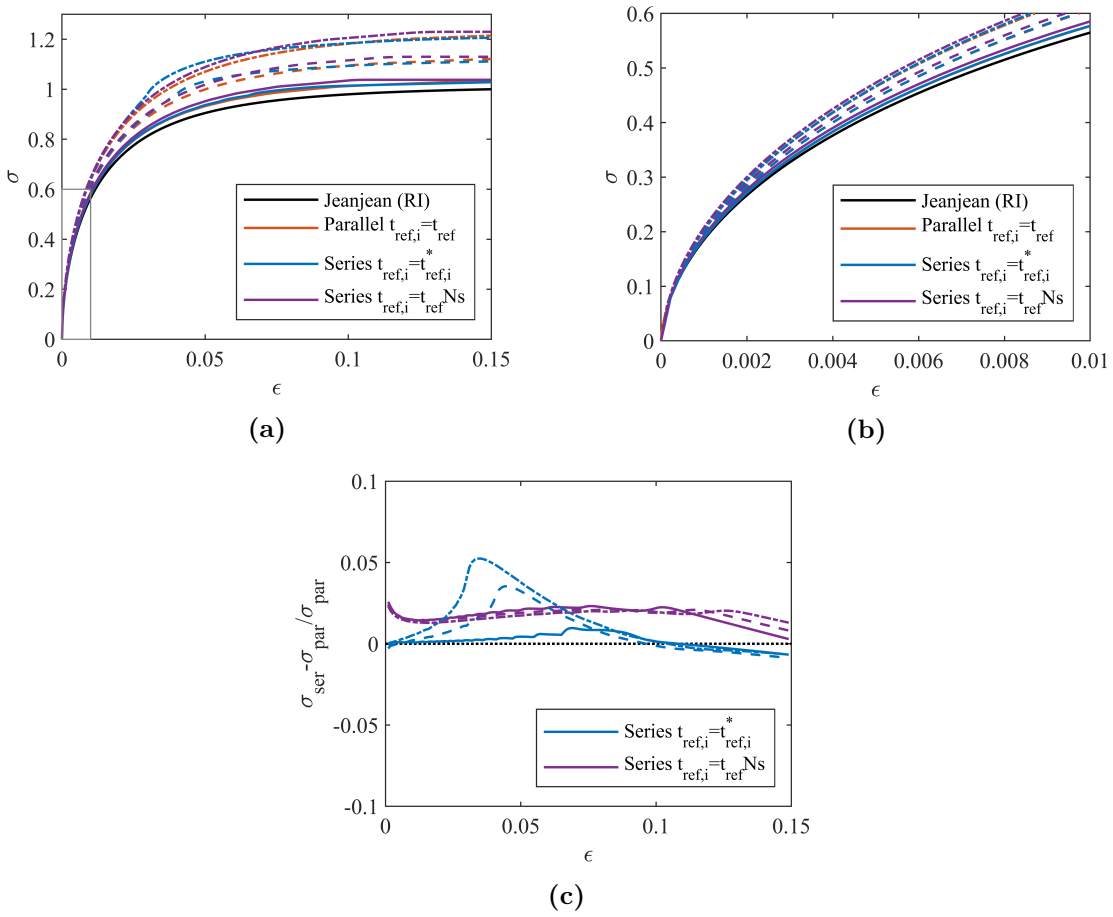

Figure 5.6: Series and parallel model (with rate process theory) computations of application of strain with constant strain rate. Rate independent backbone as per Figure 5.2a,$\eta_{10} = 0.1$, $t_{ref,G} = 1hr$. (—) $\dot{\varepsilon} = 0.1/t_{ref,G}$, (- -) $\dot{\varepsilon} = 10 * 0.1/t_{ref,G}$, (-·-) $\dot{\varepsilon} = 100 * 0.1/t_{ref,G}$. (a) and (b) computed response shown at two scales for clarity; (c) proportional difference between series and parallel predictions of stress with strain level

In Chapters 2 and 3 a more crude $t_{ref,i} = t_{ref,G}N_s$ was used to cater for the dependency of number of surfaces only.

Figure 5.6 shows RPT model computations of a monotonic application of strain at constant rate. The backbone parameters are calibrated as in Figure 5.2a with additional rate parameters $\eta_{10} = 0.1$, $t_{ref,G} = 1hr$. In the parallel model $t_{ref,i} = t_{ref,G}$, in the series both formulations discussed above are compared. As expected a 10% increase in strength is achieved per order of magnitude increase in strain rate. It is clear however that the three models do not agree.

$t^*_{ref,i}$ offers the better approximation and performs very well at low stresses. However, issues occur as the final yield surface is exceeded (where $E_{t,y} \approx 0$ and $H_{Ns} \approx 0$). $t^*_{ref,i} = t_{ref,G}\frac{H_i}{E_{t,y}}$ is then exceedingly large for all $i \neq Ns$. This causes unrealistically

high normalised strain rates, and therefore a 'kick' in the response which occurs at the yield of the final surface. The effect is greater with greater strain rates. Using $t_{ref,i} = t_{ref,G}N_s$ provides a more stable computation across all stress levels but does not agree with the parallel model.

In conclusion, it is not a trivial exercise to ensure that models based upon rate-process theory, in which dissipation is a function of local strain rate, are equivalent in series and parallel. Parallel models are better suited for rate-dependency because the strain rate of each active surface corresponds to the global plastic strain rate of the system, whereas in the series formulation plastic strain rates differ between surfaces and with magnitude of strain. If series models are to be used, the best option is to assign $t_{ref,i} = t_{ref,G}N_s$ as was done in previous chapters, this is stable with a similar response observed.

5.4 Softening

In Section 3.4.2.1, a model was proposed to reproduce the changes in secant stiffness due to repeated loading in element tests. Surface strengths are increased or decreased with a hardening parameter β_i, taken as the local plastic work as per Equation 5.4. By employing a switch parameter F_κ strength changes can be applied locally $F_\kappa = 1$, globally $F_\kappa = 0$, or as some ratio of the two $0 < F_\kappa < 1$:

$$\kappa_i = \frac{K_i}{K_{i,0}} = \kappa_{l,i}^{F_\kappa} \kappa_G^{1-F_\kappa} \tag{5.14}$$

$$\kappa_{l,i} = \left(1 + \frac{\beta_i}{\beta_{ref,i}} \left(\kappa_{ref}^{-\frac{1}{m_k}} - 1\right)\right)^{-m_k} \tag{5.15}$$

$$\kappa_G = \left(1 + \frac{\sum \beta_i}{\beta_{ref,G}} \left(\kappa_{ref}^{-\frac{1}{m_k}} - 1\right)\right)^{-m_k} \tag{5.16}$$

Since the exponents are negative, if $m_k > 0, \kappa < 1$ and softening occurs whilst if $m_k < 0, \kappa > 1$ and stiffening occurs. The former is typically the case in clays (e.g. element tests in Chapter 3) whilst the later is often observed in sand (e.g. in model pile tests by Richards, 2020).

With this formulation $\kappa_{l,i}$ develops as a function of local work β_i whilst κ_G develops with the global work $\Sigma\beta_i$. Figure 5.7 tracks β_i for two rate-independent models with

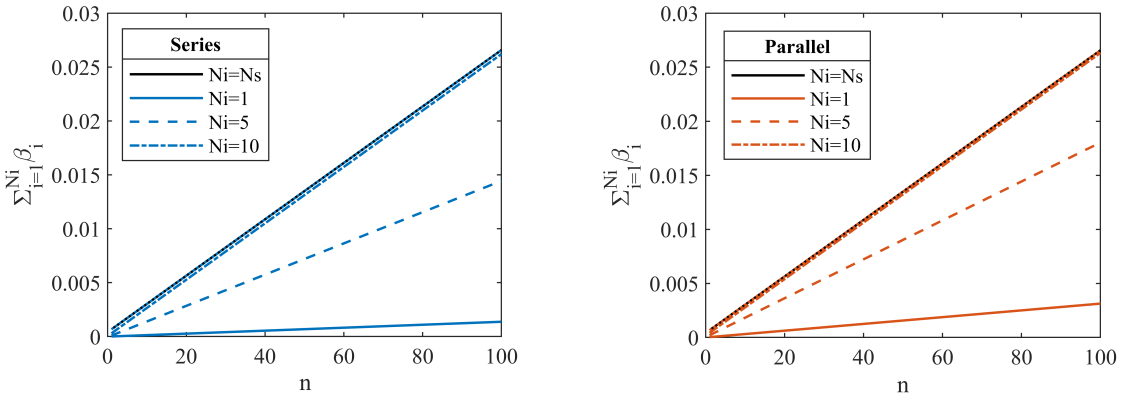

(a) **(b)**

Figure 5.7: Cumulative plastic work β_i rate-independent models with no strength changes (m_k) subject to 100 cycles of constant amplitude one-way loading $\sigma_{av} = \sigma_{cyc} = 0.25$. Models follow formulation and parameters as in Section 5.2 (a) series, (b) parallel

the same formulation and parameters as in Section 5.2, subject to 100 cycles of constant amplitude one-way loading $\sigma_{av} = \sigma_{cyc} = 0.25$. No strength changes are applied ($m_k = 0$), therefore work develops linearly with cycles. It is clear that whilst global work is equivalent in series and parallel configuration, local development differs. $\beta_{ref,i}$ should therefore be expected to differ.

Here, definitions are followed as per section 3.4.2.1:

$$\beta_{ref,i,ser} = F_{\beta,l,ser} K_i \frac{\sigma_u}{H_i} \tag{5.17}$$

$$\beta_{ref,i,par} = F_{\beta,l,par} K_i \varepsilon_u \tag{5.18}$$

where in the parallel model ε_u is an approximation of plastic strain expected with an application of σ_u, this is similar to σ_u/H_i in series. $\beta_{ref,G,par} = \beta_{ref,G,ser} = F_{\beta,G}\sigma_u\varepsilon_u$ is used, noting that $\sigma_u = \Sigma K_i$ in parallel and $\sigma_u = K_{Ns}$ in series. Broadly each aims to describe some measure of expected work on the surface or globally.

Figure 5.8 shows 100 cycles of constant amplitude $\sigma_{av} = \sigma_{cyc} = 0.25$ loading applied to similar rate-independent models, this time with softening activated. In all three models, $m_k = 0.1$, $\kappa_{ref} = 0.7$, $F_{\beta,G} = 1$. To ensure similar softening with cycles $F_{\beta l,par} = 2$ and $F_{\beta l,ser} = 14$. F_κ varies and controls the type of softening observed.

As expected the models are equivalent for global softening $F_\kappa = 0$, developing at the same rate and causing the same change to loop shape, additional ratcheting and post-cyclic softening.

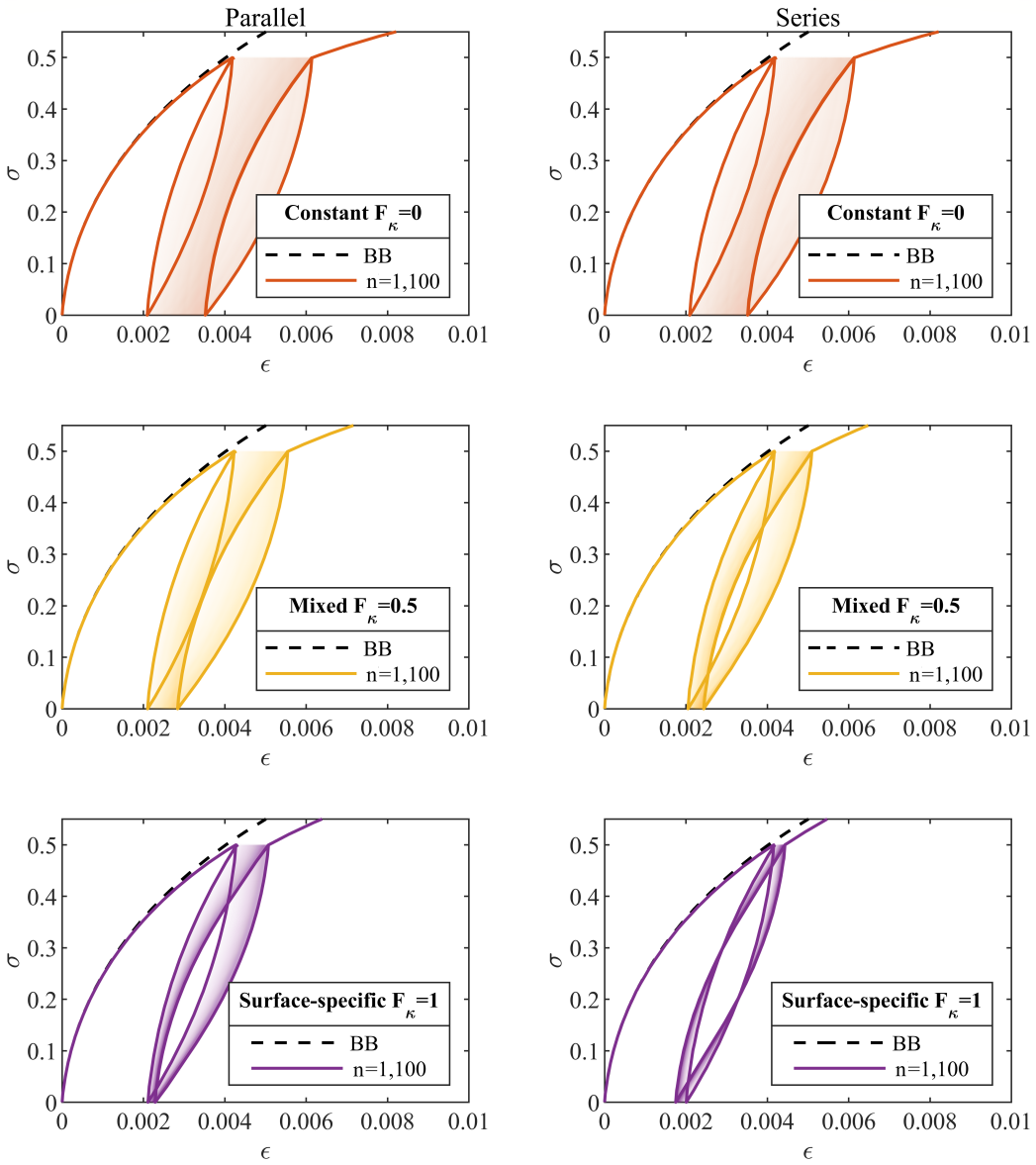

Figure 5.8: Softening model choice for a rate independent model with monotonic parameters similar to DRM OCR=1 and subject to 100 cycles of one-way loading. Left hand column – parallel model. Right hand column – series Model. $m_k = 0.1$, $\kappa_{ref} = 0.7$, $F_{\beta,G} = 1$, $F_{\beta l,par} = 2$,$F_{\beta l,ser} = 14$ and F_κ varies

However, the computed response differs when local softening is specified, $F_\kappa = 1$. As discussed in Section 3.4.2.1, when subject to constant stress amplitude cycles, series models in which yield is stress-dependent show no ratcheting or post-cyclic softening as the higher yield surfaces remain unaffected.

In parallel models, however, some limited ratcheting and post-cyclic softening develops as the higher yield stresses are gradually reduced (despite yield strains remaining fixed.

Qualitatively mixed softening in series appears similar to local softening in the parallel model. It may be possible to equate both by optimising F_κ (such that $F_{\kappa,ser} < F_{\kappa,par}$) but it is not obvious how this could be calculated analytically.

Ratcheting and post-cyclic strength reduction resulting from local softening are second order effects and are a product of fixed stress-amplitude testing. Whilst this is certainly the most common type of load applied for model calibration, fixed-strain amplitude tests or truly pseudo-random loading may also be prescribed.

With a fixed strain-amplitude these second order effects will differ. The higher surfaces will not be activated since in parallel, inactive yield strains remain the same; whilst in series, inactive yield strains increase. When subject to pseudo-random loads subtle changes are reduced as surfaces are activated and deactivated more regularly.

Finally, as described by Richards (2020), if local stiffening is required it is sensible to include some global stiffening $F_\kappa < 1$, not least to ensure that for fixed stress amplitude loads $K_i < K_{i+1}$. The risk of this occurring is reduced in the parallel model where for inactive surfaces the yield strain remains the same but yield stress is slightly increased. Simply, some post-cyclic stiffening occurs in parallel without applying a reduced F_κ.

In summary, local strength changes are not equivalent in the two models because of the variation of global work and subtle changes due to yield stress or yield strain control. In stress controlled tests, parallel models with local changes behave like series models with a small amount of global change. Perhaps this type of development is more logical; small amplitude loads largely affect the material which is being stressed most highly but has a small effect on the whole system.

These observations, however, do not provide evidence for the choice of one model or the other since the same behaviour can be achieved with an alteration of F_κ.

5.5 Ratcheting

Figures 5.9a and 5.9b show rate-independent HARM models, in which an additional ratcheting component is added in series with the underlying kinematic hardening models. These are described by energy and dissipation functions:

$$f_{par} = \sum_{i=1}^{Ns} \frac{H_i}{2}(\varepsilon - \alpha_i - \alpha_r)^2 + \frac{H_{Ns+1}}{2}(\varepsilon - \alpha_r)^2 \tag{5.19}$$

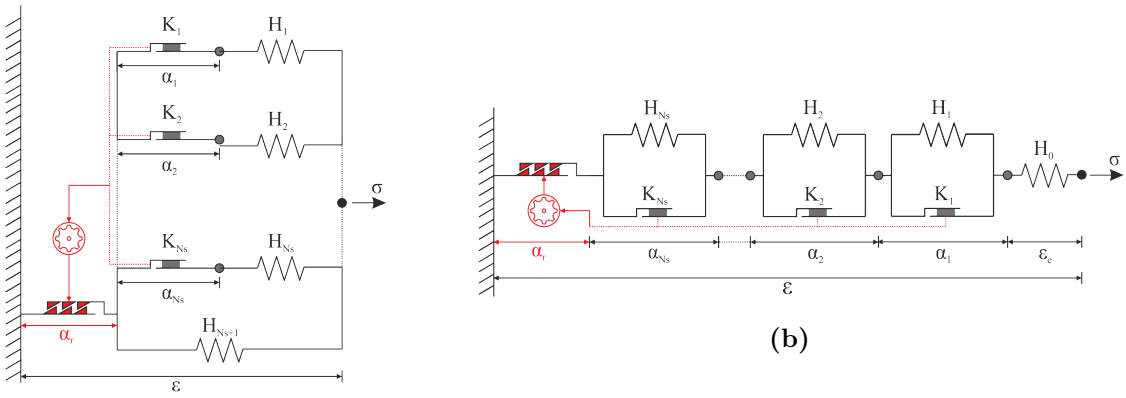

(a) (b)

Figure 5.9: Conceptual diagrams of rate-independent, multi-surface, kinematic hardening HARM models in (a) parallel configuration and (b) series configuration

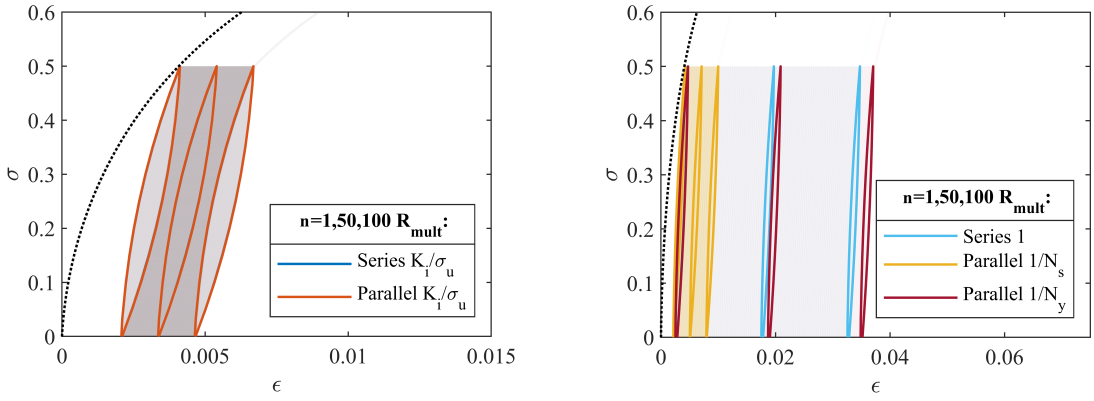

(a) (b)

Figure 5.10: Choice of ratcheting multiplier R_{mult} in series and parallel models. Rate independent model with monotonic parameters similar to Section 5.2 and $R_0 = 0.1$, subject to 100 cycles of one-way loading

$$f_{ser} = \frac{H_0}{2}\left(\varepsilon - \sum_{i=1}^{Ns}\alpha_i - \alpha_r\right)^2 + \sum_{i=1}^{Ns}\frac{H_i}{2}\alpha_i^2 \tag{5.20}$$

$$d = \left(\sum_{i=1}^{Ns} K_i|\dot{\alpha}_i|\right) + \sigma\dot{\alpha}_r \tag{5.21}$$

alongside a ratcheting constraint which can be re-written as:

$$\dot{\alpha}_r = S(\sigma)\sum_{i=1}^{Ns} R_i|\dot{\alpha}_i| \tag{5.22}$$

R_i controls the rate of ratcheting and as in Section 3.4.2.2 a modified power law is used:

$$R_i = R_{mult}.R_0\left(1 + \frac{\sum\beta_i}{\beta_{R,ref}}\left(\left(\frac{R_0}{R_{ref}\left(\frac{|\sigma|}{\sigma_u}\right)^{m_s}}\right)^{\frac{1}{m_r}} - 1\right)\right)^{-m_r} \tag{5.23}$$

such that the rate of ratcheting increases with stress level and reduces with global plastic work $\sum \beta_i$ which develops consistently in the series and parallel configurations (Figure 5.7). At a given stress level σ and assuming consistent parameters $\beta_{R,ref}, R_{ref}, m_s, m_r$, the term in outer brackets of Equation 5.23 will be the same in series and parallel (Termed C_R). For the purposes of this study Equation5.23 can then be reduced to:

$$R_i = R_{mult}.R_0.C_R \tag{5.24}$$

where, for simplicity $C_R = 1$. R_{mult} describes a multiplier which can be assigned to R_0. Section 3.4.2.2 and previously Richards (2020), use $R_{mult} = 1$ in conjunction with series models such that $R_i = R$ for all surfaces. This would result in considerably more ratcheting in the parallel equivalent since (with attention to Equation 5.22) the change in ratcheting strain is a product of the sum of the plastic strains $\sum_{i=1}^{Ns} |\dot{\alpha}_i|$. In parallel configurations this will increase with the number of active surfaces.

R_{mult} should, if possible, ensure parity between series and parallel models and for the latter ensure that behaviour does not vary with the choice of the number of surfaces. Abadie (2015) used $R_{mult} = \frac{K_i}{\sigma_u}$, making $\dot{\alpha}_r$ a function of the total incremental work. Secondarily, this causes less ratcheting on the lower surfaces, coupling with the stress-magnitude reduction (controlled by m_s).

Alternatively $R_{mult,ser} = 1$ could be used in conjunction with $R_{mult,par} = 1/N_s$ or $1/N_y$. Where N_y is the number of yielding surfaces, which can for instance be found by $N_y = \Sigma(|(S(\dot{\alpha}_i)|)$.

Figures 5.10a and 5.10b show 100 cycles of constant amplitude $\sigma_{av} = \sigma_{cyc} = 0.25$ loading applied to similar rate-independent models, based upon those presented in section 5.2. A constant ratcheting rate $R_0 = 0.1$ is used. It is clear that when $R_{mult} = \frac{K_i}{\sigma_u}$ the models agree exactly. If $R_{mult,ser} = 1$, the best equivalent is to use $R_{mult,par} = 1/N_y$ although this is not exact, $R_{mult,par} = 1/N_s$ computes much less ratcheting. The magnitude of strain differs between the two figures, such that choice of R_{mult} will impact the choice of other ratcheting parameters.

Figure 5.11 investigates the effect of number of surfaces for $N_s = 10, 40, 100$. When $N_s = 10$ the approximation of non-linearity becomes less accurate. Less work is predicted as the approximation linearises the curve (see Figure 3.9) and therefore less ratcheting is produced. The difference between $N_s = 40$ and $N_s = 100$ is removed

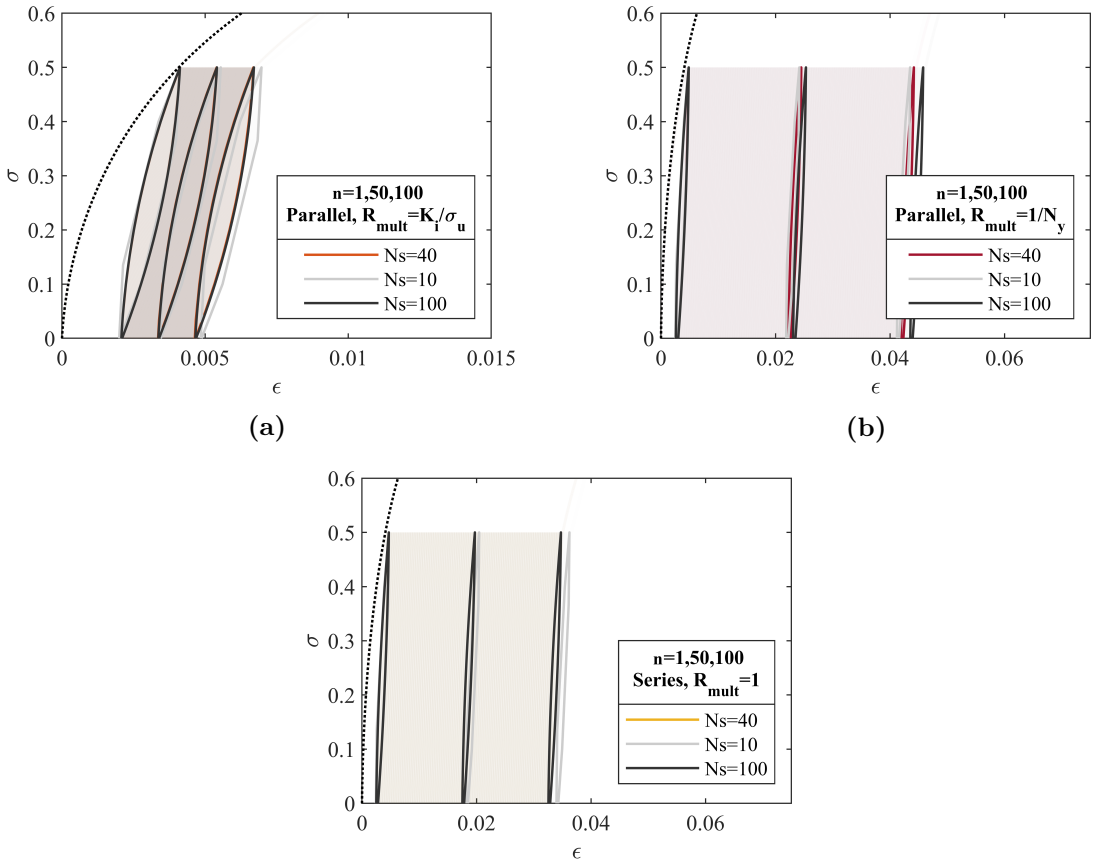

Figure 5.11: Effect of number of surfaces on ratcheting behaviour, with regards to choice of ratcheting multiplier R_{mult}. Rate independent model with monotonic parameters similar to Section 5.2 and $R_0 = 0.1$, subject to 100 cycles of one-way loading.

when $R_{mult,ser} = 1$ and $R_{mult,par} = \frac{K_i}{\sigma_u}$, and a slight disparity is observed for $R_{mult,par} = 1/N_y$.

In summary exact replication is observed if the factor $R_{mult} = \frac{K_i}{\sigma_u}$ is used, although $R_{mult,par} = 1/N_y$ serves as a good approximation of the the equation used in Richards (2020), where $R_{mult,ser} = 1$.

5.6 Summary

This chapter has appraised the equivalence and suitability of parallel and series models. Table 5.1 summarises the findings, highlighting where the models are identical (such as unidirectional rate independent models). Conclusions regarding models which develop with a hardening parameter β (e.g. stiffening or softening and ratcheting) have been limited to a work-based parameter. If a strain-based parameter were

Table 5.1: Equivalence of Series and Parallel Models for differing dimensionality and complexity

Mechanism	Model	Equivalence	Reference	Comments
Rate Independent	1Dir	✓	Figure 5.2a and (Beuckelaers, 2017)	Model computes identical response with suitably calibrated (and differing) local K_i and H_i.
	1Dir Assym.	✓	Figure 5.3c	Identical response. Local asymmetry factor $A_{f,i}$ may differ unless a constant global factor is used.
	2Dir	×	(Richards, 2020; Beuckelaers et al., 2018)	Bi-directional (σ_x, σ_y) models do not agree. As yet unable to select between the models on the basis of experimental data.
Rate Dependent	RPT	×	Figure 5.6	Local strain rate $\dot{\alpha}_i$ differs in series and parallel, therefore response is not equivalent. **Parallel models are better suited** since $\dot{\alpha}_i = \dot{\varepsilon}$. A close, stable, estimate is achieved using $t_{ref,ser,i} = t_{ref,G}.N_s$ and $t_{ref,par,i} = t_{ref,G}$.
Stiffening/ Softening	Global	✓	Figure 5.8	Development of global plastic work is equivalent, as are implication of global strength changes.
	Local	×	Figure 5.8 and 5.5b	Development of local plastic work differs. Parallel models with local changes behave like series models with a small amount of combined global change, such that model similarity is found with $F_{kappa,ser} < F_{kappa,par}$. No clear preference.
Ratcheting	Global	✓	Figure 5.10 and 5.11	Development of ratcheting with global work is comparable, although caution is needed with initial parameter choice. Here a multiplier is specified such that $R_{mult} = \frac{K_i}{\sigma_u}$ ensures equivalence or $R_{mult,par} = 1/N_y$ serves as an a good approximation of $R_{mult,ser} = 1$.

chosen, equivalence would not be met for global or local models.

Where rate-dependency is implemented following rate process theory (as in Section 3.3.2), parallel models are better defined due to a consistent strain rate on each surface. The two models are, however, close if $t_{ref,ser,i} = t_{ref,G}.N_s$ is used. Global softening and ratcheting are equivalent, although care must be given in parameter specification for the latter. Surface specific softening is not identical but the behaviour is similar provided differing choice of the switch parameter F_κ.

Rarely do the differences between the models present enough variability to establish a preferred option (Richards, 2020), and instead a choice must be made. Parallel models are better suited to rate-dependency because the strain rate of each active surface corresponds to the global plastic strain rate of the system, whereas in the series formulation plastic strain rates differ between surfaces and with magnitude of strain.

The two produce identical responses for a single direction kinematic-hardening model (Beuckelaers, 2017) and for cyclic effects which develop with global work (Abadie, 2015). However, under multi-directional loading the models produce slightly different responses (Beuckelaers et al., 2018; Richards et al., 2020). The introduction of rate-dependency and a variation on a softening-type model were also found to develop a difference in response.

Chapter 6

Development of 1D models for pile tests

6.1 Introduction

In Chapters 3 to 4, hyperplasticity models were employed to compute the response of clay samples due to repeated loading at an element scale. In this chapter, behaviour of laterally loaded monopiles is considered.

In doing so, the interaction between the pile and the ground must be modelled. Similar constitutive models may be used but implemented at various scales: 0D macro elements (Abadie, 2015; Richards, 2020), 1D Winkler-type models (Beuckelaers, 2017) or as continuum, tensorial models, in 3D FEA (Houlsby et al., 2017). The three are indicatively drawn in Figure 6.1 and represent increasing complexity and computational effort from left to right. In this Chapter macro and 1D models are used.

In pile-scale macro models the conjugate stress σ and strain ε variables represent either applied load H or moment M and a corresponding displacement u or rotation θ. In 1D models the pile is represented as a series of nodes and Gauss points, which supplements computation of pile head movement with useful information of the response down the pile. Importantly, changes to the pile dimensions do not necessitate change of calibrated soil parameters and this approach is therefore considered a more useful design tool.

The ultimate aim of this chapter is to investigate if parameters calibrated at element scale may be used at pile scale. Clearly the mechanisms of soil behaviour differ at the two scales and direct scaling of the response (such as that presented by

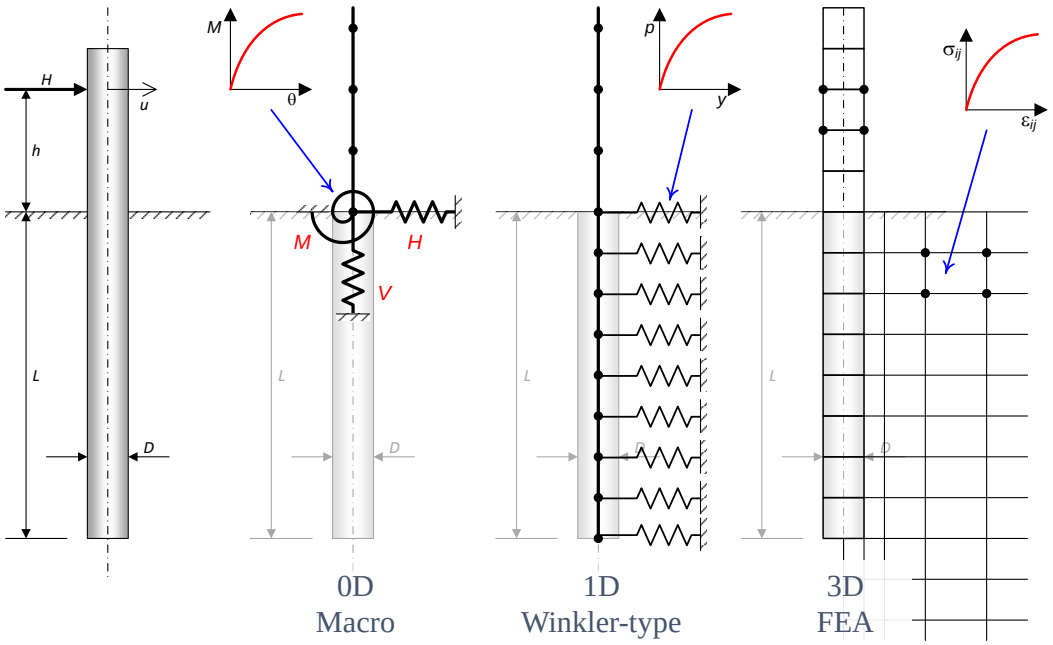

Figure 6.1: Idealised monopile (left) with possible scales of monopile foundation modelling in increasing complexity and computational cost from 0D to 3D (right). Example non-linear monotonic behaviour also shown in terms of respective stress and strain-type quantities. Figure edited from Houlsby (2020a)

Zhang and Andersen, 2017) may be over simplified. Instead this work makes use of the fact that hyperplasticity models necessarily build upon a calibrated monotonic backbone (such as those in Section 3.2). These are augmented with mechanisms which capture rate and cyclic effects and depend upon the internal variables of the backbone in terms of units, magnitude and therefore local mechanisms.

Importantly calibration of the monotonic response at continuum, p-y (or other PISA-style soil reactions) or macro level can be undertaken separately from cyclic calibration. For example, at the 1-D level, the PISA rule-based, numerical or data-based methods (Suryasentana et al., 2020) in which FEA analyses are used to derive the non-linear curves can be used. For a given pile the same can be done at macro level, deriving H-v or M-θ from 3D or 1D computations.

It is the working assumption that the rate-dependent and cyclic mechanisms and parameters presented in Sections 3.3 and 3.4 may then be used at any of the scales above, such that soil response to cycles in element tests are representative of cycles at system level. These parameters are suitably normalised such that each represents a proportional change to the monotonic response. There is some reason to believe

this may work: Beuckelaers (2017) showed that similar cyclic parameters used at macro (in Abadie, 2015) and PISA-type 1D level produced a similar response; whilst Chapter 4 showed that similar parameters could be used for both CU and DSS tests. Mapping of hyperplasticity models between element and pile has not, however, been done before.

This equivalence is tested for the Cowden data-set by using a PISA-type 1D model (OxPile) extended to include parallel hyperplasticity models (described in Section 6.4.1). The monotonic backbone is calibrated as per the PISA method, but the cyclic parameters are initially those calibrated to Cowden element tests in Section 6.2. Differences are discussed and reasons explained.

6.2 Calibration of model to Cowden laboratory tests

Non-dimensional rate and cyclic parameters are calibrated to undrained triaxial tests from the Cowden data-set presented in Chapter 2. Techniques follow those in Chapter 2 but applied to a parallel model as described in Chapter 3.

Multiple linearly hardening yield surfaces of varying stiffness H_i and yield strengths K_i are selected to reproduce a hyperbolic tangent 'Jeanjean' curve (as in Equation 3.7) fit to an anisotropically consolidated compression $CAUc$ test with initial conditions $p_0 = 67$kPa and $q_0 = -25$kPa. Local asymmetry factors $A_{f,i}$ are optimised to best fit a similarly consolidated extension $CAUe$ test as shown in Figure 6.2a.

Rate dependency is captured following rate process theory such that a viscous constant η_{10} and reference time $t_{ref,G}$ must be calibrated. This is achieved with tests of differing strain rate; the 'slow' CU tests and the initial quarter cycles of the faster CU_{cyc} tests (Figure 6.2a) as well as an isotropically consolidated compression test with stress applied at multiple rates (Figure 6.2b). $t_{ref,G} = 10^4 \text{hr}^{-1}$ is taken following data presented in Section 3.3.1, which corresponds to a test time to failure above which rate effects would be negligible. η_{10} is optimised and the backbone strength $s_{u,c,0}$ and curvature parameters a_0 recalibrated such that surface properties correspond to a test of time $t_u >> t_{ref}$.

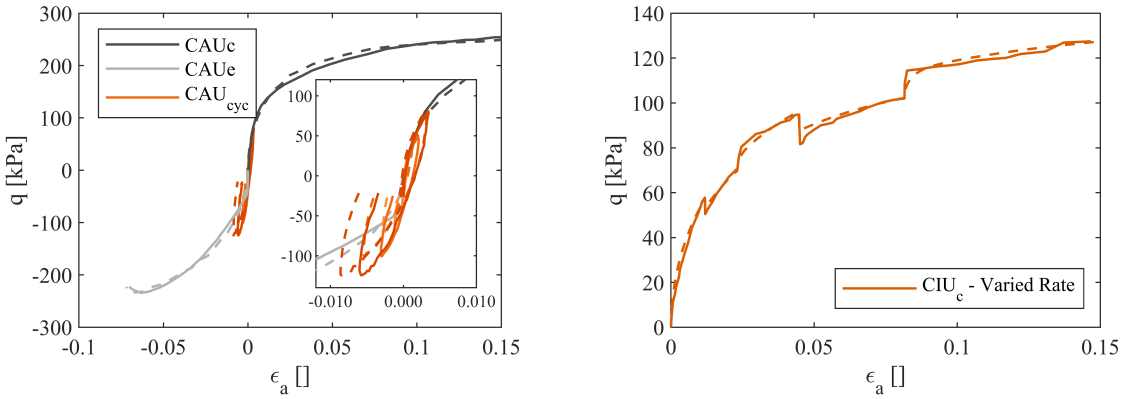

Figure 6.2: Calibration of model (dashed lines) to Cowden element test data (solid lines) (a) Monotonic and rate-dependent calibration to $CAUc$, $CAUe$ and initial cycles of CAU_{cyc} tests (plotted at two scales for clarity) and (b) Varied rate CIU_c test

Cyclic parameters are calibrated against 7 tests within the Cowden data-set, with stress conditions shown in figure 6.3a (filled markers). Figures 6.3b and 6.3c show the development of average and cyclic strain with number of cycles. This is captured by reducing the strength of each surface as a function of an incremental, surface dependent, hardening parameter β_i, here taken as local plastic work. The option to locally soften the active surfaces or soften all surfaces equally is left open with the switch parameter F_κ (Equation 5.14) and strength changes develop with power laws as described by Equations 5.15 and 5.16.

No additional ratcheting element is prescribed here; instead it is found that average and cyclic strain can be adequately captured using surface specific softening only ($F_\kappa = 1$). As noted in Section 5.4, local softening still results in some reduction in ultimate strength and therefore ratcheting. This model choice also reproduces the hysteresis loop shape (Figures 6.3d and 6.3e) well. Required parameters follow Section 5.4, such that $\kappa_{ref} = 0.7$ is fixed and m_k and $F_{\beta,l}$ chosen as a best fit. Table 6.1 summarises all calibrated parameters.

Table 6.1: Summary of calibrated Cowden CU conditions and model parameters

p_0 $[kPa]$	q_0 $[kPa]$	$\dot{\varepsilon}_{BB}$ $[hr^{-}1]$	$s_{u,c}$ $(s_{u,e})$ $[kPa]$	$\frac{E_0}{2s_{u,c}}$	$\varepsilon_{u,c}$ $(\varepsilon_{u,e})$	Af_{Ns}	η_{10}	$t_{ref,G}$	$s_{u,c,0}$ $[kPa]$	a_0	κ_{ref}	m_k	F_κ	$F_{\beta,l}$
67	-25	0.002	125 (118)	1000	0.15 (0.07)	0.94	0.1	10^4	116	2.36	0.7	0.1	1	20

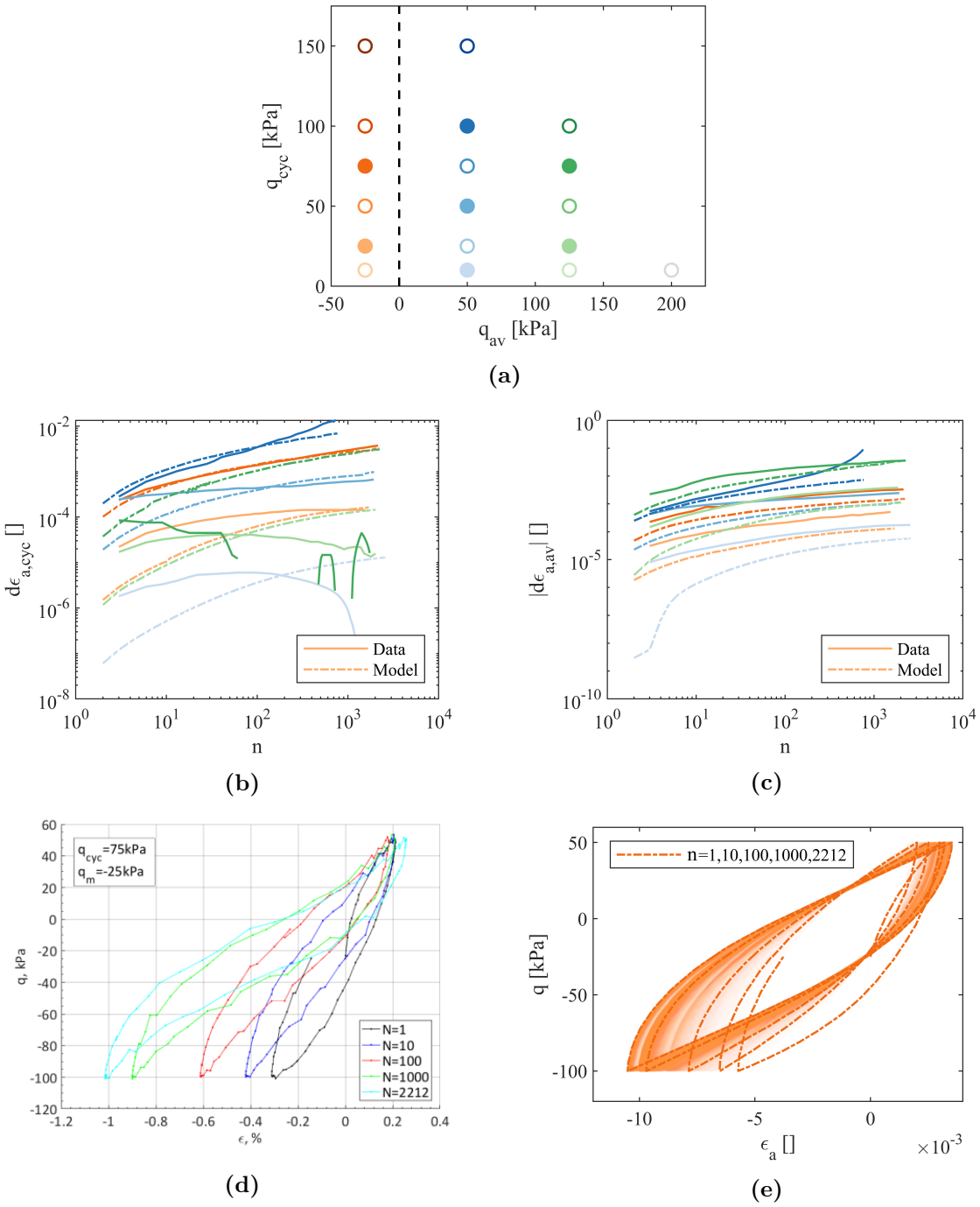

Figure 6.3: Cyclic calibration of model to Cowden element test data (a) interaction diagram showing location of CU_{cyc} tests, filled markers indicate those used for calibration (b) Change in cyclic strain against cycle number (c) Change in average strain against cycle number (d) Example measured hysteresis loops, plot taken from Ushev (2017) (e) Modelled hysteresis loops corresponding to (d)

6.3 Database of pile tests at Cowden

Whilst many authors and institutions have undertaken laterally loaded pile tests in clays in the lab, centrifuge or in the field (as outlined in Section 1.3.3), the most complete data set at scale is that of the PISA test program undertaken at Cowden (Byrne et al., 2017; PISA Academic Work Group, 2016b; PISA Academic Work Group, 2016a). Importantly, the element test program presented in Section 6.2 used material taken from the same site and therefore offers a direct comparison.

The main focus of the PISA work was to study the monotonic response of laterally loaded monopiles at low L/D ratios typically found for offshore wind turbines. Preliminary varied-rate and cyclic tests were also undertaken with a further testing program planned as part of the ongoing PICASO project (Byrne et al., 2020). In this chapter, five of the PISA tests are chosen, all with a common $L/D = 5.2$ ratio, as presented in Table 6.2. More information on the tests undertaken and investigation of the effects of various other aspects can be found in Byrne et al. (2019a) and companion papers.

Figure 6.4a shows the monotonic tests CM9 and CM1. In test CM9 loads were incrementally applied and then held until the displacement exceeded $u_{0.1D} = 76.2$mm, before unloading completely. The test ran for $T_u = 354$minutes prior to unloading at which point the pile had displaced $u = 99$mm such that the curve which passes through all load hold points can be estimated to be at a rate of $\dot{u} \approx 0.28$mm/min. $H_{0.1D} = 115$kN is taken as a reference failure load going forward and the initial stiffness of the pile $E_0 = 20$kN/mm.

In test CM1 loads were applied in a similar manner until 50kN after which the pile was initially displaced until failure at either fast $\dot{u} \approx 430$mm/min or slow $\dot{u} \approx 1.65$mm/min rates. Indicative continuous curves at each rate are shown increasing

Table 6.2: Properties of medium-scale laterally loaded piles at Cowden with common diameter and L/D ratio of 5.2

Pile Name	L [m]	D [m]	h [m]	t [mm]	Loading
CM9	4	0.762	10	11	Monotonic push to failure with load-holds
CM1	4	0.762	10	11	Monotonic push to failure at multiple rates
CM5	4	0.762	10	11	Packets of one-way (and over one-way) loads $n > 10000$
CM6	4	0.762	10	11	Packets of one-way loads $n = 55$
CM7	4	0.762	10	11	Packets of two-way loads $n > 1000$

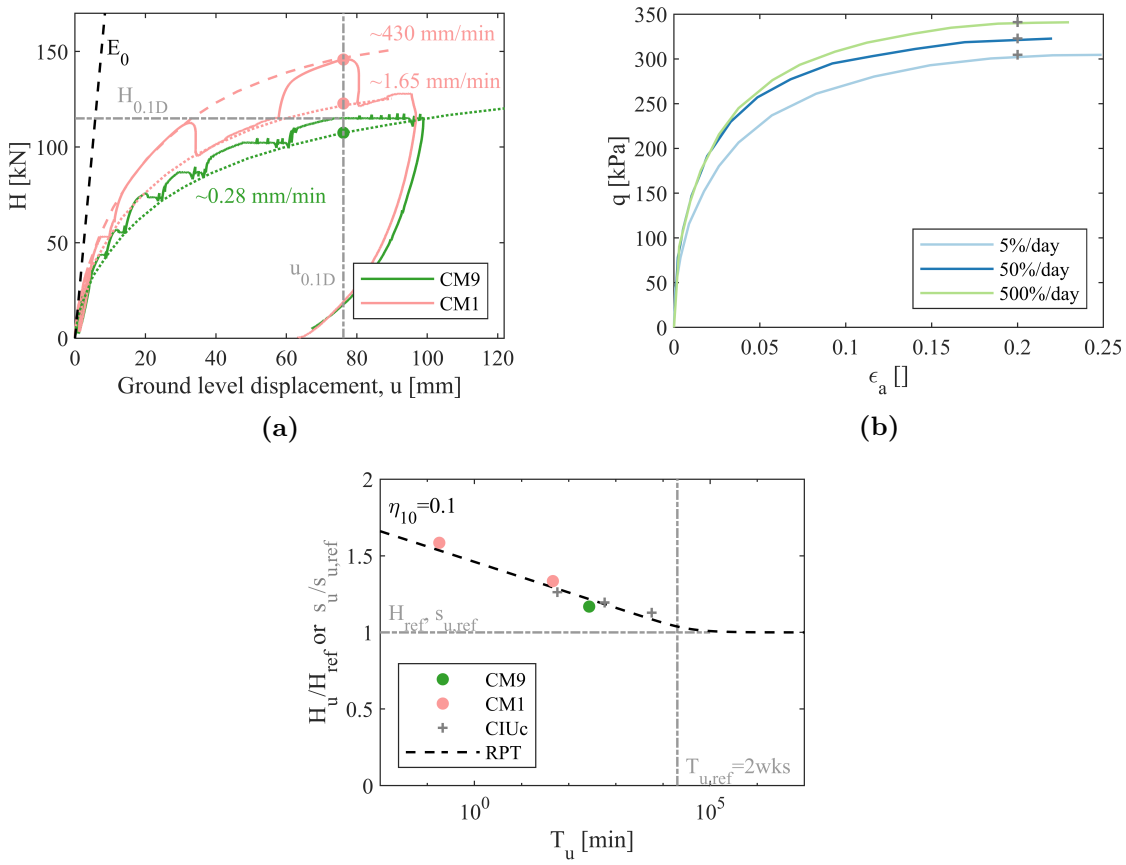

Figure 6.4: (a) Monotonic tests CM9 and CM1 (b) Undrained triaxial compression tests after Ushev, 2017 (c) Ultimate horizontal load and undrained shear strength against test time to failure alongside inverse hyperbolic sine fit (RPT)

in strength with a faster rate. The test is similar to that undertaken in triaxial conditions by Ushev and plotted in Figure 6.2b.

Figure 6.4b shows three isotropically consolidated triaxial tests $CIUc$ tests at differing strain rates from the COW data set (Ushev, 2017) with approximate $s_{u,c}$, taken at maximum deviatoric stress, indicated. These are plotted alongside lateral loads at $u_{0.1D}$ at respective test times to failure T_u in Figure 6.4c. Both are normalised by either $H_{ref} = 92$kN or $s_{u,ref} = 135$kPa. A hyperbolic sine relationship similar to Equation 3.19 is also plotted in which a consistent logarithmic increase with reducing test time is seen, boding well for a link between the two.

The cyclic loading characteristics of tests CM5, CM6 and CM7 are plotted in an interaction diagram in Figure 6.5 normalised by $H_{0.1D} = 115$kN and alongside the numbers of cycles applied. The Cowden $CUcyc$ cyclic triaxial testing program as

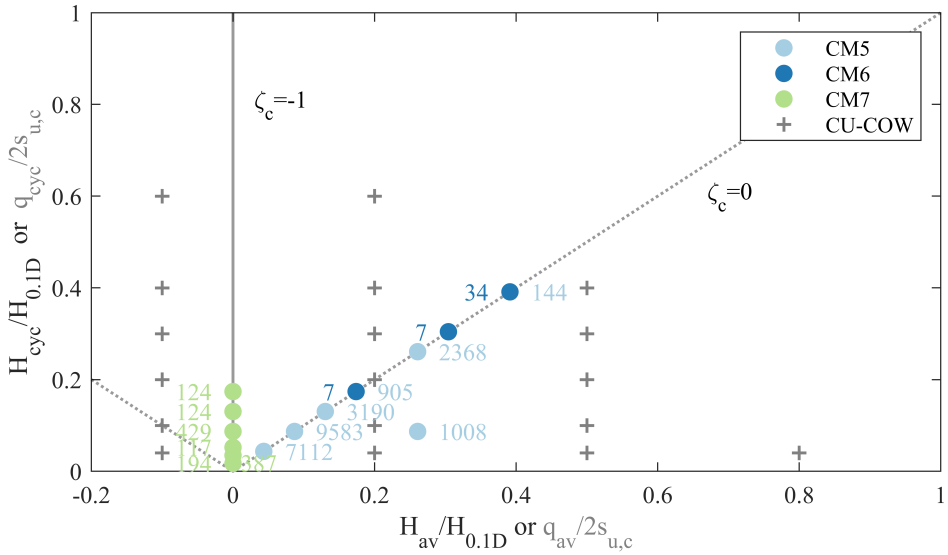

Figure 6.5: Location of PISA cyclic pile tests at Cowden

reported by Ushev (2017) is also plotted. The focus of the pile testing program was on one-way ($\zeta_c = 0$) and two-way ($\zeta_b = -1$) loading, whilst the element tests follow fixed average and cyclic stresses.

Figures 6.6 to 6.8 show each test in more detail. From time-histories of H and ground level displacement u, packets are identified and analysed in the same manner as Section 3.4.1. Accumulation of displacement, secant stiffness and energy loss factor are identified and plotted against respective cycle number in each packet. Power-laws are fitted following Equations 3.28,3.26 and 3.27.

In test CM5, three packets of one-way loading are applied in increasing magnitude before returning to smaller loads and ramping up again. The packets in grey between $3.5 - 4 * 10^5$s were not of constant amplitude and cyclic response is therefore not analysed. In test CM7 only the first 6 packets of consistent cycles are analysed.

Figure 6.9a shows cyclic secant stiffness k_f against load amplitude H_{cyc} for each packet. Only the first and final cycles are plotted with an arrow indicating increasing cycles. A continuous estimate of secant stiffness with load magnitude is also plotted for the idealised constant-rate approximations of monotonic tests CM9 and CM1 as shown in 6.4a. This assumes Masing rules such that at:

$$H_{cyc} = H \quad \rightarrow \quad k_f = H/v \tag{6.1}$$

The majority of packets follow the CM9 curve, although some CM5 packets at $H_{cyc} = 10, 15$ and 20kN are much softer (shown filled). These packets are applied after a much greater maximum load, hence some considerable changes to soil behaviour (e.g. local degradation, gapping) have already occurred due to load history. These particular packets remain outliers in Figure 6.9b where softening exponent is plotted against ζ_b. The positive exponent indicates stiffening, whilst the majority of the sets show softening.

Figure 6.9c shows energy loss factor exponent plotted against softening exponent. An inverse correlation is observed as in the element tests in Figure 3.31c. In Figure 6.9d ratcheting exponent is shown. In test CM5 this mostly increases with ζ_b although in CM6 consistent value is observed for all packets. Again the load packets in CM5 which happened after a previous maximum show greatly reduced rate.

Figure 6.9e shows the the monotonic tests CM9 and CM1 alongside a similar monotonic load applied to approximately $H_{0.1D}$ after cyclic test CM6, hence the displacement begins at approximately $1.5u_{0.1D}$. During load increase the post-cyclic response is initially much softer with a shape indicative of gapping. As the load increases this returns to behaviour similar to CM1 and CM9 but offset by the accumulated cyclic displacement. The displacement rate is, however, higher than the slow CM1 curve, possibly evidence of some limited post-cyclic softening.

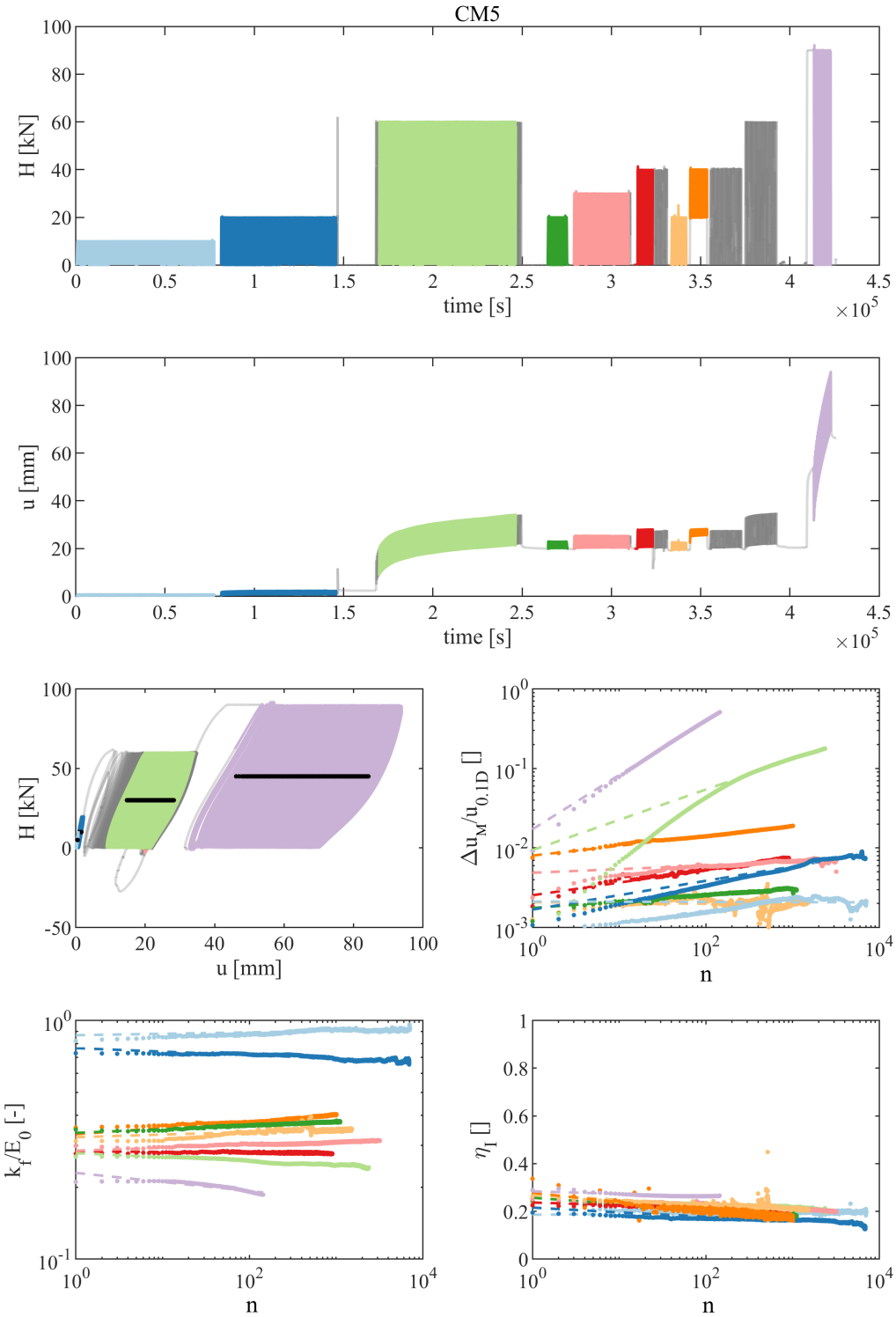

Figure 6.6: Cyclic response of test CM5 - Loads between 3.5 and 4x10^5*s* are not single amplitude packets but repetitions of three load magnitudes. Black dots in H-u plot correspond to average displacement and load at each cycle ($u_{M,n}, H_{M,n}$).

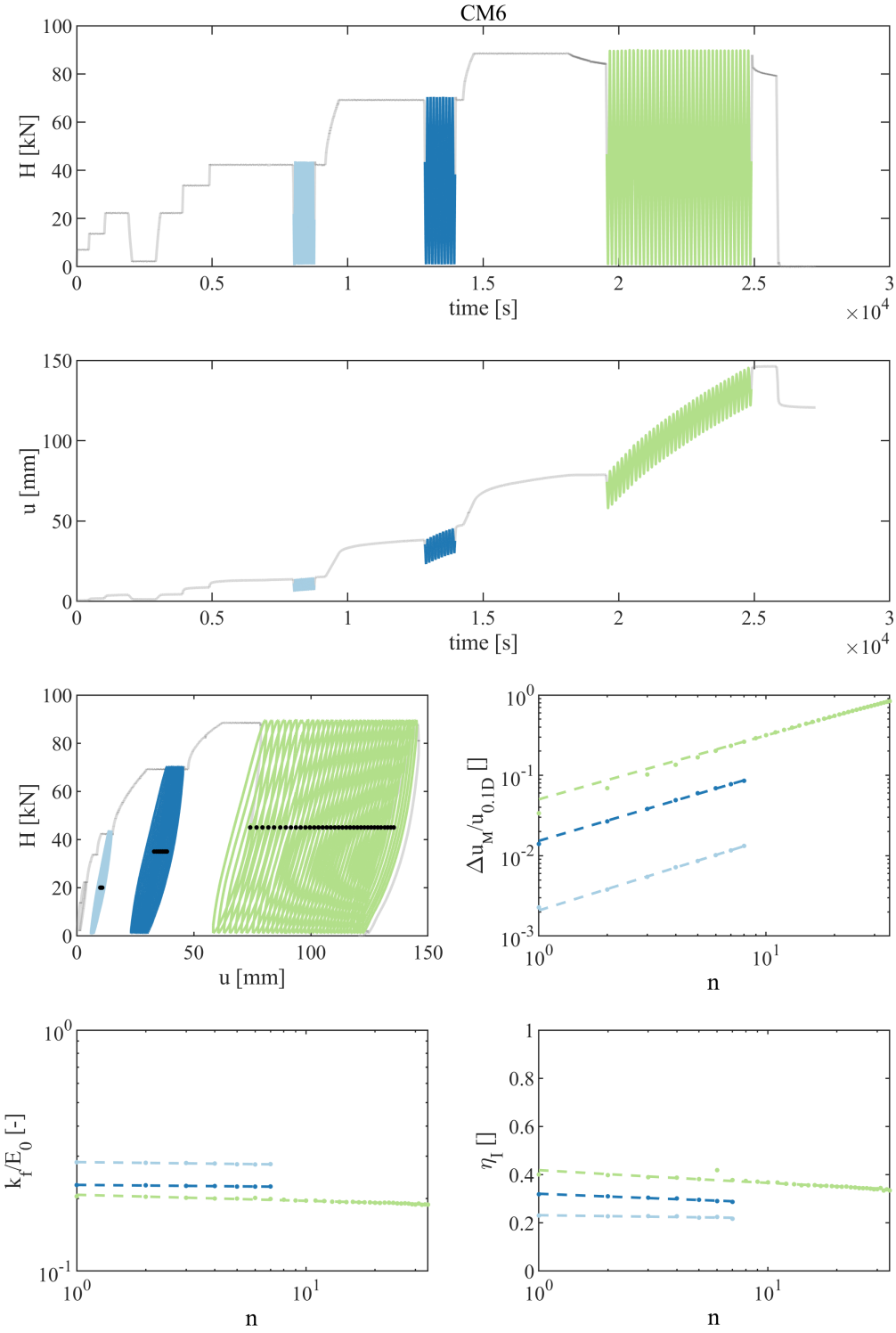

Figure 6.7: Cyclic response of test CM6. Black dots in H-u plot correspond to average displacement and load at each cycle $(u_{M,n}, H_{M,n})$.

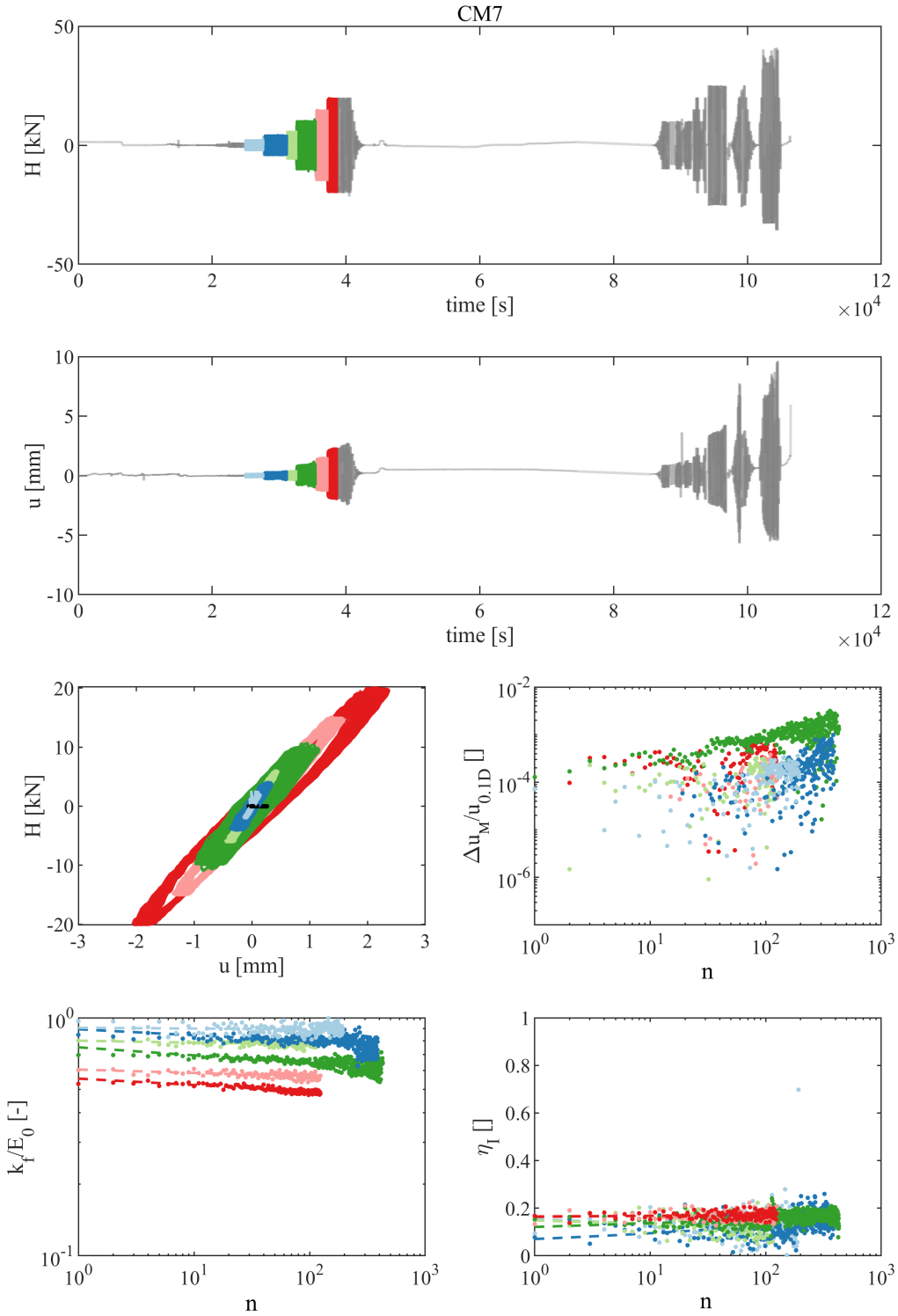

Figure 6.8: Cyclic response of test CM7 - Only the first 6 packets used in further analysis. Black dots in H-u plot correspond to average displacement and load at each cycle $(u_{M,n}, H_{M,n})$.

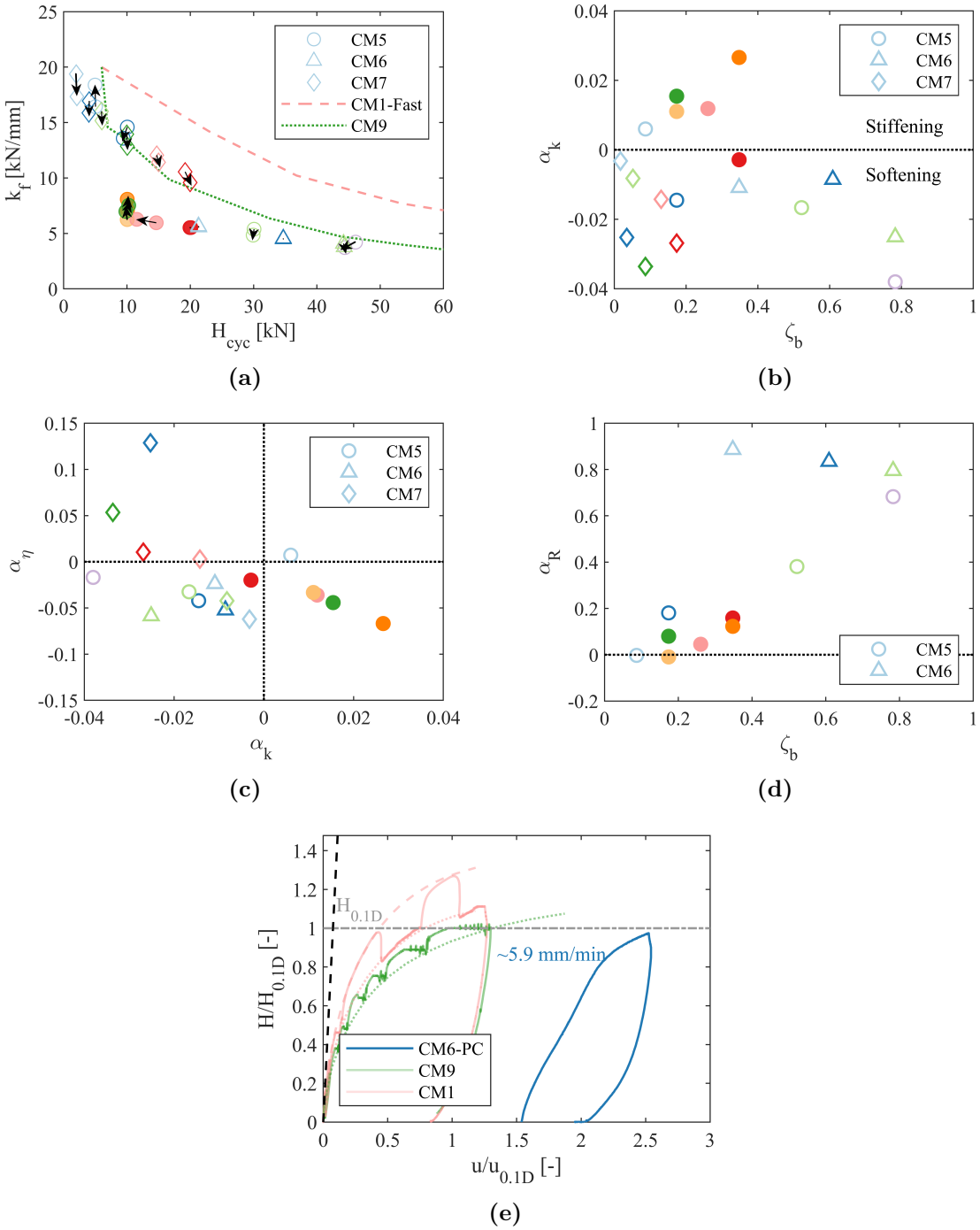

Figure 6.9: (a) Cyclic secant stiffness against amplitude for first and final cycle of each load packet, the arrow indicates direction of cycles. Secant stiffness against half-load is also plotted for monotonic tests CM9 and CM1.(b) Secant stiffness change exponent plotted against ζ_b, solid markers indicates tests which do not exceed the previous maximum (c) Energy loss exponent against secant stiffness exponent (d) Ratcheting exponent against ζ_b (e) Monotonic test to failure after cyclic test CM6 plotted alongside the tests in Figure 6.4a

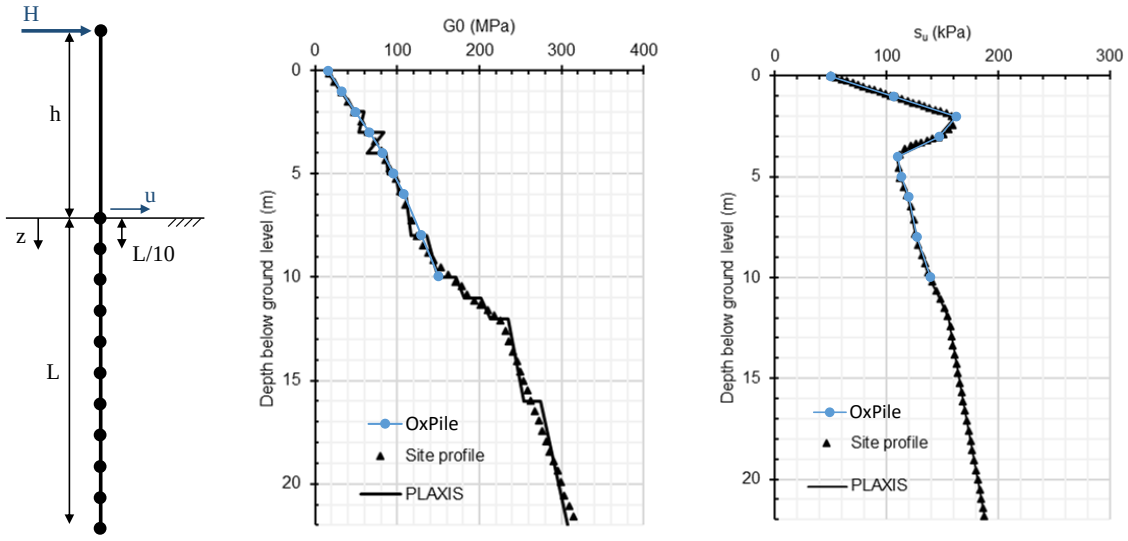

(a) **(b)** **(c)**

Figure 6.10: (a) 1D Model structure (b) G_0 variation with depth (c) s_u variation with depth (edited from Minga and Burd, 2019)

6.4 Calibration and prediction of PISA Cowden tests

In this section the extended version of the 1D Finite Element (FE) model 'OxPile' outlined in Section 6.4.1 is used to predict the pile tests at Cowden presented in Section 6.3. This includes five medium scale pile tests with consistent pile dimensions $L = 4$m, $h = 10$m, $D = 0.762$m, $t = 11$mm as outlined in Table 6.2. The 1D FE model of the pile uses 10 elements below ground level, Figure 6.10a. Throughout this section the idealised soil profiles of G_0 and s_u shown in Figures 6.10b and 6.10c are used and horizontal load H is applied to the node at h. Unless otherwise specified ground level displacement u is used as comparison. Calibration is discussed progressively in terms of extended mechanisms.

6.4.1 Extension of OxPile

OxPile is a suite of MATLAB functions which describe the PISA design model for computing the response of a monopile subject to lateral loading. This is formulated in a 1D FE framework in which the pile is represented as a line of Timoshenko beam elements. The soil is also modelled as a set of finite elements, such that each embedded

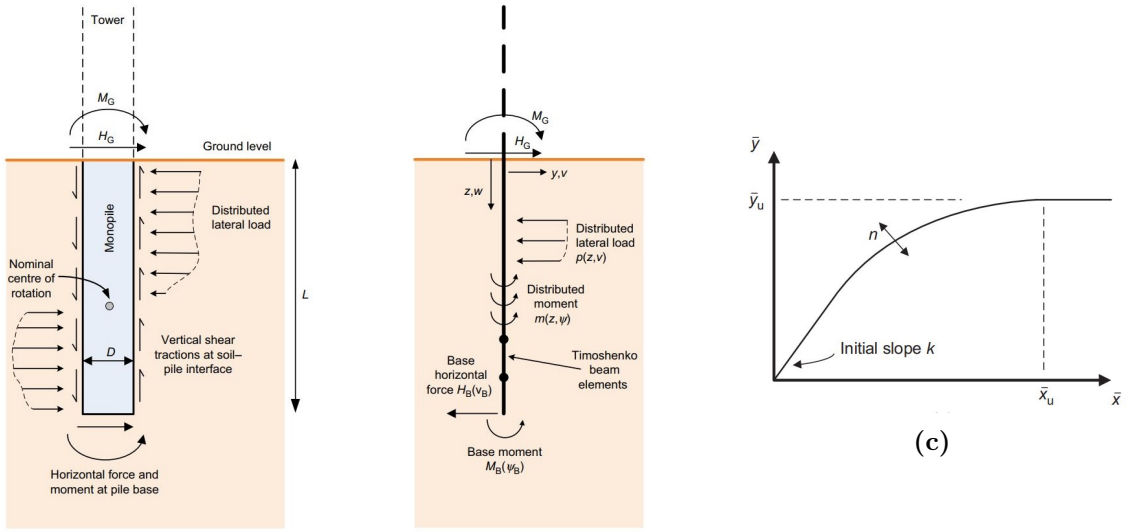

Figure 6.11: PISA design model after Byrne et al. (2019b) (a) Soil reaction components (b) PISA 1D FE model as employed in OxPile (c) Generic PISA soil reaction curve

pile element has an associated soil element at each of its nodes. This shares the same displacement and rotation along the length of each element.

In the PISA method four soil reaction components are assumed to act on the pile as shown in Figure 6.11. These are: distributed lateral loads (similar to the p-y method); distributed moment (arising from shear tractions due to vertical displacement of the pile and of soil wedges near the mudline); base shear and base moment. In the model, each is related to the local lateral displacement or rotation by calibrated four-parameter non-linear functions termed 'soil reaction curves' (Figure 6.11c). The method therefore follows a 'Winkler' assumption, such that reactions depend solely on local behaviour and does not represent any spacial coupling in the soil.

Soil reactions are integrated using four Gauss points per element. Internal $\boldsymbol{F_{int}}$ and external force vectors $\boldsymbol{F_{ext}}$ are computed at each Gauss point and solved for equilibrium using a Newton-Raphson procedure. Figure 6.12a (left hand side) shows an indicative flow chart of operation. Loads ($\boldsymbol{F_{ext}}$) are applied incrementally and displacements estimated using stiffness matrix $\boldsymbol{D}$. This is conventionally taken as the tangent stiffness at the current displacement (shown indicatively for single Gauss point in 6.12b) , calculated at each interation. The soil stiffness terms are easily evaluated for each reaction by deriving the gradient of the local soil reaction curve. The convergence criterion uses a normalised residual of the unbalanced forces divided

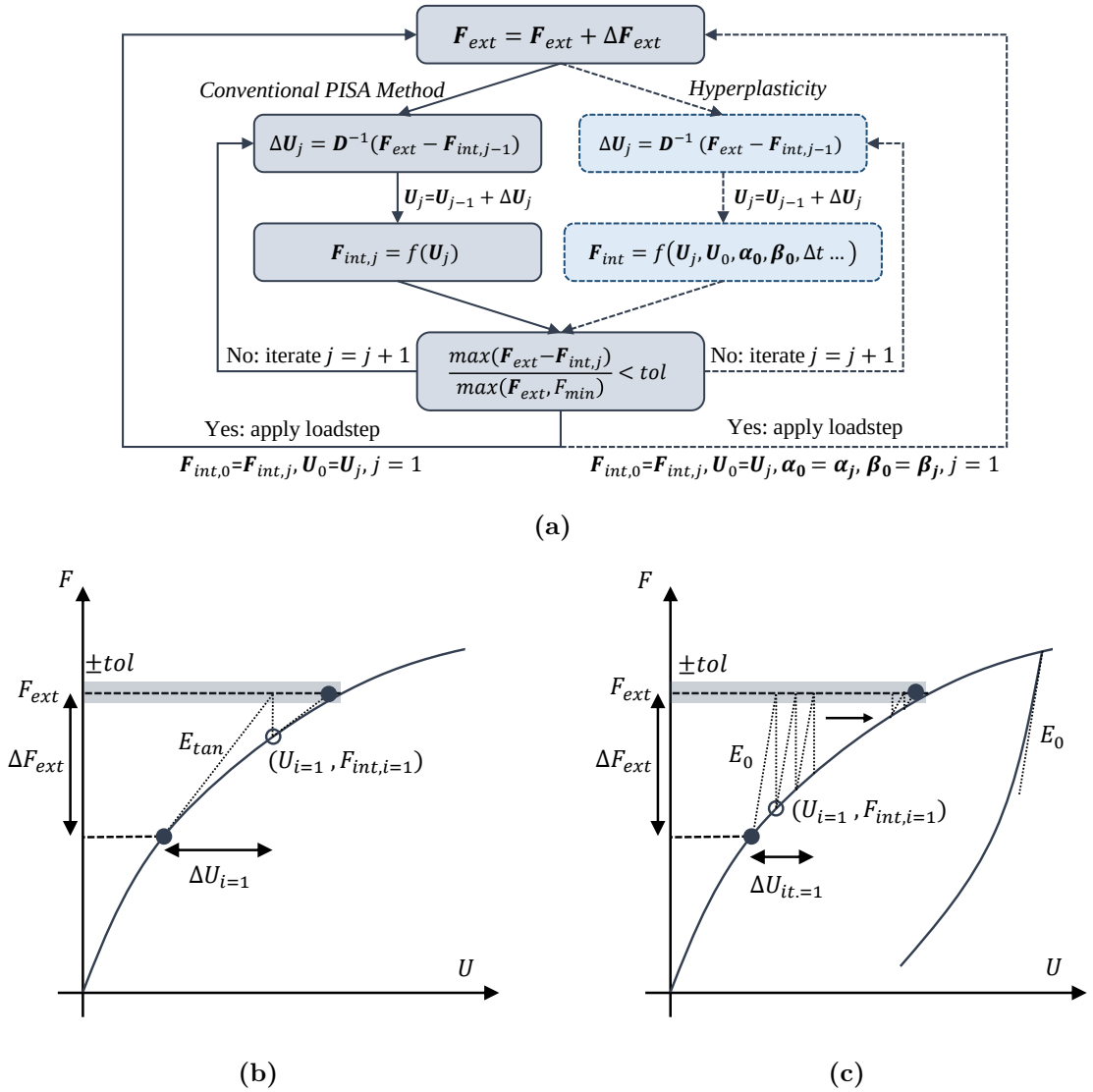

Figure 6.12: (a) Flow chart of OxPile computation under an applied external force vector F_{ext} for conventional PISA method and extended to include hyperplasticity models (b) Idealised tangential stiffness iterations at a single Gauss point (c) Idealised initial stiffness iterations at a single Gauss point

by the maximum of current external forces or a predefined F_{min} (ensuring that the denominator does not go to zero). F_{min} = 1000N and tol = 0.001 are used here. More information on the PISA project and the 1D design model can be found in Byrne et al. (2019b).

The fundamental development in this chapter is that the conventional soil reaction curves are re-framed as multi-surface kinematic hardening models in a parallel configuration (as described in Chapter 5). The non-linear reaction curves are discretised into a series of linear surfaces with strength K_i and stiffness H_i, from which further

extensions to cater for rate-dependency and cyclic effects may be added as before. This follows the work of Beuckelaers (2017) but applied to 'OxPile' and with updated evolution functions to match those presented in previous chapters.

The 1D FE model is largely unchanged except for calculation of the soil terms in the stiffness matrix and computation of F_{int}. F_{int} is now computed for an applied displacement increment using the hyperplasticity framework outlined in Appendix A. The computation at each Gauss point may now depend on internal variables $\boldsymbol{\alpha}$, hardening variables $\boldsymbol{\beta}$, time increment Δt and associated parameters. This is shown indicatively in Figure 6.12a (right). Hardening variables (used in softening and ratcheting) are only updated at the end of each load step when the solution has converged. This ensures that they are not affected by the strain paths during iterations.

Soil stiffness terms can no longer be directly derived from the soil reaction curves. Rather for each Gauss point and reaction curve, the stiffness is found by summing the stiffnesses of the surfaces which are not yet yielding (such that $y_i = 0$ if elastic and $y_i = 1$ if plastic):

$$E_{tan} = H_{Ns+1} + \sum_{i=1}^{Ns} H_i(1 - y_i) \tag{6.2}$$

A further option is also explored in which an initial stiffness Newton-Raphson method is used (Figure 6.12c) such that:

$$E_0 = \sum_{i=1}^{Ns+1} H_i \tag{6.3}$$

This results in more iterations before equilibrium but only requires a single calculation of the stiffness matrix.

For rate-independent calculations the tangent stiffness matrix is constructed for each iteration (using Equation 6.2) except for loading increments in which the direction of loading is changed, in which case the initial stiffness matrix is used (Equation 6.3). However, for rate-dependent computations the initial stiffness matrix is used throughout, removing the complexity of calculating rate-dependent stiffness. This decision is discussed in greater detail in Section 6.4.3.

Although this extension has been applied to the 1D PISA model, it is not dependent on any particular curve function, and could also therefore be applied to the

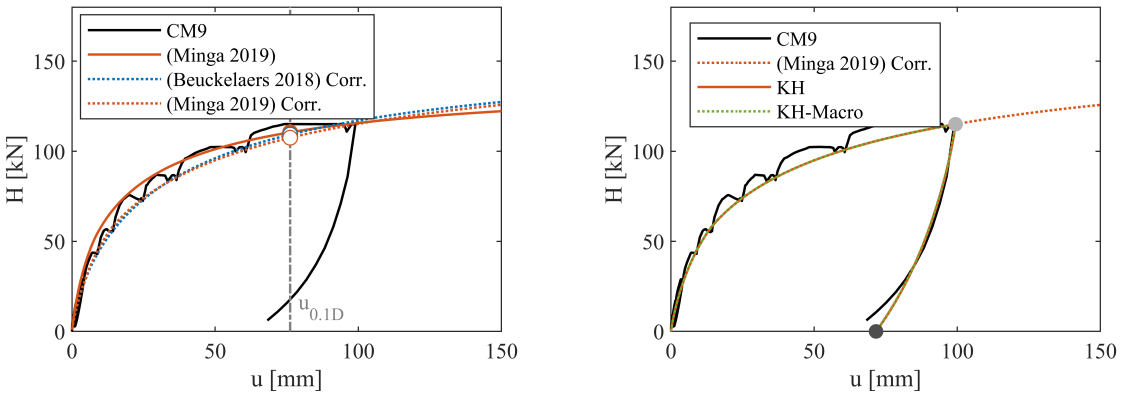

Figure 6.13: Cowden Test CM9 with OxPile model predictions (a) Comparison of various fitting parameters, markers indicate $H_{u_{0.1D}}$ (b) With multi-surface kinematic hardening extension and prediction of unload, markers indicate peak and unload prediction

p-y method in the same manner. The following sections describe each additional mechanism in more detail with comparison to the field tests.

6.4.2 Monotonic and kinematic hardening

The monotonic response is calibrated using the 'rule based' method (Byrne et al., 2019b). The four parameters of the non-dimensional PISA soil reaction curves reactions (y_u, x_u, k_0, n), as shown in Figure 6.11c, are found for each of the soil reaction components using relationships with a total of 28 previously defined 'fitting parameters' (see page 86 PLAXIS, 2018). The relationships are a function of depth z, pile diameter D and pile length L and are based upon 3D FE simulations for monopiles in idealised profiles of Cowden Till. At a particular location the dimensional soil reaction curve can then be found using the dimensionless groups defined by Byrne et al. (2019b).

Byrne et al. (2019b) present parameters derived to reproduce FEA analyses of full-scale piles at a representative Cowden site. First-stage fitting parameters are derived directly from FEA reactions down the pile and are similar to those used by Beuckelaers (2017). The PISA piles were much smaller than those in the full scale FEA analyses; direct application of the fitting parameters to the prediction of the PISA tests involves using the parameters outside of the design calibration space and may not be expected to produce close comparisons.

Byrne et al. (2019b) overcame this by a second-stage calibration of the 1D model fit, whilst Beuckelaers (2017) used local correction factors on the original PISA parameters to better predict the medium sized piles such that:

$$\sigma_u^* = A_u \sigma_u \qquad k_0^* = A_0 k_0 \qquad \varepsilon_u^* = \frac{A_u}{A_0}\varepsilon_u \qquad n^* = n \tag{6.4}$$

A_u and A_0 values are optimised for each pile and apply to all four reaction components (values shown in Table 6.3). Finally, Minga and Burd (2019) updated the calibration process using the MoDeTo design tool and found a further parameter set derived especially for the reproduction of the medium diameter pile tests.

Figure 6.13a shows monotonic computations with the original OxPile model using both parameter sets, plotted against the response of test CM9. Table 6.3 details correction factors used and shows predicted force at displacement of $u = 0.1D$, and initial stiffness E_0 fit to $H < 1kN$. An additional set of correction factors was derived for the Minga and Burd (2019) parameter set, fitted to the points of CM9 after load holds (at a slow rate). Both reproduce the measured response well.

In design, correction factors which effectively guarantee a perfect fit of measured data, could not be derived *a priori*. In that case, original soil reaction curves would be used as are also shown in Figure 6.13a where the predicted response is slightly stiffer than that observed at a slow rate; depending on the application this is likely well within expected tolerance and conservatisms in design.

In this chapter, however, correction factors are used to guarantee a perfect fit of the slow monotonic response in each individual pile. This enables the focus to lie solely on the subsequent mechanisms, largely removing any error due to the calibration of the monotonic response which is not of interest going forward. The Minga and Burd (2019) parameters and local correction factors for each pile (Table 6.4) are used in the rest of this chapter.

To capture hysteretic behaviour, the soil reaction curves are formulated as strain-controlled multi-surface kinematic hardening models in parallel configuration, as described in Section 5.2. Non-dimensional surface strengths $\bar{K}_i$ and $\bar{H}_i$ are derived from the non-dimensional PISA curves following methods described in Houlsby et al. (2017), in which $\Sigma_{i=1}^{Ns}\bar{K}_i = \sigma_u^*$ and $\Sigma_{i=1}^{Ns+1}\bar{H}_i = k_0^*$. Dimensional equivalents (K_i, H_i)

Table 6.3: Details and results of monotonic analyses of medium scale pile tests, corresponds to computations shown in Figure 6.13a with correction factors shown for CM9

Depth variation functions for soil reaction curves	Correction factors A_u	A_0	$H_{0.1D}$ [kN]	E_0 [kN/mm]
Beuckelaers (2018) corrected	0.715	0.416	109	11.2
Minga and Burd (2019)	1	1	111	17.1
Minga and Burd (2019) corrected	1.17	0.49	108	11.6

can then be found by considering the dimensionless groups for each soil-reaction such that:

$$\begin{aligned} p-v \quad &\rightarrow \quad K_i = \bar{K}_i s_u D \quad H_i = \bar{H}_i G_0 \\ m-\psi \quad &\rightarrow \quad K_i = \bar{K}_i s_u D^2 \quad H_i = \bar{H}_i G_0 D^2 \\ H-v \quad &\rightarrow \quad K_i = \bar{K}_i s_u D^2 \quad H_i = \bar{H}_i G_0 D \\ M-\psi \quad &\rightarrow \quad K_i = \bar{K}_i s_u D^3 \quad H_i = \bar{H}_i G_0 D^3 \end{aligned} \tag{6.5}$$

This is applied to the corrected soil reaction curves in Figure 6.13b in which 40 surfaces are used with equispaced K_i and an initial stiffness correction varying the location of the first yield point (See Equation 3.9). The m-ψ reactions are modelled with a single surface as the curve is linear-elastic perfectly plastic (Curvature parameter $n = 0$). Loading and unloading are applied in 1kN increments. The kinematic hardening model also allows for computation of unloading which, when compared to the CM9 response, is reproduced well. Figure 6.13b also shows the same unload and reload computed using a macro model with 40 surfaces calibrated to the global (H,u) prediction on loading. This agrees with the 1D model although the gain in computational time is insignificant at this stage (both run in less than a second).

The 1D model allows for computation of the response down the pile as well as at ground level. Figure 6.14 shows displacement and bending moment along the pile

Table 6.4: Correction factors for Cowden pile tests using Minga (2019) soil reaction curves

Test	A_u	A_0
CM1	1.16	0.75
CM5	1.46	0.75
CM6	1.09	0.31
CM7	1.46	0.75
CM9	1.17	0.49

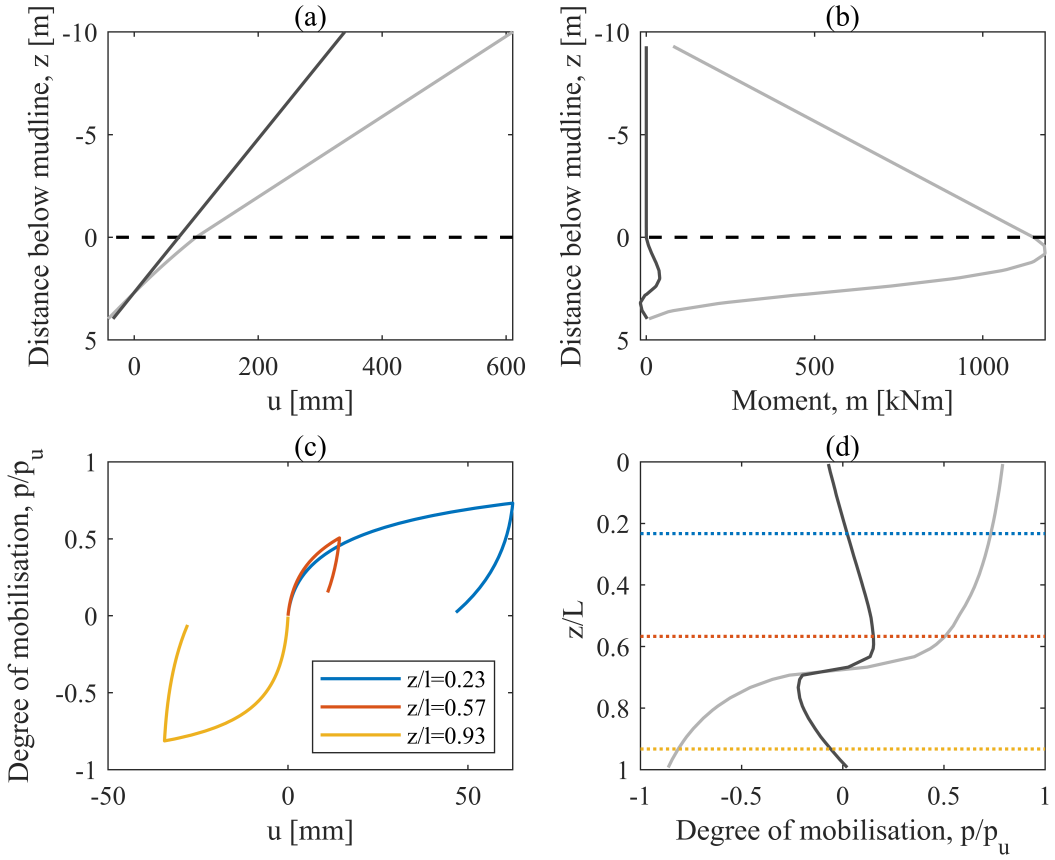

Figure 6.14: Computed behaviour with pile length associated with 'KH' in Figure 6.13b (a) Lateral displacement u and (b) bending moment m with depth below mudline z at peak load and unload (c) Normalised distributed lateral reaction response 'degree of mobilisation' at three depths (d) Depth varying degree of mobilisation at peak load and unload

length at peak load and at unload (as shown by markers in Figure 6.13b). Permanent displacement on unload is predicted as well as residual bending moment in the pile below ground level. Measured bending moment profiles were not available for CM9, but for other piles are compared to predictions in the following sections. Distributed lateral reaction response is shown at three depths, and shown normalised by the depth varying ultimate value p_u, and termed 'degree of mobilisation'. This is also shown depth-wise at peak load and unload. In this case the point of rotation can be seen at approximately $z/L = 0.68$.

6.4.3 Rate dependency

Pile response in clays is rate-dependent (see Figure 6.4a). Models presented in Section 5.3, based upon rate process theory, capture similar behaviour. However, the

incremental solutions in Appendix A require small timesteps to ensure numerical stability. At a macro-scale this is acceptable but at 1D where computations are required at each Gauss point for many load steps, computational expense may be too high.

Beuckelaers (2017) overcame this by approximating rate process theory using a modified rule. Rather than capturing the elastic, elastic-viscoplastic and viscoplastic ranges (as in Equation 5.9) only the elastic and viscoplastic areas are modelled. This is achieved by varying the strengths of each surface during each iteration, such that:

$$K_{d,i} = K_i\left(1 + \eta \sinh^{-1}\left(|\dot{\varepsilon}|t_{ref}\right)\right) \tag{6.6}$$

where $\eta = \eta_{10}/\ln(10)$ is the viscous parameter, t_{ref} is a reference time and $\dot{\varepsilon}$ is the strain rate for the corresponding reaction at a certain Gauss point. This was shown to approximate the response due to varied loading rate well, and allows for rate-independent implementation $(f - y)$ to be achieved for a rate-dependent model. Hence the number of increments can be greatly reduced. For each soil reaction the the same viscous parameter η_{10} and reference test time to failure, $T_{u,ref}$ is assumed. From this a local reference time is computed for rotation or displacement reaction curves:

$$t_{ref,v} = \frac{1}{\dot{v}_{ref}} = \frac{T_{u,ref}}{v_u} \tag{6.7}$$

$$t_{ref,\psi} = \frac{1}{\dot{\psi}_{ref}} = \frac{T_{u,ref}}{\psi_u} \tag{6.8}$$

where v_u and ψ_u are global displacement and rotation variables corresponding to the monotonic response at approximately $T_{u,ref}$.

Figure 6.15 shows computations of tests CM9 and CM1 using the modified rate process theory model (RPT) with input parameters described in Table 6.5. The load-time input is down-sampled from the original data such that there are 10 steps per load ramp and load hold. Rate-independent (RI) computations are also shown with a further set of correction factors calibrated for test CM1 to ensure a suitable prediction for the response at the end of each load hold.

Table 6.5: Rate-dependency parameters used for tests CM1 and CM9

$T_{u,ref}$ mins	η_{10} -	v_u m	ψ_u rads
272	0.1	0.1D	$2\pi/180$

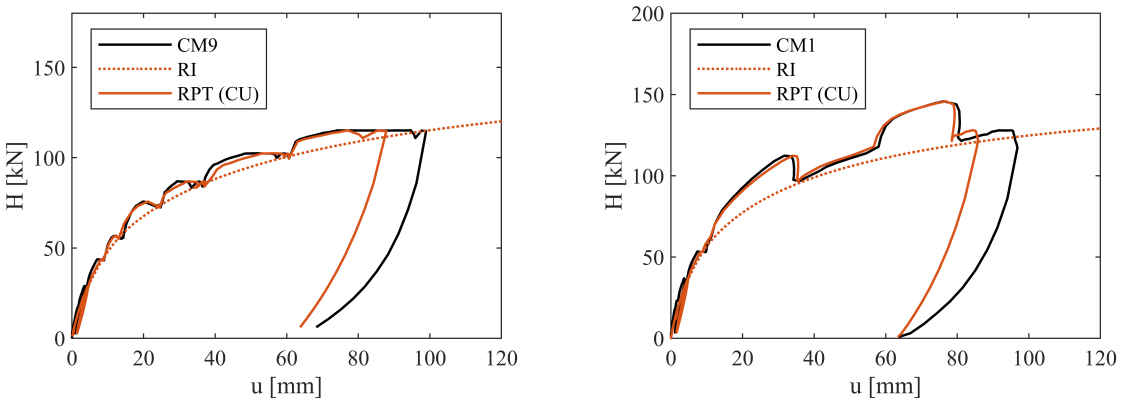

Figure 6.15: Rate-independent (RI) and rate-dependent (RPT) computations of (a) Test CM9 (b) Test CM1, model parameters shown in Table6.5

$T_{u,ref}$ = 272mins is taken as the approximate time to $v_u = 0.1D$ after the slow isotach curve to which the RI case is calibrated. At this displacement the pile is rotated to approximately 2° such that $\psi_u = 2\pi/180$. $\eta_{10} = 0.1$ is calibrated to the element tests in Section 6.2. In using a smaller $T_{u,ref}$ and therefore t_{ref}, minimal rate effects are computed for strain rates below this value. Alternatively a much larger $T_{u,ref}$, similar to the assumed value in element tests (say 1 month), could be used. The PISA soil reaction curve parameters would then require recalibration to ensure the predicted RI response matched that expected close to zero displacement-rate (as per Section 3.3.3).

The predictions match the measured response well, suggesting that the non-dimensional viscous parameter η_{10} can be calibrated at element scale and applied to field tests. This is perhaps expected given the results in Figure 6.4c but is an important conclusion for potential use in design.

Figure 6.16(a) shows the same computations for CM1 alongside a macro H-v model prediction with the same rate parameters and load input as the 1D model. Agreement is not as good as in the rate-independent case, particularly at high load magnitudes and slow rates. This may be due to a difference in relative rate-dependent strength in rotation and displacement reactions or perhaps disparity at the iteration level in the 1D model. This is further discussed at the end of this section.

Figure 6.16(b) shows the predicted moment distribution with embedded length at two peak loads and on unload as indicated in Figure 6.16(a). Measured bending

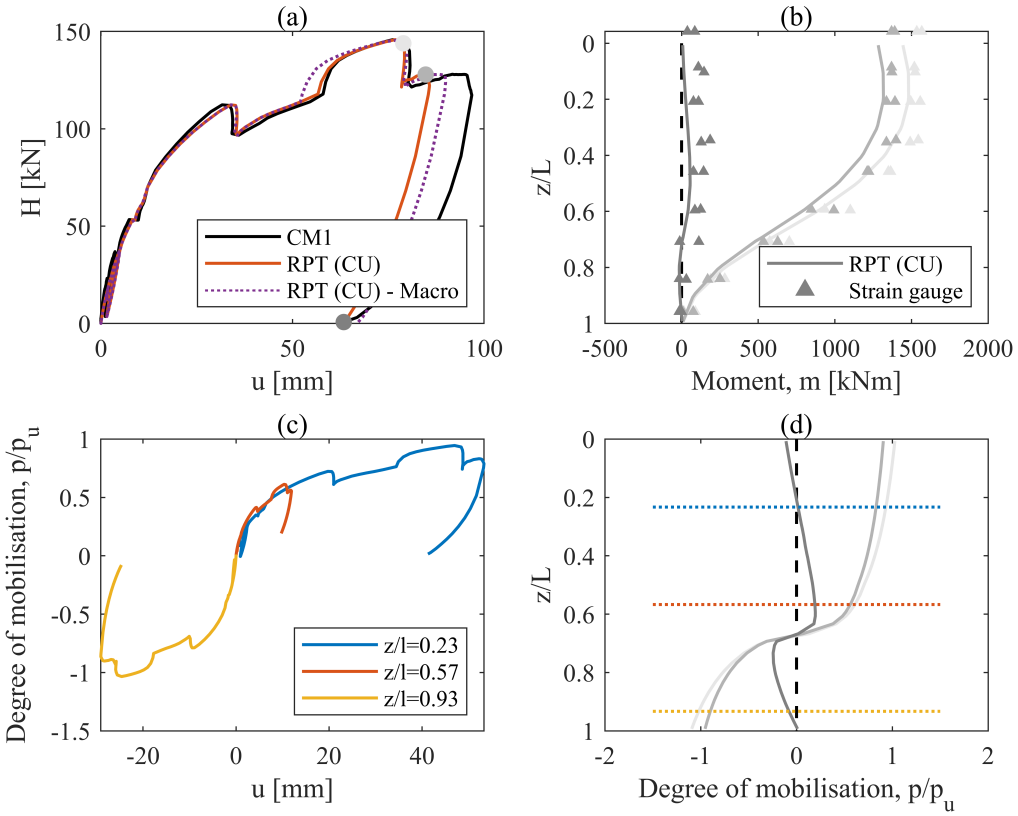

Figure 6.16: (a)RPT computations of Cowden Test CM1 with equivalent macro model (b) bending moment m with depth below mudline z at peak loads and unload as shown in (a), (c) Normalised distributed lateral reaction response 'degree of mobilisation' at three depths (d) Depth varying degree of mobilisation at peak loads and unload

moments calculated from fibre-optic strain-gauges on either side of the instrumented pile are also shown. A good prediction of the distribution is achieved at all three points. Figure 6.16(c) and (d) show distributed lateral reaction response at three depths and along the embedded pile length. Additional strength due to increased rate means that degree of mobilisation exceeds 1 at high rates both near the surface and at the pile tip.

In summary, rate-dependency at pile level is well reproduced with models based upon rate process theory and for this data-set normalised viscous parameters scale well between element and pile.

As described in Section 6.4.1, the initial stiffness matrix is used for Newton-Raphson iterations. In fact this is a poor estimate of the behaviour at each Gauss point, particularly at load reversals where viscosity causes an increase in displacement

whilst load decreases (negative stiffness). This is still computed but can require many iterations and poor initial guesses. As displacement rate reduces to almost zero, oscillations can occur, in this case the soil elements of the stiffness matrix are increased to 10 times initial stiffness ($10E_0$). With this addition the model converges for the cases used in this chapter.

While using the Newton-Raphson procedure in this way, displacement over a given time is estimated. Since the internal force is then a function of strain rate, there may be more than a single possible solution. A more robust method may be to solve the expected displacement using both a stiffness matrix (rate of change of displacement) and dissipation matrix (rate of change of displacement rate) which could be calculated numerically.

6.4.4 Cyclic effects

This section aims to capture the effects of many cycles. The primary focus is capturing ratcheting behaviour (as per SLS design in Section 1.2.2.2), although stiffness and loop shape changes (energy loss factor) are also considered. A local softening model, calibrated to element tests in Section 6.2, is initially employed and compared to global softening and ratcheting (HARM) models. The latter has previously been successfully applied to the same data-set (Beuckelaers, 2017) and to model piles in sands (Richards, 2020; Abadie, 2015). Both softening and HARM-type models are described in Chapter 5, and are implemented as extensions to the parallel multi-surface kinematic hardening model in Section 6.4.2.

In the softening model incremental changes to the yield strengths at each Gauss point are calculated following Equation A.25. Local (surface-specific) or global changes are controlled by the switch parameter F_κ. The magnitude of softening is controlled by hardening variable β_i taken as the local plastic work as per Equation 5.4. In the 1D model β_i is only updated after convergence is achieved such that softening does not depend upon the strain paths prior to convergence.

The HARM (ratcheting) model is implemented with an additional ratcheting unit as per Section 5.5, in which the evolution of ratcheting strain is controlled by Equations 5.22 and 5.23 with $R_{mult} = \frac{K_i}{\sigma_u}$. Again the plastic work related hardening parameters at each Gauss point and soil reaction are updated after convergence. The

derivation of incremental behaviour is updated following Appendix A with a subtle change. In previous models an acceleration factor a between 0 and 1 ensured numerical stability if yield is exceeded, although here a sub-stepping procedure is employed which ensures that yield is met exactly and ratcheting updated correctly during each step and iteration (see pg. 127 of Beuckelaers, 2017 for more detail).

The models can be used jointly and with or without rate-dependency (as per Section 6.4.3). Initially a rate-independent model is used.

6.4.4.1 Rate independent and cyclic effects

Three sets of analyses are undertaken with varying underlying models and parameters as shown in Table 6.6:

- CU - Local softening only in which the parameters follow those calibrated to element tests.
- GS - Global softening calibrated to best fit the accumulation of strain in test CM6.
- HARM - Ratcheting model (without any softening) calibrated to best fit the accumulation of strain in CM6, starting with similar values to those used by (Richards, 2020).

Reference hardening values, $\beta_{ref,i} = F_{\beta,l} K_i \varepsilon_u$, $\beta_{ref,G} = F_{\beta,G} \sigma_u \varepsilon_u$ and $\beta_{ref,R} = F_{\beta,G} \sigma_u \varepsilon_u$ follow those used in Chapter 5, where for each Gauss point $\sigma_u = \Sigma K_{0,i}$ and $\varepsilon_u = K_{0,Ns}/H_{Ns}$. K_0 indicates initial yield strengths prior to any softening or rate changes.

For each parameter-set the backbone must be recalibrated since the cyclic effects begin as soon as plastic strains develop. Here the same method described in Section

Table 6.6: Cyclic model parameters used in analyses

	m_k	κ_{ref}	$F_{\beta,l}$	F_κ	$F_{\beta,G}$	$A_{u,rec}$	$A_{n,rec}$
CU	0.1	0.7	20	1	–	1.101	1
Soft	0.4	0.7	–	0	0.3	1	1
	R_0	R_{ref}	$F_{\beta,R}$	m_r	m_s	$A_{e,rec}$	$A_{n,rec}$
HARM	1	0.1	25	1.5	4	0.445	0.97

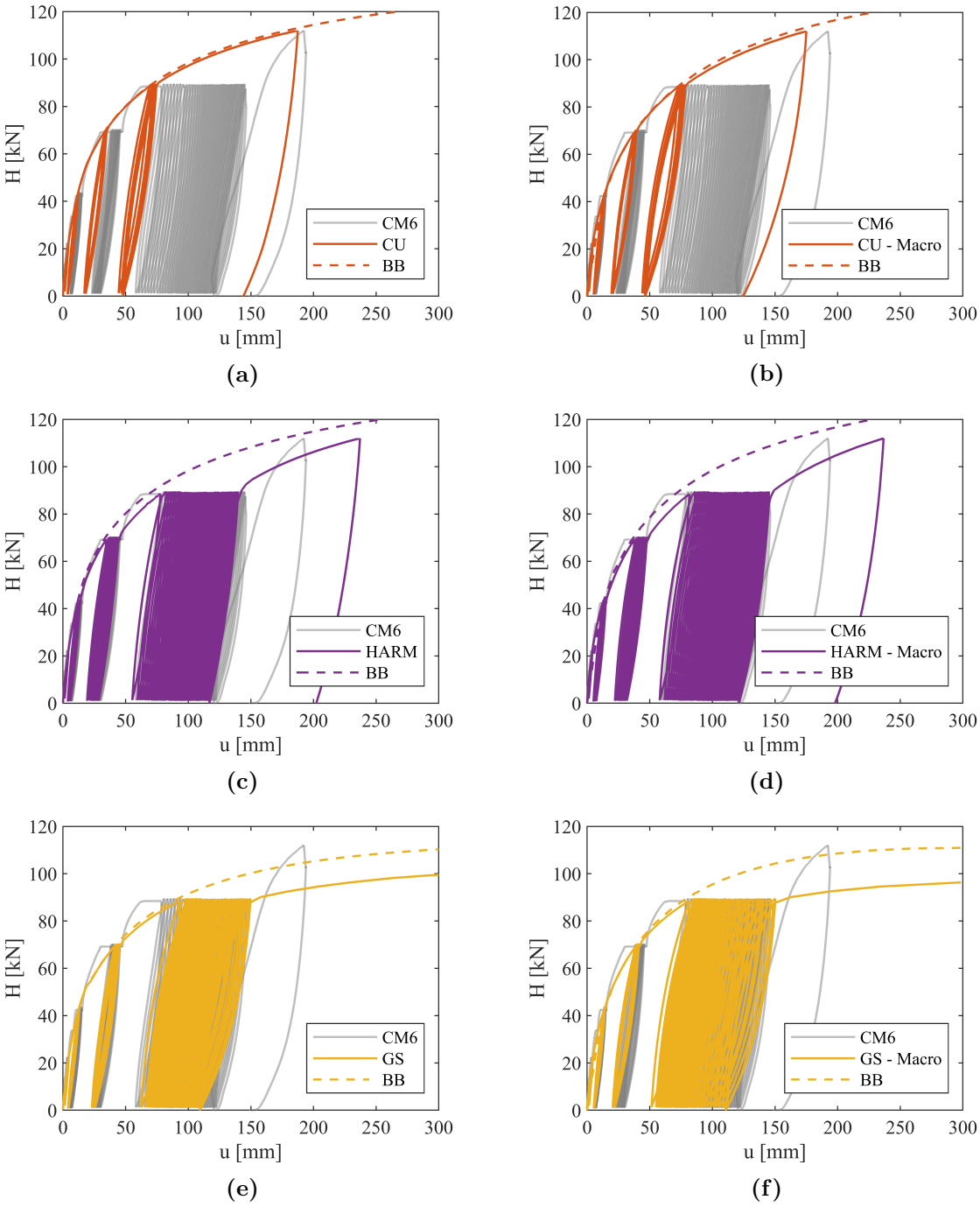

Figure 6.17: Computation of test CM6 with 1D (left hand column) and macro models (right hand column); (a),(b) CU local softening parameters calibrated to element tests; (c),(d) HARM ratcheting model calibrated at pile level; (e),(f) GS global softening model calibrated at pile level

3.4.3 is used. Optimising global recalibration factors which are applied in a similar way to the 'correction factors', such that Equation 6.4 is updated to:

$$\sigma_u^* = A_u A_{u,rec} \sigma_u \qquad k_0^* = A_0 k_0 \qquad \varepsilon_u^* = \frac{A_u}{A_0} A_{e,rec} \varepsilon_u \qquad n^* = A_{n,rec} n \tag{6.9}$$

For independent ratcheting models $A_{u,rec} = 1$ and in softening models $A_{e,rec} = 1$. Recalibration factors are not applied to the linear elastic perfectly plastic (curvature parameter $n = 0$) M-ψ curves. For the GS calibration set no recalibration factors are used, the softening required to produce the correct amount of ratcheting causes rapid reduction of strength at high magnitudes (similar to post-peak softening) but relatively little at low strains.

This method allows recalibration using just two or three parameters across all Gauss points, alternatively each stiffness or strength value can be recalibrated independently. The two methods can result in a subtly different response (Balaam and Kragelund, 2020).

Figures 6.17(a,c and e) show 1-D and macro level computations of test CM6. The original time histories from the PISA tests are re-sampled with 50 steps per load ramp or cycle and 20 per load hold. The CU model does not reproduce the ratcheting behaviour, grossly under-predicting the accumulation of strain. In contrast, the HARM model is, unsurprisingly, well calibrated. Global softening reproduces the ratcheting behaviour; however, the post-cyclic response is far too soft, failing before unloading. In this case, as discussed in detail in 5.4, ratcheting can only occur if the ultimate strength is reduced.

Macro element model computations are also shown (Figures 6.17 b,d and f) calibrated to the rate-independent 1D model response. These are far less computationally expensive and produce largely similar responses. Subtle differences are predominantly due to the recalibrated backbone (shown dashed) response which differs slightly, particularly in the softening models. This reinforces the importance of the backbone response on subsequent effects due to repeated loads. Importantly, the similarity between the two modelling scales suggests that normalised cyclic parameters can be calibrated at a macro level and applied to the 1D model. This is useful, particularly if calibrating from field tests. Alternatively, macro models could be used as a much faster predictive tool for the response of single piles in which down pile behaviour may not be required.

Figure 6.18 shows displacement time history alongside accumulation of displacement, secant stiffness and energy loss factor with cycles. Where possible exponents are fit to both measured and computed data following Section 6.3. It is clear that the

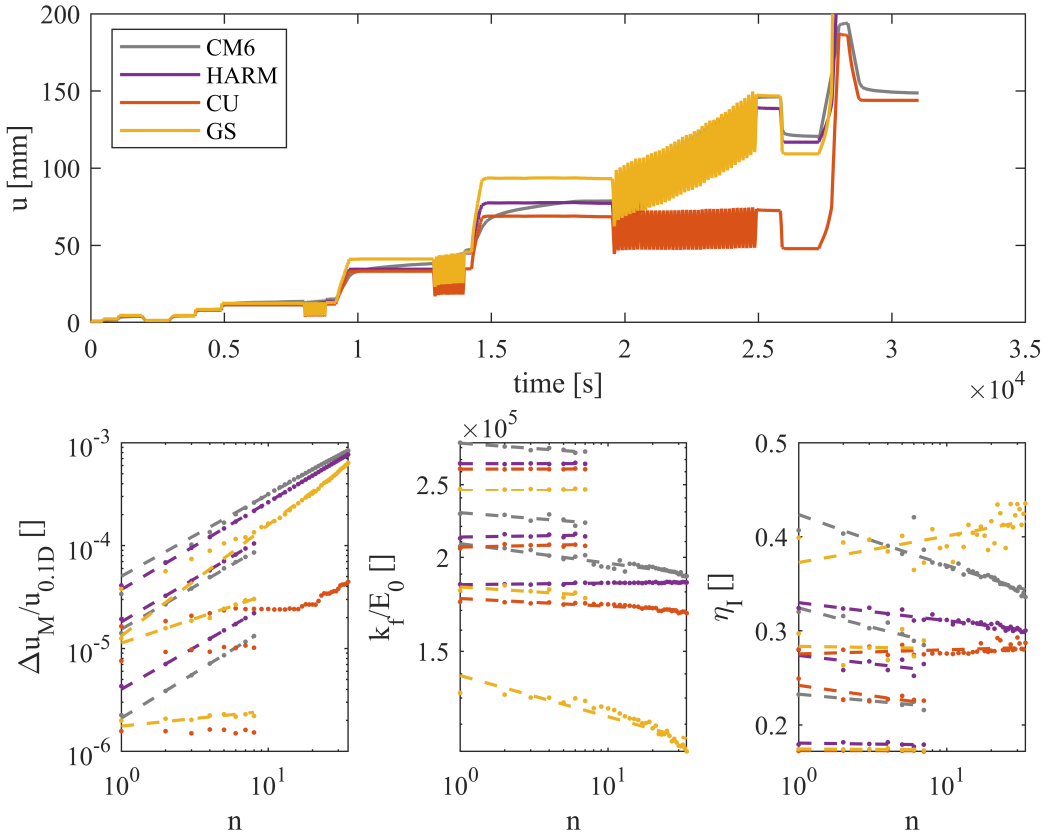

Figure 6.18: Test CM6 and model computations. Displacement, accumulation of displacement, stiffness and energy loss factor

HARM model reproduces the development of ratcheting well whilst CU shows little to no change. GS broadly reproduces the ratcheting development during the final, most intense, packets but under-predicts the lower intensity packets.

Stiffness predictions of the initial cycles (at n=1) are underestimated in all models, suggesting a softer backbone than required. This would probably be improved with the addition of rate-dependency and associated stiffer response at higher rates. The effect is more pronounced in GS in which the backbone is intensely reduced with stress magnitude. Stiffness reduction with cycles increases with the intensity of calibrated softening: no change in the HARM model; very little in the CU model; and much greater changes in the GS, leading to an over-prediction in high magnitude cycles.

Energy loss factor decreases in all batches of the measured tests. Global softening predicts an increase with cycles in the final packet as the loop shape becomes more open. This is largely unchanged in the CU model but reduces in the HARM model

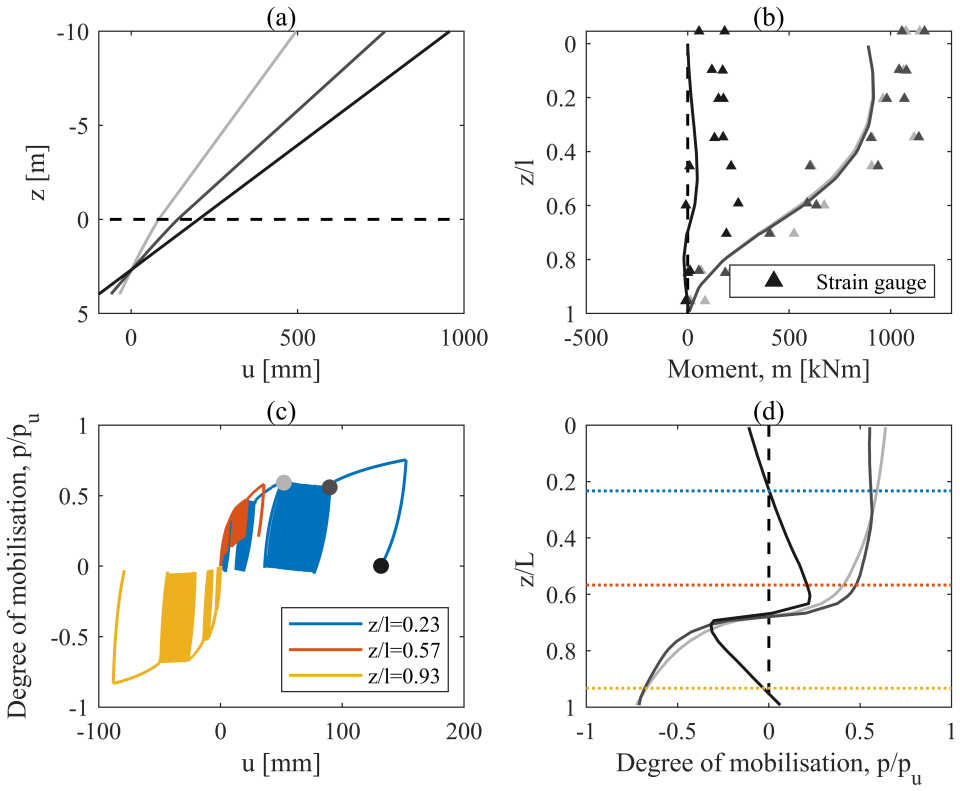

Figure 6.19: Computed behaviour of test CM6 with pile length associated with 'HARM' in Figure 6.17c (a) Lateral displacement u and (b) bending moment m with depth below mudline z at peak loads and unload (c) Normalised distributed lateral reaction response 'degree of mobilisation' at three depths (d) Depth varying degree of mobilisation at peak load and unload

as energy dissipation due to ratcheting follows the reducing rate of displacement accumulation.

Figure 6.19 shows down pile prediction using the HARM model only. Pile displacement, moment distribution and soil mobilisation are shown at the first and last peaks of the final packet and at final unload as indicated in continuous p-y curves in Figure 6.19(c). Figure 6.19(b) shows the predicted moment distribution with embedded length. Measured bending moments (from fibre-optic strain-gauges) are also shown. A good prediction of moment distribution at peak loads is achieved with little change before and after cycling. On unload the residual bending moment is underpredicted, although the distribution shows a peak close to $z/L = 0.6$ in both. Figure 6.19(d) show distributed lateral reaction response along the embedded pile length. Peak and unload behaviour are similar to those shown in Figure 6.16. With cycles,

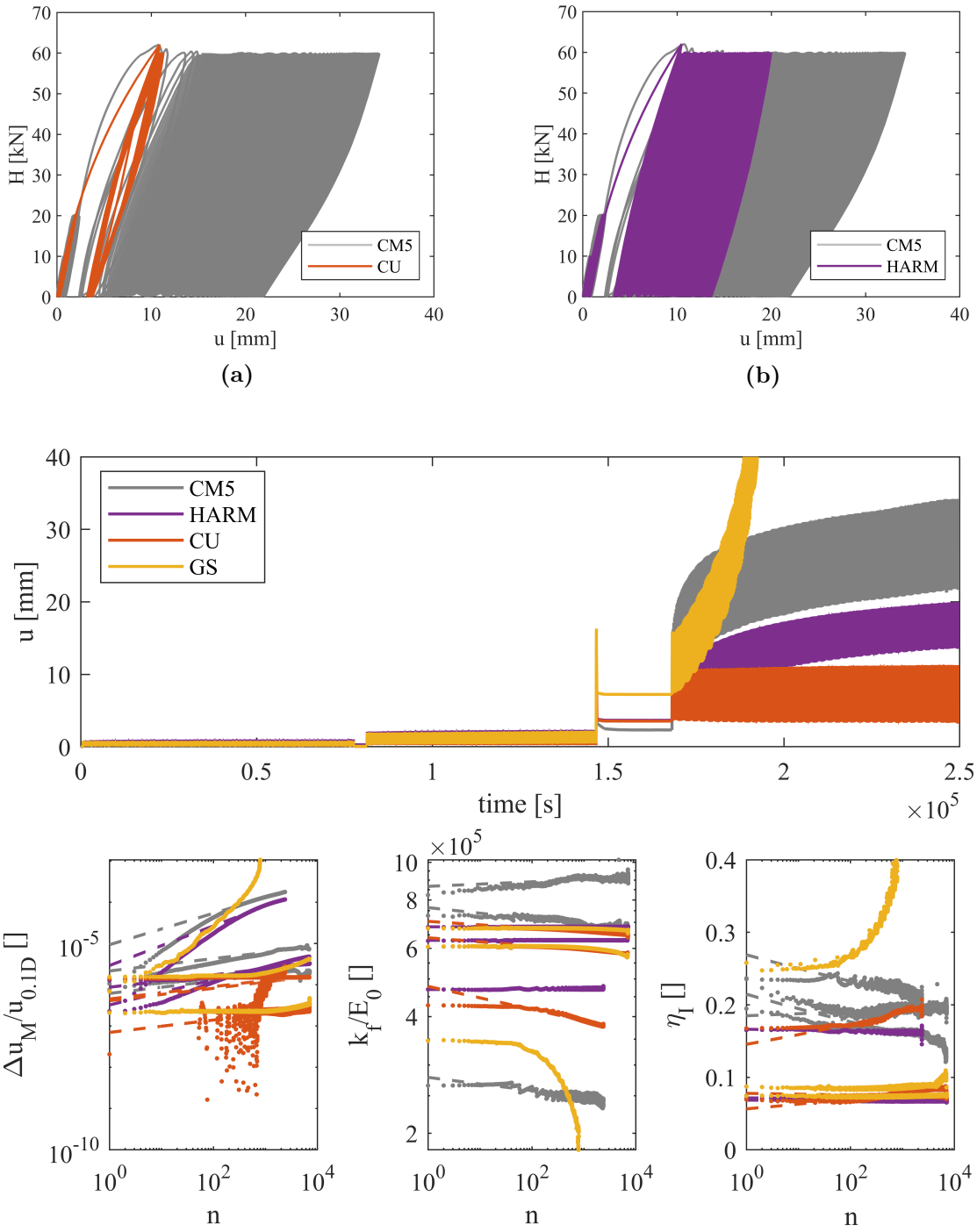

Figure 6.20: Computation of test CM5 (a) CU (b) HARM (c) Accumulated displacement, secant stiffness and energy loss factor with cycles

the distribution becomes more balanced above and below the pivot point. As displacement (ratcheting) occurs more in the most highly mobilised depths, so pressures are redistributed to less mobilised locations (closer to the pivot).

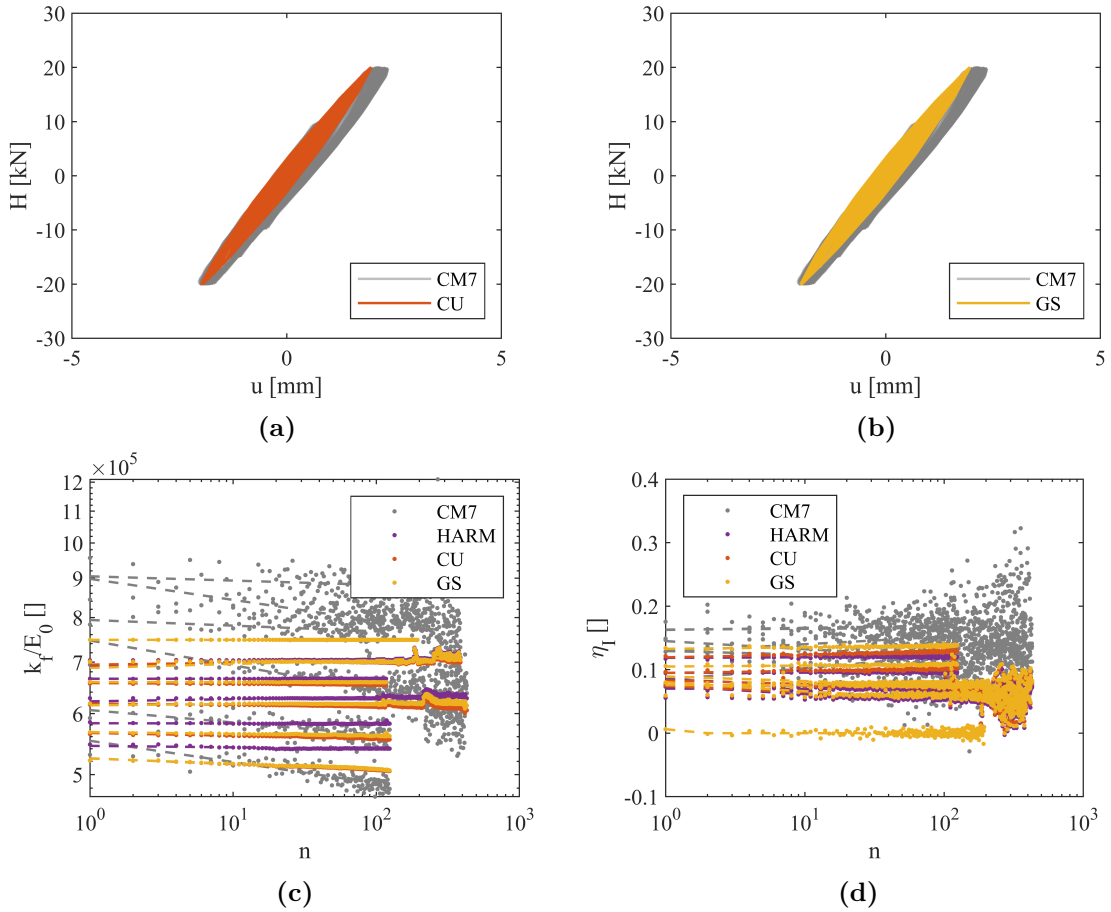

Figure 6.21: Computation of test CM7 (a) CU (b) GS (c) Stiffness change with cycles (d) Energy loss factor with cycles

Macro models with similar cyclic parameters are used to compute tests CM5 and CM7. The original load history is down-sampled with 20 steps per cycle owing to the high number of cycles. Figure 6.20 shows predictions of test CM5 with low-magnitude one-way cycles to cycles of $n > 1000$. The initial backbone is again slightly too stiff in all models but the difference in strain development is clear. With higher numbers of cycles GS fails as yield strengths are reduced too rapidly, little ratcheting occurs in CU although stiffness reduction is well modelled. The HARM model reproduces the development of ratcheting well despite underpredicting the magnitude.

Figure 6.21 shows similar models applied to the first 5 batches of low-amplitude two-way loading in test CM7. Both softening models develop with plastic work and therefore at such low stress magnitudes little change occurs. This does show that the models do not spuriously develop softening at very low strains. The same is true of ratcheting in Figure 6.20.

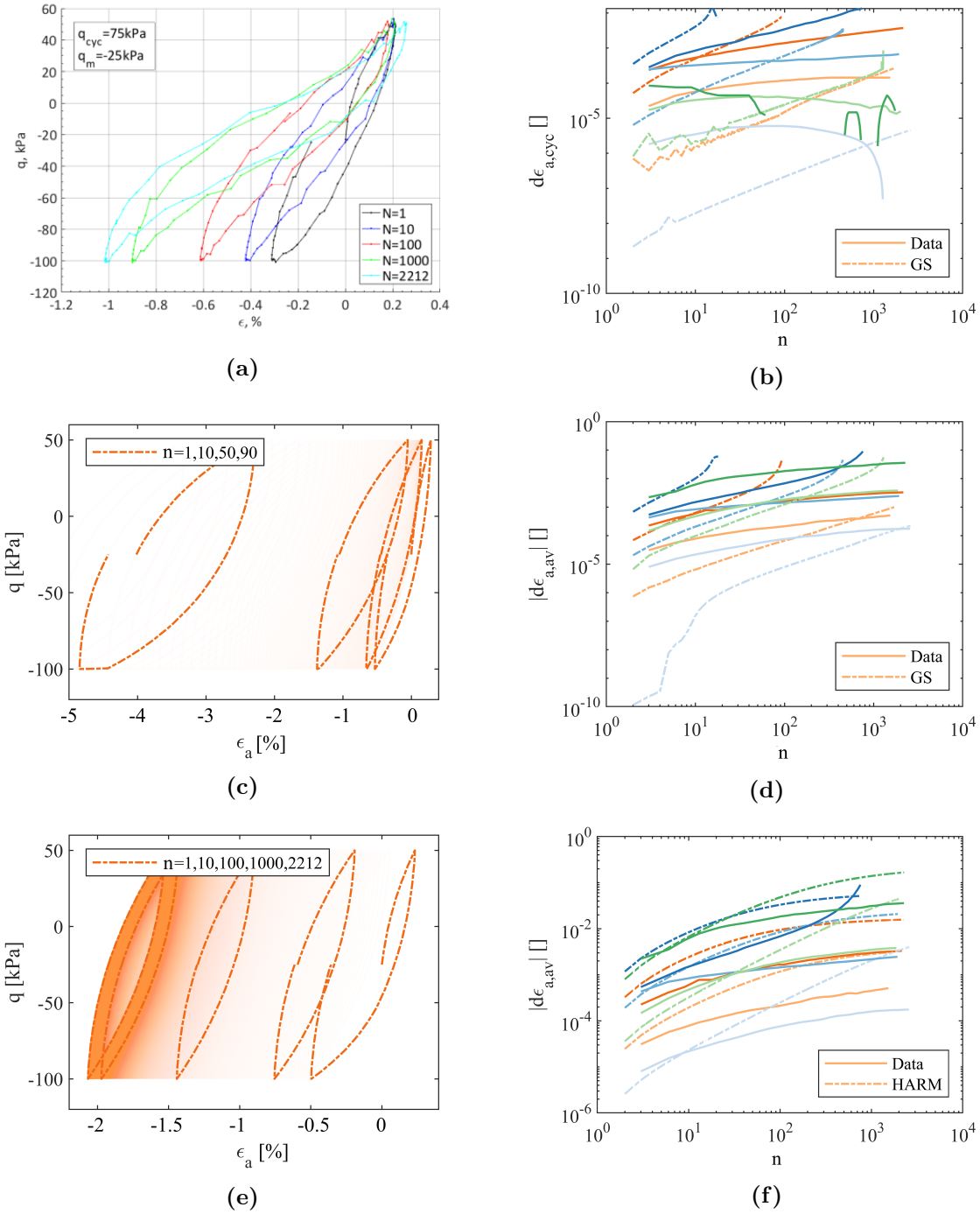

Figure 6.22: Computations of Cowden element tests with parameters calibrated to pile scale response (a) Example measured hysteresis loops, plot taken from Ushev (2017) (b),(c) and (d) GS Global softening model, change in cyclic strain,modelled hysteresis loops corresponding to (a), and average strain (e),(f) HARM model, modelled hysteresis loops and change in average strain

It is clear from this section that the dimensionless softening parameters calibrated at an element scale do not reproduce the behaviour at pile scale well when applied at

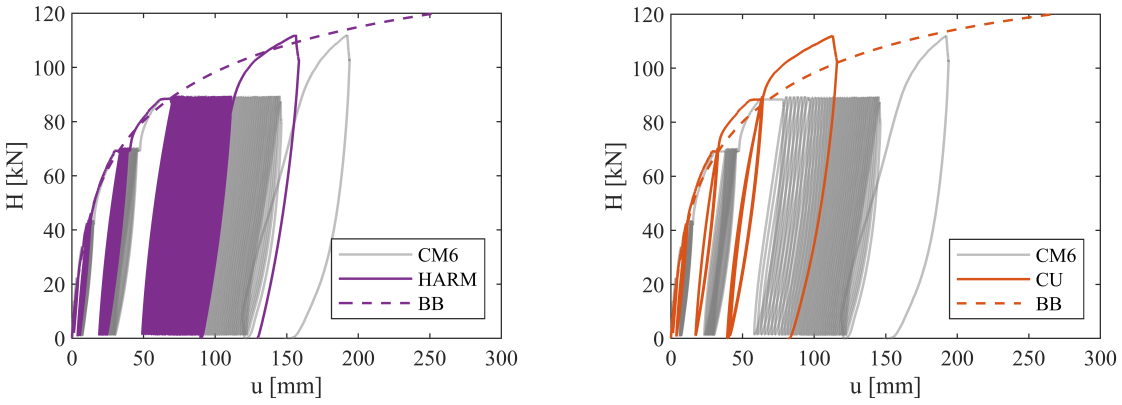

Figure 6.23: Computation of test CM6 using a rate dependent model (a) HARM (b) CU

a 1-D or macro level. Instead, to capture the accumulation of displacement, softening models with a high degree of global yield strength reduction or HARM models were used. Figure 6.22 shows this applied in reverse, calibrated pile level parameters applied to the element scale, to ensure the issue is not with the calibration process.

Figure 6.22 (b) to (d) show GS model predictions, these greatly overpredict the increase in cyclic and average strain and in (c) fail rapidly. Figure 6.22 (e) and (f) show HARM model predictions which offer a more accurate prediction of average strain, although with no changes to secant stiffness. The development of cycles for the test shown is approximately double the measured strains but more importantly loop shapes develop in a different manner.

6.4.4.2 Rate dependent and cyclic effects

In this section, both rate-dependency and cyclic effects are combined. Figure 6.23 shows computations of CM6 with parameters as per Tables 6.7 and 6.5. Periods of load hold and resulting displacement prior to each set cycle of cycles are well predicted by the model. In the HARM model, ratcheting rate is reduced slightly due to the reduction in plastic strains and therefore ratcheting strain. In the softening model no additional ratcheting is computed due to rate-dependency, due to the the load holds.

Table 6.7: Cyclic model parameters used in rate dependent analyses

m_k	κ_{ref}	$F_{\beta,l}$	F_κ	$F_{\beta,G}$	R_0	R_{ref}	$F_{\beta,R}$	m_r	m_s	$A_{u,rec}$	$A_{e,rec}$	$A_{n,rec}$
0.1	0.7	5	1	–	1	0.1	55	1.5	4	1.101	0.445	0.97

Some additional creep would be produced with a higher $T_{u,ref}$ although this is likely to be small.

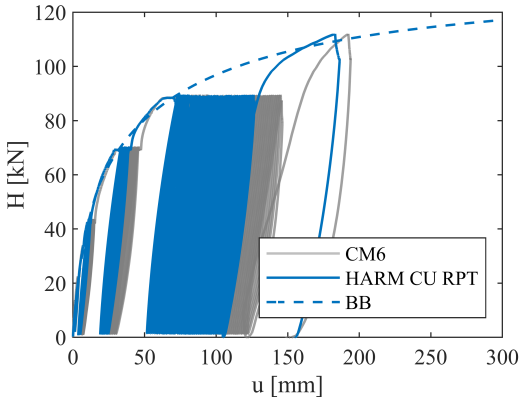

(a)

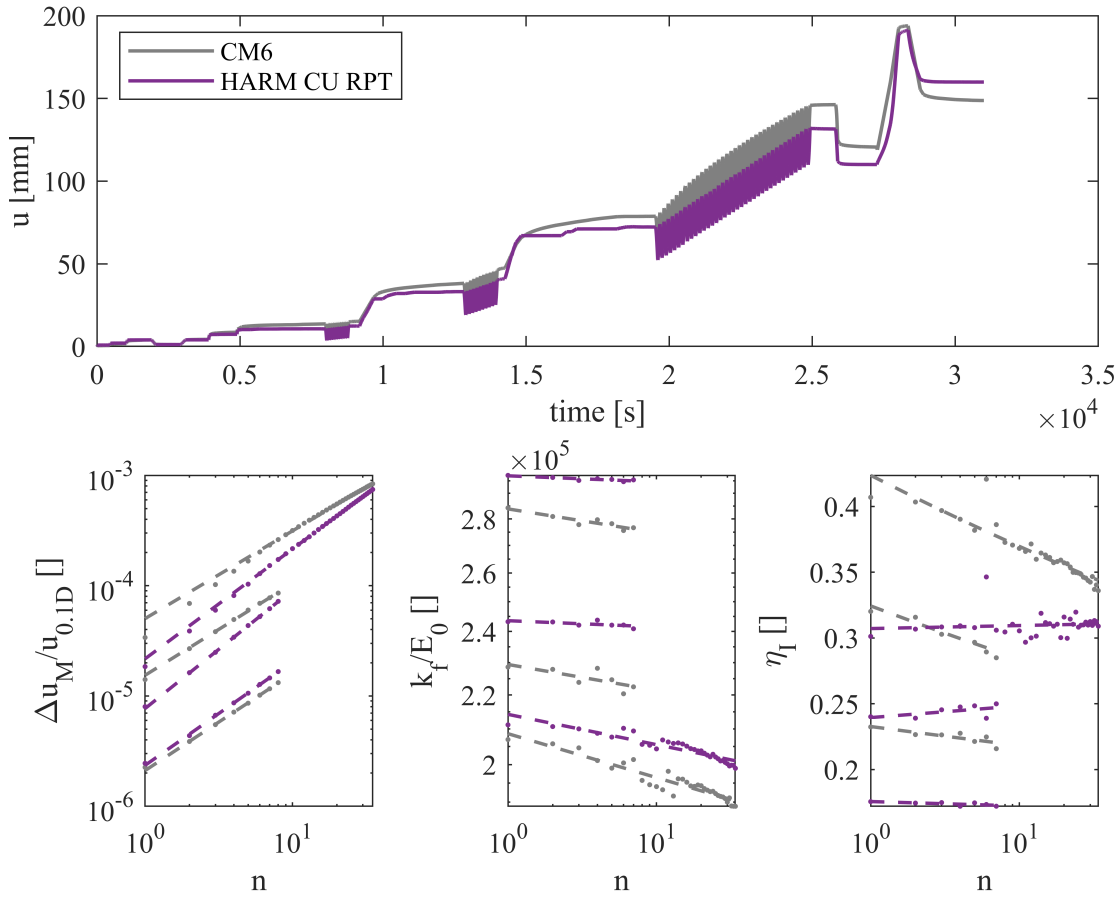

(b)

Figure 6.24: Computation of test CM6 using a RPT model with ratcheting and softening (HARM and CU) (a) Hysteretic behaviour (b) Accumulated displacement, secant stiffness and energy loss factor with cycles

Figure 6.24 shows a final best-fit model with parameters defined in Table 6.7, this is similar to that presented by Beuckelaers, 2017 but using the updated ratcheting relationship and with local softening catering for stiffness development. Intensity of softening is increased slightly by reducing $F_{\beta l}$ from 15 to 5 thereby softening earlier. Ratcheting intensity is increased to allow for the reduction in rate-dependent strains, by increasing $F_{\beta R}$ from 25 to 55.

6.5 Storm load behaviour

The models presented in this section can be used to predict pile displacement and rotation for any input loading. Macro models could be used for computational efficiency on similar piles, whilst the 1D models could be applied to piles of varying properties in similar conditions and allow for down-pile behaviour to be computed.

Here, the response of pile CM6 is computed for an example 9-hour storm load using the 1D model. A rate-independent HARM model is used with parameters as in Table 6.6. The load history is the same as that introduced in Section 2.7.1 and is shown in Figure 6.25a (top). It has been suitably scaled with a safety factor of 1.35 on the maximum ULS design load such that $H_{max} = H_{ref}/1.35$, where $H_{ref} = H_{0.1D} = 90.5kN$.

Figure 6.25a also shows computed displacement and rotation with time. As in Section 4.2, considerable increases occur at high amplitude loads with a small amount of ratcheting between peaks. Over double the SLS limit θ_{SLS} is predicted by the end of the storm. In fact, this is particularly severe loading: unidirectional with a high bias and with a peak load at the ULS design limit.

The embedded response of the model is shown in Figure 6.26 at load maximum, minimum and at the end of loading. Down-pile behaviour is further interrogated to characterise the degree of mobilisation (in terms of lateral pressure) across the embedded length. This is achieved in a similar manner to Section 2.7.1, deriving average and cyclic pressure for each half cycle at each Gauss point. Each individual half cycle is plotted in an interaction diagram (Figure 6.28) with the Gauss points plotted in Figure 6.26(a) highlighted. The further from the pivot point the more intense the mobilisation, particularly in terms of amplitude.

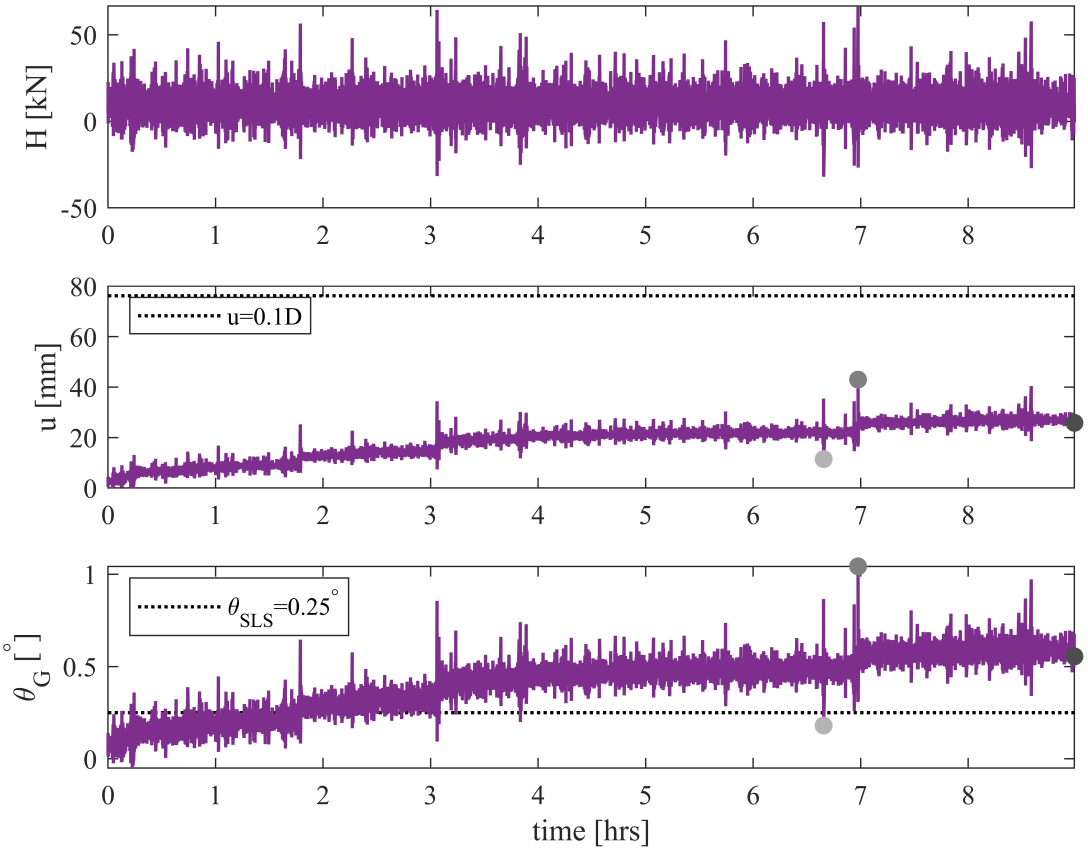

(a)

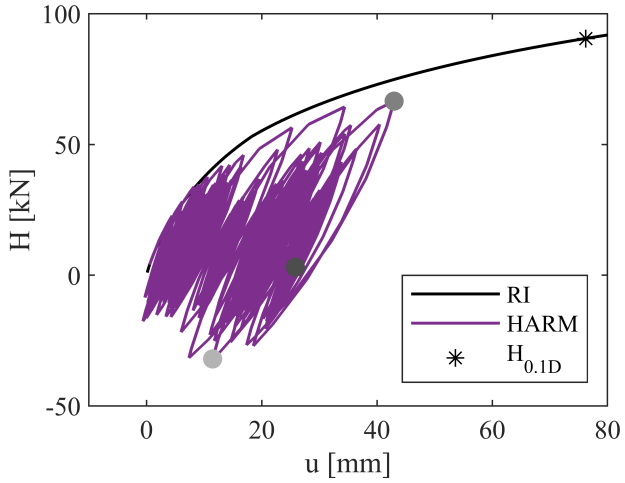

(b)

Figure 6.25: Computation of response to 9 hour storm load applied to pile CM6 (a) Load, displacement, and rotation with time CU (b) hysteretic response

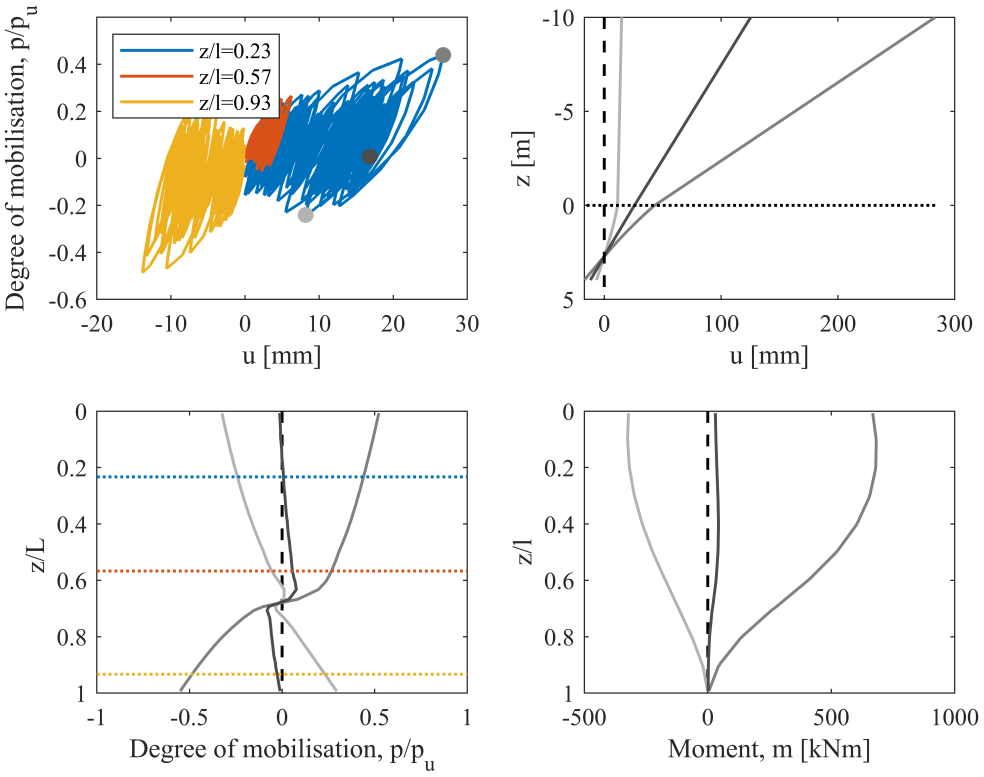

Figure 6.26: Computed response to storm load with pile length associated with Figure 6.25 (a) Normalised distributed lateral reaction response 'degree of mobilisation' at three depths (b) Lateral displacement u with depth (c) Depth varying degree of mobilisation at peak load and unload(d) bending moment m with depth below mudline

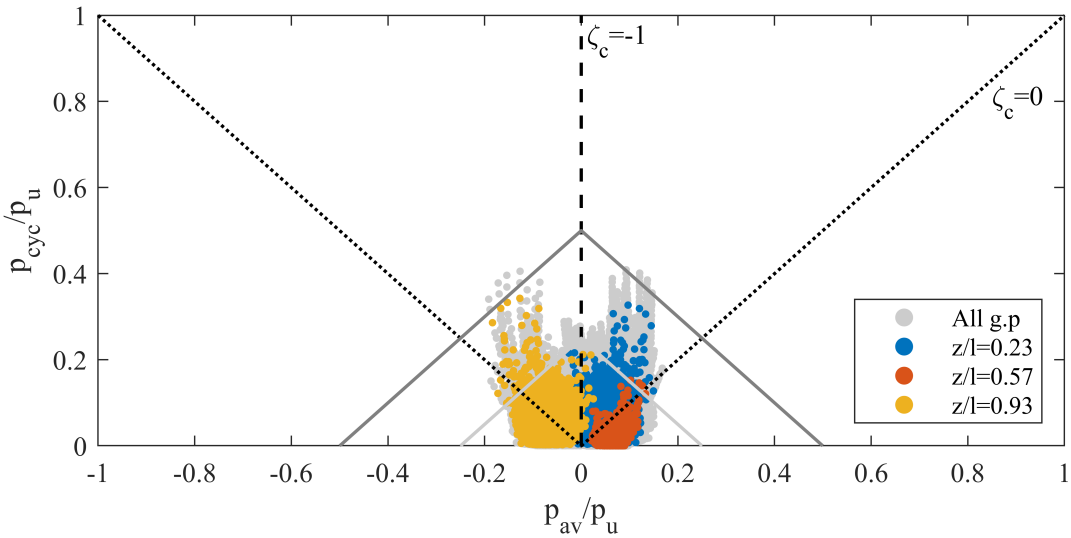

Figure 6.27: Load characterisation of all Gauss point half-cycles in terms of average and cyclic degree of mobilisation.

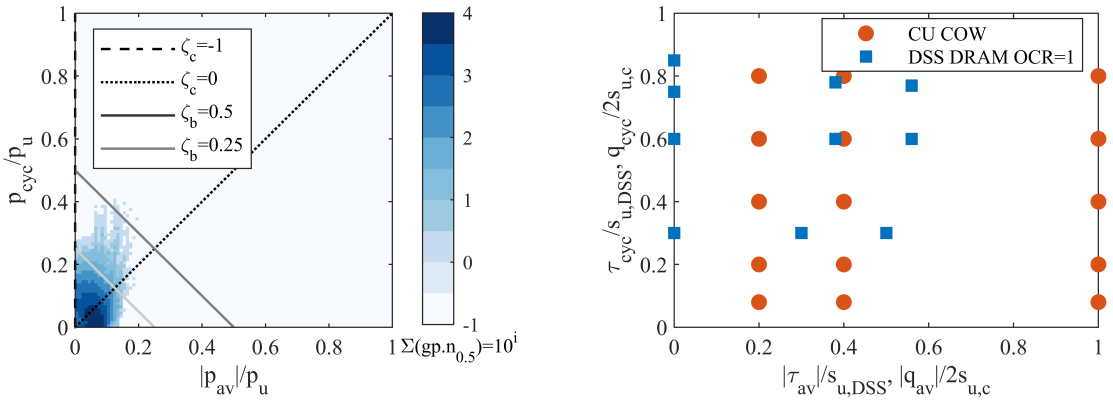

(a) **(b)**

Figure 6.28: (a) Heat map of Gauss point degree of mobilisation (b) Location of element tests regimes, CU COW as per Section 6.2 and DSS tests of Drammen clay which form the initial contour diagrams as in Section 4.1.2

Figure 6.28a shows the same data plotted as a heatmap in which the absolute value of average lateral pressure is used, removing directionality. The vast majority of cycles occur with a maximum mobilisation of $p_{max}/p_u < 0.25$. Figure 6.28b shows locations of element tests normalised by respective undrained shear strength in CU (Cowden) and DSS (Drammen) conditions. Direct comparison of loading intensity between lateral pressure and shear stress can be made if one assumes $\tau/s_u \approx p/p_u$ as postulated by (Zhang and Andersen, 2017). This relationship only considers the integrated behaviour and not .

Although the $\tau/s_u \approx p/p_u$ relationship does not capture local lateral changes in shear stress, which would be much higher close to the pile, it is clear that element tests in these example sets are specified at far higher magnitudes than would be experienced by much of the soil volume during this fairly severe storm load. Regardless of modelling method used, this suggests behaviour observed in the element tests would need to be extrapolated (to the lower stress magnitudes) when modelling the pile response. It is also true, however, that the majority of the cycles at low amplitude contribute very little to the overall response and that element tests undertaken at such magnitudes would probably show very little strain development. It may, of course, be possible to discount loading below a certain threshold. It should be noted that rate-dependency of the reference quantity (s_u or p_u) is not considered in this comparison.

Element testing should be defined to be at stress levels expected in soil. This is true for cyclic loading too. In applying an example storm load to the 1D model and deriving the magnitude of lateral pressure down the pile a comparison can be made between the scales, aiding the specification of constant amplitude tests.

6.6 Summary

In this chapter, 1D Winkler-type models were extended to include parallel multi-surface kinematic hardening models with additional mechanisms to capture rate-dependency and the effects of many cycles. Computation of a selection of PISA pile tests were used to compare normalised parameters calibrated at element scale for use at field scale. Suitably calibrated macro models reproduced the ground level of the 1D model well, offering a useful and rapid alternative for calibration or prediction of similar dimensioned pile tests.

The monotonic response of the 1D model was computed using the PISA method with parameters reported by Minga and Burd (2019), locally altered to reproduce each pile response. This method is widely accepted and can be applied with varying accuracy at various stages of the design cycle by employing 'rule-based' or 'numerical-based' calibration. Multiple surfaces with kinematic hardening allow for computation of unload and hysteresis, retaining the accuracy of the loading response prediction.

Rate and cyclic effects were implemented as per Chapter 5, building upon the calibrated monotonic response. For monotonic pile tests at varied rates the normalised viscous parameter η_{10}, calibrated to CU tests, works well. This suggests a promising route to calibration for design .

A 'local softening' model captured the cyclic response at element level well. Applying similar parameters at field scale did not capture the observed response, particularly with regards to ratcheting. In softening models, any ratcheting which develops is due to global strength reduction. As such a 'global softening' model was calibrated to reproduce the displacement accumulation, although this resulted in excessive post-cyclic softening. Instead a separate, HARM, ratcheting element was used and calibrated to the pile response. To truly model behaviour correctly, a ratcheting

element is necessary at pile scale, which is not the case for laboratory tests in the same material.

In summary, if calibrating a PISA-type 1D monopile model from laboratory tests only, rate and stiffness change parameters may be used directly from a macro model calibrated to cyclic laboratory tests. This may be *CU* tests (as in this chapter) or *DSS* tests, since the results of Section 4.1 showed that similar parameters were used for both test types in the same soil. Ratcheting would likely be underestimated in this case, therefore HARM parameters may be derived from previous pile tests at laboratory or field scale. Further ideas for calibration of the additional ratcheting are suggested below.

Looking forward, with regards to cycling, the evidence presented in this section suggests there is a further mechanism which is not being captured when behaviour at element scale is mapped to the soil reactions of a 1D model. The problem is, of course, a boundary value problem and the difference may be due to gapping, local softening in the gap or dissipation of pore-pressures. It may also be true that integration of cyclic effects from an element of soil to the soil reaction curves may not be simply be achieved with normalised parameters. Further work is required to ascertain and quantify the difference.

Additional work is likely to involve further experimental evidence, such as in the PICASO project, in which a considerable number of cyclic element tests and pile tests will be undertaken providing a larger data-set to draw upon. Mapping of cyclic mechanisms and parameters could also be the subject of a numerical study of the effects of integration from continuum to the 1D soil reactions. A similar rate-independent continuum model could by implemented in FEA and used to model the full pile behaviour to cyclic lateral loads. Resulting cyclic parameters for the soil reactions could be derived, in a similar exercise to the PISA numerical method for the monotonic curves. The evidence in this section suggests that the additional mechanism may well be an accumulation of displacement only, such that it may be sufficient to calibrate a HARM model at for each soil reaction from the FEA analyses.

Chapter 7

Development of effective stress models

7.1 Introduction

Effective stress changes are not explicitly considered in the total stress models presented in Chapters 3 to 4, which results in some inherent limitations. Firstly, consolidation (volumetric change) is not computed, instead the backbone is derived from post-consolidation behaviour. Whilst this may be suitably normalised for isotropically consolidated samples, it was found that anisotropically consolidated tests were not represented in a satisfactory way (Figure 3.13a). Secondly, it is clear from evidence such as that presented in Figure 3.34, that cyclic loading in undrained conditions causes progressive changes in effective stress. This is not considered, but rather the effects on strain development were modelled by softening yield strengths and/or inclusion of a ratcheting element.

Explicit prediction of effective stress may therefore have some benefits and provide further insight into behaviour of clays due to cyclic loading. This chapter does so by developing a multi-surface Modified Cam Clay (MCC) model in the hyperplasticity framework. This is a model at early stages of development, therefore only provisional ideas of the direction of this work are presented.

7.2 Methodology - Modified Cam Clay

The Modified Cam Clay (Roscoe and Burland, 1968) model makes use of the critical state framework (Schofield and Wroth, 1968) to describe the behaviour of soft clays.

The most basic MCC model requires only a few, easily calibrated, parameters to describe fully much of the key behaviour observed in deforming soft clays: elastic behaviour at low stresses, plastic behaviour at yield, and the coupling between volume and strength changes. It is widely used as a constitutive model in many Finite Element programs and computations of soil behaviour.

Basic MCC models have their limitations *i.e.*: not capturing non-linearity at small strains and less accurate representation of the behaviour of heavily over-consolidated clays. However, as noted by Muir Wood (1990), relatively straightforward changes can be made to incorporate more realistic features of soil response. It therefore serves as an obvious first choice as the basis for developing a model to cater for effective stress modelling of clays.

Houlsby (2000) present a formulation of a conventional MCC model in the hyperplasticity framework, which is extended to multiple surfaces and then continuous hyperplasticity. Likitlersuang and Houlsby (2007) then included linear viscosity and successfully reproduced triaxial tests on Bangkok clay. Cassiani et al. (2017) extend a conventional MCC model with a rate-dependent yield surface with an empirical power law on volumetric strain rates.

In this chapter a simple MCC model is developed which :

- is formulated in $p' - q$ space
- is rate-dependent, following the underlying physics of rate process theory
- is extended to employ multiple surfaces
- allows for combined stress and strain control, such that undrained constant stress amplitude cycles can be applied

The model is able to predict consolidation (isotropic and anisotropic) and subsequent monotonic or cyclic shearing and is validated against selected triaxial tests from the Wenzhou clay database presented in Chapter 3.

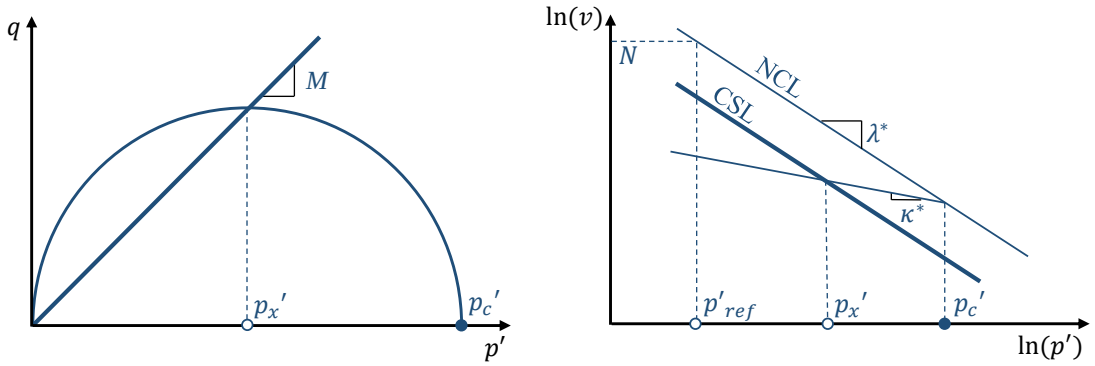

Figure 7.1: Definitions of Modified Cam Clay parameters

7.3 Single surface model

7.3.1 Rate independent

The model is formulated in terms of triaxial stress variables p', q and conjugate strains $\varepsilon_v, \varepsilon_q$, p is used in place of p' throughout this section. Houlsby and Puzrin (2006) and earlier Collins and Houlsby (1997) show that the conventional MCC model can be derived from at least two possible pairs of energy and dissipation functions. Here the Helmholtz free energy and dissipation function are defined as:

$$f = p_r \kappa^* exp\left(\frac{1}{\kappa^*}(\varepsilon_v - \alpha_v) + \frac{3g}{2\kappa^*}(\varepsilon_q - \alpha_q)^2\right) \tag{7.1}$$

$$d = p_x\left(\dot{\alpha_v} + \sqrt{\dot{\alpha_v}^2 + M^2\dot{\alpha_q}^2}\right) \tag{7.2}$$

with

$$2p_x = p_c = p_r exp\left(\frac{\alpha_v}{\lambda^* - \kappa^*}\right) \tag{7.3}$$

κ^*, λ^* and M correspond to MCC parameters as defined in Figure 7.1. g is the shear modulus number and is defined by:

$$g = \frac{1}{\kappa^*}\frac{3(1-2\nu)}{2(1+\nu)} \tag{7.4}$$

where ν is the constant Poisson's ratio on the isotropic axis. p_r is a reference pressure (taken as a default value of 1kPa) and corresponds to p_c when $\alpha_v = 0$. Internal variables α_v, α_q are associated with equivalent plastic strains and conjugate generalised

stresses χ_p, χ_q are derived in equations 7.13 to 7.15. Stress variables p, q are found by differentiating the energy function:

$$p = \frac{\delta f}{\delta \varepsilon_v} = p_r exp\left(\frac{1}{\kappa^*}\left(\varepsilon_v - \alpha_v\right) + \frac{3g}{2\kappa^*}\left(\varepsilon_q - \alpha_q\right)^2\right) \tag{7.5}$$

$$q = \frac{\delta f}{\delta \varepsilon_q} = 3g(\varepsilon_q - \alpha_q)p_r exp\left(\frac{1}{\kappa^*}\left(\varepsilon_v - \alpha_v\right) + \frac{3g}{2\kappa^*}\left(\varepsilon_q - \alpha_q\right)^2\right) = 3gp(\varepsilon_q - \alpha_q) \tag{7.6}$$

further differentiation of 7.5 and 7.6 gives:

$$\begin{aligned}\dot{p} &= \left(\frac{1}{\kappa^*}\left(\dot{\varepsilon}_v - \dot{\alpha}_v\right)\frac{3g}{2\kappa^*}\left(\varepsilon_q - \alpha_q\right)(\dot{\varepsilon}_q - \dot{\alpha}_q)\right)p_r exp\left(\frac{1}{\kappa^*}\left(\varepsilon_v - \alpha_v\right) + \frac{3g}{2\kappa^*}\left(\varepsilon_q - \alpha_q\right)^2\right) \\ &= \frac{p}{\kappa^*}\left(\varepsilon_v - \alpha_v\right) + \frac{q}{\kappa^*}\left(\varepsilon_q - \alpha_q\right) \qquad (7.7) \\ \dot{q} &= 3g\dot{p}(\varepsilon_q - \alpha_q) + 3gp(\dot{\varepsilon}_q - \dot{\alpha}_q) \\ &= \frac{q}{\kappa^*}(\dot{\varepsilon}_v - \dot{\alpha}_v) + \left(\frac{q^2}{p\kappa^*} + 3gp\right)(\dot{\varepsilon}_q - \dot{\alpha}_q) \qquad (7.8)\end{aligned}$$

This can be re-written in the more conventional elastic stiffness matrix form, where $\dot{\varepsilon}^e = \dot{\varepsilon} - \dot{\alpha}$:

$$\begin{bmatrix}\dot{p} \\ \dot{q}\end{bmatrix} = \begin{bmatrix}\frac{p}{\kappa^*} & \frac{q}{\kappa^*} \\ \frac{q}{\kappa^*} & \left(\frac{q^2}{p\kappa^*} + 3gp\right)\end{bmatrix}\begin{bmatrix}\dot{\varepsilon}_v^e \\ \dot{\varepsilon}_q^e\end{bmatrix} \tag{7.9}$$

Hence the bulk modulus $K = p/\kappa^*$ and shear modulus $3G = 3gp + q^2/p\kappa^*$ are pressure dependent and differ slightly from conventional MCC. This is consistent with Houlsby et al. (2019) in which normalised bulk stiffness $k = K/p = 1/\kappa^*$ and $g = G/p$ on the isotropic axis.

λ^* and κ^* also have slightly different meanings from those of conventional MCC, with the consolidation and swelling lines considered straight in $ln(p)$,$ln(v)$ space, as suggested by Butterfield, 1979, rather than $ln(p)$,v (Figure 7.1 right). Isotropic consolidation can be considered by rearranging Equations 7.3 and 7.5, noting that on the Normal Consolidation Line (NCL) $p_c = p$ and $\varepsilon_q = \alpha_q = 0$:

$$p = p_r exp\left(\frac{1}{\kappa^*}\left(\varepsilon_v - \alpha_v\right)\right) \Rightarrow \varepsilon_v = \kappa^* ln\left(\frac{p}{p_r}\right) + \alpha_v \tag{7.10}$$

$$p_c = p = p_r exp\left(\frac{\alpha_v}{\lambda^* - \kappa^*}\right) \Rightarrow \alpha_v = (\lambda^* - \kappa^*) ln\left(\frac{p}{p_r}\right) \tag{7.11}$$

by combining and assuming logarithmic strains:

$$\begin{aligned}\varepsilon_v &= \kappa^* ln\left(\frac{p}{p_r}\right) + (\lambda^* - \kappa^*) ln\left(\frac{p}{p_r}\right) \\ &= ln\left(\frac{p}{p_r}\right)(\lambda^*) \\ ln\left(\frac{v}{v_0}\right) &= ln\left(\frac{p}{p_r}\right)(\lambda^*)\end{aligned} \tag{7.12}$$

The swelling line (κ^*) is found in 7.10 by considering elastic strains only, $\dot{\alpha_v} = 0$. The complete constitutive behaviour can be derived from:

$$\overline{\chi_p} = -\frac{\delta f}{\delta \alpha_v} = p_r exp\left(\frac{1}{\kappa^*}\left(\varepsilon_v - \alpha_v\right) + \frac{3g}{2\kappa^*}\left(\varepsilon_q - \alpha_q\right)^2\right) = p \tag{7.13}$$

$$\overline{\chi_q} = -\frac{\delta f}{\delta \alpha_q} = 3g(\varepsilon_q - \alpha_q) p_r exp\left(\frac{1}{\kappa^*}\left(\varepsilon_v - \alpha_v\right) + \frac{3g}{2\kappa^*}\left(\varepsilon_q - \alpha_q\right)^2\right) = q \tag{7.14}$$

$$\chi_p = -\frac{\delta d}{\delta \dot{\alpha_v}} = p_x\left(1 + \frac{\dot{\alpha_v}}{\sqrt{\dot{\alpha_v}^2 + M^2 \dot{\alpha_q}^2}}\right) \tag{7.15}$$

$$\chi_q = -\frac{\delta d}{\delta \dot{\alpha_q}} = p_x\left(\frac{M^2 \dot{\alpha_q}}{\sqrt{\dot{\alpha_v}^2 + M^2 \dot{\alpha_q}^2}}\right) \tag{7.16}$$

Employing the condition $(\overline{\chi_p}, \overline{\chi_q}) = (\chi_p, \chi_q)$ gives:

$$\begin{aligned}\chi_p = \overline{\chi_p} \Rightarrow \chi_p - p_x &= p_x\left(\frac{\dot{\alpha_v}}{\sqrt{\dot{\alpha_v}^2 + M^2 \dot{\alpha_q}^2}}\right) \\ \chi_q = \overline{\chi_q} \Rightarrow \frac{\chi_q}{M} &= p_x\left(\frac{M\dot{\alpha_q}}{\sqrt{\dot{\alpha_v}^2 + M^2 \dot{\alpha_q}^2}}\right)\end{aligned} \tag{7.17}$$

The conventional yield function y is obtained by summing the squares of the volumetric and shear components of Equation 7.17. At yield, when $|\dot{\alpha_v}| + |\dot{\alpha_q}| \neq 0$:

$$\begin{aligned}(\chi_p - p_x)^2 + \left(\frac{\chi_q}{M}\right)^2 &= p_x^2\left(\frac{\dot{\alpha}_v^2}{\dot{\alpha_v}^2 + M^2 \dot{\alpha_q}^2}\right) + p_x^2\left(\frac{M^2 \dot{\alpha}_q^2}{\dot{\alpha_v}^2 + M^2 \dot{\alpha_q}^2}\right) \\ y = (\chi_p - p_x)^2 + \left(\frac{\chi_q}{M}\right)^2 - p_x^2 &= 0\end{aligned} \tag{7.18}$$

The incremental behaviour can then be derived following the methods presented in Appendix Section A.4, assuming a general control statement:

$$Sd\sigma + Ed\varepsilon = Tdt \tag{7.19}$$

where S and E are switch matrices, T is a rate array and dt is the time-step (which for rate-independent models is arbitrary). This allows for combined stress and strain control. For example, an undrained ($d\varepsilon_v = 0$) of dq over dt can be written:

$$\begin{bmatrix} 0 & 0 \\ 0 & 1 \end{bmatrix} \begin{bmatrix} dp \\ dq \end{bmatrix} + \begin{bmatrix} 1 & 0 \\ 0 & 0 \end{bmatrix} \begin{bmatrix} d\varepsilon_v \\ d\varepsilon_q \end{bmatrix} = \begin{bmatrix} 0 \\ \frac{dq}{dt} \end{bmatrix} dt \tag{7.20}$$

The control statement is specified for each increment of stress and/or strain application. The model is fully described by input parameters, M, λ^*, κ^* (shown in Figure 7.1), ν, $p_{x,0}$ and p_0. Stress is initialised at zero strain $\varepsilon_{v,0} = \varepsilon_{q,0} = 0$ where:

$$p = \chi_{p,0} = p_0 \quad q = \chi_{q,0} = 0 \quad p_x = p_{x,0} \tag{7.21}$$

and $p_0 \leq 2p_{x,0}$. Plastic strain $\alpha_v = \alpha_q = 0$ begins at $(p_{ref}, 0)$, so Equation 7.3 becomes:

$$\alpha_{v,0} = ln\left(\frac{2p_{x,0}}{p_r}\right)(\lambda^* - \kappa^*) \tag{7.22}$$

To capture changes in specific volume, N is defined corresponding to the initial specific volume at $p_{ref} = 1kPa$. Considering Figure 7.1, at p_0:

$$ln(v_0) = ln(N) - (\lambda^* - \kappa^*)ln\left(\frac{2p_{x,0}}{p_r}\right) - \kappa^* ln\left(\frac{p_0}{p_r}\right) \tag{7.23}$$

Figure 7.2 shows example model computations for an arbitrary material with parameters as shown in Table 7.1. A drained and an undrained test are computed in which both are subject to initial conditions $p_0 = p_{x,0} = 5kPa$ and isotropic consolidation of $dp = 95kPa, dq = 0kPa$ before:

- Drained application of $dp = 50kPa$, $dq = 150kPa$, or
- Undrained application of $d\varepsilon_v = 0$,$d\varepsilon_q = 0.15$.

Computations behave as expected, with an initial elastic change in volume until $p = p_{c,0} = 10kPa$ at which point consolidation follows the specified λ^*. A weaker response is shown in undrained conditions with no further consolidation and a reduction

Table 7.1: MCC parameters for an idealised clay

RI					+ RPT	
M	λ^*	κ^*	ν	N	η_{10}	t_{ref} [hrs]
1.2	0.12	0.02	0.2	3.5	0.1	10^4

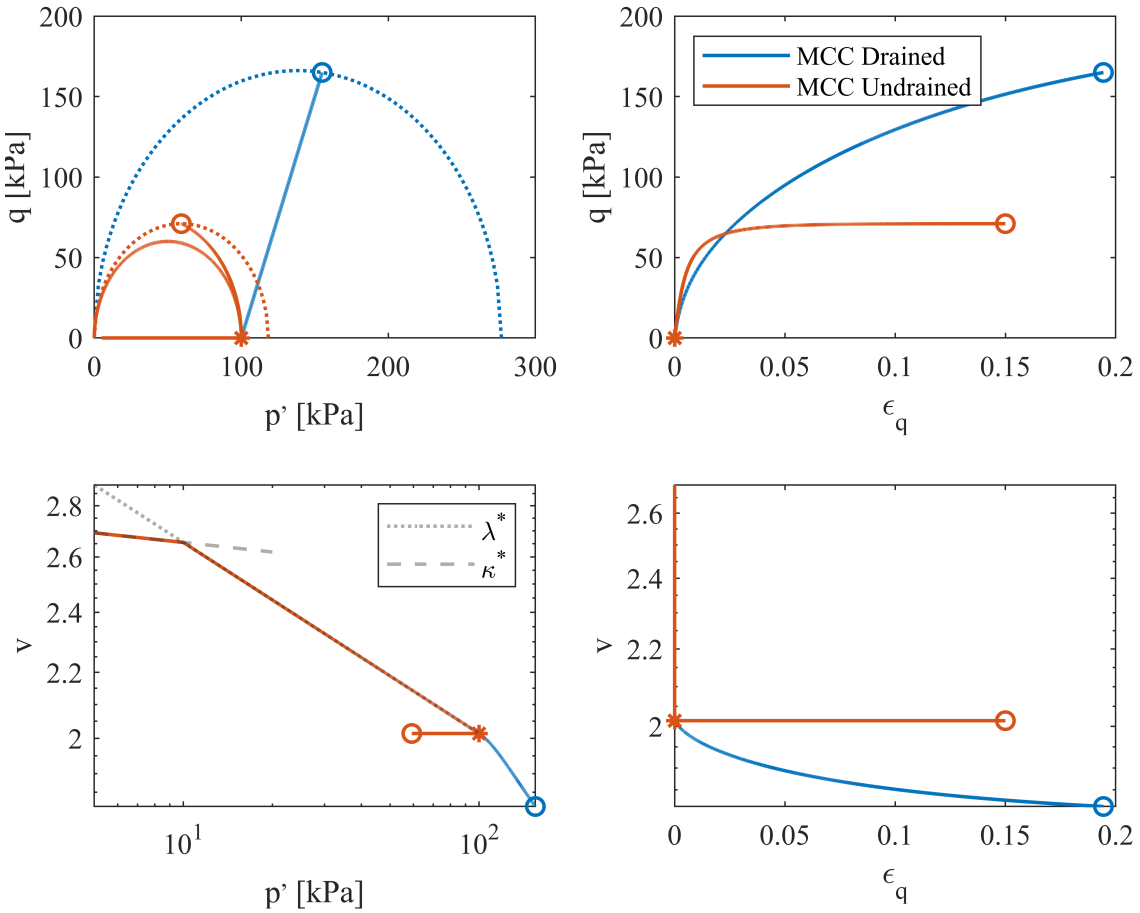

Figure 7.2: Single Surface MCC Model prediction of an isotropically consolidated sample with subsequent drained and undrained shearing

in mean effective stress p. These results are conventional and not novel, but allows for a MCC model codified in the hyperplasticity framework to be further extended in the following sections.

7.3.2 Rate dependent model

Rate dependency is introduced in a similar way to Section 3.3 following rate process theory. Rate-dependent dissipation can now be written as the flow potential:

$$w = \frac{\mu}{t_{ref}^2}\left(\cosh\left(\frac{t_{ref}\langle\sqrt{x} - p_x\rangle}{\mu}\right) - 1\right) \tag{7.24}$$

$$x = (\chi_p - p_x)^2 + \frac{\chi_q}{M}^2 \tag{7.25}$$

where t_{ref} is the time constant at which rate-dependent behaviour changes from linear to logarithmic and μ is a viscous parameter which here is described as $\mu = p_c t_{ref}\eta$

using a non-dimensional viscous parameter $\eta = \eta_{10}/ln(10)$. Equation 7.24 is then written:

$$w = \frac{p_c \eta}{t_{ref}} \left(\cosh \left(\frac{\langle \sqrt{x} - p_x \rangle}{p_c \eta} \right) - 1 \right) \tag{7.26}$$

Further constitutive behaviour follows Section 7.3.1 with a general control statement as in Equation 7.19. Incremental behaviour is derived in Appendix Section A.4.1.

Figure 7.3a shows example model computations for an arbitrary material with parameters as shown in Table 7.1. Undrained tests are computed, in which the consolidation time and shearing time (and therefore rates) are varied. Initial conditions $p_0 = p_{x,0} = 5kPa$ as before, followed by:

- Isotropic consolidation of $dp = 95kPa, dq = 0kPa$ over time $t = T_c$ with a constant stress rate $dp/dt = 95/T_c$
- Undrained application of $d\varepsilon_v = 0$,$d\varepsilon_q = 0.15$ over time $t = T_u$, with a constant strain rate $d\varepsilon_q/dt = 0.15/T_u$.

T_c =1 year or 1 week and T_u =1 day, 1 week or 1 month. A rate-independent (RI) analysis is also shown as a baseline. Here it can be seen that the time history of consolidation and the rate of subsequent shearing become important. At failure, the undrained shear strength unsurprisingly increases with shearing rate (reduction of T_u); however, it also increases with consolidation time (T_c). With T_c =1 year, consolidation follows the rate-independent case applied at a suitably low rate. With T_c=1 week, consolidation (i.e. plastic volumetric strain α_v) is reduced, affecting the location of the yield surface prior to shearing. This restates the argument that s_u is not a fundamental property of soil behaviour and is dependent upon history of loading (in this case rate). Pre-failure behaviour also differs; at fast shearing rates and long consolidation times the initial response is highly elastic.

Importantly this shows that for an accurate prediction of response when using a rate-dependent model, all aspects of soil history must be modelled diligently and correctly.

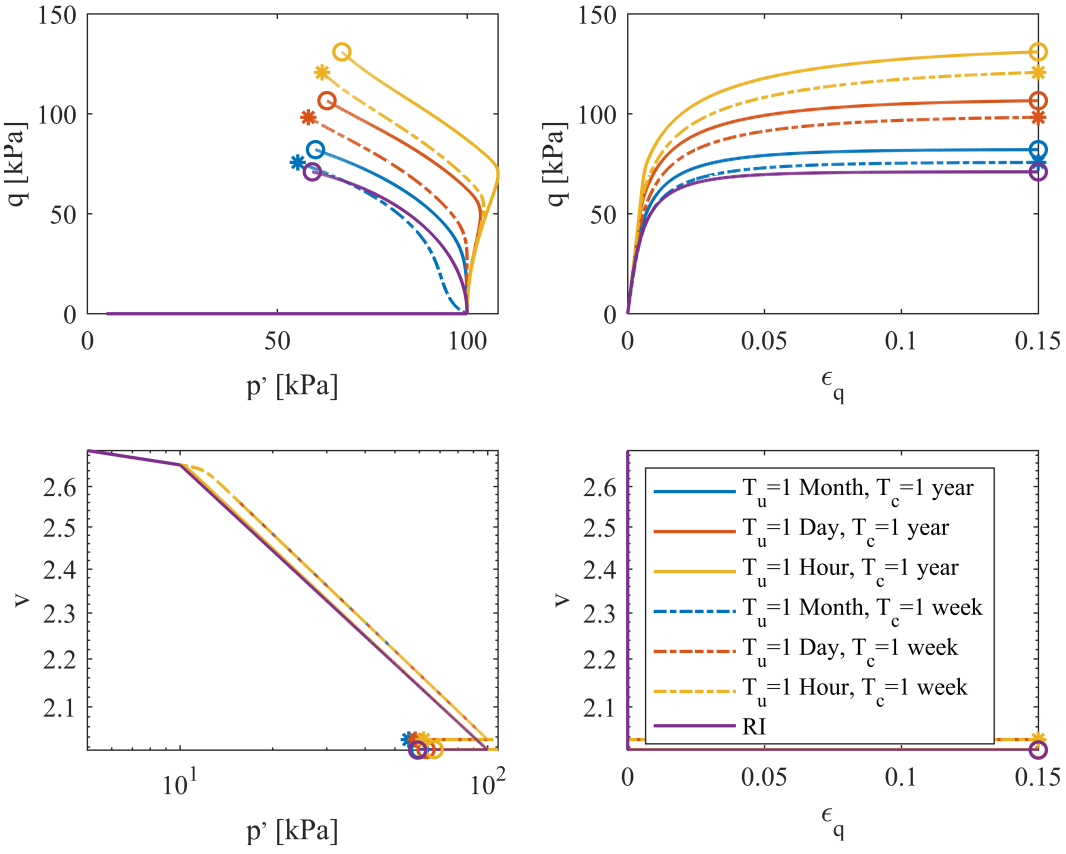

(a)

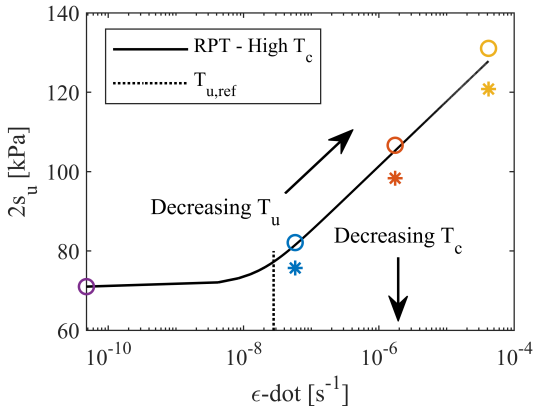

(b)

Figure 7.3: (a) Single Surface MCC Model prediction of a sample subject to constant stress rate isotropic consolidation over time T_c and subsequent undrained shearing to failure $\varepsilon_q = 0.15$ over time T_u (b) Twice undrained shear strength with shearing time (corresponding to points in (a)), also shown rate process theory equation with similar parameters as per Equation 3.19

7.4 Extension to multiple surfaces

Here the rate-dependent model is extended to multiple surfaces. Multiple versions of the single surface model are employed in which some property is varied and each is subject to a weighting factor Ω_i, where i indicates surface number from 1 to the number of surfaces N_s. This is a similar structure to the PIMS model by Whyte et al. (2020). Here the elastic stiffness is varied by changing κ^* by a factor κ_{fac}:

$$\kappa_i^* = \frac{\kappa^*}{\kappa_{fac,i}} \tag{7.27}$$

$$\sum_{i=1}^{Ns} \Omega_i = 1 \tag{7.28}$$

The energy function and flow potential can then be written:

$$f = \sum_{i=1}^{Ns} \Omega_i f_i \quad \rightarrow \quad f_i = p_r \kappa_i^* exp\left(\frac{1}{\kappa_i^*}\left(\varepsilon_v - \alpha_{v,i}\right) + \frac{3g_i}{2\kappa_i^*}\left(\varepsilon_q - \alpha_{q,i}\right)^2 \right) \tag{7.29}$$

$$w = \sum_{i=1}^{Ns} \Omega_i w_i \quad \rightarrow \quad w_i = \frac{p_{c,i}\eta}{t_{ref}} \left(\cosh\left(\frac{\langle \sqrt{x_i} - p_{x,i} \rangle}{p_{c,i}\eta} \right) - 1 \right) \tag{7.30}$$

$$x_i = (\chi_{p,i}^* - p_{x,i})^2 + \frac{\chi_{q,i}^*}{M}^2 \tag{7.31}$$

where $\chi_i^* = \chi_i \Omega_i$ and:

$$2p_{x,i} = p_{c,i} = p_{r,i} exp\left(\frac{\alpha_{v,i}}{\lambda^* - \kappa_i^*} \right) \tag{7.32}$$

$$g_i = \frac{1}{\kappa_i^*} \frac{3(1-2\nu)}{2(1+\nu)} \tag{7.33}$$

If for all i, $\kappa_{fac,i} = 1$, the model reduces to the single surface equivalent. Incremental behaviour can be derived in the usual way and is shown in full in Appendix A.4. The model is defined with the same parameters as before although the initialisation varies:

$$p = p_0, \quad \chi_{p,i,0}^* = \Omega_i p_0, \quad q = \chi_{q,0}^* = 0, \quad p_{x,i,o} = \Omega_i p_{x,0}, \quad p_{r,i} = \Omega_i p_r \tag{7.34}$$

$$\alpha_{v,i,0} = ln\left(\frac{2p_{x,i,0}}{p_{r,i}} \right) (\lambda^* - \kappa_i^*) \tag{7.35}$$

$$v_0 = \sum_{i=1}^{Ns} \left(exp\left((ln(\Omega_i N) - (\lambda^* - \kappa_i^*) ln\left(\frac{2p_{x,i,0}}{p_{r,i}} \right) - \kappa_i^* ln\left(\frac{\chi_{p,i,0}^*}{p_{r,i}} \right) \right) \right) \tag{7.36}$$

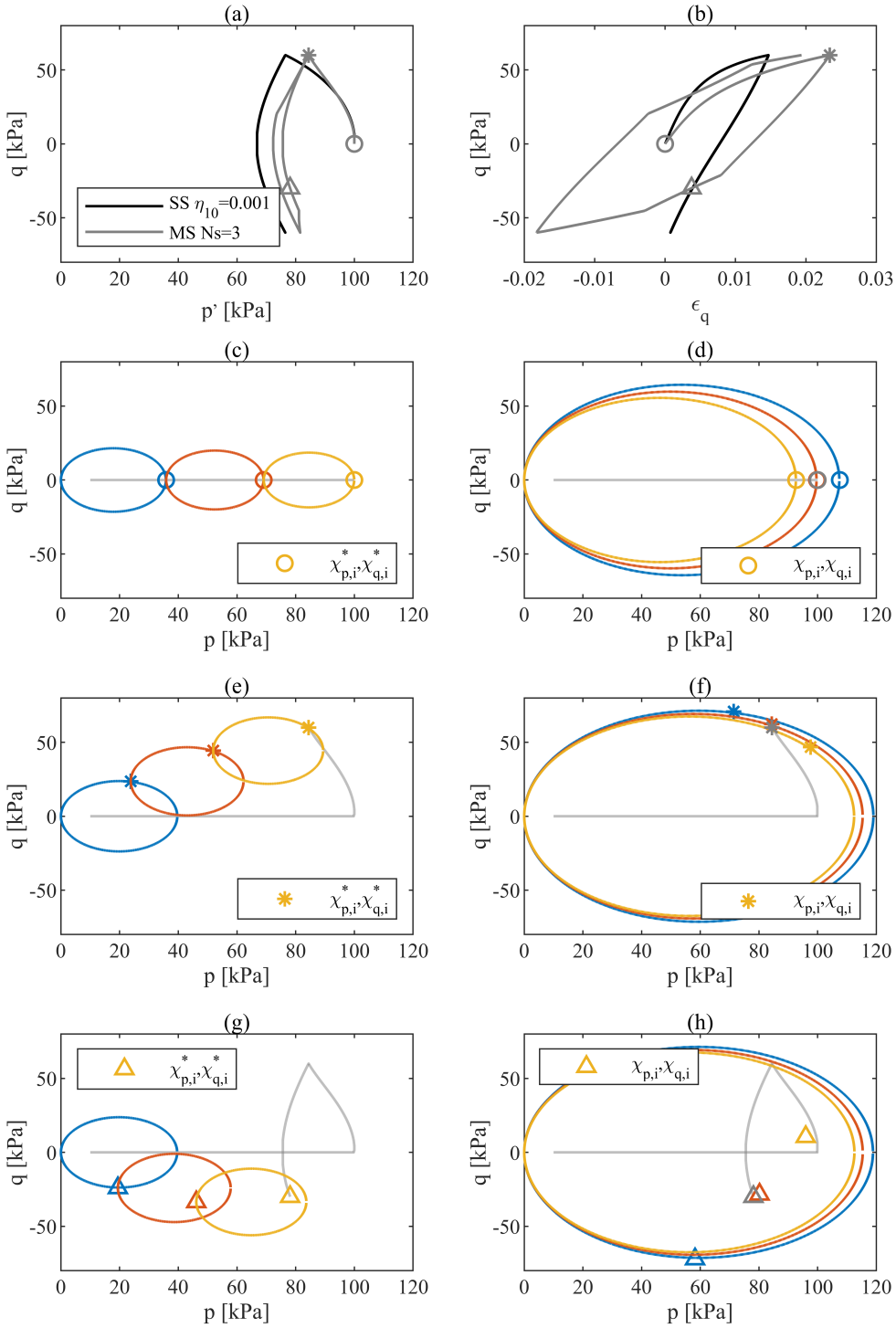

Figure 7.4: (a) and (b) Comparison of a single surface and multi-surface (equal weighting) pseudo rate independent model ($\eta_{10} = 0.001$) subject to undrained loading, unloading and reloading, input parameters as in Table 7.1 with multi-surface weightings defined in Equation 7.37. (c-h) Depiction of multi-surface model development at various points during loading history and in two forms for completeness: (c,e,g) 'Daisy chain' of the sum of local yield surfaces and weighted stresses ($\chi^*_{p,i}$, $\chi^*_{q,i}$), where $p = \sum(\chi^*_p)$,(d,f,h) 'Weighted average' of local yield surfaces and local stresses ($\chi_{p,i}$, $\chi_{q,i}$) where p is the centroid of the local stresses

Figure 7.4a and b show a comparison of a single surface and multi-surface model with input parameters as per Table 7.1 but with $\eta_{10} = 0.001$ such that the models are pseudo-rate-independent. Surface factors are specified with equal weightings as:

$$\kappa_{fac} = \begin{bmatrix} 1 \\ 0.5 \\ 0.2 \end{bmatrix}, \quad \Omega = \begin{bmatrix} 1 \\ 1 \\ 1 \end{bmatrix} = \begin{bmatrix} 1/3 \\ 1/3 \\ 1/3 \end{bmatrix} \tag{7.37}$$

where for ease of input $\Omega = \Omega/\Sigma(\Omega)$. Both models are subject to slow constant stress rate isotropic consolidation $T_c = 48$hrs followed by undrained 'saw-tooth' loading, unloading and reloading to $q = \pm 60$kPA at a constant stress rate $dq/dt = 2.4kPa/s$.

In the single surface model the response is elastic on unload and reload, tracing the same path in stress $(q - p)$ and strain $(q - \varepsilon_q)$ space. With multiple surfaces, a hysteresis loop and reduction in effective stress is shown. The development of stress can be displayed in two ways; as a 'daisy chain' or a 'weighted average', both of which are shown for completeness. This is a choice of presentation and does not affect the underlying model. Figure 7.4c,e and g show the 'daisy chain' method in which detail of the local weighted internal stress (χ_p^*, χ_q^*) location and yield surface at four points in the loading history. The corresponding yield surfaces are shown subject to weight and varied stiffness. Since the global stress (p, q) is the sum of the local stresses, each yield surface is shown offset with its origin at the previous surface's current stress co-ordinate. **Note that each yield surface remains pinned to it's local isotropic axis**. Figure 7.4d,f and h show the 'weighted average' presentation where internal stress (χ_p, χ_q) location and yield surfaces are shown without weighting at the same three points in the loading history. The corresponding yield surfaces remain roughly the same with subtle changes due to varying κ^*.(p, q) is now the centroid of local stresses (in this case a triangle). During consolidation (c,d) and initial loading (e,f) local stresses lie on the yield surface. On unloading each surface behaves elastically until (g,h) when just one further surface yields altering the global strain behaviour. Surfaces then progressively yield but at differing locations on the yield surface such that plastic strains due to associated flow will also differ. This gives rise to the hysteresis behaviour observed.

Figure 7.5 shows the same analysis but with varied weights on each model, where:

$$\kappa_{fac} = \begin{bmatrix} 1 \\ 0.5 \\ 0.2 \end{bmatrix}, \quad \Omega = \begin{bmatrix} 3 \\ 2 \\ 1 \end{bmatrix} = \begin{bmatrix} 1/2 \\ 1/3 \\ 1/6 \end{bmatrix} \tag{7.38}$$

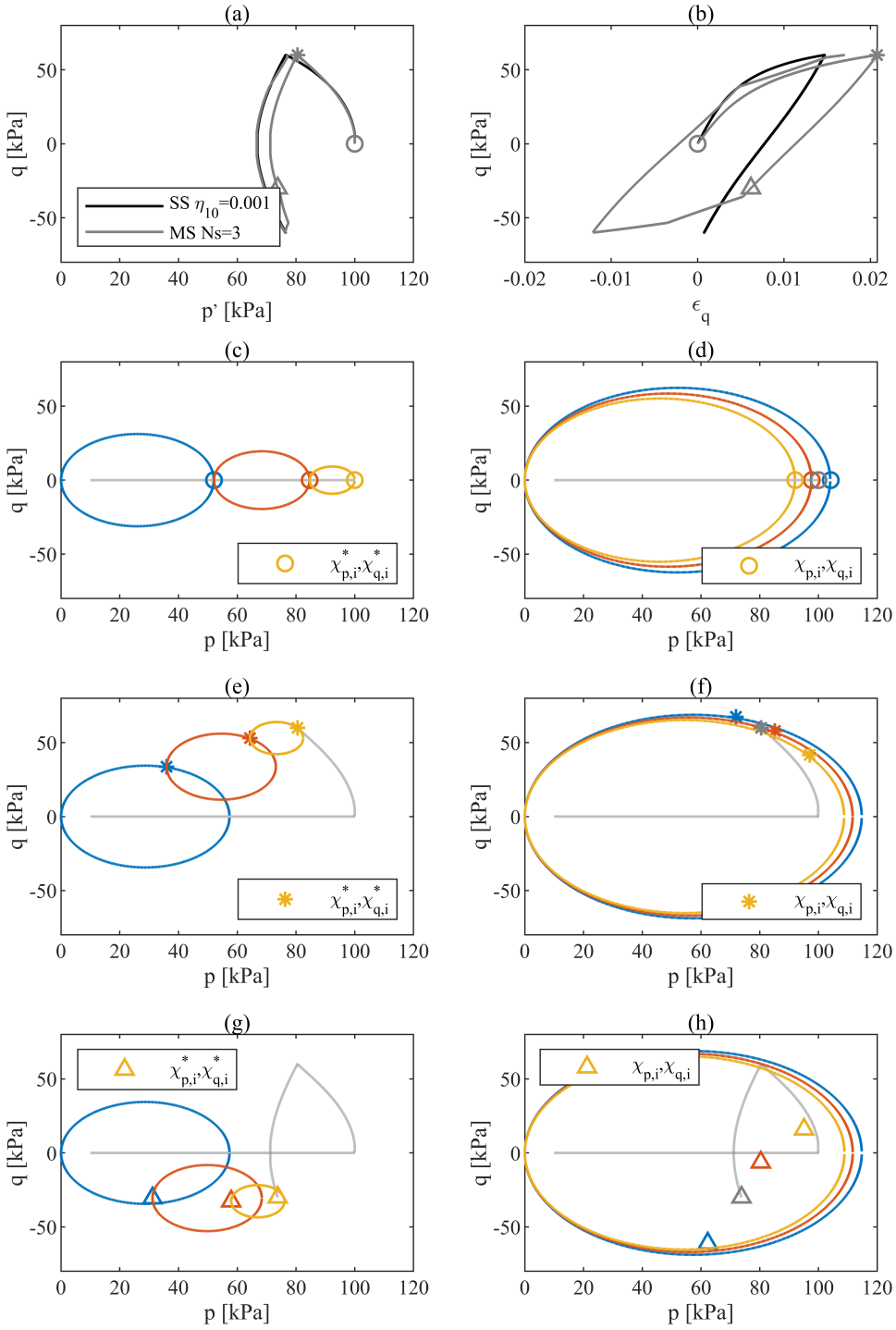

Figure 7.5: (a,b) Comparison of a single surface and multi-surface (varied weight) pseudo rate independent model ($\eta_{10} = 0.001$) subject to undrained loading, unloading and reloading, input parameters as in Table 7.1 and Equation 7.38. (c-h) Depiction of multi-surface model development at various points during loading history and in two forms for completeness: (c,e,g) 'Daisy chain' of the sum of local yield surfaces and weighted stresses $(\chi^*_{p,i}, \chi^*_{q,i})$, where $p = \sum(\chi^* p)$ (d,f,h) 'Weighted average' of local yield surfaces and local stresses $(\chi_{p,i}, \chi_{q,i})$ where p is the **weighted** centroid of the local stresses

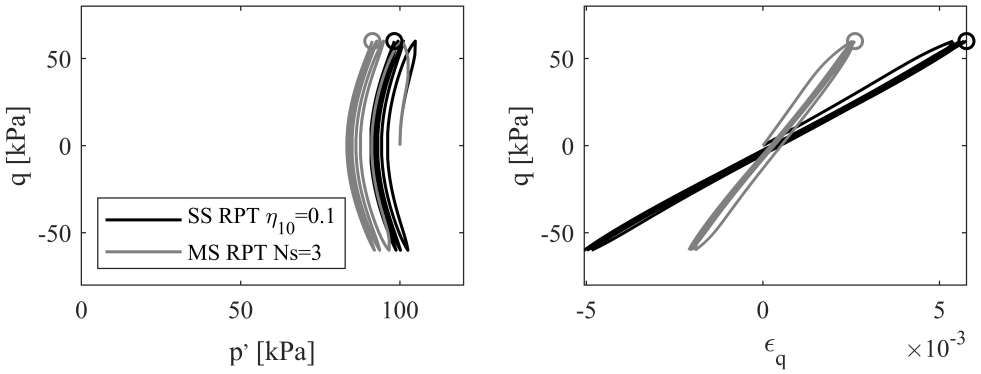

Figure 7.6: Comparison of a single surface and multi-surface (varied weighting) pseudo rate dependent model ($\eta_{10} = 0.1$) subject to undrained loading and three cycles of loading and reloading, input parameters as in Table 7.1 with multi-surface weightings defined in Equation 7.38

Behaviour is similar, although the highly weighted surface dominates the global response. This is most easily observed in the 'daisy chain' presentation (Figure 7.5c,e,g). In the weighted average depiction, Figure 7.5d,f,h, the yield surfaces remain similar but the weighting shifts the global strength towards the point with higher weight, i.e. a centroid of the weighted mass. With a suitable selection of k_{fac} and Ω, the response in strain space could be calibrated to experimental tests.

The effects of the addition of rate dependency (by returning to $\eta_{10} = 0.1$) is shown in Figure 7.6, where the same load (now over 3 cycles) and input parameters are applied to a model with the same local weightings as in Equation 7.38. The single surface model shows a reduction of effective stress and some hysteresis on unloading, although as discussed in Section 7.3.2, this is heavily dependent upon consolidation history.

7.5 Application of the model

In this section the model is applied to triaxial tests in Wenzhou soft clay, introduced in Chapter 3 with the notation 'WEN'. The majority of the data comes from papers by Cai et al., 2017 and Guo et al., 2018, with some further data kindly shared by the authors. K_0 consolidated triaxial tests subject to undrained monotonic shearing and cyclic loading are reproduced. This unit is chosen as time histories of consolidation are available, facilitating modelling and comparison of the full history of loading.

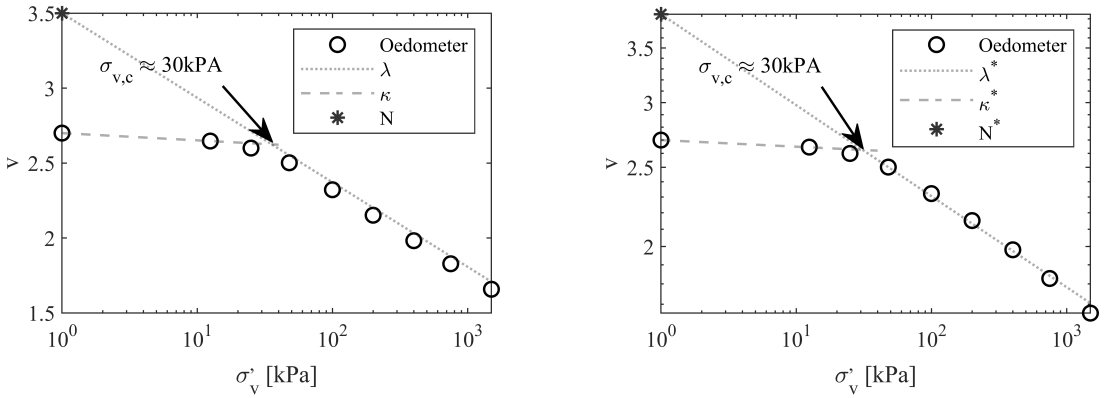

Figure 7.7: Oedometer compression date after Guo et al., 2018 with (a) Conventional linear-log consolidation and swelling lines (b) log-log consolidation and swelling lines

Much of the data is presented in terms of q, σ_r and ϵ_a, ϵ_r whilst the model formulation follows q, p, thus conversion is required following:

$$p = \frac{\sigma_a + 2\sigma_r}{3} \qquad q = \sigma_a - \sigma_r \qquad \varepsilon_v = \varepsilon_a + 2\varepsilon_r \qquad \varepsilon_q = \frac{2}{3}(\varepsilon_a - \varepsilon_r) \tag{7.39}$$

$$\sigma_a = p + \frac{2}{3}q \qquad \sigma_r = p - \frac{1}{3}q \qquad \varepsilon_a = \frac{1}{3}\varepsilon_v + \varepsilon_q \qquad \varepsilon_r = \frac{1}{3}\varepsilon_v - \frac{1}{2}\varepsilon_q \tag{7.40}$$

MCC parameters λ^*,κ^* and N^* are calibrated from conventional Oedometer tests shown in Figure 7.7. Figure 7.7a shows parameters calibrated as straight lines in linear v-log p space where $\lambda = 0.245$ and $\kappa = 0.021$, similar to those presented by Li et al. (2011) in the same material. Gradients in log-log space can then be estimated by:

$$\kappa^* = \frac{\kappa}{v_{av}} \approx \frac{\lambda}{2.6}, \quad \lambda^* = \frac{\lambda}{v_{av}} \approx \frac{\lambda}{2.2} \tag{7.41}$$

where v_{av} is the average specific volume of the test on the swelling and consolidation lines respectively. This is useful if full data were unavailable. Figure 7.7b shows the resulting fit in log$v$-log p, as used in this chapter. A Poisson's ratio of ν=0.2 is assumed.

Rate dependent parameters are calibrated to three isotropically consolidated compression tests $CIUc$ at varied rates (0.01%/ min,0.05%/ min and 0.1%/ min). Figure 7.8a shows the measured response (dashed) alongside model predictions. Consolidation history is not known and is therefore assumed to be applied at constant stress rate over 3 days. $t_{ref} = 10^4$hr is assumed following Section 3.3.1 and previous literature

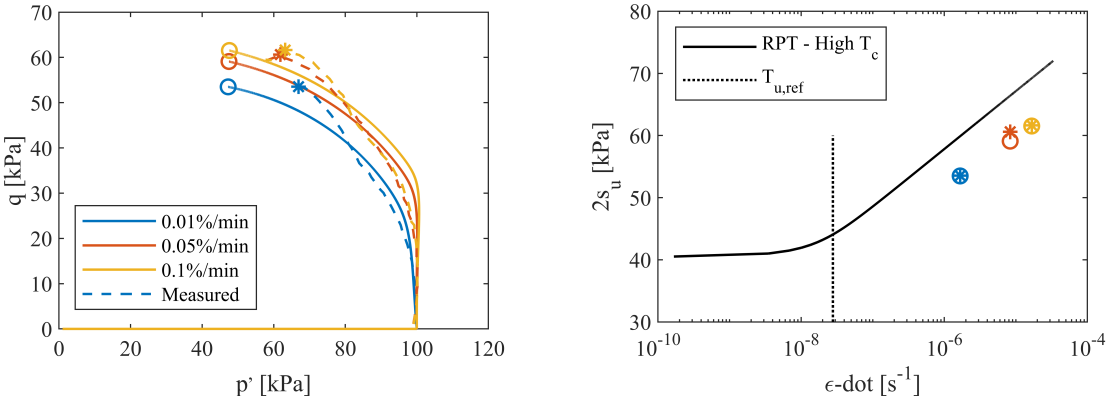

(a) **(b)**

Figure 7.8: (a) $CIUc$ tests at three strain rates, (- -) Measured (-) Model (b) s_u against shearing rate corresponding to a (*) Measured (o) Model, predicted rate-process theory curve for high consolidation time T_c shown.

(i.e. Vaid and Campanella, 1977). $\eta_{10} = 0.1$ is calibrated to the change in undrained shear strength whilst MCC parameter M must be recalibrated to an equivalent value at zero rate $M_{\dot{\varepsilon}\to 0} = 0.81$ after an infinite consolidation time. Figure 7.8b shows predicted and modelled s_u alongside the RPT curve at high consolidation time. As in Figure 7.3b the points are likely to fall below this curve since T_c is relatively small.

Further monotonic and cyclic tests were undertaken on anisotropically consolidated specimens with an assumed $K_0 = 0.55$. The consolidation history is shown in Figure 7.9a alongside the assumed profile for the CIU_c tests. Stresses are increased following the assumed K_0 behaviour over ≈ 1.5 days before being held for ≈ 3 days to allow for creep (controlled by σ_r and σ_v). The sample was then sheared to failure at a rate of $0.01\%/min$. Figure 7.9b shows the measured response in comparison to a CIU_c test sheared at the same rate. Although the final strengths are similar, the M value differs considerably. This is a surprising anomaly and is assumed to be fundamental to a given material at consistent rates. To overcome this discrepancy, when modelling the CAU_c tests (as is the focus of the remainder of this chapter) a different zero rate M is assigned $M_{A,\dot{\varepsilon}\to 0} = 0.99$.

Table 7.2: MCC parameters for Wenzhou clay

RI				+ RPT		
λ^*	κ^*	N^*	ν	η_{10}	t_{ref} [hrs]	$M_{A,\dot{\varepsilon}\to 0}$ ($M_{I,\dot{\varepsilon}\to 0}$)
0.111	0.008	3.85	0.2	0.1	10^4	0.99 (0.81)

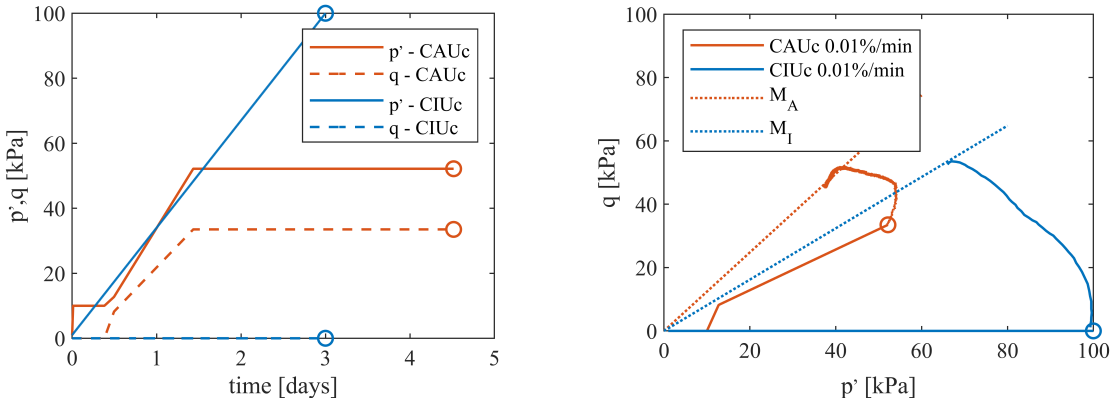

(a) **(b)**

Figure 7.9: (a) Consolidation history of $CAUc$ and $CIUc$ (assumed) tests (b) Measured response of $CAUc$ and $CIUc$ tests at shearing rate of $0.01\%/min$ in which considerable difference in M values are observed

Final model parameters for a single surface rate-dependent model are summarised in Table 7.2. The consolidation phase of the $CAUc$ test is applied as stress control (following Figure 7.10a where $p_0 = p_{ref} = 1kPa$). With the subsequent shearing phase to failure applied at a constant shearing rate to $d\varepsilon_q$=0.15. $p_{c,0}$ is estimated subject to the previous in-situ stress conditions and is derived from the Oedometer data in Figure 7.7 where $\sigma_{vc} = 30kPa$. Assuming $K_0 = 0.55$ and following definitions in Equation 7.39, $p_c = 22kPa$ and $q_c = 13.5kPa$, so that for an elliptical yield surface with $M \approx 1$, $p_c \approx 30kPa$. Clearly there is some uncertainty about this value due to potential sample disturbance but this is a best estimate and is important for prediction of the consolidation strains.

Figure 7.10b shows a comparison of the predicted and measured axial strain during consolidation alongside the predicted radial strain. True K_0 consolidation is not predicted as $\varepsilon_r \neq 0$. An increase in axial strain and subsequent creep phase is predicted well although the magnitude of strain is not well reproduced. During the shearing phase Figure 7.10c and d, the effective stress changes and axial strain development are accurately reproduced. Here rate-dependency of the response is key, producing an in initially elastic response before subsequent increase in strain and reduction of effective stress.

Next a multi-surface model is employed to predict a similarly consolidated CAU_{cyc} test in which sinusoidal cycles of $q_{av} = 44.7kPa$, $q_{cyc} = 11.2kPa$ and frequency $1Hz$

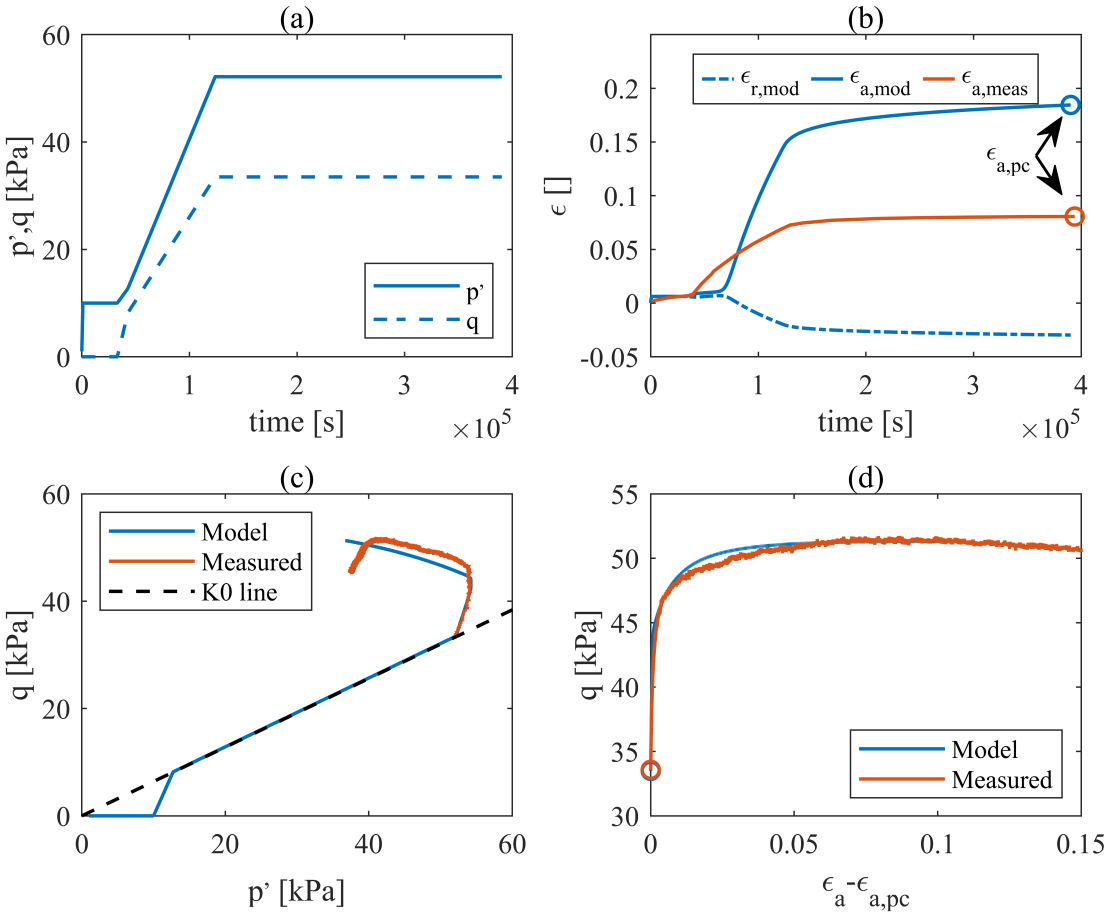

Figure 7.10: Single surface rate dependent (RPT) predictions of a $CAUc$ test (a) Consolidation stress history (b) Predicted axial and radial strains during consolidation phase compared to measured axial strains (c) Measured and modelled $p-q$ development during consolidation and subsequent shearing (d) Axial strain during undrained shearing

are applied. This builds upon the single surface model with 6 surfaces employed and:

$$\kappa_{fac} = \begin{bmatrix} 4 \\ 2 \\ 1 \\ 0.5 \\ 0.25 \\ 0.1 \end{bmatrix}, \quad \Omega = \begin{bmatrix} 1 \\ 1 \\ 1 \\ 1 \\ 1 \\ 1 \end{bmatrix} = \begin{bmatrix} 1/6 \\ 1/6 \\ 1/6 \\ 1/6 \\ 1/6 \\ 1/6 \end{bmatrix} \tag{7.42}$$

At first equal weighting is chosen, since with a greater number of surfaces subtle changes to weighting become less important. Although 6 additional parameters are assigned this could also be described as a maximum and minimum κ_{fac} with some distribution of stiffnesses in between; reducing the additional required parameters to three ($\kappa_{fac,max}$,$\kappa_{fac,min}$,N_s) regardless of surface numbers.

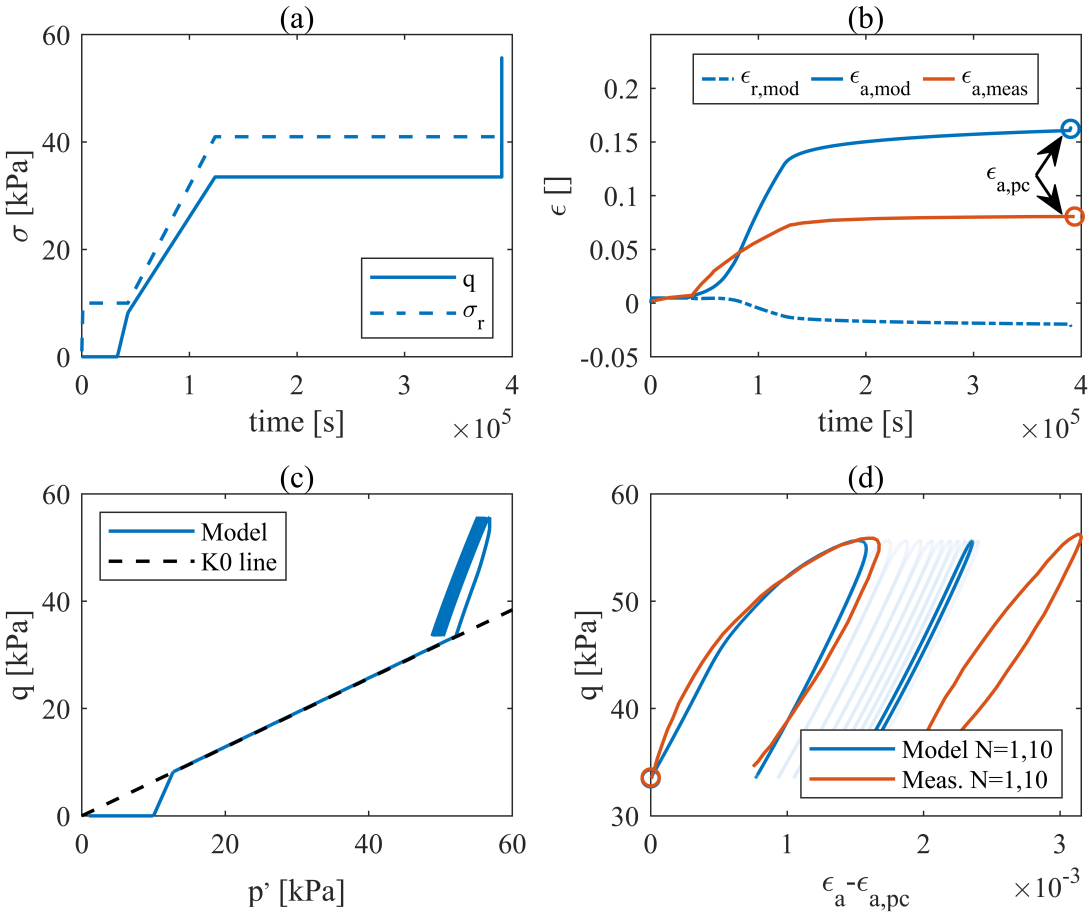

Figure 7.11: Multi-surface rate dependent (RPT) predictions of a *CAUcyc* test (a) Consolidation stress history (b) Predicted axial and radial strains during consolidation phase compared to measured axial strains (c) Modelled $p-q$ development during consolidation and subsequent shearing (d) Measured and modelled axial strain during undrained shearing at cycles N=1, N=10

Figure 7.11 shows model predictions in which consolidation behaviour is largely unaffected. The initial cycle of axial strain (Figure 7.11d) is reproduced well. With rate-dependency, an accurate representation of curved loops along with some ratcheting of axial strain and reduction of effective stress is produced. To achieve further development of strain and stress with cycles, degradation of the yield surfaces could be employed. This is briefly described in the following section. On unloading and reloading the model is largely elastic as the yield surfaces are not met, a function of the relatively few surfaces. More surfaces with more varied stiffnesses or potentially a series formulation where the yield strengths greatly differ would give rise to more open loops.

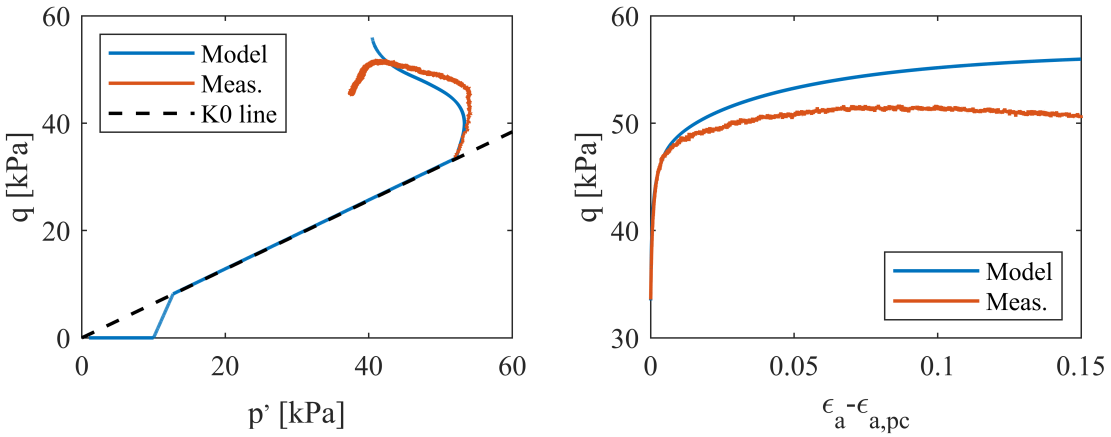

Figure 7.12: Multi-surface rate dependent (RPT) predictions of a $CAUc$ test, (Left) Modelled and measured $p-q$ development during consolidation and subsequent shearing (Right) Measured and modelled axial strain during undrained shearing

Figure 7.12 shows the same multi-surface model applied to the monotonic CAU_c test as in Figure 7.10. Additional surfaces result in a poorer comparison with the measured strains in this case, predicting a stiffer response. An optimisation routine (similar to that presented in Section 3.3.3 for rate prediction of slow monotonic and fast cyclic tests) could be employed to ensure both are suitably reproduced, although this is not pursued here.

7.6 Summary

In this Chapter, preliminary work aiming to capture effective stress stress changes in triaxial conditions was presented. This builds upon the Modified Cam Clay model, formulating in the hyperplasticity framework and including rate-dependency and an extension to include multiple surfaces.

In formulating the model following the underlying physics of rate process theory, time-dependent changes to undrained shear strength and pre-failure behaviour are captured. It was shown that as expected, in an undrained test, behaviour depends not only on the rate of shearing but also on the rate and time of consolidation. It is therefore crucial that the full time-history of loading is modelled accurately.

Multiple surfaces are employed in parallel and a single property is altered (in this case κ^*). By assigning weights to each surface additional control of response is achieved. With correctly calibrated parameters this produces hysteresis on unloading,

expanding upon the elastic response of a single surface model. An example model fit to a database of tests in Wenzhou soft clay shows the early stages of calibration and some promising results.

Although in the early stages of development, the model could quite simply be extended to include:

- Extensive and compressive asymmetry of strength. Included in a similar way to Section 3.2.2 by changing all occurrences of:

$$M^2 \dot{\alpha_q}^2 \quad \rightarrow \quad M_c^2 \langle \dot{\alpha_q} \rangle^2 + M_c^2 \langle -\dot{\alpha}_q \rangle^2 \tag{7.43}$$

$$\left(\frac{\chi_q}{M}\right)^2 \quad \rightarrow \quad \left(\frac{\langle \chi_q \rangle}{M}\right)^2 + \left(\frac{\langle -\chi_q \rangle}{M}\right)^2 \tag{7.44}$$

  with subsequent changes to derivatives.

- Yield surface softening. In the macro model applied to element tests, the yield strength degraded with plastic shear strain or work (Section 3.4.2.1). In the MCC Model, yield strength (controlled by p_c) increases as a function of volumetric plastic strain, Equation 7.3. This could be supplemented by an additional term decreasing p_c with the increment of plastic shear strain or work:

$$p_{c,\kappa} = p_c f(\beta) \tag{7.45}$$

  where $\dot{\beta} = |\dot{\alpha_q}|$ or $\dot{\beta} = |\dot{\alpha_q}| M p_{c,\kappa}$ and f indicates some appropriate reduction function, e.g. modified power law as in Equation 3.33. As before, local and global softening could be included straightforwardly.

Both would offer more control, and ultimately, a more accurate representation of the behaviour of clays under repeated loading.

Chapter 8

Conclusions

This thesis has explored the response of clays to repeated loading primarily at element scale but also at pile scale, under regular single amplitude loading and more realistic pseudo-random loads. The database of element tests collated from literature and private communication have facilitated the development of total stress and effective stress models formulated in the hyperplasticity framework to capture key features of behaviour. Models were then applied to more complex cases by reproducing industry standard contour diagrams and predicting truly irregular tests. Finally, a comparison of normalised parameters and underlying mechanisms from element to pile scale was made using similarly configured 1D models. This chapter describes the key contributions and possible directions of future work following this work.

8.1 Key contributions

A consistent framework for cyclic loading

To facilitate the comparison of cyclic element tests and cyclic pile tests, a consistent framework for the interpretation of cyclic loading and response was developed. This focused on describing the pertinent features of behaviour in monopile design (Section 1.2.2). Definitions of cycles, strain, stiffness and energy loss factor were suggested in Chapter 2 which rigorously describe response under both simple and complex loading.

Element test response of fine-grained soils

Key behaviour under cyclic loading was established from a database of cyclic element tests of fine-grained soils using the above framework:

(i) Non-linearity of response with stress magnitude and approximate Masing-type behaviour on unloading (Section 3.2). In *CU* tests this varies in extension and compression due to anisotropy (Section 3.2.2).

(ii) Strain-rate dependency (Section 3.3.1), where an increase in strength and stiffness is observed at higher rates. During fast cycling the continuous change in strain rate causes subtle effects such as viscous, curved peaks and some accumulation of strain due to creep.

(iii) With the application of many constant-amplitude cycles the secant stiffness typically reduces and the loop shape varies, characterised by energy loss factor (Sections 3.4.1.1 and 3.4.1.2).

(iv) If the applied load is biased or strength is direction dependent, ratcheting of strain is observed (Section 3.4.1.3).

(v) In undrained testing, changes in strain response are typically accompanied by a reduction effective stress which can induce sample failure. As failure is approached the strain response varies considerably (Section 3.4.1.4).

(vi) In those tests which do not fail, post-cyclic strength showed little or no change relative to the monotonic response. This is often despite considerable changes to secant stiffness (Section 3.4.1.5).

The relative importance of the above features was shown to depend heavily on the load magnitude, cycle asymmetry and frequency.

Development of models at element scale

Total stress, multi-surface, kinematic hardening Hyperplasticity models were shown to adequately capture hysteresis (i) and rate-dependency (ii), with the addition of a model based upon rate process theory (Section 3.3.2). The effects of many cycles were reproduced using a plastic work or strain dependent degradation of yield strength. In allowing degradation to occur both locally and globally (i.e. Section 3.4.2.1), post cyclic strength, accumulation of strain and secant stiffness changes can be suitably controlled (iii,iv,vi). Where required an additional ratcheting model (HARM) was used to supplement accumulation of strain (iv). This choice is left open, although for

many datasets careful specification of the mix of local and global softening reproduced the results with adequate accuracy. Calibration methods from constant amplitude tests were suggested for each mechanism.

Explicit prediction of effective stress changes (v) provide a more accurate depiction of soil behaviour. Therefore, a rate-dependent, hyperplasticity model in triaxial stress space (q-p') was described, building upon the conventional MCC model (Chapter 7). This highlighted the importance of consolidation history on soil response and represents a first stage for further development.

Application of the model at element scale

Two projects in conjunction with Norwegian Geotechnical Institute (NGI) aimed to test the proposed total stress modelling framework outside the calibrated range (Chapter 4). Firstly, the model successfully reproduced industry-standard 'contour diagrams' of CU and DSS testing from synthetic model tests. This served as a novel validation tool as well as a powerful demonstration of the suitability of proposed models to predict the behaviour across a range of test types. In using a mechanistic model, the original diagrams were described in terms of physical processes. The same normalised cyclic parameters were used in both CU and DSS tests suggesting a possible mapping between the two.

The second application involved genuine 'Class C' (Lambe, 1973) predictions of multi-amplitude, Direct Simple Shear (DSS) tests. Calibration was achieved from monotonic and constant-amplitude cyclic (DSS and DSS_{cyc}) tests in the same soil unit, successfully reproducing much of the behaviour observed under more complex loading. The exercise showed the ability of hyperplasticity models to predict long, multi-amplitude tests quickly and reasonably accurately with default (or simple to calibrate) parameters.

Model structure subtleties

There are several possible ways of structuring the multi-surface models used in this thesis. The implications of configuring units in series or in parallel were therefore investigated (summarised in Table 5.1). In one dimension, behaviour is identical

(with differing but well defined parameters) for rate-independent models and evolution mechanisms which depend on global quantities, such as global softening and additional ratcheting (HARM) models. If changes occur locally to the surface (i.e. rate process theory and local-softening) the two models are not equivalent. The response is similar, however, if suitable parameters are chosen (RPT -$t_{ref,ser,i} = t_{ref,G}.Ns$ and Softening - Varied F_κ). It is not clear which, if any, is the better formulation. However, if rate-dependency is implemented following rate process theory, parallel models are better defined due to a consistent strain rate on each surface. With derivation of stress or strain control as per Appendix A either may be implemented for a given application; however, the thesis has shown that caution is required in correctly deriving parameters and model formulation if both are to be used or compared.

Application to 1D modelling

Similar models were applied at pile scale using extended 1D 'Winkler' type models. These build upon the successful PISA method which allows monotonic response to be accurately derived using FEA analyses. Normalised non-dimensional model parameters calibrated to element tests of Cowden till were applied to predict cyclic laterally loaded pile tests in the same unit. Rate-dependent parameters were found to map directly (Section 6.4.3); however, the cyclic parameters did not (Section 6.4.4). Whilst in general the behaviour at element and pile scale is similar, more ratcheting occurs at pile level with respect to the softening. Little to no post-cyclic reduction of strength was observed, therefore behaviour is best modelled using the HARM framework (rather than a degradation model only). Rate and stiffness change parameters may be used directly from a macro model calibrated to CU tests or DSS tests but HARM parameters may preliminarily be derived from previous pile tests at laboratory or field scale. With a suitably calibrated model, typical storm loading was applied and cyclic response identified down the pile as mobilisation of lateral pressure. Comparisons between this and typical element tests leads to better assessment of suitable element testing for a prescribed load.

8.2 Future work

Constitutive models

The total stress models primarily used in this thesis were shown to predict behaviour of cyclic element tests in fine-grained soils well. In order to truly predict the effective stress behaviour, further extension of the MCC model to include degradation of yield strength and anisotropy could be implemented as described in Section 7.6. Further work might further investigate the structure of such models, be it parallel, series or otherwise to best predict the hysteretic behaviour. Behaviour of coarse-grained, frictional soils is likely to require a different modelling strategy, although work is already under way at Oxford with this in mind; see the work of Luc Simonin (Simonin, 2022), who is developing the 'Hysand' model which builds upon previous work by Houlsby and Mortara (2004) .

Formulating as continuum models, rather than at macro scale, would facilitate application in FEA predictions of monopiles. Although computationally expensive, 3D FE models calibrated to element tests could inform parameters for use in more efficient 1D Winkler or pile scale macro models.

Specification of element tests

The element test database used in this thesis was taken from a variety of sources, each with its own purpose. Specification of tests specifically for calibration of models for cyclic monopile design could be refined. Section 6.5 predicted that mobilisation of soil around a monopile subject to cyclic storm load was far less intense than that applied in typical laboratory testing regimes, in which relatively high magnitude loads tend to be applied to failure after relatively few cycles. This is at odds with the numerous cycles of relatively low loads experienced by an OWT structure. Further work might also investigate the possibility of using more complex testing to calibrate the model (such as multi-amplitude or truly pseudo-random loads). This could facilitate more efficient testing of retrieved samples, with greater potential to repeat tests and quantify sample variability.

Application at pile-scale

1D Winkler models using the PISA framework offer a quick and useful design tool

in which changes to the pile dimensions do not necessitate change of calibrated soil parameters. Extension to include rate dependency and the effects of many cycles was implemented in the same way as macro models, applied at each soil reaction. This is a promising solution for cyclic design and there is much scope for model improvement: (i) more robust methods for the solution of rate-dependent models, where the expected displacement could be calculated using both a stiffness matrix (rate of change of displacement) and dissipation matrix (rate of change of displacement rate); (ii) inclusion of multi-directionality to allow for the varied direction of true offshore loads, building upon bi-directional models implemented at a macro level (e.g. by Richards, 2020); (iii) further investigation to identify the disparity between normalised parameters from element to pile scale, mapping using 3D FEA computations in a similar manner to the PISA numerical method.

Practical cyclic monopile design

Cyclic loading of soils and subsequent response is complex. Simplifications are made to identify key behaviours, typically single amplitude repeated loads. Section 4.2 showed that when more realistic, multi-amplitude, loads where applied in DSS_{cyc} conditions the largest loads dominate behaviour. This was well reproduced by the models used and agrees with results from previous model pile tests by Richards, 2020. For design, it is possible that much of a given loading history could be removed from model predictions, greatly reducing computational effort. Numerical studies, using models validated by large-scale field tests, could be used to investigate this. Finally, applying loads unidirectionally is inaccurate. Real loads are likely to be multi-directional, changing the direction of load bias and mobilising greater volumes of soil. By correctly modelling multi-directional response, more accurate predictions of the lifetime accumulation of pile rotation could be made.

8.3 Summary

This thesis has provided insights and tested modelling options for capturing the effects of repeated loading on clay soils, capturing non-linearity, rate dependency, degradation, ratcheting and effective stress changes. In successfully applying methods previ-

ously used to predict monopile behaviour to element testing this thesis provides the first step in the potential route to calibration.

This forms part of a wider effort by Oxford University to better predict the response of monopiles to cyclic loading, building upon previous experimental and numerical work and preceding a large-scale project PICASO (Pile Cyclic Analysis: Oxford and Ørsted) which aims to facilitate the use of new design methods with extensive laboratory testing, field testing and numerical work.

References

Abadie, C.N. (2015). "Cyclic lateral loading of monopile foundations in cohesionless soils". DPhil Thesis. University of Oxford.

Abadie, C.N., G.T. Houlsby, and B.W. Byrne (2019). "A method for calibration of the Hyperplastic Accelerated Ratcheting Model (HARM)". *Comput. Geotech.* 112, pp. 370–385. DOI: 10.1016/j.compgeo.2019.04.017.

Achmus, M., K. Abdel-Rahman, and Y.S. Kuo (2007). "Behavior of Large Diameter Monopiles Under Cyclic Horizontal Loading". *Proc. 12th Int. Colloq. Struct. Geotech. Eng.* Cairo.

Achmus, M., J. Albiker, and K. Abdel-Rahman (2011). "Investigations on the behavior of large diameter piles under cyclic lateral loading". *Proc. 2nd Int. Symp. Front. Offshore Geotech.* Perth, pp. 471–476.

Andersen, K.H. (1976). "Behaviour of clay subject to cyclic loading". *NGI Reports* NR. 114, pp. 33–44.

— (2009). "Bearing capacity under cyclic loading — offshore, along the coast, and on land". *Can. Geotech. J.* 46.5, pp. 513–535. DOI: 10.1139/T09-003.

— (2015). "Cyclic soil parameters for offshore foundation design". *Proc. 3rd Int. Symp. Front. Offshore Geotech.* Oslo.

Andersen, K.H., A. Kleven, and D. Heien (1988). "Cyclic Soil Data for Design of Gravity Structures". *J. Geotech. Eng.* 114.5, pp. 517–539. DOI: 10.1061/(ASCE)0733-9410(1988)114:5(517).

Andersen, K.H. et al. (1980). "Cyclic and Static Laboratory Tests on Drammen Clay". *J. Geotech. Eng. Div. ASCE* 106.5, pp. 499–529.

Anusic, I., G.R. Eiksund, and M.A. Liingaard (2016). "Comparison of pile driveability methods based on a case study from an offshore wind farm in North Sea". *Proc. 17th Nord. Geotech. Meet. Challenges Nord. Geotech.* Reykjavik, pp. 1037–1046.

API (2011). *Geotechnical and Foundation Design Considerations. IS0 19901-4:2003.* Washington.

Arany, L. et al. (2016). "Closed form solution of Eigen frequency of monopile supported offshore wind turbines in deeper waters incorporating stiffness of substructure and SSI". *Soil Dyn. Earthq. Eng.* 83, pp. 18–32. DOI: 10.1016/j.soildyn.2015.12.011.

Arany, L. et al. (2017). "Design of monopiles for offshore wind turbines in 10 steps". *Soil Dyn. Earthq. Eng.* 92.September 2016, pp. 126–152. DOI: 10.1016/j.soildyn.2016.09.024.

Arnold, G. and S. Werkmeister (2010). *Pavement thickness design charts derived from a rut depth finite element model.* Tech. rep. NZ Transport Agency research report 427, p. 84.

Balaam, T.D. and J.J. Kragelund (2020). *HARM models applied to PISA type 1D models – comparison of OU and Ørsted software*. Tech. rep. Oxford University Internal Report.

Barksdale, R.D. (1971). "Laboratory evaluation of rutting in base course materials". *Int. Conf. Struct. Des. Asph. Pavements*. London, pp. 161–174.

Beuckelaers, W.J.A.P. (2015). "Fatigue life calculation of monopiles for offshore wind turbines using a kinematic hardening soil model". *Gr. Eng.*

— (2017). "Numerical Modelling of Laterally Loaded Piles for Offshore Wind Turbines". DPhil Thesis. University of Oxford.

Beuckelaers, W.J.A.P., G.T. Houlsby, and H.J. Burd (2018). "A comparison of the series and parallel Masing-Iwan model in 2D". *Numer. Methods Geotech. Eng. IX*. Porto, pp. 173–177. DOI: 10.1201/9781351003629-22.

Bjerrum, L. (1967). "Engineering Geology of Norwegian Normally-Consolidated Marine Clays as Related to Settlements of Buildings". *Géotechnique* 17.2, pp. 83–118. DOI: 10.1680/geot.1967.17.2.83.

Bredmose, H. et al. (2016). "DeRisk — Accurate Prediction of ULS Wave Loads. Outlook and First Results". *Energy Procedia* 94, pp. 379–387. DOI: 10.1016/j.egypro.2016.09.197.

Brodersen, M.L., A. Bjørke, and J. Høgsberg (2017). "Active tuned mass damper for damping of offshore wind turbine vibrations". *Wind Energy* 20.5, pp. 783–796. DOI: 10.1002/we.2063.

Buckley, R.M. et al. (2020). "Pile behavior in low-medium density chalk: preliminary results from the ALPACA project". *Int. Symp. Front. Offshore Geotech.* Austin.

Butterfield, R. (1979). "A natural compression law for soils". *Géotechnique* 29.4, pp. 469–480. DOI: 10.1680/geot.1979.29.4.469.

Byrne, B.W. and G.T. Houlsby (2003). "Foundations for offshore wind turbines". *Philos. Trans. R. Soc. London. Ser. A Math. Phys. Eng. Sci.* 361.1813. Ed. by J. M. T. Thompson, pp. 2909–2930. DOI: 10.1098/rsta.2003.1286.

Byrne, B.W. et al. (2017). "PISA: New Design Methods for Offshore Wind Turbine Monopiles". *Proc. 8th Int. Conf. Offshore Site Investig. Geotech.* London, pp. 142–161.

Byrne, B.W. et al. (2019a). "Monotonic laterally loaded pile testing in a stiff glacial clay till at Cowden". *Géotechnique*, pp. 1–16. DOI: 10.1680/jgeot.18.PISA.003.

Byrne, B.W. et al. (2019b). "PISA design model for monopiles for offshore wind turbines: application to a stiff glacial till". *Géotechnique*, pp. 1–19. DOI: 10.1680/jgeot.18.p.277.

Byrne, B.W. et al. (2020). "PICASO: Cyclic lateral loading of offshore wind turbine monopiles." *Int. Symp. Front. Offshore Geotech.* Austin.

Cai, Y.Q. et al. (2017). "Stress–strain response of soft clay to traffic loading". *Géotechnique* 67.5, pp. 446–451. DOI: 10.1680/jgeot.15.P.224.

Carswell, W. et al. (2016). "Natural frequency degradation and permanent accumulated rotation for offshore wind turbine monopiles in clay". *Renew. Energy* 97, pp. 319–330. DOI: 10.1016/j.renene.2016.05.080.

Cassiani, G., A. Brovelli, and T. Hueckel (2017). "A strain-rate-dependent modified Cam-Clay model for the simulation of soil/rock compaction". *Geomech. Energy Environ.* 11, pp. 42–51. DOI: 10.1016/j.gete.2017.07.001.

Cheung, L.W. (1994). "Laboratory assessment of pavement foundation materials". PhD Thesis. University of Nottingham.

Collins, I.F. and G.T. Houlsby (1997). "Application of thermomechanical principles to the modelling of geotechnical materials". *Proc. R. Soc. A Math. Phys. Eng. Sci.* 453.1964, pp. 1975–2001. DOI: 10.1098/rspa.1997.0107.

Di Prisco, C. and D.M. Wood (2012). *Mechanical Behaviours of Soils under Environmentally Induced Cyclic Loads*. New York: Springer.

DNVGL (2018). *Support structures for wind turbines*. Tech. rep. DNVGL-ST-0126. Oslo: Det Norske Veritas.

Downing, S. and D. Socie (1982). "Simple rainflow counting algorithms". *Int. J. Fatigue* 4.1, pp. 31–40. DOI: 10.1016/0142-1123(82)90018-4.

Dyvik, R. et al. (1987). "Comparison of truly undrained and constant volume direct simple shear tests". *Géotechnique* 37.1, pp. 3–10. DOI: 10.1680/geot.1987.37.1.3.

Evans, S. (2019). "Analysis: Record-low price for UK offshore wind cheaper than existing gas plants by 2023". *Carbon Br.*

Garnier, J. (2013). "Advances in lateral cyclic pile design : Contribution of the SOLCYP project". *Proc. TC 209 Work. 18th ICSMGE*. Ed. by A. Puech. Vol. 1. Paris, pp. 59–68.

Green, E.I. (1955). "The Story of Q". *Am. Sci.* 43, pp. 584–595.

Grimstad, G., L. Andresen, and H.P. Jostad (2012). "NGI-ADP: Anisotropic shear strength model for clay". *Int. J. Numer. Anal. Methods Geomech.* 36.4, pp. 483–497. DOI: 10.1002/nag.1016.

Guo, L. et al. (2018). "Undrained behaviour of intact soft clay under cyclic paths that match vehicle loading conditions". *Can. Geotech. J.* 55.1, pp. 90–106. DOI: 10.1139/cgj-2016-0636.

He, B., L. Wang, and Y. Hong (2017). "Field testing of one-way and two-way cyclic lateral responses of single and jet-grouting reinforced piles in soft clay". *Acta Geotech.* 12.5, pp. 1021–1034. DOI: 10.1007/s11440-016-0515-z.

Houlsby, G.T. (2000). "Critical state models and small-strain stiffness". *Dev. Theor. Geomech. Proc. Booker Meml. Symp.* C63–1:18.

— (2016). "Interactions in offshore foundation design". *Géotechnique* 66.10, pp. 791–825. DOI: 10.1680/jgeot.15.RL.001.

— (2020a). *Cyclic Loading for Geotechnical Engineering Problems*. Presnetation at ETH Winter School 2020.

— (2020b). *On the structure of multi-surface kinematic hardening models*. Tech. rep. University of Oxford: Private Communication.

Houlsby, G.T., A. Amorosi, and F. Rollo (2019). "Non-linear anisotropic hyperelasticity for granular materials". *Comput. Geotech.* 115, p. 103167. DOI: 10.1016/j.compgeo.2019.103167.

Houlsby, G.T. and G. Mortara (2004). "A continuous hyperplasticity model for sands under cyclic loading". *Cycl. Behav. Soils Liq. Phenom.* Ed. by T. Triantafyllidis, pp. 1–6. DOI: 10.1201/9781439833452.ch3.

Houlsby, G.T. and A.M. Puzrin (2000). "Thermomechanical framework for constitutive models for rate-independent dissipative materials". *Int. J. Plast.* 16.9, pp. 1017–1047. DOI: 10.1016/S0749-6419(99)00073-X. arXiv: 6(9),10171047.

Houlsby, G.T. and A.M. Puzrin (2002). "Rate-dependent plasticity models derived from potential functions". *J. Rheol. (N. Y. N. Y).* 46.1, pp. 113–126. DOI: 10.1122/1.1427911.

— (2006). *Principles of Hyperplasticity*. London: Springer.

Houlsby, G.T. et al. (2017). "A model for nonlinear hysteretic and ratcheting behaviour". *Int. J. Solids Struct.* 120, pp. 67–80. DOI: 10.1016/j.ijsolstr.2017.04.031.

Huang, M. and Y. Liu (2015). "Axial capacity degradation of single piles in soft clay under cyclic loading". *Soils Found.* 55.2, pp. 315–328. DOI: 10.1016/j.sandf.2015.02.008.

IEA (2015). *World Energy Outlook*. Tech. rep. International Energy Agency.

Inman, D.J. (2014). *Engineering Vibration*. 4th ed. Boston: Pearson.

IPCC (2014). *AR5 Synthesis Report: Climate Change 2014*. Tech. rep.

Jardine, R.J. (2014). "Advanced laboratory testing in research and practice: the 2nd Bishop Lecture". *Geotech. Res.* 1.1, pp. 2–31. DOI: 10.1680/geores.14.00003.

Jeanjean, P. et al. (2017). "A Framework for Monotonic P-Y Curves in Clays". *Proc. 8th Int. Conf. Offshore Site Investig. Geotech.* London, pp. 108–142.

Jostad, H.P. et al. (2014). "A FE procedure for foundation design of offshore structures - Applied to study a potential OWT monopile foundation in the Korean Western Sea". *Geotech. Eng.* 45.4, pp. 63–72.

Kallehave, D., C.L. Thilsted, and A. Troya (2015a). "Observed variations of monopile foundation stiffness". *Proc. 3rd Int. Symp. Front. Offshore Geotech.* Oslo, pp. 978–1. DOI: 10.1201/b18442-98.

Kallehave, D. et al. (2015b). "Optimization of monopiles for offshore wind turbines". *Philos. Trans. R. Soc. A Math. Phys. Eng. Sci.* 373.2035, p. 20140100. DOI: 10.1098/rsta.2014.0100.

Klar, A. and M.F. Randolph (2008). "Upper-bound and load–displacement solutions for laterally loaded piles in clays based on energy minimisation". *Géotechnique* 58.10, pp. 815–820. DOI: 10.1680/geot.2007.00197.

Knight, S. (2019). "What comes after the monopile - and what will load it?" *Marit. J.*

Kramer, S. (1996). *Geotechnical Earthquake Engineering*. Prentice Hall.

Kuo, Y. (2008). "On the behavior of large-diameter piles under cyclic lateral load". PhD Thesis. Leibniz Hannover.

Lambe, T.W. (1973). "Predictions in soil engineering". *Géotechnique* 23.2, pp. 151–202. DOI: 10.1680/geot.1973.23.2.151.

Lau, B.H. (2015). "Cyclic behaviour of monopile foundations for offshore wind farms". PhD thesis. University of Cambridge.

Leblanc Thilstead, C. (2019). *Future Design Challenges in Offshore Wind*. Glasgow.

Leblanc, C., B.W. Byrne, and G.T. Houlsby (2010a). "Response of stiff piles to random two-way lateral loading". *Géotechnique* 60.9, pp. 715–721. DOI: 10.1680/geot.09.T.011.

Leblanc, C., G.T. Houlsby, and B.W. Byrne (2010b). "Response of stiff piles in sand to long-term cyclic lateral loading". *Géotechnique* 60.2, pp. 79–90. DOI: 10.1680/geot.7.00196.

Lekarp, F., U. Isacsson, and A. Dawson (2000). "State of the Art. II: Permanent Strain Response of Unbound Aggregates". *J. Transp. Eng.* 126.1, pp. 76–83. DOI: 10.1061/(ASCE)0733-947X(2000)126:1(76).

Li, L., H. Dan, and L. Wang (2011). "Undrained behavior of natural marine clay under cyclic loading". *Ocean Eng.* 38.16, pp. 1792–1805. DOI: 10.1016/j.oceaneng.2011.09.004.

Liedtke, E. et al. (2019). "Monotonic and Cyclic Soil Properties of Gulf of Mexico Clays The database". *Offshore Technol. Conf.* Houston.

Likitlersuang, S. and G.T. Houlsby (2007). "Predictions of a continuous hyperplasticity model for Bangkok clay". *Geomech. Geoengin.* 2.3, pp. 147–157. DOI: 10.1080/17486020701561479.

Lindsey, R. (2020). "Climate Change: Atmospheric Carbon Dioxide". *Underst. Clim.*

Long, J.H. and G. Vanneste (1994). "Effects of Cyclic Lateral Loads on Piles in Sand". *J. Geotech. Eng.* 120.1, pp. 225–244. DOI: 10.1061/(ASCE)0733-9410(1994)120:1(225).

Løvholt, F., C. Madshus, and K.H. Andersen (2020). "Intrinsic Soil Damping from Cyclic Laboratory Tests with Average Strain Development". *Geotech. Test. J.* 43.1. DOI: 10.1520/GTJ20170411.

Lunne, T. and K.H. Andersen (2007). "Soft Clay Shear Strength Parameters for Deepwater Geotechnical Design". *Proc. 6th Int. Offshore Site Investig. Geotech. Conf.* London, pp. 11–13.

Matešić, L. and M. Vucetic (2003). "Strain-Rate Effect on Soil Secant Shear Modulus at Small Cyclic Strains". *J. Geotech. Geoenvironmental Eng.* 129.6, pp. 536–549. DOI: 10.1061/(ASCE)1090-0241(2003)129:6(536).

Mayall, R.O. et al. (2018). "Modelling of foundation response to scour and scour protection for offshore wind turbine structures". *9th Int. Conf. Phys. Model. Geotech.* London.

Minga, E. and H.J. Burd (2019). *Validation report of PLAXIS MoDeTo based on the Cowden clay PISA field tests.*

Mitchell, J.K. and K. Soga (2005). *Fundamentals of Soil Behaviour.* Wiley.

Muir Wood, D. (1990). *Soil Behaviour and Critical State Soil Mechanics.* Cambridge University Press.

Murff, J.D. and J.M. Hamilton (1993). "P -Ultimate for Undrained Analysis of Laterally Loaded Piles". *J. Geotech. Eng.* 119.1, pp. 91–107. DOI: 10.1061/(ASCE)0733-9410(1993)119:1(91).

Niemunis, A., T. Wichtmann, and T. Triantafyllidis (2005). "A high-cycle accumulation model for sand". *Comput. Geotech.* 32.4, pp. 245–263. DOI: 10.1016/j.compgeo.2005.03.002.

Noren-Cosgriff, K., H.P. Jostad, and C. Madshus (2015). "Idealized load composition for determination of cyclic undrained degradation of soils". *Proc. 3rd Int. Symp. Front. Offshore Geotech.* Oslo, pp. 1097–1102.

NREL (2018). *IEA WInd TCP Task 26: Offshore Wind Energy International Comparative Analysis.* Tech. rep., p. 71.

Okur, D.V. and A. Ansal (2007). "Stiffness degradation of natural fine grained soils during cyclic loading". *Soil Dyn. Earthq. Eng.* 27.9, pp. 843–854. DOI: 10.1016/j.soildyn.2007.01.005.

Page, A.M. et al. (2018). "A macro-element pile foundation model for integrated analyses of monopile-based offshore wind turbines". *Ocean Eng.* 167, pp. 23–35. DOI: 10.1016/j.oceaneng.2018.08.019.

Paute, J.L., P. Hornych, and J.P. Benaben (1993). "Repeated load triaxial testing of granular materials in the French network of Laboratoires des Ponts et Chaussees." *Eur. Symp. Flex. pavements*. Lisbon, pp. 53–64.

Peralta, P. et al. (2017). "Dynamic and cyclic pile-soil response curves for monopile design". *Proc. 8th Int. Conf. Offshore Site Investig. Geotech.* London, pp. 1054–1061.

PISA Academic Work Group (2016a). *PISA Damping*. Tech. rep.

— (2016b). *PISA Final Report*. Tech. rep.

PLAXIS (2018). *PLAXIS MoDeTo Manual*.

Prévost, J. (1977). "Mathematical modelling of monotonic and cyclic undrained clay behaviour". *Int. J. Numer. Anal. Methods Geomech.* 1.2, pp. 195–216. DOI: 10.1002/nag.1610010206.

Puech, A. and J. Garnier (2017). *Design of Piles Under Cyclic Loading - SOLCYP Recommendations*. London: John Wiley & Sons.

Qiao, Y. et al. (2015). "Calculating rutting of some thin flexible pavements from repeated load triaxial test data". *Int. J. Pavement Eng.* 16.6, pp. 467–476. DOI: 10.1080/10298436.2014.943127.

Rajashree, S.S. and R. Sundaravadivelu (1996). "Degradation model for one-way cyclic lateral load on piles in soft clay". *Comput. Geotech.* 19.4, pp. 289–300. DOI: 10.1016/S0266-352X(96)00008-0.

Randolph, M.F. and S. Gourvenec (2011). *Offshore Geotechnical Engineering*. Abingdon: Spon Press.

Reese, L.C., W.R. Cox, and F.D. Koop (1974). "Analysis of Laterally Loaded Piles in Sand". *Offshore Technol. Conf.* Offshore Technology Conference. DOI: 10.4043/2080-MS.

Reyno, A.J. and D.W. Airey (2005). "Influence of height and boundary conditions in simple shear tests". *Proc. 1st Int. Symp. Front. Offshore Geotech.* Perth, pp. 1101–1108.

Richards, I.A. (2020). "Monopile foundations under complex cyclic lateral loading in sand". DPhil Thesis. University of Oxford.

Richards, I.A. et al. (2020). "Cyclic Loading Definitions: A Review and Recommendations". *In Preperation*.

Roscoe, K.H. and J.B. Burland (1968). "On the Generalised Stress-Strain Behaviour of Wet Clay". *Eng. Plast.* Ed. by J. Heyman and F.A. Leckie. Cambridge University Press, pp. 535–610.

Sánchez, S. et al. (2019). "Foundations in Offshore Wind Farms: Evolution, Characteristics and Range of Use. Analysis of Main Dimensional Parameters in Monopile Foundations". *J. Mar. Sci. Eng.* 7.12, p. 441. DOI: 10.3390/jmse7120441.

Schofield, A. and P. Wroth (1968). *Critical State Soil Mechanics*. McGraw Hill.

Schroeder, F.C. et al. (2015). "Predicting monopile behaviour for the godewind offshore wind farm". *Proc. 3rd Int. Symp. Front. Offshore Geotech.* Oslo, pp. 735–740.

Sheng, D., S.W. Sloan, and H.S. Yu (2000). "Aspects of finite element implementation of critical state models". *Comput. Mech.* 26.2, pp. 185–196. DOI: 10.1007/s004660000166.

Simonin, L. (2022). "Hysand, an effective stress model in the hyperplastic framework for sand under cyclic loading". DPhil Thesis. University of Oxford.

Skau, K.S. et al. (2020). "Response of over-consolidated clay under irregular cyclic loading and comparison with predictions from the strain accumulation procedure". *Submitt. to Géotechnique*.

Staubach, P. and T. Wichtmann (2020). "Long-term deformations of monopile foundations for offshore wind turbines studied with a high-cycle accumulation model". *Comput. Geotech.* 124, p. 103553. DOI: 10.1016/j.compgeo.2020.103553.

Su, D. et al. (2014). "Cyclic Degradation of a Multidirectionally Laterally Loaded Rigid Single Pile Model in Compacted Clay". *J. Geotech. Geoenvironmental Eng.* 140.5, p. 06014002. DOI: 10.1061/(ASCE)GT.1943-5606.0001084.

Suryasentana, S.K et al. (2020). "Comparison of machine learning models in a data-driven approach for scalable and adpative design of laterally-loaded monopile foundations". *Int. Symp. Front. Offshore Geotech.* Austin.

Sweere, G.T.H (1990). "Unbound Granular Bases for Roads". PhD Thesis. University of Delft.

Taborda, D.M.G., D.M. Potts, and L. Zdravković (2016). "On the assessment of energy dissipated through hysteresis in finite element analysis". *Comput. Geotech.* 71, pp. 180–194. DOI: 10.1016/j.compgeo.2015.09.001.

Truong, P. et al. (2019). "Empirical approach based on centrifuge testing for cyclic deformations of laterally loaded piles in sand". *Géotechnique* 69.2, pp. 133–145. DOI: 10.1680/jgeot.17.P.203.

United Nations (2015). *Framework Convention on Climate Change - Paris Agreement.* Tech. rep.

Ushev, E. (2017). "Laboratory Investigation of the Mechanical Properties of Cowden Till under Static and Cyclic Conditions". PhD Thesis. Imperial College London.

Vaid, Y.P. and R.G. Campanella (1977). "Time-dependent behavior of an undisturbed clay". *J. Geotech. Eng. Div., ASCE* 103.7, pp. 693–709.

Van Vledder, G.P. (2013). "On Wind-Wave Misalignment, Directional Spreading and Wave Loads". *Vol. 5 Ocean Eng.* American Society of Mechanical Engineers. DOI: 10.1115/OMAE2013-11393.

Vucetic, M. (2016). *Some Recent Advances in (understanding) the Cyclic Behaviour of Soils*. Long Beach.

Vucetic, M. and R. Dobry (1988). "Degradation of Marine Clays under Cyclic Loading". *J. Geotech. Eng.* 114.2, pp. 133–149. DOI: 10.1061/(ASCE)0733-9410(1988)114:2(133).

Werkmeister, S. (2003). "Design of Granular Pavement Layers Considering Climatic Conditions". PhD Thesis. TU Dresden. DOI: 10.3141/1837-07.

Whittle, A.J. and M.J. Kavvadas (1994). "Formulation of MIT-E3 Constitutive Model for Overconsolidated Clays". *J. Geotech. Eng.* 120.1, pp. 173–198. DOI: 10.1061/(ASCE)0733-9410(1994)120:1(173).

Whyte, S.A. et al. (2020). "Formulation and implementation of a practical multi-surface soil plasticity model". *Comput. Geotech.* 117, p. 103092. DOI: 10.1016/j.compgeo.2019.05.007.

Wichtmann, T. (2019). *Personal Webiste of Prof. Dr.-Ing. habil. Torsten Wichtmann.*

Wichtmann, T., A. Niemunis, and T. Triantafyllidis (2005). "Strain accumulation in sand due to cyclic loading: drained triaxial tests". *Soil Dyn. Earthq. Eng.* 25.12, pp. 967–979. DOI: 10.1016/j.soildyn.2005.02.022.

— (2009). "Validation and Calibration of a High-Cycle Accumulation Model Based on Cyclic Triaxial Tests on Eight Sands". *Soils Found.* 49.5, pp. 711–728. DOI: 10.3208/sandf.49.711.

Wichtmann, T. and T. Triantafyllidis (2016). "An experimental database for the development, calibration and verification of constitutive models for sand with focus to cyclic loading: part I—tests with monotonic loading and stress cycles". *Acta Geotech.* 11.4, pp. 739–761. DOI: 10.1007/s11440-015-0402-z.

— (2018). "Monotonic and cyclic tests on kaolin: a database for the development, calibration and verification of constitutive models for cohesive soils with focus to cyclic loading". *Acta Geotech.* 13.5, pp. 1103–1128. DOI: 10.1007/s11440-017-0588-3.

Wichtmann, T. et al. (2013). "Cyclic tests on high-quality undisturbed block samples of soft marine Norwegian clay". *Can. Geotech. J.* 50.4, pp. 400–412. DOI: 10.1139/cgj-2011-0390.

Wind Europe (2020a). *Offshore Wind in Europe*. Tech. rep. DOI: 10.1016/S1471-0846(02)80021-X.

— (2020b). *Wind energy in Europe in 2019 Trends and statistics*. Tech. rep.

WMO (2019). *WMO Provisional Statement on the State of the Global Climate in 2019*. Tech. rep. World Meteorological Organization.

Yong, R.N. and R.D. Japp (1967). "Stress-Strain Behavior of Clays in Dynamic Compression". *Vib. Eff. Earthquakes Soils Found.* ASTM International, pp. 233–233–30. DOI: 10.1520/STP33643S.

Yu, J., M. Huang, and C. Zhang (2015). "Three-dimensional upper-bound analysis for ultimate bearing capacity of laterally loaded rigid pile in undrained clay". *Can. Geotech. J.* 52.11, pp. 1775–1790. DOI: 10.1139/cgj-2014-0390.

Zdravković, L. et al. (2019). "Ground characterisation for PISA pile testing and analysis". *Géotechnique*, pp. 1–16. DOI: 10.1680/jgeot.18.PISA.001.

Zhang, Y. and K.H. Andersen (2017). "Scaling of lateral pile p-y response in clay from laboratory stress-strain curves". *Mar. Struct.* 53, pp. 124–135. DOI: 10.1016/j.marstruc.2017.02.002.

Zhang, Y. et al. (2016). "Monotonic and Cyclic p-y Curves for Clay Based on Soil Performance Observed in Laboratory Element Tests". *Proc. Offshore Technol. Conf.* Houston, pp. 1–12. DOI: 10.4043/26942-MS.

Zhu, F.Y. et al. (2017). "The response of suction caissons to long-term lateral cyclic loading in single-layer and layered seabeds". *Géotechnique* Accepted October 2017. DOI: 10.1680/jgeot.17.P.129.

Ziegler, H. (1977). *An Introduction to Thermomechanics*. Amsterdam: North-Holland.

Zografou, D., S. Gourvenec, and C.D. O'Loughlin (2019). "Response of normally consolidated kaolin clay under irregular cyclic loading and comparison with pre-

dictions from the accumulation procedure". *Geotechnique* 69.2, pp. 106–121. DOI: 10.1680/jgeot.16.P.340.

Appendices

Appendix A

Standard incremental derivation

Throughout this thesis models derived in the hyperplasticity framework (Houlsby and Puzrin, 2006; Houlsby et al., 2017) are used. This is a rigorous approach to modelling plastic behaviour which makes use of internal variables to describe the history of loading. Multi-surface kinematic hardening models can be formulated in parallel, series or nested configurations. They may be rate-dependent or independent in both derived form and behaviour (Beuckelaers, 2017). And as discussed in Chapter 3, can include additional mechanisms such as: strength asymmetry, softening/stiffening and ratcheting.

Regardless of model complexity, constitutive behaviour is fully described by a single energy function and a single dissipation function. Standardised methods can then be used to derive incremental behaviour. This appendix aims to:

- Describe derivation of incremental behaviour
- Show a fully worked example for a simple model
- Present all required derivatives for the models presented in Chapters 3 to 6

This is not novel work and is well described in previous publications (e.g. Houlsby and Puzrin, 2000; Houlsby and Puzrin, 2002). It is presented in full here to facilitate the implementation of models. Only macro model (with a single scalar σ and conjugate strain ε) formulation is presented. This is described by Helmholtz free energy f and dissipation function d from which yield functions y or flow potential w, and further incremental behaviour is derived. Models may also be described by the Gibbs free energy g (as in Richards, 2020) and but this is not pursued.

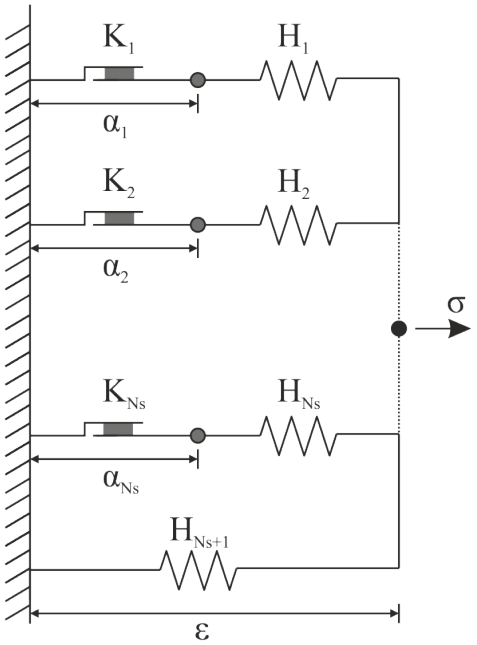

Figure A.1: Rate-independent parallel kinematic hardening model

A.1 Rate independent framework

Here incremental derivation of a rate-independent multi-surface parallel model with kinematic hardening and a single unidirectional stress and conjugate strain is shown (Figure A.1).

A.1.1 Derivation of yield function

The model is fully defined by:

$$f = \sum_{i=1}^{Ns} \frac{H_i}{2}(\varepsilon - \alpha_i)^2 + \frac{H_{Ns+1}}{2}\varepsilon^2 \tag{A.1}$$

$$d = \sum_{i=1}^{Ns} K_i|\dot{\alpha}_i| \tag{A.2}$$

where ε is strain-type scalar. H_i and K_i correspond to surface stiffnesses and strengths and α_i corresponds to the internal variables of each surface which represent plastic strains. The constitutive behaviour can be derived as:

$$\sigma = \frac{\partial f}{\partial \varepsilon} = \sum_{i=1}^{Ns} H_i(\varepsilon - \alpha_i) + H_{Ns+1}\varepsilon \tag{A.3}$$

$$\bar{\chi_i} = \frac{-\partial f}{\partial \alpha_i} = H_i(\varepsilon - \alpha_i) \tag{A.4}$$

$$\chi_i = \frac{-\partial d}{\partial \dot{\alpha}_i} = K_i S(\dot{\alpha}_i) \tag{A.5}$$

where σ is the conjugate stress-type variable of ε. χ_i represents the conjugate generalised stresses to internal variables α_i and is representative of the stress in each of the unit springs. $S(X)$ refers to the modified signum function. By utilising Ziegler's orthogonality assumption (Ziegler, 1977), energy is dissipated at the maximum rate and:

$$\bar{\chi_i} = \chi_i \rightarrow H_i(\varepsilon - \alpha_i) = k_i S(\alpha_i) \tag{A.6}$$

The yield function can be derived from Equation A.6. Such that at yield when $\dot{\alpha}_i \neq 0$ and $S(\alpha_i) = 1$ or -1:

$$y_i = |H_i(\varepsilon - \alpha_i)| - k_i = |\chi_i| - k_i = 0 \tag{A.7}$$

A.1.2 Standard derivation of incremental behaviour

A.1.2.1 Strain control

Assuming strain control (prescribed $d\varepsilon$) and knowledge of f and y, incremental behaviour can now be derived. Here N_{int} is the number of internal variables (α) and N_s the number yield surfaces (y) which may differ. In general terms:

$$f = f(\varepsilon, \boldsymbol{\alpha}), \boldsymbol{y} = \begin{bmatrix} y_1 = f(\boldsymbol{\chi}, \varepsilon, \boldsymbol{\alpha}) \\ y_2 = f(\boldsymbol{\chi}, \varepsilon, \boldsymbol{\alpha}) \\ \vdots \\ y_{Ny} = f(\boldsymbol{\chi}, \varepsilon, \boldsymbol{\alpha}) \end{bmatrix} \tag{A.8}$$

and:

$$\sigma = \frac{\partial f}{\partial \varepsilon}, \boldsymbol{\chi} = \begin{bmatrix} \chi_1 = \frac{-\partial f}{\partial \alpha_1} \\ \chi_2 = \frac{-\partial f}{\partial \alpha_2} \\ \vdots \\ \chi_{Nint} = \frac{-\partial f}{\partial \alpha_{Nint}} \end{bmatrix}, \boldsymbol{\alpha} = \begin{bmatrix} \alpha_1 \\ \alpha_2 \\ \vdots \\ \alpha_{Nint} \end{bmatrix} \tag{A.9}$$

such that incremental response is derived as:

$$d\sigma = \frac{\partial^2 f}{\partial \varepsilon \partial \varepsilon} d\varepsilon + \frac{\partial^2 f}{\partial \varepsilon \partial \boldsymbol{\alpha}} d\boldsymbol{\alpha} \tag{A.10}$$

$$d\boldsymbol{\chi} = -\frac{\partial^2 f}{\partial \boldsymbol{\alpha} \partial \varepsilon} d\varepsilon - \frac{\partial^2 f}{\partial \boldsymbol{\alpha} \partial \boldsymbol{\alpha}} d\boldsymbol{\alpha} \tag{A.11}$$

where:

$$\frac{\partial^2 f}{\partial\varepsilon\partial\varepsilon} = \frac{\partial^2 f}{\partial\varepsilon\partial\varepsilon}, \frac{\partial^2 f}{\partial\varepsilon\partial\boldsymbol{\alpha}} = \begin{bmatrix} \frac{\partial^2 f}{\partial\varepsilon\partial\alpha_1} & \cdots & \frac{\partial^2 f}{\partial\varepsilon\partial\alpha_{Nint}} \end{bmatrix}$$
$$\frac{\partial^2 f}{\partial\boldsymbol{\alpha}\partial\varepsilon} = \begin{bmatrix} \frac{\partial^2 f}{\partial\alpha_1\partial\varepsilon} \\ \vdots \\ \frac{\partial^2 f}{\partial\alpha_{Nint}\partial\varepsilon} \end{bmatrix}, \frac{\partial^2 f}{\partial\boldsymbol{\alpha}\partial\boldsymbol{\alpha}} = \begin{bmatrix} \frac{\partial^2 f}{\partial\alpha_1\partial\alpha_1} & \cdots & \frac{\partial^2 f}{\partial\alpha_1\partial\alpha_{Nint}} \\ \vdots & \ddots & \vdots \\ \frac{\partial^2 f}{\partial\alpha_{Nint}\partial\alpha_1} & \cdots & \frac{\partial^2 f}{\partial\alpha_{Nint}\partial\alpha_{Nint}} \end{bmatrix} \tag{A.12}$$

The consistency condition and flow rule at yield can be written:

$$d\boldsymbol{y} = -a\boldsymbol{y} = \frac{\partial\boldsymbol{y}}{\partial\boldsymbol{\chi}}d\boldsymbol{\chi} + \frac{\partial\boldsymbol{y}}{\partial\varepsilon}d\varepsilon + \frac{\partial\boldsymbol{y}}{\partial\boldsymbol{\alpha}}d\boldsymbol{\alpha} \tag{A.13}$$

$$d\boldsymbol{\alpha} = \left(\boldsymbol{\Lambda}\frac{\partial\boldsymbol{y}}{\partial\boldsymbol{\chi}}\right)^T = \frac{\partial\boldsymbol{y}}{\partial\boldsymbol{\chi}}^T\boldsymbol{\Lambda}^T \tag{A.14}$$

where a is a factor between 0 and 1 which ensures numerical stability if yield is exceeded (typically taken as 0.5) and $\boldsymbol{\Lambda}$ is an array of arbitrary non-negative multipliers. In Equation A.14 the transpose ensures consistency with the shape of the $\boldsymbol{\alpha}$ array in Equation A.9. Derivatives are defined as:

$$\frac{\partial\boldsymbol{y}}{\partial\boldsymbol{\chi}} = \begin{bmatrix} \frac{\partial y_1}{\partial\chi_1} & \cdots & \frac{\partial y_1}{\partial\chi_{Nint}} \\ \vdots & \ddots & \vdots \\ \frac{\partial y_{Ny}}{\partial\chi_1} & \cdots & \frac{\partial y_{Ny}}{\partial\chi_{Nint}} \end{bmatrix}, \frac{\partial\boldsymbol{y}}{\partial\varepsilon} = \begin{bmatrix} \frac{\partial y_1}{\partial\varepsilon} \\ \vdots \\ \frac{\partial y_{Ny}}{\partial\varepsilon} \end{bmatrix}, \frac{\partial\boldsymbol{y}}{\partial\boldsymbol{\alpha}} = \begin{bmatrix} \frac{\partial y_1}{\partial\alpha_1} & \cdots & \frac{\partial y_1}{\partial\alpha_{Nint}} \\ \vdots & \ddots & \vdots \\ \frac{\partial y_{Ny}}{\partial\alpha_1} & \cdots & \frac{\partial y_{Ny}}{\partial\alpha_{Nint}} \end{bmatrix} \tag{A.15}$$
$$\Lambda = \begin{bmatrix} \Lambda_1 & \ldots & \Lambda_{Ny} \end{bmatrix}$$

Equations A.11 and A.14 are then substituted into A.13 to solve the plastic multipliers Λ_i as a function of strain increment $d\varepsilon$:

$$-a.\boldsymbol{y} = \frac{\partial\boldsymbol{y}}{\partial\boldsymbol{\chi}}\left(-\frac{\partial^2 f}{\partial\boldsymbol{\alpha}\partial\varepsilon}d\varepsilon - \frac{\partial^2 f}{\partial\boldsymbol{\alpha}\partial\boldsymbol{\alpha}}\frac{\partial\boldsymbol{y}}{\partial\chi}^T\boldsymbol{\Lambda}^T\right) + \frac{\partial\boldsymbol{y}}{\partial\varepsilon}d\varepsilon + \frac{\partial\boldsymbol{y}}{\partial\boldsymbol{\alpha}}\frac{\partial\boldsymbol{y}}{\partial\boldsymbol{\chi}}^T\boldsymbol{\Lambda}^T$$

$$\left(\frac{\partial\boldsymbol{y}}{\partial\boldsymbol{\alpha}} - \frac{\partial\boldsymbol{y}}{\partial\boldsymbol{\chi}}\frac{\partial^2 f}{\partial\boldsymbol{\alpha}\partial\boldsymbol{\alpha}}\right)\frac{\partial\boldsymbol{y}}{\partial\boldsymbol{\chi}}^T\boldsymbol{\Lambda}^T = -a.\boldsymbol{y} - \left(\frac{\partial\boldsymbol{y}}{\partial\varepsilon} - \frac{\partial\boldsymbol{y}}{\partial\boldsymbol{\chi}}\frac{\partial^2 f}{\partial\boldsymbol{\alpha}\partial\varepsilon}\right)d\varepsilon \tag{A.16}$$

With $\boldsymbol{\Lambda}$ found, incremental behaviour (Equations A.14, A.11 and A.10) can be computed.

A.1.2.2 Stress control

If stress control is required (prescribed $d\sigma$), incremental behaviour can be derived by re-arranging Equation A.10 to give:

$$\frac{\delta^2 f}{\delta\varepsilon\delta\varepsilon}d\varepsilon = d\sigma - \frac{\delta^2 f}{\delta\varepsilon\delta\boldsymbol{\alpha}}d\boldsymbol{\alpha} \tag{A.17}$$

and obtaining a compliance matrix:

$$C = \left(\frac{\delta^2 f}{\delta\varepsilon\delta\varepsilon}\right)^{-1} \tag{A.18}$$

which are combined to give:

$$d\varepsilon = C\left(d\sigma - \frac{\delta^2 f}{\delta\varepsilon\delta\boldsymbol{\alpha}}\boldsymbol{d\alpha}\right) \tag{A.19}$$

Plastic multipliers Λ_i are then solved in a similar manner to Equation A.16, by combining Equations A.11, A.14, A.13 and A.19:

$$\begin{aligned} -a\boldsymbol{y} = \frac{\partial \boldsymbol{y}}{\partial \boldsymbol{\chi}}\Bigg(-\frac{\partial^2 f}{\partial\boldsymbol{\alpha}\partial\varepsilon}C\left(d\sigma - \frac{\delta^2 f}{\delta\varepsilon\delta\boldsymbol{\alpha}}\frac{\partial \boldsymbol{y}}{\partial \boldsymbol{\chi}}^T\boldsymbol{\Lambda}^T\right) - \frac{\partial^2 f}{\partial\boldsymbol{\alpha}\partial\boldsymbol{\alpha}}\frac{\partial \boldsymbol{y}}{\partial \boldsymbol{\chi}}^T\boldsymbol{\Lambda}^T\Bigg) + \\ \frac{\partial \boldsymbol{y}}{\partial\varepsilon}C\left(d\sigma - \frac{\delta^2 f}{\delta\varepsilon\delta\boldsymbol{\alpha}}\frac{\partial \boldsymbol{y}}{\partial \boldsymbol{\chi}}^T\boldsymbol{\Lambda}^T\right) + \frac{\partial \boldsymbol{y}}{\partial\boldsymbol{\alpha}}\frac{\partial \boldsymbol{y}}{\partial \boldsymbol{\chi}}^T\boldsymbol{\Lambda}^T \end{aligned}$$

$$\begin{aligned} \left(\left(\frac{\partial \boldsymbol{y}}{\partial\varepsilon} - \frac{\partial \boldsymbol{y}}{\partial \boldsymbol{\chi}}\frac{\partial^2 f}{\partial\boldsymbol{\alpha}\partial\varepsilon}\right)C\frac{\partial^2 f}{\partial\boldsymbol{\alpha}\partial\varepsilon} - \left(\frac{\partial \boldsymbol{y}}{\partial\boldsymbol{\alpha}} - \frac{\partial \boldsymbol{y}}{\partial \boldsymbol{\chi}}\frac{\partial^2 f}{\partial\boldsymbol{\alpha}\partial\boldsymbol{\alpha}}\right)\right)\frac{\partial \boldsymbol{y}}{\partial \boldsymbol{\chi}}^T\boldsymbol{\Lambda}^T \\ = a\boldsymbol{y} + \left(\frac{\partial \boldsymbol{y}}{\partial\varepsilon} - \frac{\partial \boldsymbol{y}}{\partial \boldsymbol{\chi}}\frac{\partial^2 f}{\partial\boldsymbol{\alpha}\partial\varepsilon}\right)Cd\sigma \end{aligned} \tag{A.20}$$

From which incremental behaviour (Equations A.14,A.19 and A.11) can be computed.

A.1.2.3 Example

For the model shown in Figure A.1 and described by Equations A.1 and A.7, incremental behaviour is now derived following Section A.1.2.1. $f(\varepsilon, \boldsymbol{\alpha})$, $y(\boldsymbol{\chi})$ and in this case $N_{int} = N_s$. The required derivatives are:

$$\frac{\partial^2 f}{\partial\varepsilon\partial\varepsilon} = \sum_{i=1}^{Ns+1} H_i, \frac{\partial^2 f}{\partial\varepsilon\partial\boldsymbol{\alpha}} = \begin{bmatrix} -H_1 & -H_2 & \dots & -H_{Ns} \end{bmatrix}$$

$$\frac{\partial^2 f}{\partial\boldsymbol{\alpha}\partial\varepsilon} = \begin{bmatrix} -H_1 \\ -H_2 \\ \vdots \\ -H_{Ns} \end{bmatrix}, \frac{\partial^2 f}{\partial\boldsymbol{\alpha}\partial\boldsymbol{\alpha}} = \begin{bmatrix} H_1 & 0 & \dots & 0 \\ 0 & H_2 & \dots & 0 \\ \vdots & \vdots & \ddots & \vdots \\ 0 & 0 & \dots & H_{Ns} \end{bmatrix}$$

$$\frac{\partial \boldsymbol{y}}{\partial \boldsymbol{\chi}} = \begin{bmatrix} S(\chi_1) & 0 & \dots & 0 \\ 0 & S(\chi_2) & \dots & 0 \\ \vdots & \vdots & \ddots & \vdots \\ 0 & 0 & \dots & S(\chi_{Ns}) \end{bmatrix}, \frac{\partial \boldsymbol{y}}{\partial\varepsilon} = \begin{bmatrix} 0 \\ 0 \\ \vdots \\ 0 \end{bmatrix}, \frac{\partial \boldsymbol{y}}{\partial\boldsymbol{\alpha}} = \begin{bmatrix} 0 & 0 & \dots & 0 \\ 0 & 0 & \dots & 0 \\ \vdots & \vdots & \ddots & \vdots \\ 0 & 0 & \dots & 0 \end{bmatrix} \tag{A.21}$$

Now Equation A.16 combined with A.21 reduces to:

$$\frac{\partial \boldsymbol{y}}{\partial \boldsymbol{\chi}} \frac{\partial^2 f}{\partial \boldsymbol{\alpha} \partial \boldsymbol{\alpha}} \frac{\partial \boldsymbol{y}}{\partial \boldsymbol{\chi}}^T \boldsymbol{\Lambda}^T = -\frac{\partial \boldsymbol{y}}{\partial \boldsymbol{\chi}} \frac{\partial^2 f}{\partial \boldsymbol{\alpha} \partial \varepsilon} d\varepsilon - a\boldsymbol{y} \tag{A.22}$$

$$\begin{bmatrix} H_1 S(\chi_1)^2 \Lambda_1 \\ H_2 S(\chi_2)^2 \Lambda_2 \\ \vdots \\ H_{Ns} S(\chi_{Ns})^2 \Lambda_{Ns} \end{bmatrix} = \begin{bmatrix} H_1 S(\chi_1) d\varepsilon - a y_1 \\ H_2 S(\chi_2) d\varepsilon - a y_2 \\ \vdots \\ H_{Ns} S(\chi_{Ns}) d\varepsilon - a y_{Ns} \end{bmatrix} \tag{A.23}$$

from which increments of plastic strain may be found (Equation A.14):

$$d\boldsymbol{\alpha} = \frac{\partial \boldsymbol{y}}{\partial \boldsymbol{\chi}}^T \boldsymbol{\Lambda}^T = \begin{bmatrix} d\varepsilon - a y_1 \frac{S(\chi_1)}{H_1} \\ \vdots \\ d\varepsilon - a y_{Ns} \frac{S(\chi_{Ns})}{H_{Ns}} \end{bmatrix} \tag{A.24}$$

where the second term caters for the overshoot when the surface first yields. This can also be achieved by ensuring strain steps meet yield exactly (e.g. as by Beuckelaers, 2017), thus ensuring $y_i = 0$ and Equation A.24 reduces to $d\alpha_i = d\varepsilon$.

Alternatively the same expression may be derived by re-arranging Equation A.6 to find the plastic strain when yielding. This will occur in the same direction as total strain such that $S(\alpha_i) = S(\varepsilon)$, and:

$$\alpha_i = \varepsilon - \frac{K_i S(\varepsilon)}{H_i} \tag{A.25}$$

assuming no changes to K_i or H_i, $d\alpha_i = d\varepsilon$ (when yielding). However, this can not be applied generally to any model as the derivation in Sections A.1.2.1.

A.2 Rate dependent framework

Here incremental derivation of a rate-dependent multi-surface parallel model with kinematic hardening and a single unidirectional stress and conjugate strain is shown (Figure A.2).

A.2.1 Derivation of flow potential

The model is fully defined by the same energy function as the rate-independent example:

$$f = \sum_{i=1}^{Ns} \frac{H_i}{2} (\varepsilon - \alpha_i)^2 + \frac{H_{Ns+1}}{2} \varepsilon^2 \tag{A.26}$$

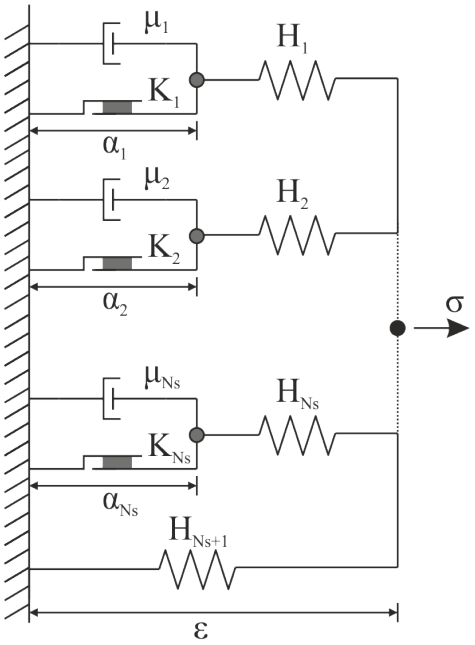

Figure A.2: Conceptual diagram of rate-dependent, multi-surface, kinematic Hardening models in parallel configuration.

and dissipation function following rate process theory (as in Section 3.4.2):

$$d = \sum_{i=1}^{Ns} K_i|\dot{\alpha}_i| + \sum_{i=1}^{Ns} \frac{\mu_i}{t_{ref,i}}\dot{\alpha}_i \sinh^{-1}\left(|\dot{\alpha}_i| t_{ref,n}\right) \tag{A.27}$$

which is related to the force potential z by:

$$d = \frac{\partial z}{\partial \dot{\boldsymbol{\alpha}}}\dot{\boldsymbol{\alpha}} \tag{A.28}$$

For rate-independent behaviour this reduces to $d = z$. Finally the flow potential is derived via a Legendre transform such that:

$$w = \boldsymbol{\chi}^T\dot{\boldsymbol{\alpha}} - z = d - z \tag{A.29}$$

More detail can be found in Houlsby and Puzrin (2002). Equations A.27, A.28 and A.29 combine to give:

$$w = \sum_{i=1}^{Ns} \frac{\mu_i}{{t_{ref,i}}^2}\left(\cosh\left(\frac{t_{ref}\langle|\chi_i| - K_i\rangle}{\mu_i}\right) - 1\right) \tag{A.30}$$

A.2.2 Standard derivation of incremental behaviour

Plastic strain increments are derived from Equation A.29:

$$d\dot{\boldsymbol{\alpha}} = \frac{d\boldsymbol{\alpha}}{dt} = \frac{\delta w}{\delta \boldsymbol{\chi}} \tag{A.31}$$

with incremental behaviour following Equations A.11 and A.10 (for stress control) or A.19 (for strain control) as per the rate-independent case.

For the example shown, Equation A.30 is combined with A.31 to give:

$$d\alpha_i = \frac{\delta w}{\delta \chi_i} dt = \frac{S(\chi_i)}{t_{ref,i}} \sinh\left(\frac{t_{ref}\langle|\chi_i| - K_i\rangle}{\mu_i}\right) dt \tag{A.32}$$

$$d\boldsymbol{\alpha} = \begin{bmatrix} d\alpha_1 \\ \vdots \\ d\alpha_{Ns} \end{bmatrix} \tag{A.33}$$

Clearly the implementation and derivation of rate-dependent models is much more straightforward than equivalent rate-independent cases. It is therefore often used even for rate-independent materials with arbitrarily low viscous parameters (Abadie, 2015). However, for stability, small steps are required and as such rate-independent models are much faster (Beuckelaers, 2017). Both are implemented in this thesis.

A.3 Derivatives for all presented models

Table A.1 presents required derivatives for incremental implementation of multi-surface kinematic hardening models. The table includes formulation in series and in parallel, for which the dissipative functions in both the rate-independent (RI) and rate-dependent (RPT) are the same. It must, however, be noted that the various parameters (e.g. K_i,H_i and α_i) take different meanings and therefore quantities, as discussed in detail in Chapter 5.

Table A.2 presents required derivatives for extended models which include an additional ratcheting unit (HARM models). Further model descriptions can be found in Sections 3.4.2.2 and 5.5. An additional internal strain parameter, α_r is included which controls an additional accumulated strain and is defined by the constraint:

$$c = \dot{\alpha}_r - S(\sigma) \sum_{i=1}^{N_s} R_i |\dot{\alpha}_i| = 0 \tag{A.34}$$

where R_i controls the rate of accumulation on each surface. α_r can simply be implemented as an additional internal parameter such that $N_{int} = N_s + 1$. Matrix sizes are therefore changed in line with Equations A.9 and A.8. Since σ now appears in the dissipation and yield functions not all RI derivatives are consistent between the two models. For clarity $E_0 = H_0 = \sigma_{i=1}^{Ns+1} H_i$ is used in the parallel cases.

Changes to yield strengths, either to model stiffness change (as per Section 5.4) or modified rate-dependency (as per Section 6.4.1) can be implemented within each increment simply by updating the values of K_i. Therefore energy functions and derivatives remain unchanged.

Asymmetry of strength was introduced in Section 3.2.2 and 5.2.1 in which the rate-independent dissipation function changed from Equation A.2 to:

$$d = \sum_{i=1}^{Ns} K_{n,c}\langle\dot{\alpha}_i\rangle + K_{n,e}\langle-\dot{\alpha}_i\rangle \tag{A.35}$$

This can be implemented in the derivatives in Tables A.1 and A.2 simply by changing:

$$|\chi_i| - K_i \rightarrow |\chi_i| - \mathcal{H}(\chi_i)K_{c,i} - \mathcal{H}(-\chi_i)K_{e,i} \tag{A.36}$$

where $\mathcal{H}(X)$ corresponds to the Heaviside step function.

A general algorithm structure may now be written which includes all features presented. An example is shown in Algorithm 1 which computes σ_{out} for n_{step} increments of ε (strain control), this is easily changed to stress control by swapping σ and ε, deriving the compliance matrix and changing respective equations as per Section A.1.2.2. Each step (j) is divided into further substeps, defined by n_{sub} which is particularly useful for rate-independent models (discussed in the following section). Strength changes, ratcheting variables and the hardening parameter are implemented incrementally. Each preceding model (with features switched off) can then be seen as a special case, defined by the careful specification of parameters.

A.3.1 Notes on rate dependent implementation

When using the rate-dependent formulation the algorithm requires small stress-steps to achieve convergence. The smaller the steps the higher the computational effort and therefore time. Efficient choice of steps size is therefore important to reduce computation time whilst retaining accuracy. Load histories tend have a fixed sample fixed frequency f_s, and therefore constant dt. By employing substeps, the model output remains similar to the input but changes may be made to ensure convergence; the number of substeps n_{sub} can be fixed or more efficiently decided by:

(i) **Set incremental maxima**: Such that 'steep' increases in stress are allowed smaller time steps than shallower sections where little is changing. This is depicted in Figure A.3a where :

$$n_{sub} = ceil\left(max\left(\frac{(\sigma_j - \sigma_{j-1})}{\sigma_{max}}, \frac{(t_j - t_{j-1})}{t_{max}}, 3\right)\right)$$

for strain control σ is replaced by ε. A minimum number of sub steps of 3 is defined such that this method may be used in conjunction with the next.

(ii) **Automated sub-stepping**: Assuming 3 subsets per increment, model stability can be checked. This is done by taking the two rolling products of the gradients of the previous three substeps (including those of the previous step):

$$P_1 = \frac{d\sigma_{j_{sub}-2}}{d\varepsilon_{j_{sub}-2}}.\frac{d\sigma_{j_{sub}-1}}{d\varepsilon_{j_{sub}-1}} \quad \text{and} \quad P_2 = \frac{d\sigma_{j_{sub}-1}}{d\varepsilon_{j_{sub}-1}}.\frac{d\sigma_{j_{sub}}}{d\varepsilon_{j_{sub}}}$$

If both are positive the model is stable and stress is increasing or decreasing. If one is positive and the other negative the model is stable and the stress has changed direction. However, if both are negative then the model is oscillating (as shown in Figure A.3b). The number of sub steps within that step can be increased and the section re-computed. Since this may include the previous, it is more robust to apply this method from the preceding step. This automated sub-stepping can increase computational efficiency considerably and can be used in conjunction with the previous method. A limit is required to ensure that tests which truly 'fail' (exceed final yield) do end.

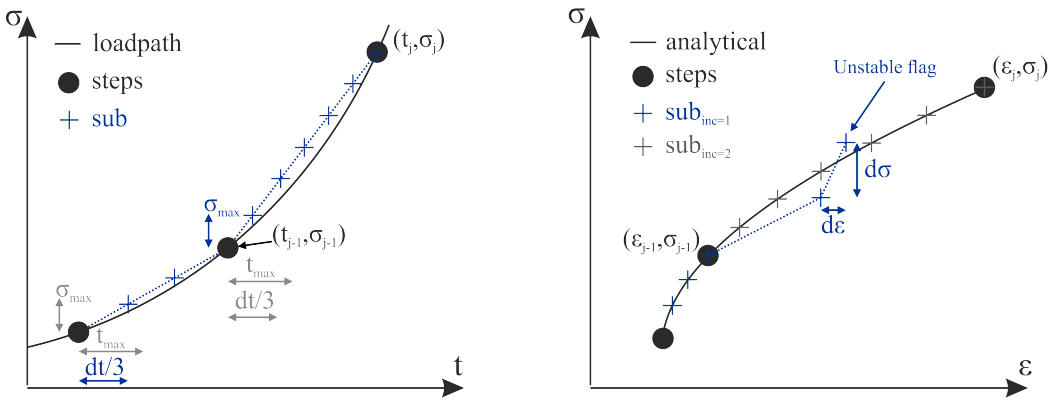

(a) **(b)**

Figure A.3: Incremental implementation for rate-dependent model with steps and substeps (a) substeps decided by predefined limits (b) substeps computed automatically to ensure stability

Algorithm 1: Example implementation of a general multi-surface kinematic hardening hyperplasticity model with stiffness changes and ratcheting

Data: $\boldsymbol{\varepsilon}$,$\boldsymbol{t}$,$\boldsymbol{K_0}$,$\boldsymbol{H}$,$\boldsymbol{C}$,n_{sub}
Result: $\boldsymbol{\sigma_{out}}$
Define: $f,\frac{\partial f^2}{\partial\varepsilon\partial\varepsilon},\frac{\partial f^2}{\partial\varepsilon\partial\boldsymbol{\alpha}},\frac{\partial f^2}{\partial\boldsymbol{\alpha}\partial\varepsilon},\frac{\partial f^2}{\partial\boldsymbol{\alpha}\partial\boldsymbol{\alpha}}$; // Table A.2
Initialise (zero): σ,$\boldsymbol{\alpha}$,$\boldsymbol{\chi}$,$\boldsymbol{\beta}$;
n_{step} =length($\boldsymbol{\varepsilon}$);
for $j = 2 : n_{step}$ **do**
  $d\varepsilon = (\varepsilon_j - \varepsilon_{j-1})/n_{sub}$;
  $dt = (t_j - t_{j-1})/n_{sub}$;
  for $j_{sub} = 1 : n_{sub}$ **do**
    $\boldsymbol{K}$=$\boldsymbol{K_0}f(\boldsymbol{\beta},\boldsymbol{C})$; // Update yield strengths (e.g. Equation 5.14)
    $\boldsymbol{R}$=$f(\boldsymbol{\beta},\sigma,\boldsymbol{C})$; // Update ratcheting variable (e.g. Equation 5.23)
    if *Rate Independent* **then**
      Update: $\boldsymbol{y},\frac{\partial\boldsymbol{y}}{\partial\boldsymbol{\chi}},\frac{\partial\boldsymbol{y}}{\partial\boldsymbol{\alpha}},\frac{\partial\boldsymbol{y}}{\partial\varepsilon}$; // Table A.2
      Solve: $\boldsymbol{\Lambda}$; // Equation A.16
      $d\boldsymbol{\alpha} = \boldsymbol{\Lambda}\frac{\partial\boldsymbol{y}}{\partial\boldsymbol{\chi}}$;
    else
      Update:$\frac{\delta w}{\delta\boldsymbol{\chi}}$; // Table A.2
      $d\boldsymbol{\alpha} = \frac{\delta w}{\delta\boldsymbol{\chi}}dt$;
    end
    Solve:$d\boldsymbol{\chi}$,$d\sigma$,$d\boldsymbol{\beta}$; // Equations A.11,A.10 and 5.4
    Update:$\boldsymbol{\alpha}$,$\boldsymbol{\chi}$,σ,$\boldsymbol{\beta}$
  end
  $\sigma_{out,j} = \sigma$; // Save output
end

Table A.1: Constitutive equations and required derivatives for rate-independent (RI) and rate-dependent (with Rate Process Theory RPT) multi-surface kinematic-hardening models formulated in parallel and series

		Parallel	Series
	f	$\sum_{i=1}^{Ns+1} \frac{H_i}{2}(\varepsilon-\alpha_i)^2 + \frac{H_{Ns+1}}{2}\varepsilon^2$	$\frac{H_0}{2}\left(\varepsilon - \sum_{i=1}^{Ns}\alpha_i\right)^2 + \sum_{i=1}^{Ns}\frac{H_i}{2}\alpha_i^2$
	$\frac{\partial^2 f}{\partial\varepsilon\partial\varepsilon}$	$\sum_{i=1}^{Ns} H_i$	H_0
	$\frac{\partial^2 f}{\partial\varepsilon\partial\boldsymbol{\alpha}}$	$\begin{bmatrix}-H_1 & -H_2 & \dots & -H_{Ns}\end{bmatrix}$	$\begin{bmatrix}-H_0 & -H_0 & \dots & -H_0\end{bmatrix}$
	$\frac{\partial^2 f}{\partial\boldsymbol{\alpha}\partial\varepsilon}$	$\begin{bmatrix}-H_1\\-H_2\\\vdots\\-H_{Ns}\end{bmatrix}$	$\begin{bmatrix}-H_0\\-H_0\\\vdots\\-H_0\end{bmatrix}$
	$\frac{\partial^2 f}{\partial\boldsymbol{\alpha}\partial\boldsymbol{\alpha}}$	$\begin{bmatrix}H_1 & 0 & \dots & 0\\0 & H_2 & \dots & 0\\\vdots & \vdots & \ddots & \vdots\\0 & 0 & \dots & H_{Ns}\end{bmatrix}$	$\begin{bmatrix}H_0+H_1 & H_0 & \dots & H_0\\H_0 & H_0+H_2 & \dots & H_0\\\vdots & \vdots & \ddots & \vdots\\H_0 & H_0 & \dots & H_0+H_{Ns}\end{bmatrix}$
RI	d	$\sum_{i=1}^{Ns} K_i\lvert\dot{\alpha}_i\rvert$	
	$\boldsymbol{y}$	$\begin{bmatrix}\lvert\chi_1\rvert - K_1\\\lvert\chi_2\rvert - K_2\\\vdots\\\lvert\chi_{Ns}\rvert - K_{Ns}\end{bmatrix}$	
	$\frac{\partial\boldsymbol{y}}{\partial x}$	$\frac{\partial\boldsymbol{y}}{\partial\boldsymbol{\chi}} = \begin{bmatrix}S(\chi_1) & 0 & \dots & 0\\0 & S(\chi_2) & \dots & 0\\\vdots & \vdots & \ddots & \vdots\\0 & 0 & \dots & S(\chi_{Ns})\end{bmatrix}$, $\frac{\partial\boldsymbol{y}}{\partial\varepsilon} = \begin{bmatrix}0\\0\\\vdots\\0\end{bmatrix}$, $\frac{\partial\boldsymbol{y}}{\partial\boldsymbol{\alpha}} = \begin{bmatrix}0 & 0 & \dots & 0\\0 & 0 & \dots & 0\\\vdots & \vdots & \ddots & \vdots\\0 & 0 & \dots & 0\end{bmatrix}$	
RPT	d	$\sum_{i=1}^{Ns} K_i\lvert\dot{\alpha}_i\rvert + \sum_{i=1}^{Ns}\frac{\mu_i}{t_{ref,i}}\dot{\alpha}_i \sinh^{-1}\left(\lvert\dot{\alpha}_i\rvert t_{ref,i}\right)$	
	w	$\sum_{i=1}^{Ns}\frac{\mu_i}{{t_{ref,i}}^2}\left(\cosh\left(\frac{t_{ref,i}\langle\lvert\chi_i\rvert-K_i\rangle}{\mu_i}\right)-1\right)$	
	$\frac{\partial w}{\partial\boldsymbol{\chi}}$	$\begin{bmatrix}\frac{S(\chi_1)}{t_{ref,1}}\sinh\left(\frac{t_{ref,1}\langle\lvert\chi_1\rvert-K_1\rangle}{\mu_i}\right)\\\frac{S(\chi_2)}{t_{ref,2}}\sinh\left(\frac{t_{ref,2}\langle\lvert\chi_2\rvert-K_2\rangle}{\mu_i}\right)\\\vdots\\\frac{S(\chi_{Ns})}{t_{ref,Ns}}\sinh\left(\frac{t_{ref,Ns}\langle\lvert\chi_{Ns}\rvert-K_{Ns}\rangle}{\mu_i}\right)\end{bmatrix}$	

Table A.2: Constitutive equations and required derivatives for rate-independent (RI) and rate-dependent (with Rate Process Theory RPT) multi-surface kinematic-hardening HARM models formulated in parallel. Here $\alpha_r = \alpha_{Ns+1}$ and in the parallel model $H_0 = \sum_{i=1}^{Ns+1} H_i$

		Parallel	Series
	f	$\sum_{i=1}^{Ns} \frac{H_i}{2}(\varepsilon - \alpha_i - \alpha_r)^2 + \frac{H_{Ns+1}}{2}(\varepsilon - \alpha_r)^2$	$\frac{H_0}{2}\left(\varepsilon - \sum_{i=1}^{Ns}\alpha_i - \alpha_r\right)^2 + \sum_{i=1}^{Ns}\frac{H_i}{2}\alpha_i^2$
	$\sigma = \frac{\partial f}{\partial \varepsilon}$	$H_0(\varepsilon - \alpha_r) - \sum_{i=1}^{Ns} H_i(\alpha_i)$	$H_0\left(\varepsilon - \sum_{i=1}^{Ns}\alpha_i - \alpha_r\right)$
	$\frac{\partial^2 f}{\partial \varepsilon \partial \varepsilon}$	$\sum_{i=1}^{Ns+1} H_i = H_0$	H_0
	$\frac{\partial^2 f}{\partial \varepsilon \partial \boldsymbol{\alpha}}$	$\begin{bmatrix} -H_1 & -H_2 & \dots & -H_{Ns} & -H_0 \end{bmatrix}$	$\begin{bmatrix} -H_0 & -H_0 & \dots & -H_0 & -H_0 \end{bmatrix}$
	$\frac{\partial^2 f}{\partial \boldsymbol{\alpha} \partial \varepsilon}$	$\begin{bmatrix} -H_1 \\ -H_2 \\ \vdots \\ -H_{Ns} \\ -H_0 \end{bmatrix}$	$\begin{bmatrix} -H_0 \\ -H_0 \\ \vdots \\ -H_0 \\ -H_0 \end{bmatrix}$
	$\frac{\partial^2 f}{\partial \boldsymbol{\alpha} \partial \boldsymbol{\alpha}}$	$\begin{bmatrix} H_1 & 0 & \dots & 0 & H_1 \\ 0 & H_2 & \dots & 0 & H_2 \\ \vdots & \vdots & \ddots & \vdots & \vdots \\ 0 & 0 & \dots & H_{Ns} & H_{Ns} \\ H_1 & H_2 & \dots & H_{Ns} & H_0 \end{bmatrix}$	$\begin{bmatrix} H_0 + H_1 & H_0 & \dots & H_0 & H_0 \\ H_0 & H_0 + H_2 & \dots & H_0 & H_0 \\ \vdots & \vdots & \ddots & \vdots & \vdots \\ H_0 & H_0 & \dots & H_0 + H_{Ns} & H_0 \\ H_0 & H_0 & \dots & H_0 & H_0 \end{bmatrix}$
RI	d	$\sum_{i=1}^{Ns} K_i\lvert\dot{\alpha}_i\rvert + \sigma\dot{\alpha}_r$	
	$\boldsymbol{y}$	$\begin{bmatrix} \lvert\chi_1\rvert - K_1 + R_1(\lvert\chi_r\rvert - \lvert\sigma\rvert) \\ \lvert\chi_2\rvert - K_2 + R_2(\lvert\chi_r\rvert - \lvert\sigma\rvert) \\ \vdots \\ \lvert\chi_{Ns}\rvert - K_{Ns} + R_{Ns}(\lvert\chi_r\rvert - \lvert\sigma\rvert) \end{bmatrix}$	
	$\frac{\partial \boldsymbol{y}}{\partial \boldsymbol{\chi}}$	$\begin{bmatrix} S(\chi_1) & 0 & \dots & 0 & R_1 S(\chi_r) \\ 0 & S(\chi_2) & \dots & 0 & R_2 S(\chi_r) \\ \vdots & \vdots & \ddots & \vdots & \vdots \\ 0 & 0 & \dots & S(\chi_{Ns}) & R_{Ns} S(\chi_r) \end{bmatrix}$	
	$\frac{\partial \boldsymbol{y}}{\partial \varepsilon}$	$\begin{bmatrix} -R_1 H_0 S(\sigma) \\ -R_2 H_0 S(\sigma) \\ \vdots \\ -R_{Ns} H_0 S(\sigma) \end{bmatrix}$	
	$\frac{\partial \boldsymbol{y}}{\partial \boldsymbol{\alpha}}$ PAR	$\begin{bmatrix} R_1 H_1 S(\sigma) & 0 & \dots & 0 & R_1 H_0 S(\sigma) \\ 0 & R_2 H_2 S(\sigma) & \dots & 0 & R_2 H_0 S(\sigma) \\ \vdots & \vdots & \ddots & \vdots & \vdots \\ 0 & 0 & \dots & R_{Ns} H_{Ns} S(\sigma) & R_{Ns} H_0 S(\sigma) \end{bmatrix}$	
	$\frac{\partial \boldsymbol{y}}{\partial \boldsymbol{\alpha}}$ SER	$\begin{bmatrix} R_1 H_0 S(\sigma) & 0 & \dots & 0 & R_1 H_0 S(\sigma) \\ 0 & R_2 H_0 S(\sigma) & \dots & 0 & R_2 H_0 S(\sigma) \\ \vdots & \vdots & \ddots & \vdots & \vdots \\ 0 & 0 & \dots & R_{Ns} H_0 S(\sigma) & R_{Ns} H_0 S(\sigma) \end{bmatrix}$	
RPT	d	$\sum_{i=1}^{Ns} K_i\lvert\dot{\alpha}_i\rvert + \sum_{i=1}^{Ns} \frac{\mu_i}{t_{ref,i}}\dot{\alpha}_i \sinh^{-1}\left(\lvert\dot{\alpha}_i\rvert t_{ref,i}\right) + \sigma\dot{\alpha}_r$	
	w	$\sum_{i=1}^{Ns} \frac{\mu_i}{{t_{ref,i}}^2}\left(\cosh\left(\frac{t_{ref,i}\langle\lvert\chi_i\rvert - K_i + R_i(\lvert\chi_r\rvert - \lvert\sigma\rvert)\rangle}{\mu_i}\right) - 1\right)$	
	$\frac{\partial w}{\partial \boldsymbol{\chi}}$	$\begin{bmatrix} \frac{S(\chi_1)}{t_{ref,1}} \sinh\left(\frac{t_{ref,1}\langle\lvert\chi_1\rvert - K_1 + R_1(\lvert\chi_r\rvert - \lvert\sigma\rvert)\rangle}{\mu_i}\right) \\ \frac{S(\chi_2)}{t_{ref,2}} \sinh\left(\frac{t_{ref,2}\langle\lvert\chi_2\rvert - K_2 + R_2(\lvert\chi_r\rvert - \lvert\sigma\rvert)\rangle}{\mu_i}\right) \\ \vdots \\ \frac{S(\chi_{Ns})}{t_{ref,Ns}} \sinh\left(\frac{t_{ref,Ns}\langle\lvert\chi_{Ns}\rvert - K_{Ns} + R_{Ns}(\lvert\chi_r\rvert - \lvert\sigma\rvert)\rangle}{\mu_i}\right) \end{bmatrix}$	

A.4 Notes on MCC model

Here incremental derivation of a Modified Cam Clay model, as presented in Chapter 7, is shown. Firstly as a single surface model with and without rate dependency and then extension of the rate dependent model to multiple surfaces. A key difference is that two stress quantities are specified (p, q) with conjugate strains $(\varepsilon_v, \varepsilon_q)$. Effectively this follows the previous section with $N_{int} = 2$ and $N_s = 1$. Incremental behaviour is derived with stress and strain control, such that drained and undrained tests are easily specified.

A.4.1 Single surface

In general terms, the model is specified by:

$$f = f(\boldsymbol{\varepsilon}, \boldsymbol{\alpha}), \quad y = f(\boldsymbol{\chi}, \boldsymbol{\varepsilon}, \boldsymbol{\alpha}) \quad or \quad w = f(\boldsymbol{\chi}, \boldsymbol{\varepsilon}, \boldsymbol{\alpha}) \tag{A.37}$$

and:

$$\boldsymbol{\varepsilon} = \begin{bmatrix} \varepsilon_v \\ \varepsilon_q \end{bmatrix}, \quad \boldsymbol{\alpha} = \begin{bmatrix} \alpha_v \\ \alpha_q \end{bmatrix}, \quad \boldsymbol{\sigma} = \begin{bmatrix} p = \frac{\partial f}{\partial \varepsilon_v} \\ q = \frac{\partial f}{\partial \varepsilon_q} \end{bmatrix}, \quad \boldsymbol{\chi} = \begin{bmatrix} \chi_v = \frac{-\partial f}{\partial \alpha_v} \\ \chi_q = \frac{-\partial f}{\partial \alpha_q} \end{bmatrix} \tag{A.38}$$

such that incremental response is derived as:

$$d\boldsymbol{\sigma} = \frac{\partial^2 f}{\partial \boldsymbol{\varepsilon} \partial \boldsymbol{\varepsilon}} d\boldsymbol{\varepsilon} + \frac{\partial^2 f}{\partial \boldsymbol{\varepsilon} \partial \boldsymbol{\alpha}} d\boldsymbol{\alpha} \tag{A.39}$$

$$d\boldsymbol{\chi} = -\frac{\partial^2 f}{\partial \boldsymbol{\alpha} \partial \boldsymbol{\varepsilon}} d\boldsymbol{\varepsilon} - \frac{\partial^2 f}{\partial \boldsymbol{\alpha} \partial \boldsymbol{\alpha}} d\boldsymbol{\alpha} \tag{A.40}$$

A general control statement is assumed of the form:

$$\boldsymbol{S} d\boldsymbol{\sigma} + \boldsymbol{E} d\boldsymbol{\varepsilon} = \boldsymbol{T} dt \tag{A.41}$$

where

$$\boldsymbol{S} = \begin{bmatrix} S_{1,1} & S_{1,2} \\ S_{2,1} & S_{2,2} \end{bmatrix}, \quad \boldsymbol{E} = \begin{bmatrix} E_{1,1} & E_{1,2} \\ E_{2,1} & E_{2,2} \end{bmatrix} \quad \boldsymbol{T} = \begin{bmatrix} T_1 \\ T_2 \end{bmatrix} \tag{A.42}$$

Equation A.39 is substituted into A.41 and rearranged to give:

$$\begin{aligned} \boldsymbol{S}\left(\frac{\partial^2 f}{\partial \boldsymbol{\varepsilon} \partial \boldsymbol{\varepsilon}} d\boldsymbol{\varepsilon} + \frac{\partial^2 f}{\partial \boldsymbol{\varepsilon} \partial \boldsymbol{\alpha}} d\boldsymbol{\alpha} \right) + E d\boldsymbol{\varepsilon} = T dt \\ d\boldsymbol{\varepsilon} = P\left(T dt - S \frac{\partial^2 f}{\partial \boldsymbol{\varepsilon} \partial \boldsymbol{\alpha}} d\boldsymbol{\alpha} \right) \end{aligned} \tag{A.43}$$

where

$$\boldsymbol{P} = \left(\boldsymbol{E} + \boldsymbol{S} \frac{\partial^2 f}{\partial \boldsymbol{\varepsilon} \partial \boldsymbol{\varepsilon}} \right)^{-1} \tag{A.44}$$

If y is known and a rate independent model is specified, the consistency condition and flow rule at yield can be written:

$$dy = -ay = \frac{\partial y}{\partial \boldsymbol{\chi}} d\boldsymbol{\chi} + \frac{\partial y}{\partial \boldsymbol{\varepsilon}} d\boldsymbol{\varepsilon} + \frac{\partial y}{\partial \boldsymbol{\alpha}} d\boldsymbol{\alpha} \tag{A.45}$$

$$d\boldsymbol{\alpha} = \left(\Lambda \frac{\partial y}{\partial \boldsymbol{\chi}} \right)^T = \frac{\partial y}{\partial \boldsymbol{\chi}}^T \Lambda \tag{A.46}$$

where a is a factor between 0 and 1 which ensures numerical stability if yield is exceeded (typically taken as 0.5). Λ is an arbitrary non-negative multiplier which is found by substituting equations A.40, A.46 and A.43 into A.45 and solving as a function of modified control statement parameters $\boldsymbol{P}, \boldsymbol{S}, \boldsymbol{T}$:

$$\left(\left(\frac{\partial y}{\partial \boldsymbol{\varepsilon}} - \frac{\partial y}{\partial \boldsymbol{\chi}} \frac{\partial^2 f}{\partial \boldsymbol{\varepsilon} \partial \boldsymbol{\alpha}} \right) \boldsymbol{P}.\boldsymbol{S} \frac{\partial^2 f}{\partial \boldsymbol{\varepsilon} \partial \boldsymbol{\alpha}} - \left(\frac{\partial y}{\partial \boldsymbol{\alpha}} - \frac{\partial y}{\partial \boldsymbol{\chi}} \frac{\partial y}{\partial \boldsymbol{\alpha}} d\boldsymbol{\alpha} \right) \right) \frac{\partial y}{\partial \boldsymbol{\chi}}^T \Lambda = a.y + \left(\frac{\partial y}{\partial \boldsymbol{\varepsilon}} - \frac{\partial y}{\partial \boldsymbol{\chi}} \frac{\partial^2 f}{\partial \boldsymbol{\varepsilon} \partial \boldsymbol{\alpha}} \right) \boldsymbol{P}.\boldsymbol{T} dt \tag{A.47}$$

With Λ found, plastic strain increments are found following Equation A.46.

If w is known and a rate-dependent model specified, plastic strain increments are derived from Equation A.29, such that:

$$d\dot{\boldsymbol{\alpha}} = \frac{d\boldsymbol{\alpha}}{dt} = \frac{\delta w}{\delta \boldsymbol{\chi}} \tag{A.48}$$

The remaining incremental behaviour (Equations A.40, A.43 and A.39) can then be computed. All required derivatives are specified in Table A.3.

A.4.2 Multiple surfaces - rate dependent

In Section 7.4 multiple versions of the single surface model are employed in which some property is varied and each is subject to a weighting factor Ω_i, where i indicates surface number from 1 to the number of surfaces N_s. The energy function and flow potential can then be written:

$$f = \sum_{i=1}^{Ns} \Omega_i f_i, \quad w = \sum_{i=1}^{Ns} \Omega_i w_i \tag{A.49}$$

and:

$$\boldsymbol{\varepsilon} = \begin{bmatrix} \varepsilon_v \\ \varepsilon_q \end{bmatrix}, \quad \boldsymbol{\alpha_i} = \begin{bmatrix} \alpha_{v,i} \\ \alpha_{q,i} \end{bmatrix}, \quad \boldsymbol{\sigma} = \begin{bmatrix} p = \frac{\partial f}{\partial \varepsilon_p} \\ q = \frac{\partial f}{\partial \varepsilon_q} \end{bmatrix}, \quad \boldsymbol{\chi_i} = \begin{bmatrix} \chi_{v,i} = \Omega_i \frac{-\partial f_i}{\partial \alpha_{v,i}} \\ \chi_{q,i} = \Omega_i \frac{-\partial f_i}{\partial \alpha_{q,i}} \end{bmatrix} \tag{A.50}$$

such that local incremental response is derived as:

$$d\dot{\boldsymbol{\alpha}}_{\boldsymbol{i}} = \frac{d\boldsymbol{\alpha_i}}{dt} = \frac{\delta w_i}{\delta \boldsymbol{\chi_i}}, \quad d\boldsymbol{\chi_i} = -\Omega_i \frac{\partial^2 f_i}{\partial \boldsymbol{\alpha_i} \partial \boldsymbol{\varepsilon}} d\boldsymbol{\varepsilon} - \Omega_i \frac{\partial^2 f_i}{\partial \boldsymbol{\alpha_i} \partial \boldsymbol{\alpha_i}} d\boldsymbol{\alpha_i} \tag{A.51}$$

and global incremental response:

$$d\boldsymbol{\sigma} = \sum_{i=1}^{Ns} \left(\Omega_i \frac{\partial^2 f_i}{\partial \boldsymbol{\varepsilon} \partial \boldsymbol{\varepsilon}} d\boldsymbol{\varepsilon} + \Omega_i \frac{\partial^2 f_i}{\partial \boldsymbol{\varepsilon} \partial \boldsymbol{\alpha_i}} d\boldsymbol{\alpha_i} \right), \quad d\boldsymbol{\varepsilon} = \sum_{i=1}^{Ns} \left(\boldsymbol{P}_i \left(\boldsymbol{T} dt - \boldsymbol{S} \Omega_i \frac{\partial^2 f_i}{\partial \boldsymbol{\varepsilon} \partial \boldsymbol{\alpha_i}} d\boldsymbol{\alpha_i} \right) \right) \tag{A.52}$$

where

$$\boldsymbol{P}_i = \left(\boldsymbol{E} + \boldsymbol{S} \Omega_i \frac{\partial^2 f_i}{\partial \boldsymbol{\varepsilon} \partial \boldsymbol{\varepsilon}} \right)^{-1} \tag{A.53}$$

Derivatives for each surface i remain as defined in Table A.3 with some locally varying properties. In Section 7.4 this was κ^* but it is deliberately left general here.

Table A.3: Constitutive equations and required derivatives for single surface rate-independent (RI) and rate-dependent (with Rate Process Theory RPT) Modified Cam Clay (MCC) model. These may also be applied to the mulit-surface model for each local surface

		MCC
	f	$p_r\kappa^* exp\left(\frac{1}{\kappa^*}\left(\varepsilon_v-\alpha_v\right)+\frac{3g}{2\kappa^*}\left(\varepsilon_q-\alpha_q\right)^2\right)$
	$\frac{\partial f}{\partial \boldsymbol{\varepsilon}}$	$\begin{bmatrix}p\\q\end{bmatrix}=\begin{bmatrix}p_r exp\left(\frac{1}{\kappa^*}\left(\varepsilon_v-\alpha_v\right)+\frac{3g}{2\kappa^*}\left(\varepsilon_q-\alpha_q\right)^2\right)\\3g(\varepsilon_q-\alpha_q)p_r exp\left(\frac{1}{\kappa^*}\left(\varepsilon_v-\alpha_v\right)+\frac{3g}{2\kappa^*}\left(\varepsilon_q-\alpha_q\right)^2\right)=3gp(\varepsilon_q-\alpha_q)\end{bmatrix}$
	$\frac{\partial f}{\partial \boldsymbol{\alpha}}$	$\begin{bmatrix}-\chi_p\\-\chi_q\end{bmatrix}=\begin{bmatrix}-p_r exp\left(\frac{1}{\kappa^*}\left(\varepsilon_v-\alpha_v\right)+\frac{3g}{2\kappa^*}\left(\varepsilon_q-\alpha_q\right)^2\right)=-p\\-3g(\varepsilon_q-\alpha_q)p_r exp\left(\frac{1}{\kappa^*}\left(\varepsilon_v-\alpha_v\right)+\frac{3g}{2\kappa^*}\left(\varepsilon_q-\alpha_q\right)^2\right)=-q\end{bmatrix}$
	$\frac{\partial^2 f}{\partial a\partial b}$	$\frac{\partial^2 f}{\partial \boldsymbol{\varepsilon}\partial \boldsymbol{\varepsilon}}=\frac{\partial^2 f}{\partial \boldsymbol{\alpha}\partial \boldsymbol{\alpha}}=\begin{bmatrix}\frac{p}{\kappa^*} & \frac{q}{\kappa^*}\\ \frac{q}{\kappa^*} & \frac{q^2}{\kappa^* p}+3gp\end{bmatrix}$, $\frac{\partial^2 f}{\partial \boldsymbol{\varepsilon}\partial \boldsymbol{\alpha}}=\frac{\partial^2 f}{\partial \boldsymbol{\alpha}\partial \boldsymbol{\varepsilon}}=\begin{bmatrix}-\frac{p}{\kappa^*} & -\frac{q}{\kappa^*}\\ -\frac{q}{\kappa^*} & -\frac{q^2}{\kappa^* p}-3gp\end{bmatrix}$
RI	d	$p_x\left(\dot{\alpha_v}+\sqrt{\dot{\alpha_v}^2+M^2\dot{\alpha_q}^2}\right)$
	y	$(\chi_p-p_x)^2+\left(\frac{\chi_q}{M}\right)^2-p_x^2$
	p_x	$\frac{p_r}{2}exp\left(\frac{\alpha_v}{\lambda^*-\kappa^*}\right)$
	$\frac{\partial \boldsymbol{y}}{\partial a}$	$\frac{\partial \boldsymbol{y}}{\partial \boldsymbol{\chi}}=\begin{bmatrix}2(\chi_p-p_x)\\ \frac{2\chi_q}{M^2}\end{bmatrix}$, $\frac{\partial \boldsymbol{y}}{\partial \boldsymbol{\varepsilon}}=\begin{bmatrix}0\\0\end{bmatrix}$, $\frac{\partial \boldsymbol{y}}{\partial \boldsymbol{\alpha}}=\begin{bmatrix}-\chi_p(\lambda^*-\kappa^*)2p_x\\0\end{bmatrix}$
RPT	w	$\frac{p_c\eta}{t_{ref}}\left(\cosh\left(\frac{\langle\sqrt{x}-p_x\rangle}{p_c\eta}\right)-1\right)$
	x	$(\chi_p-p_x)^2+\frac{\chi_q}{M}^2$
	$\frac{\partial w}{\partial \boldsymbol{\chi}}$	$\begin{bmatrix}\frac{1}{t_{ref}}\sinh\left(\frac{\langle\sqrt{x}-p_x\rangle}{p_c\eta}\right)\left(\frac{\chi_p-p_x}{x^{0.5}}\right)\\ \frac{1}{t_{ref}}\sinh\left(\frac{\langle\sqrt{x}-p_x\rangle}{p_c\eta}\right)\left(\frac{\chi_q}{M^2x^{0.5}}\right)\end{bmatrix}$